

A multifaceted investigation of tris(2-phenylpyridine)iridium

by

Jordan R. Fine

A Dissertation Presented to the
FACULTY OF THE USC GRADUATE SCHOOL
UNIVERSITY OF SOUTHERN CALIFORNIA
In Partial Fulfillment of the
Requirements for the Degree
DOCTOR OF PHILOSOPHY
(CHEMISTRY)

October 2012

Copyright 2012

Jordan R. Fine

DEDICATION

To my wife Lydia for her love and devotion

To my mother Sherri for pushing me to achieve what she knew I could

And my puppies for showing me what unconditional love is

ACKNOWLEDGMENTS

To be sure I would not have been as successful in my graduate career had it not been for the help and guidance of my family, friends, and coworkers.

I am forever indebted to my advisor Curt Wittig. Many people in the chemical physics community know that Curt is a talented and insightful scientist. But, Curt is also a generous and thoughtful individual. He has impressed to me that he cares about me and my future. There were times when Curt would push me to excel, whether I wanted to or not. But, I know it was because he wanted me to accomplish what was within my potential. I could not have asked for a better mentor.

I would like to thank Professors Andre Vilesov, Hanna Reisler, Anna Krylov, Steve Bradforth, and Vitaly Kresin. I am fortunate to have learned from their teaching and guidance. I hold each of them in high regard.

I was very blessed to have worked alongside so many wonderful people. Among these are Dr. Christopher Nemirow, Dr. Zhou Lu, Dr. Oscar Robolledo-Mayoral, Jamie Stomberg, Stephanie McKean, Lee Ch'ng, Dr. Chirantha Rodrigo, Dr. Russell Sliter, Dr. Luis Gomez, Dr. Sergey Malyk, Anton Zadorozhnyy and Bill Schroeder. I am happy to know each and every one of you. Thank you for making graduate school such a great experience.

I would also like to thank the staff of the USC Chemistry Department and the USC Machine shop. You were instrumental in my success and I am extremely grateful for all of your hard work.

Finally, I want to thank my family. Graduate school and life in general would be much harder if I did not have your love and support. I hope you know how much you all mean to me.

TABLE OF CONTENTS

Dedication	ii
Acknowledgments	iii
List of Tables	vii
List of Figures	ix
Abstract	xxi
Chapter 1: Introduction	1
1.1 Chapter contents	3
1.2 References	8
Chapter 2: Experimental techniques	10
2.1 Photoionization	10
2.1.1 Stepwise ionization spectroscopy	13
2.1.2 Fragmentation	17
2.2 Time-of-flight mass spectrometry	19
2.2.1 Overview	19
2.2.2 Resolution	22
2.3 Gas phase UV-Vis absorption spectroscopy of room temperature solids	24
2.4 Helium droplet matrix isolation	30
2.4.1 Helium droplet production and characteristics	31
2.4.2 Pulsed Helium Droplet Production	34
2.4.3 The pick-up process	35
2.5 Electron impact ionization	36
2.5.1 Interpretation of σ_{\max}	38
2.6 Production and detection of the ethynyl radical	40
2.6.1 Experiments and results	44
2.6.2 Discussion	53
2.6.3 Conclusion	55
2.7 References	56
Chapter 3: Photoionization of tris(2-phenylpyridine)iridium	64
3.1 Introduction	64
3.2 Experimental methods and results	73
3.2.1 Multiphoton ionization	78
3.2.2 Two-photon ionization	82
3.2.3 One-photon ionization	88
3.3 Discussion	88
3.3.1 Low-lying electronically excited states	90
3.3.2 Photoionization	96
3.3.3 Ion yield spectrum	99

3.3.4	Disposition of vibrational energy	100
3.3.5	Comparison with electronic structure theory and previous work	102
3.4	Summary	106
3.5	References	108
Chapter 4: Electronic structure of tris(2-phenylpyridin)iridium: electronically excited and ionized states		112
4.1	Introduction	112
4.2	Computational details	115
4.3	Results and discussion	117
4.3.1	Equilibrium structures	118
4.3.2	Molecular orbitals	125
4.3.3	Ultraviolet absorption spectrum	132
4.3.4	Phosphorescence from T ₁	137
4.3.5	Vibrational energy distribution	138
4.4	Summary	143
4.5	References	146
Chapter 5: Investigation of He₄⁺ formation via electron impact and the photoionization of tris(2-phenylpyridine)iridium in helium droplets		149
5.1	Introduction	149
5.2	Experimental	150
5.3	Results and discussion	152
5.3.1	Droplet sizes	153
5.3.2	Pulse profile	158
5.3.3	Current Dependence	161
5.3.4	Electron energy dependence	162
5.3.5	Pulse duration dependence	164
5.3.6	Photoionization of tris(2-phenylpyridine)iridium in helium droplets	170
5.4	References	177
Chapter 6: Future Work		179
6.1	Introduction	179
6.2	Experimental	180
6.3	Discussion	184
6.4	References	186
Bibliography		187
Appendices		200
Appendix A: A brief introduction to density functional theory		200
Appendix B: Supplementary Material for Chapter 4		206
Appendices References		242

LIST OF TABLES

Table 2.1	Ionization potential and C–H bond energy for acetylene and the ethynyl radical. The 193.3 nm absorption cross-section of acetylene is for room temperature.	45
Table 3.1	Bond lengths (Å) for S_0 , T_1 , and D_0 states of $\text{Ir}(\text{ppy})_3$.	103
Table 4.1	Bond lengths (Å) for S_0 , T_1 , and D_0 states of $\text{Ir}(\text{ppy})_3$.	119
Table 4.2	Bond lengths (Å) for S_0 and D_0 <i>mer</i> - $\text{Ir}(\text{ppy})_3$.	121
Table 4.3	Koopmans IE's (eV) for the six highest energy occupied MO's of <i>fac</i> - $\text{Ir}(\text{ppy})_3$.	125
Table 4.4	BNL percent spin density for <i>fac</i> - $\text{Ir}(\text{ppy})_3$ at the S_0 , T_1 , and D_0 equilibrium geometries. For T_1 and D_0 , only the main contributions are listed.	126
Table 4.5	Vertical and adiabatic IE's (eV) for <i>fac</i> - $\text{Ir}(\text{ppy})_3$ from S_0 and T_1 states at their equilibrium geometries	131
Table 4.6	Orbital character and leading amplitude for the four lowest energy triplet states at the S_0 and T_1 equilibrium geometries: Energies are relative to that of S_0 at its equilibrium geometry.	133
Table 4.7	Orbital character and leading amplitude for the three lowest energy singlet excited states at the S_0 and T_1 equilibrium geometries. Energies are relative to that of S_0 at its equilibrium geometry.	134
Table 5.1	$\text{Ir}(\text{ppy})_3$ vapor pressure vs. temperature	174
Table B.1	Z-matrix for S_0 equilibrium geometry	207
Table B.2	S_0 Standard Nuclear Orientation (Å)	209
Table B.3	Z-matrix for T_1 equilibrium geometry	211
Table B.4	T_1 Standard Nuclear Orientation (Å)	213
Table B.5	Z-matrix for D_0 equilibrium geometry	215

Table B.6	D ₀ Standard Nuclear Orientation (Å)	217
Table B.7	Shell populations of first six HOMO's at S ₀ equilibrium geometry	219
Table B.8	Mulliken charges and spin density the S ₀ equilibrium geometry	225
Table B.9	Mulliken charges and spin density the T ₁ equilibrium geometry	227
Table B.10	Mulliken charges and spin density the D ₀ equilibrium geometry	229
Table B.11	BNL TDDFT excited states – S ₀ equilibrium geometry	231
Table B.12	ωB97X TDDFT excited states – S ₀ equilibrium geometry	235
Table B.13	Calculated vibrational frequencies for the S ₀ geometry. B3LYP – lanl2dz for Ir, 6-31+G* for all other atoms	237

LIST OF FIGURES

- Figure 1.1** Ground electronic state structure for Ir(ppy)₃'s most stable isomer (*fac*-Ir(ppy)₃). H atoms are omitted for clarity. Color scheme: green = Ir; blue = N; gray = C. 1
- Figure 1.2** The diagram illustrates the effect of triplet harvesting. In organometallic compounds with transition metal centers, such as Ir(ppy)₃, excited singlet states relax to a low lying singlet state where they show a fast intersystem crossing (ISC) to the lowest triplet state (T₁). On the other hand, excited triplets states simply trickle down the triplet manifold to the lowest triplet state. Thus, T₁ harvests both singlet and triplet excitation energy and can efficiently emit. In principle, a triplet emitter can — in the limit of vanishing radiationless decay — exhibit 100% luminescence quantum efficiency. 2
- Figure 2.1** Three possible multiphoton excitation schemes are shown above. (a) One-color multiphoton ionization resonance enhanced at the initial transition. (b) A double resonance variant of REMPI; ν_1 is fixed to resonantly enhance the initial two-photon transition while ν_2 is scanned to probe the spectroscopy of the second transition. (c) Two-color multistep photoionization is shown, where ν_1 is fixed and ν_2 is scanned to reveal the various ionization thresholds. 12
- Figure 2.2** Schematic representing a stepwise one-color two-photon photoionization pathway. $|0\rangle$ represents the ground state, $|1\rangle$ is a real intermediate absorbing state, and $|2\rangle$ is a state that lies above the ionization energy. The absorption cross-sections for transition $|1\rangle \leftarrow |0\rangle$ and $|2\rangle \leftarrow |1\rangle$ are σ_1 and σ_2 , respectively. The photon energy ($h\nu$) is considered much larger than the thermal energy ($k_B T$). 14
- Figure 2.3** Depiction of two fragmentation schemes of multistep ionization. (a) Continued absorption by the parent ion opens up a variety of dissociation channels, which can eventually lead to atomization. (b) Dissociation of the intermediate state will lead to neutral fragments that can be ionized and/or dissociate further. 18

- Figure 2.4** Schematic of a basic TOF system. The interaction region has a height of $2s$ and is between the repeller and extractor plates, which hold voltages V_1 and V_2 , respectively. A second acceleration region is above the interaction region and has a height of d . The field free region allows the accelerated ions of different mass time to separate. Ions that collide with the micro-channel plate detector (MCP) cause a cascade of electrons creating a small current, which is detected by an oscilloscope monitoring the MCP. 20
- Figure 2.5** Diagram showing the origin of the decreased TOF mass resolution as a result of the initial kinetic energy distribution U_0 . (a) Two identical particles with translational energy U_0 but in opposite directions are shown. A is moving away from the detector, B is moving toward the detector. (b) The applied field must counter the initial kinetic energy of A causing it to reverse direction and return to its initial position with energy U_0 towards the detector, whereas B is simply accelerated toward the detector. 23
- Figure 2.6** Basic operation of a standard spectrophotometer. A tungsten lamp generates a continuous white light source that is collimated and passes through the absorbing medium. The transmitted light is then scattered using a rotatable grating and slowly passed over a photodetector. Current generated from the transmitted light striking the detector is sent to a recorder that displays the resultant spectrum. 26
- Figure 2.7** A plot of the $\text{Ir}(\text{ppy})_3$ vapor pressure vs. temperature. 28
- Figure 2.8** Depiction of the (a) UV-Vis vacuum cell, (b) and copper sleeve with end caps. The $\text{Ir}(\text{ppy})_3$ must be added to the cell prior to evacuation. After the cell has been thoroughly pumped, the side port is sealed and the cell is inserted into the sleeve in the order indicated in (c). 29
- Figure 2.9** Plot of the gas phase $\text{Ir}(\text{ppy})_3$ absorption spectrum at $270\text{ }^\circ\text{C}$. 30
- Figure 2.10** The pressure-temperature phase diagram for ^4He . Dashed lines show typical trajectories for supercritical (upper) and subcritical (lower) expansion isentropes. 32

- Figure 2.11** Average number of helium atoms per droplet for various backing pressure and nozzle temperatures. The right axis corresponds to the average droplet diameter under the same expansion conditions. Images of the subcritical (lower) and supercritical (upper) expansions are shown. 33
- Figure 2.12** The total absolute cross-sections for (a) helium and (b) acetylene along with their corresponding theoretical fit calculated using the BEB method. The electron energy at the point of maximum cross-section is displayed for both experiment and BEB. 37
- Figure 2.13** Image showing how the polarizability volume acts as an effective cross-section for the process of an incoming electron ejecting a bound electron from a target species. 38
- Figure 2.14** Schematic representation of the potential energy surfaces involved in the 193.3 nm photodissociation of acetylene. Formation of excited C_2H ($A^2\Pi$) occurs via two possible routes: (a) tunneling to the continuum through the potential barrier on the A^1A'' curve and/or (b) through internal conversion to the dissociative $2^1A'$ state. Formation of vibrationally excited C_2H ($X^2\Sigma^+$) occurs by (c) internal conversion to the $2^1A'$ state followed by subsequent diabatic surface hopping to the $1^1A'$ state at the $2^1A'/1^1A'$ avoided crossing. 42
- Figure 2.15** Calculated adiabatic potential energy curves for the lowest $^2\Sigma^+$ and $^2\Pi$ states of C_2H as functions of the C–H bond length. Full lines represent Σ^+ symmetry, and dashed lines Π symmetry. 43
- Figure 2.16** Experimental apparatus used for acetylene photolysis. The base pressures were, 2×10^{-6} (torr) in the expansion chamber, 10^{-7} (torr) in the interaction chamber (where the gas was ionized), and 10^{-8} (torr) at the MCP detector. The total length of the TOF was 1 m and voltages of 1500, 1350, and -3500 were used for the repeller, extractor and MCP bias, respectively. The nozzle was set approximately 2 cm away from a 1 mm diameter skimmer and ~ 15 cm away from the interaction region of the TOF. 45

- Figure 2.17** Calibration line for the actual electron energy as a function of the electron gun control panel electron energy. The ionization potentials for acetylene and helium as well as appearance potentials of doubly ionized argon and the C_2H ion were used as references for the actual electron energy. 46
- Figure 2.18** Pulsed valve expansion profile using argon. The initial part of the profile is consistent with the 250 μs open time. The long tail is attributed to a mechanical delay in the nozzle's closing. 48
- Figure 2.19** (a) TOF mass spectrum of acetylene seeded in argon, taken with an electron energy of 60 eV. The inset in (a) is magnified by 4x to better show the acetylene cracking pattern. (b) TOF spectra at several electron impact energies demonstrate the disappearance of the C_2H peak at sufficiently low electron energy. An electron energy of ~ 18.4 eV was used in all subsequent experiments to better discern photolyzed C_2H signal from that of fragmented acetylene. (c) The acetylene depletion signal when photolysing directly in front of the nozzle, as opposed to (d), which is the depletion when photolysing in front of the skimmer ~ 1.5 cm downstream. The FWHM of (c) is roughly 30 μs while that of (d) is only 15 μs , indicating that photolysing in front of the nozzle disturbs the supersonic expansion. 50
- Figure 2.20** (a) Schematic showing the three regions where photolysis of acetylene was attempted. (b) Representation of the suprasil tube attached to the nozzle. 51
- Figure 2.21** (a) Acetylene and ethynyl peaks recorded with 193.3 nm beam directly in front of ionization region of TOF. Pure acetylene and a laser power was ~ 4.9 J cm^{-2} was used for this measurement. (b) Difference spectrum for laser on minus laser off. The inset in (b) is the region of the difference spectrum corresponding to C_2H^+ , between 2.2 and 2.35 μs , and shows that a very small amount of photolyzed C_2H is present. 53

Figure 3.1 This schematic indicates important features of an OLED (not to scale, typical dimensions are given in parentheses). Electrons are injected from the cathode through a thin protection layer into the electron transport layer, which typically consists of an amorphous organic material. Holes are injected into the hole transport layer from an optically transparent anode (typically an $\text{In}_2\text{O}_3 / \text{SnO}_2$ composite) that permits light to exit the device. In the recombination and emission layer, electron-hole pairs form excitons that relax to the dopant excited states (indicated by an asterisk *) that emit photons.

65

Figure 3.2 (a) Organic molecules (negligible spin-orbit coupling) emit only from the lowest excited singlet S_1 . Because $T_1 \rightarrow S_0$ emission is extremely weak, triplet excitation is lost through radiationless decay rather than photon emission, and consequently the maximum quantum yield is 25%. (b) In triplet harvesting, electron-hole recombination leads to excitons having a triplet-to-singlet population ratio of 3:1. Excitation cascades down the triplet and singlet manifolds, with internal conversion (IC) and intersystem crossing (ISC) resulting in excitation ultimately residing in the lowest triplet, $^3\text{MLCT}$ (T_1), which emits photons. An organometallic compound (in which spin-orbit coupling (SOC) is strong) such as $\text{Ir}(\text{ppy})_3$ experiences relatively fast ISC and efficient $T_1 \rightarrow S_0$ phosphorescence. This can result in quantum yield approaching 100%.

67

- Figure 3.3** (a) Photoexcitation of ligand-centered ${}^1\text{LC}(\pi \pi^*)$ is accompanied by rapid radiationless decay: IC to ${}^1\text{MLCT}$ followed by ISC to the levels labeled T_1 (energies are not to scale). (b) Absorption spectrum of $\text{Ir}(\text{ppy})_3$ in dimethylformamide at 414 K. Note the large σ_1 absorption cross-sections (*i.e.*, units of 10^{-16} cm^2). The yellow boxed region, $34\,150 - 35\,775 \text{ cm}^{-1}$ ($4.234 - 4.435 \text{ eV}$), corresponds to the portion of the ${}^1\text{LC} \leftarrow S_0$ system examined in this work. Inset: changing the temperature over the range 295 – 414 K has a minimal effect on the absorption spectrum in the energy range of interest; only slight broadening is observed. In order, from the top trace, the temperatures are: 295, 333, 353, 383, 408, and 414 K. The vertical axis in the inset is not labeled, as the curves are offset from one another for clarity. They are nearly identical over the indicated range. (c) Absorption spectrum of solution phase 2-phenylpyridine, adapted from reference 30. The ${}^1\text{LC} \leftarrow S_0$ feature is analogous to the one in $\text{Ir}(\text{ppy})_3$. 70
- Figure 3.4** Schematic of the experimental arrangement: (a) The main vacuum chamber has a base pressure of 2×10^{-9} Torr. (b) Details of the time-of-flight mass spectrometer (TOFMS): Typical mass resolution was $m/\Delta m \sim 200$. 74
- Figure 3.5** With $415 \mu\text{J cm}^{-2}$ of $35\,673 \text{ cm}^{-1}$ (4.423 eV) radiation, only the $\text{Ir}(\text{ppy})_3^+$ parent ion is observed (*vide infra* Figure 3.8). The $\text{Ir}(\text{ppy})_3^+$ peak consists of contributions from the major isotopologues (see text for details). (a) The experimental curve (red) is the average of several traces, each of which is comprised of ~ 1000 individual spectra. The blue curve is obtained using the natural isotope abundances and assigning a 2.35 amu FWHM to each mass, as indicated in (b). This fits the experimental trace [red curve in (a)] rather well. 76
- Figure 3.6** At a fluence of 1500 mJ cm^{-2} and photon energy of $35\,774 \text{ cm}^{-1}$ (4.435 eV), the mass spectrum is dominated by Ir^+ , albeit with an IrC^+ contribution that is $\sim 15\%$ as large as that of Ir^+ . Contributions from $\text{Ir}(\text{ppy})_2^+$ and $\text{Ir}(\text{ppy})_3^+$ (not shown) are smaller by an order of magnitude. The hydrocarbon peaks are due to impurity. 79

- Figure 3.7** (a) Action spectrum obtained by monitoring Ir^+ while varying the photon energy. Laser fluence was approximately 1400 mJ cm^{-2} . (b) Expanded view: The vertical dashed lines indicate transitions of (neutral) atomic iridium.³⁷ Note that the spectra are not offset from zero, *i.e.*, there is an underlying broad continuum. 81
- Figure 3.8** Mass spectra recorded at different fluences: The laser frequency is $35\,357 \text{ cm}^{-1}$ (4.383 eV). At low fluence (bottom trace), photoionization produces the $\text{Ir}(\text{ppy})_3^+$ ion exclusively. As the fluence is increased, fragmentation results in the appearance of the $\text{Ir}(\text{ppy})_2^+$ ion. At high fluence (top trace), the Ir^+ peak dominates, indicating severe fragmentation of $\text{Ir}(\text{ppy})_3$ and its photofragments. 83
- Figure 3.9** $\text{Ir}(\text{ppy})_3^+$ signal versus fluence, Φ , recorded with a photon energy of $35\,420 \text{ cm}^{-1}$ (4.391 eV) The straight line has a slope of 2, in accord with 2-photon ionization. 84
- Figure 3.10** (a) The black trace is the $\text{Ir}(\text{ppy})_3^+$ signal, divided by fluence squared, versus photon energy. The blue dashed trace is the absorption cross-section σ_1 of gas phase $\text{Ir}(\text{ppy})_3$ at $\sim 500 \text{ K}$ (arb. units). Different ratios of rhodamine 590 and 610 and the corresponding energy regions are designated by horizontal double-sided arrows: (a) 100% 590 (279.5 – 283.1 nm); (b) 590:610 = 9:1 (281.5 – 284.3 nm); (c) 590:610 = 4:1 (283.2 – 286.8 nm); (d) 590:610 = 7:3 (286.2 – 288.1 nm); (e) 590:610 = 3:2 (287.8 – 290.5 nm); (f) 100% 610 (290.2 – 292.8 nm). (b) The ion signal (scaled by Φ^{-2}) in (a) has been divided by the (blue dashed) absorption spectrum of $\sim 500 \text{ K}$ gas phase $\text{Ir}(\text{ppy})_3$ also shown in (a). This indicates that the undulation with $\sim 270 \text{ cm}^{-1}$ spacing is due to σ_2 . 86

- Figure 3.11** Some important properties and processes of low-lying electronic states are indicated schematically (not to scale). Rapid radiationless decay processes (IC and ISC, with respective lifetimes τ_{IC} and τ_{ISC}) ensure efficient T_1 production. Spontaneous emission lifetimes (τ_{rad}) for the T_1 sub-levels indicated on the far right differ considerably, despite the fact that these levels are close in energy, *i.e.*, 116, 6.4, and 0.2 μ s for 19 693, 19 712, and 19 863 cm^{-1} , respectively, in CH_2Cl_2 solvent. At room temperature, an observed phosphorescence lifetime of 1.6 μ s reflects the complex interplay that exists between the T_1 levels. The horizontal lines (above the electronic origins) whose spacing decreases with energy indicate (schematically) vibrational levels. 92
- Figure 3.12** Ultraviolet absorption spectra of *fac*-Ir(ppy)₃. The calculated spectrum (red) was obtained from the stick spectrum by assigning to each stick a Gaussian FWHM of 0.43 eV. The experimental spectrum (black) was recorded at room temperature in dichloromethane. Peak and shoulder positions (vertical arrows) are in eV. All stick heights have been increased by the same constant factor for viewing convenience, and curve height has been adjusted such that the maximum absorptions are equal. The low-energy, low-intensity wing due to $T_1 \leftarrow S_0$ (2.56 eV) is absent in the calculated spectrum because SOC was not included. 105
- Figure 4.1** Ground electronic state structures and atom numbering for (a) *fac*-Ir(ppy)₃ and (b) *mer*-Ir(ppy)₃. H atoms are omitted. Color scheme: green = Ir; blue = N; gray = C. Tables 4.1 and 4.2 list geometrical parameters. 118
- Figure 4.2** Six highest occupied MO's and three lowest virtual MO's for *fac*-Ir(ppy)₃ at S_0 geometry using BNL: Orbital labeling follows Hay. Energies of occupied orbitals (Koopmans IE's) are given in Table 4.3. 122
- Figure 4.3** Shapes of the electron hole wave functions obtained from Koopmans analyses for cations at the (a) S_0 , (b) T_1 , and (c) D_0 equilibrium geometries. 128

- Figure 4.4** Ir(ppy) corresponding to Table 4.4: For the T₁ equilibrium geometry, C1, C2, and C3 correspond to carbons labeled 48, 52, and 50 in Figure 4.1(a) [see also Figure 4.3(b)]. For the D₀ equilibrium geometry C1, C2, and C3 correspond to carbons labeled 23, 25, and 27 in Figure 4.1(a) [see also Figure 4.3(c)]. 129
- Figure 4.5** Orbitals giving rise to T₁ excitation (HOMO and LUMO of S₀): left and right columns correspond, respectively, to S₀ and T₁ equilibrium geometries. 131
- Figure 4.6** Ultraviolet absorption spectra of *fac*-Ir(ppy)₃. The calculated spectrum (red) was obtained from the stick spectrum by assigning to each stick a Gaussian FWHM of 0.43 eV. The experimental spectrum (black) was recorded at room temperature in dichloromethane. Peak and shoulder positions (vertical arrows) are in eV. All stick heights have been increased by the same constant factor for viewing convenience, and curve height has been adjusted such that the maximum absorptions are equal. The low-energy, low-intensity wing due to T₁ ← S₀ (2.56 eV) is absent in the calculated spectrum because SOC was not included. Inset: The BNL (red) and ωB97X (blue) spectra differ considerably, the latter being far out of registry with the experimental spectrum. 133
- Figure 4.7** The first six BNL excited states at S₀ and T₁ geometries (in eV). Note that the adiabatic ionization energy (AIE) is 5.86 eV. 136
- Figure 4.8** (a) Photoexcitation transports populated S₀ vibrational levels to ¹LC, which undergoes radiationless decay on a subpicosecond timescale, resulting ultimately in T₁ electronic excitation. This maps $P(E_{vib})$ to T₁ with additional T₁ vibrational energy given by $h\nu - E_{TL}$, as indicated in (b) and in Figure 4.9. 139

- Figure 4.9** The red curve is a plot of equation 4.2 with $T = 500$ K; see text for details. Following photoexcitation, the total vibrational energy in T_1 is given by $h\nu - E_{T1} + E_{vib}$. The probability density for E_{vib} is $P(E_{vib})$, and $h\nu - E_{T1} = 15\,000$ cm^{-1} is chosen as a representative value. When all frequencies are changed by $\pm 10\%$, the $P(E_{vib})$ plots change accordingly (blue and black curves). However, the main qualitative feature is preserved. Namely, a considerable amount of T_1 vibrational energy is distributed with a FWHM that is modest relative to the energy of maximum $P(E_{vib})$, e.g., 7800 versus 31 000 cm^{-1} , respectively, for the red curve. 141
- Figure 5.1** (Schematic of the pulsed droplet apparatus. The machine consists of 3 vacuum chambers (1 - 3). Chamber (1) contains the pulsed helium droplet source (B) mounted on a closed cycle cryostat (A) with beam skimmer (C). The source chamber is pumped by a 3000 L/s diffusion pump (P1) backed in series by a roots blower followed by a rotary pump. Chamber (2) houses a ceramic pickup cell (D) wrapped in a tungsten filament. Chamber (2) is pumped by a 1000 L/s turbo-molecular pump (P2). Chamber (3) contains a combination reflectron / linear time-of-flight (TOF) spectrometer (F) as well as an axial quadrupole mass spectrometer (E) followed by a BaF_2 window (G). This UHV chamber is pumped by two 170 L/s turbo molecular pumps (P3 & P4). 151
- Figure 5.2** Time dependence of the quadrupole mass spectrometer signal set at $M = 8$ and $M = 16$, as indicated, and measured at nozzle temperatures of 18 K (a) and 10.3 K (b). The duration of the nozzle pulse was chosen to be 220 μs in order to give the most intense signal with the shortest open duration. Time zero corresponds to a delay with respect to the nozzle trigger of 2.99 ms and 3.96 ms in panels (a) and (b), respectively. 153
- Figure 5.3** Typical TOF mass spectra at 18K (a) and 10.3K (b) with important peaks labeled. The considerable water ($M = 18$) and protonated water cluster peaks ($M = n \cdot 18 + 1$) indicates pickup of multiple water molecules, due to the relatively high background pressure (10^{-6} mbar) in our pick up chamber during the experiments. 155

- Figure 5.4** Comparison of I_{16}/I_8 measured with quadrupole (a) and TOF (b) mass spectrometers at various nozzle temperatures with repetition rates indicated. Both plots exhibit a sharp initial decrease followed by a moderate leveling when moving from low to high temperature albeit with different absolute ratios. The TOF ratios here were measured with 1 mA current, 2 μ s pulse duration, and 95 eV e-Energy. 157
- Figure 5.5** TOF pulse intensity profile vs. delay for small (a) and large (b) droplets as measured with TOF. In (a) and (b), signal for mass 16 was multiplied by 4 and 3 for small and large droplets respectively. (c) and (d) show the delay dependence of I_{16}/I_8 throughout the pulse profiles for small and large droplets, respectively. The average value (red line) of each ratio taken over their respective profile (endpoints indicated in red and 95% confidence curves in blue) was 0.058 ± 0.004 and 0.059 ± 0.0035 for small and large droplets respectively. 159
- Figure 5.6** Current dependence of the TOF mass spectrometer peak intensities at $M = 4, 8, 12,$ and 16 for small (a) and large droplets (b), as well as I_{16}/I_8 for small (c) and large (d) droplets measured at ionization currents ranging from 1 to 5 mA. Intensities for mass 4, 12, and 16 are multiplied by 5 and by 2.5 in (a) and (b), respectively. 161
- Figure 5.7** Intensity of the TOF mass 4, 8, 12, and 16 peaks vs. electron energy are shown for small (a) and large (b) droplets as well as I_{16}/I_8 for small (c) and large (d) droplets, respectively. In (a) and (b) masses 4, 12, and 16 are multiplies by factors of 5 and 2.5, respectively. 163
- Figure 5.8** TOF peak intensity vs. duration of the ionization pulse for small (a) and large (b) droplets followed by I_{16}/I_8 for small (c) and large (d) droplets. All ionization pulses were initiated at the maximum intensity of their respective droplet pulse, see Figure 5.5. In (a) and (b) intensities of mass 12 and 16 peaks were multiplied by a factor of 3. 164
- Figure 5.9** The effect of the ionizing pulse duration on background H_2O^+ TOF intensity at various electron currents. 166

- Figure 5.10** Plot of I_{16}/I_8 for large droplet subtracted by I_{16}/I_8 for small droplets. Data is fit the equation $y = a[1 - \exp(-kt)]^2 + b$. Optimized values for a , b , k are 0.1551, -0.0102, and 0.11442, respectively. 168
- Figure 5.11** Diagram of the crucible pick-up cell used to imbed $\text{Ir}(\text{ppy})_3$ in helium droplets. The droplet beam was aligned through the crucible openings and the solid $\text{Ir}(\text{ppy})_3$ was placed in the lower half of the crucible. Tungsten wire was wrapped around the crucible and heated. The temperature was measured by a thermocouple just below the exit orifice. 171
- Figure 5.12** Full (a) and zoomed in (b) mass spectra of the droplet beam after pickup of $\text{Ir}(\text{ppy})_3$. The inset in (a) is an expanded view of the droplet signal. The oven temperature in both (a) and (b) is 192 °C. (c) $\text{Ir}(\text{ppy})_3^+$ and $(\text{Ir}(\text{ppy})_3)_2^+$ progression upon increase of the oven temperature. $M = 655$ and $M = 1310$ signals reach a maximum at 192 °C and 200 °C, respectively. 173
- Figure 5.13** Photoionization mass spectra of $\text{Ir}(\text{ppy})_3$ doped helium droplets. The fluences of (a) and (b) were $\sim 5 \text{ mJ cm}^{-2}$ and $< 1 \text{ mJ cm}^{-2}$, respectively. The peak at $M = 0$ in (a) and (b) is scatter from the 266 nm radiation, which served as the $t = 0$ reference. 174
- Figure 6.1** Depiction of the nozzle and discharge assembly. The nozzle operates on a current loop mechanism. Attached to the grounded nozzle faceplate is a Teflon spacer followed by a negatively biased copper electrode. Both spacer and electrode are encased in a Teflon shroud. 181
- Figure 6.2** (a) side view of the proposed vacuum chamber. The distance between the nozzle and TOF stack is less than 10 cm. Window 1, 2, and 3 correspond to path 1, 2, and 3 in part (b), respectively. The operating pressures in the source and detection regions are expected to be 10^{-5} torr and mid 10^{-7} torr, respectively. (b) shows a top view of the proposed vacuum chamber. Three optical paths are illustrated. Path 1 passes directly in front of the nozzle, path 2 crosses the center of the detection region, and path 3 overlaps the molecular beam with anti-parallel propagation. 183

ABSTRACT

Arguably the most important green phosphor used in organometallic light emitting devices (OLEDs), tris(2-phenylpyridine)iridium ($\text{Ir}(\text{ppy})_3$), is investigated. One- and two-photon photoionization studies are presented and yield a conservative estimate for the upper bound to the ionization energy (6.4 eV). Observed undulations in the two-photon study are due to structure in the ionizing transition that originates from the lowest triplet state (T_1), which is populated via fast intersystem crossing (ISC) from the lowest singlet. At low fluence and 500 K – the conditions under which the experiments were carried out – $\text{Ir}(\text{ppy})_3^+$ is produced without fragmentation, despite the large amount of vibrational energy distributed over its 177 vibrational degrees of freedom. It is concluded that vibrational energy is transferred efficiently to the cation. Complementary density functional theory (DFT) results using long-range corrected functionals (BNL and ωB97X) affirm this conclusion. Time-dependent DFT is used to compute excited singlet and triplet states to just below the computed ionization energy (5.88 eV). A UV absorption spectrum, in which transitions are vertical from the S_0 equilibrium geometry, agrees with the room temperature experimental spectrum and indicates that transitions are dominated by Frank-Condon factors with $\Delta v_i = 0$. Computed $\text{Ir}(\text{ppy})_3$ equilibrium geometries for the ground state (S_0), lowest triplet state (T_1), and lowest cationic state (D_0) reveal very similar geometries owing to the diffuseness of the molecular orbitals. Calculated $\text{Ir}(\text{ppy})_3$ vibrational frequencies were used to estimate the probability density $P(E_{\text{vib}})$ at 500 K. In combination with

the vibrational energy imparted through relaxation and ISC following photoexcitation, it is seen that a mean value of nearly 31,000 cm^{-1} of vibrational energy appears in T_1 , and consequently $\text{Ir}(\text{ppy})_3^+$. Considerable effort was directed toward removing this excess energy prior to ionization. To this end, it proved possible to photoionize $\text{Ir}(\text{ppy})_3$ embedded in helium droplets with 266 nm radiation. The resultant TOF spectra show a strong similarity to the corresponding gas phase spectra. Additionally, low fluence experiments exclusively produced $\text{Ir}(\text{ppy})_3^+$. The combined data suggests a two-photon ionization mechanism for the low fluence experiments.

Chapter 1

Introduction

The central theme of this dissertation is a comprehensive study of tris(2-phenylpyridine) iridium ($\text{Ir}(\text{ppy})_3$). Both experimental and theoretical approaches are explored. $\text{Ir}(\text{ppy})_3$ is best known for its role in organometallic light emitting devices (OLED's).¹ The utility of $\text{Ir}(\text{ppy})_3$ lies in its ability to efficiently phosphoresce following photoexcitation and / or charge carrier recombination in a solid matrix. The latter means of excitation is attractive from the point of view of display technologies.

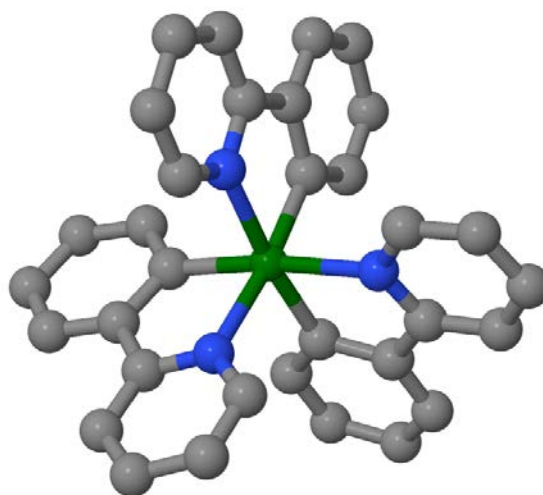


Figure 1.1. Ground electronic state structure for $\text{Ir}(\text{ppy})_3$'s most stable isomer (*fac*- $\text{Ir}(\text{ppy})_3$). H atoms are omitted for clarity. Color scheme: green = Ir; blue = N; gray = C.

High photoluminescence quantum efficiency in organometallic complexes, such as $\text{Ir}(\text{ppy})_3$, originates from the large amount of spin-orbit coupling (SOC) introduced by the heavy metal center. This dramatically increases the rate of intersystem crossing (ISC) in the system, which quickly funnels all singlet excited states into the triplet manifold.²⁻⁵

As a result, both singlet and triplet excited states ultimately populate the lowest triplet state (T_1), a phenomenon known as triplet harvesting (Figure 1.2).^{1,6,7} Moreover, the strong SOC significantly increases the phosphorescence rate, which surpasses radiationless decay as the dominant relaxation mechanism and enables quantum yields near 100% to be achieved.^{8,9}

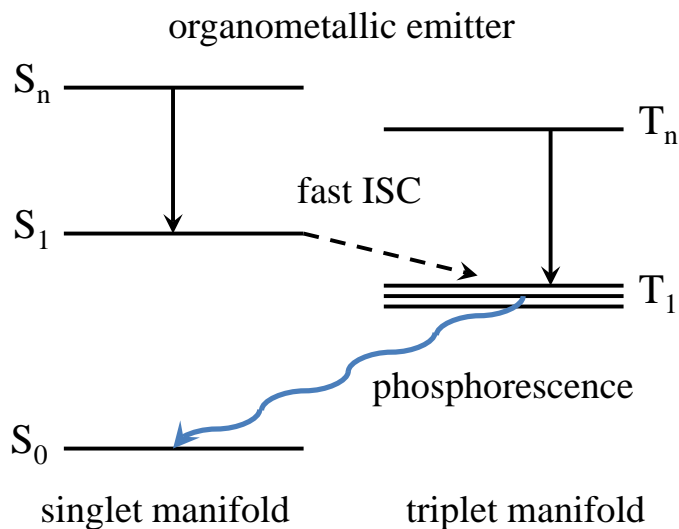


Figure 1.2. The diagram illustrates the effect of triplet harvesting. In organometallic compounds with transition metal centers, such as $\text{Ir}(\text{ppy})_3$, excited singlet states relax to a low lying singlet state where they show a fast intersystem crossing (ISC) to the lowest triplet state (T_1). On the other hand, excited triplets states simply trickle down the triplet manifold to the lowest triplet state. Thus, T_1 harvests both singlet and triplet excitation energy and can efficiently emit. In principle, a triplet emitter can — in the limit of vanishing radiationless decay — exhibit 100% luminescence quantum efficiency.

Although a great deal of research has been performed on $\text{Ir}(\text{ppy})_3$, most studies have focused on the relaxation and emission properties due to their role in OLED applications,^{3,5,8-17} with only a handful of experimental studies focused on other aspects of this system.^{4,18-20} Consequently, measurements of even the most fundamental quantities for $\text{Ir}(\text{ppy})_3$ are either absent or controversial. For example, the only known

experimental value of the Ir(ppy)₃ ionization energy (IE) is 7.2 eV based upon gas-phase electron energy loss spectroscopy (EELS).²⁰ However, the theoretical work of Hay presents an IE near 6.0 eV.²¹ It is shown in Chapters 3 and 4 that an IE of 7.2 eV is inconsistent with recent experimental and theoretical work and that a value of 6.0 is more reasonable.

In this manuscript, experimental and theoretical studies of Ir(ppy)₃ shed light on the various ground and excited state properties of Ir(ppy)₃, including the ionization energy. Results from these complementary approaches are used to describe the behavior of Ir(ppy)₃ over a range of conditions. A detailed description of each chapter is given below.

1.1 Chapter Contents

This dissertation is organized as follows: Chapter 2 discusses several experimental techniques used to complete the work presented in chapters 3 – 5. Specifically, photoionization, time-of-flight mass spectrometry (TOFMS), gas phase UV-Vis absorption of room temperature solids, helium droplet production and characteristics, and electron impact ionization are all presented in detail. Each section is meant as a basic introduction to the technique. Additionally, a final section in chapter 2 discusses preliminary experiments on the production and detection of the ethynyl radical (C₂H) using 193.3 nm photolysis and electron impact ionization / TOFMS, respectively.

Chapter 3 concentrates on the photoionization of gas phase Ir(ppy)₃. Experiments using one- and two-photon photoionization schemes coupled with TOF mass

spectrometry were carried out to yield a conservative estimate for the upper bound to the ionization energy of Ir(ppy)₃, i.e. 6.4 eV. This assumes that vibrational energy is transported efficiently to the cation. The one-photon experiment used 193 nm radiation, while the two-photon experiments used tunable UV radiation to excite the ligand-centered (¹LC) state, which quickly decays to the lowest ³MLCT state (T₁), followed by a second transition to the ionization continuum. An undulation in the two-photon action spectrum was observed. Comparison of the two-photon action spectrum with the UV absorption spectrum of gas phase Ir(ppy)₃ show the undulation is due to structure in the transition that originates from T₁.

Chapter 4 presents a computational study of Ir(ppy)₃ using density functional theory (DFT). Two long-range-corrected (LRC) functionals (BNL and ωB97X) were used in this study. Equilibrium geometries for the ground (S₀), lowest triplet (T₁), and lowest cationic state (D₀) were calculated for the *facial* isomer, and S₀ and D₀ were computed for the *meridional* isomer. Ground state energies of the *facial* and *meridional* isomers are compared. It is found that the *facial* isomer is more stable than the *meridional* isomer by ~ 220 meV. Because of this *fac*-Ir(ppy)₃ dominates in most environments. Therefore, focus is on this species. Time dependent density functional theory (TDDFT) is used to calculate excited states of Ir(ppy)₃. A UV absorption spectrum, in which transitions are vertical from the S₀ equilibrium geometry, was constructed from the TDDFT results and is compared with the room temperature experimental spectrum. The calculated absorption spectrum is in good agreement with the experimental spectrum, which is consistent with Franck-Condon factors dominated by Δv_i = 0 and the delocalized

nature of the orbitals. The calculated $T_1 - S_0$ energy gap (2.30 eV) is in reasonable agreement with the experimental value of 2.44 eV. Several ionization energies are obtained: adiabatic (5.86 eV); vertical from the S_0 equilibrium geometry (5.88 eV); and vertical ionization of T_1 at its equilibrium geometry (5.87 eV). These agree with a calculation by Hay (5.94 eV), and with the conservative experimental upper bound of Chapter 3 (6.4 eV). Finally, the 177 $\text{Ir}(\text{ppy})_3$ vibrational frequencies were calculated and used to estimate the probability density $P(E_{vib})$ for finding the molecule in a small energy interval at 500 K, i.e. the temperature at which the experiments in Chapter 3 were carried out. In combination with the vibrational energy imparted through $^1\text{LC} \leftarrow S_0$ photoexcitation, it is seen in Chapter 3 that a large amount of vibrational energy appears in $\text{Ir}(\text{ppy})_3^+$ without causing fragmentation. Specifically, for $h\nu - E_{T1} = 15\,000\text{ cm}^{-1}$, the probability density for *total* vibrational energy peaks at $\sim 31\,000\text{ cm}^{-1}$ with a 7800 cm^{-1} width.

Chapter 5 is comprised of three main topics: the characterization of helium droplets produced by a pulsed nozzle, the origin of the increased $\text{He}_4^+/\text{He}_2^+$ ratio with increasing droplet size, and the embedding and photoionization of $\text{Ir}(\text{ppy})_3$ in helium droplets. Droplets were generated by expanding cold gaseous helium at high pressure through a solenoid type pulsed nozzle. The average droplet size was determined by computing the mass 16 to mass 8 intensity ratio (I_{16}/I_8) using quadrupole mass spectrometric measurements and comparing it to the measurements of Gomez et al.²² This process was repeated for a range of temperatures. Quadrupole measurements are consistent with the results in reference 11 and show a sharp increase in I_{16}/I_8 with

decreasing T_0 indicating a corresponding rise in droplet size. The quadrupole measurements were compared to TOF measurements under similar conditions and show that the quadrupole I_{16}/I_8 is up to $\sim 5x$ larger than that of the TOF. This discrepancy arises from the dramatically different time scales intrinsic to each spectrometer. Additional TOF measurements of the droplet beam were used to characterize the droplet pulse. All characterization experiments were performed with a nozzle temperature of either 10 K or 18 K, which correspond to an average droplet size of 3×10^5 and 5×10^4 , respectively. It is observed that the droplet size is constant throughout the pulse. The effect of electron current and impact energy on the droplets were also tested. The droplet signal shows a linear dependence on electron current, which is consistent with only one electron colliding with a droplet. The changing TOF mass signal vs. electron impact energy reveals that the electron impact ionization cross-section for the droplet is a maximum near that of gaseous helium. The origin of the increased I_{16}/I_8 ratio for large droplets is due to the increased probability of forming two exciplex He_2^* molecules within the same droplet, which then combine to form He_4^+ . This chapter closes with results from embedding gaseous tris(2-phenylpyridine)iridium ($\text{Ir}(\text{ppy})_3$) in helium droplets followed by photoionization. Low fluence photoionization at 266 nm exclusively produced $\text{Ir}(\text{ppy})_3^+$ indicating that it follows a two-photon ionization mechanism.

This dissertation concludes with a description of future experiments. It is proposed that efficient production of the ethynyl radical (C_2H) will be achieved via pulsed electrical discharge of an acetylene / argon mixture. The nascent ethynyl radicals can then be detected using electron impact / TOFMS. Initial estimates of the C_2H

concentration at the detection region are on the order of 10^{10} molecules cm^{-3} based upon the work by Van Beek et al.²³ Revised electron impact parameters reveal a 100x increase in the C_2H ionization efficiency, compared to that calculated in section 2.6. The combined estimates predict approximately 10^7 C_2H^+ molecules cm^{-3} are generated for detection. Additionally, the proposed vacuum chamber introduces three very different optical paths that ensure all opportunities to spectroscopically probe C_2H are explored.

1.2 References

1. Yersin, H. Ed.; *Highly Efficient OLEDs with Phosphorescent Materials*; Wiley-VCH Verlag: Weinheim, Germany, **2008**.
2. Hedley, G. J.; Ruseckas, A.; Samuel, I. D. W. *J. Phys. Chem. A Lett.* **2008**, *113*, 2.
3. Hedley, G. J.; Ruseckas, A.; Samuel, I. D. W. *Chem. Phys. Lett.* **2008**, *450*, 292.
4. Hedley, G. J.; Ruseckas, A.; Liu, Z.; Lo, S. C.; Bum, P. L.; Samuel, I. D. W. *J. Am. Chem. Soc.* **2008**, *130*, 11842.
5. Tsuboi, T. *J. Lumin.* **2006**, *119/120*, 288.
6. Yersin, H.; Rausch, A. F.; Czerwieniec, R.; Hofbeck, T.; Fischer, T. *Coordin. Chem. Rev.* **2011**, *255*, 2622.
7. Yersin, H. *Top. Curr. Chem.* **2004**, *241*, 1.
8. Adachi, C.; Baldo, M. A.; Thompson, M. E.; Forrest, S. R. *J. Appl. Phys.* **2001**, *90*, 5048.
9. Adachi, C.; Baldo, M. A.; Forrest, S. R.; Thompson, M. E. *Appl. Phys. Lett.* **2000**, *77*, 904.
10. Hofbeck, T.; Yersin, H. *Inorg. Chem.* **2010**, *49*, 9290.
11. Tang, K.; Liu, K. L.; Chen, I. *Chem. Phys. Lett.* **2004**, *386*, 437.
12. Finkenzeller, W. J.; Yersin, H. *Chem. Phys. Lett.* **2003**, *377*, 299.
13. Vacha, M.; Koide, Y.; Kotani, M.; Sato, H. *J. Lumin.* **2004**, *107*, 51.
14. Tsuboi, T.; Alaroudi, N. *Phys. Rev. B* **2005**, *72*, 125109.
15. Stampor, W.; Mezyk, J.; Kalinowski, J. *Chem. Phys.* **2004**, *300*, 189.

16. Breu, J.; Stossel, P.; Schrader, S.; Starukhin, A.; Finkenzeller, W. J.; Yersin, H. *Chem. Mater.* **2005**, *17*, 1745.
17. Rausch, A. F.; Thompson, M. E.; Yersin, H. *J. Phys. Chem. A* **2009**, *113*, 5927.
18. Holzer, W.; Penzkofer, A.; Tsuboi, T. *Chem. Phys. Lett.* **2005**, *308*, 93.
19. Deaton, J. C.; Switalski, S. C.; Kondakov, D. Y.; Young, R. H.; Pawlik, T. D.; Giesen, D. J.; Harkins, S. B.; Miller, A. J. M.; Mickenberg, S. F.; Peters, J. C. *J. Am. Chem. Soc.* **2010**, *132*, 9499.
20. Kukhta, A. V.; Kukhta, I. N.; Bagnich, S. A.; Kazakov, S. M.; Andreev, V. A.; Neyra, O. L.; Meza, E. *Chem. Phys. Lett.* **2007**, *434*, 11.
21. Hay, P. J. *J. Phys. Chem. A* **2002**, *106*, 1634.
22. Gomez, L. F.; Loginov, E.; Sliter, R.; Vilesov, A. F. *J. Chem. Phys.* **2011**, *135*, 154201.
23. Van Beek, M. C.; Ter Meulen, J. J. *Chem. Phys. Lett.* **2010**, *337*, 237.

Chapter 2

Experimental techniques

A variety of experimental techniques were used to complete the work described in this manuscript. Discussing each and every one is unnecessary as most have been exhaustively described elsewhere. For example, detailed reviews of molecular beams – both effusive¹ and supersonic² – as well as various methods of laser spectroscopy³⁻⁸ are readily available. This chapter focuses on a few experimental techniques that were an integral part of the work described in chapters 3, 4, and 5. The first three sections address the techniques used in the work described in chapters 3 and 4, and include photoionization, TOF mass spectrometry, and gas-phase UV-Vis absorption of room temperature solids. The next two sections address helium droplet matrix isolation and electron impact ionization, which are the basis of the experiments in chapter 5. This chapter ends with a standalone section, which describes experiments that investigated 193.3 nm photolysis of acetylene and the detection of its photoproducts.

2.1 Photoionization

Before the invention of the laser, photoionization spectroscopy was limited in its application because it relied on the use of electrical discharge and arc lamps.⁹ These conventional light sources were only of marginal utility as the vast majority of chemical systems demand short wavelengths and large spectral intensities to induce atomic or molecular photoionization.³ Once high intensity lasers were developed, experiments

where a single atom or molecule could interact with multiple photons soon followed. Consequently, spectroscopists were now in a position to examine highly excited states, multiphoton transitions, and even photoionization for a wide range of systems. The observation of multiphoton transitions and the resultant excited state can either proceed by detecting fluorescence from the excited state, or by further exciting the system to the ionization continuum.¹⁰⁻¹² While a great deal of information can be gleaned from the fluorescence spectrum, this text will focus on photoionization.

There exist a number of variants to the multiphoton photoionization (MPI) technique. The vast majority of such experiments use resonance-enhanced multiphoton ionization (REMPI). Unfortunately, the literature is rife with ambiguous terminology, and even the term REMPI is not confined to one type of experiment. Figure 2.1 provides a sample of the various photoionization schemes.¹³ The most common form of REMPI is depicted in Figure 2.1a. While MPI spectroscopy can be complicated with the large laser intensities required to excite the system of interest, it has nonetheless proven to be an effective means of obtaining spectroscopic information. For example, single photon transitions between states of the same parity are forbidden, but when an even number of photons are used to induce a transition the excited state becomes accessible.^{14,15} Thus, new spectroscopic information about the system can be inferred from the multiphoton spectrum.

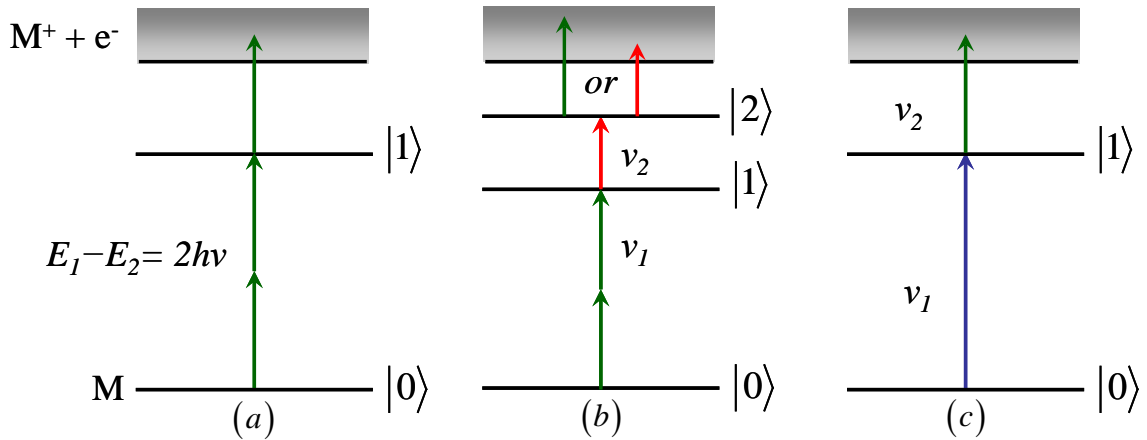


Figure 2.1. Three possible multiphoton excitation schemes are shown above. (a) One-color multiphoton ionization resonance enhanced at the initial transition. (b) A double resonance variant of REMPI; ν_1 is fixed to resonantly enhance the initial two-photon transition while ν_2 is scanned to probe the spectroscopy of the second transition. (c) Two-color multistep photoionization is shown, where ν_1 is fixed and ν_2 is scanned to reveal the various ionization thresholds.¹³

In contrast to multiphoton photoionization, a series of resonant single photon transitions can be used for ionization (Figure 2.1c). This multistep, or stepwise, photoionization technique is extremely versatile because at low laser intensities each transition may be treated independently. Additionally, precise control over the transitions opens up a multitude of pathways through which the system can be studied. For example, employing multiple laser pulses separated by time delays facilitates probing dynamical processes as they unfold. Also, action spectra generated by multistep photoionization yield spectroscopic information about all transitions involved. Another advantage of the multistep approach is that the single photon transitions have absorption cross-sections that are on average $\sim 10^{30}$ times larger than multiphoton transitions.^{15,16} Thus, the demand for very intense laser pulses is decreased.

In systems with sufficiently low ionization, modern lasers are capable of producing frequencies in which a single absorption event is sufficient to produce ions.

For example, the 193 nm photon produced by an ArF laser was able to ionize gas-phase tris(2-phenylpyridine)iridium without ionizing other gaseous molecules present in the vacuum chamber (Section 3.2.3).

The work presented in this manuscript exclusively used multistep and single photon photoionization, and therefore will be the focus of this text. Many authoritative reviews and books on the various forms of multiphoton methods are available.^{3,10,13-15}

2.1.1 Stepwise ionization spectroscopy

It is worthwhile to consider in detail the rate equations involved in a two-step photoionization process because it provides insight into what information may be extracted from the experiment. In general, the stimulated absorption/emission rates from an initial state to a final state are of the form:⁸

$$\frac{dN_i}{dt} = \pm N_i B_{i \rightarrow f} \rho(\nu) \quad (2.1)$$

where $B_{i \rightarrow f}$ is a constant, N_i is the number of particles in the initial state, $\rho(\nu)$ is the photon energy density, and \pm corresponds to absorption and emission, respectively. For spontaneous emission, the depopulation rate is:

$$\frac{dN_f}{dt} = -A_{f \rightarrow i} N_f \quad (2.2)$$

where $A_{i \rightarrow f}$ is a constant and N_f is the number of particles in the excited state. It is useful to rewrite equations 2.1 and 2.2 using more convenient quantities. $A_{i \rightarrow f}$ can be replaced with $1/\tau$ (units of s^{-1}), where τ is the spontaneous emission lifetime of the excited state,

and $B_{i \rightarrow f} \rho(\nu)$ may be written as $\sigma_i \Phi$, where σ_i is the absorption cross-section for transition i (units of cm^2) and Φ is the photon flux (units of photons $\text{cm}^{-2} \text{s}^{-1}$).

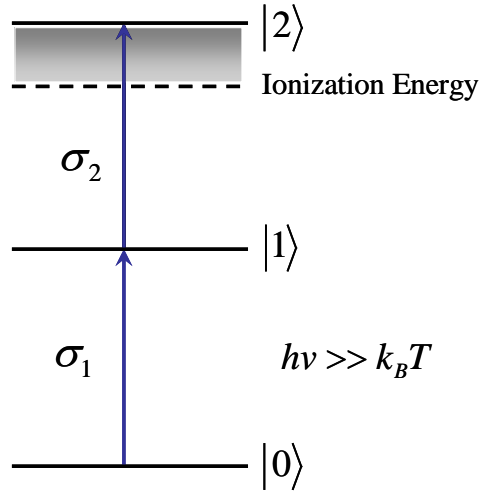


Figure 2.2. Schematic representing a stepwise one-color two-photon photoionization pathway. $|0\rangle$ represents the ground state, $|1\rangle$ is a real intermediate absorbing state, and $|2\rangle$ is a state that lies above the ionization energy. The absorption cross-sections for transition $|1\rangle \leftarrow |0\rangle$ and $|2\rangle \leftarrow |1\rangle$ are σ_1 and σ_2 , respectively. The photon energy ($h\nu$) is considered much larger than the thermal energy ($k_B T$).

Now consider the two-photon photoionization scheme in Figure 2.2. If the light source is a monochromatic square pulse of length T , then the transition rates for all three states are:

$$\frac{dN_0}{dt} = -N_0\sigma_1\Phi + \frac{N_1}{\tau} + N_1\sigma_1\Phi \quad (2.3)$$

$$\frac{dN_1}{dt} = N_0\sigma_1\Phi - \frac{N_1}{\tau} - N_1\sigma_1\Phi - N_1\sigma_2\Phi \quad (2.4)$$

$$\frac{dN_2}{dt} = N_1\sigma_2\Phi \quad (2.5)$$

Notice that equation 2.5 assumes that the cationic state has an infinite spontaneous emission lifetime. Adding equations 2.1 and 2.2 and solving for dN_0/dt yields:

$$\frac{dN_0}{dt} = -\left(\frac{dN_1}{dt} + N_1\sigma_1\Phi\right) \quad (2.6)$$

Differentiating equation 2.4 and substituting it into equation 2.6 yields a second order differential equation in N_1 :

$$\frac{d^2N_1}{dt^2} + \left[(2\sigma_1 + \sigma_2)\Phi + \frac{1}{\tau}\right]\frac{dN_1}{dt} + N_1\sigma_1\sigma_2\Phi^2 = 0 \quad (2.7)$$

The general solution to which is:¹⁷

$$N_2 = \frac{N_0\sigma_1\sigma_2\Phi^2}{\lambda_2 - \lambda_1} \left[\frac{1}{\lambda_2} \{\exp(-\lambda_2 T) - 1\} - \frac{1}{\lambda_1} \{\exp(-\lambda_1 T) - 1\} \right] \quad (2.8)$$

with

$$\lambda_2 = b + \sqrt{b^2 - \omega^2}$$

$$\lambda_1 = b - \sqrt{b^2 - \omega^2}$$

$$2b = (2\sigma_1 + \sigma_2)\Phi + \frac{1}{\tau}$$

$$\omega^2 = \sigma_1\sigma_2\Phi^2$$

In the limit of low flux and a long-lived intermediate state ($T \ll \tau$ and $\Phi T \ll 1$), the exponential terms in equation 2.8 may be expanded in a Taylor series. The expanded terms taken to the second order are

$$\exp(-\lambda T) = 1 - \lambda T + \frac{(\lambda T)^2}{2} \quad (2.9)$$

Substituting equation 2.9 into 2.8 and simplifying gives a convenient expression for the number of ions created:

$$N_2 = \frac{N_0 \sigma_1 \sigma_2 \Phi^2 T^2}{2} = \frac{N_0 \sigma_1 \sigma_2 \varphi^2}{2} \quad (2.10)$$

where φ is the laser fluence (units of photons cm^{-2}). This result shows that at low fluence, the number of particles ionized from the two-step photoionization scheme is dependent on the square of the laser fluence. A similar result is derived if the above approximations ($T \ll \tau$ and $\Phi T \ll 1$) are used from the outset, i.e. the stimulated and spontaneous emission terms in equations 2.3 and 2.4 are neglected. Thus, with the above constraints, each transition may be treated independently. Moreover, if the first transition is characterized by an absorption spectrum, then the spectroscopic information of the second transition may be extracted from a photoionization action spectrum (Section 3.2.2).

From the above derivation it should be clear that laser intensity has significant influence over the steps by which photoionization occurs. In general, a stepwise photoionization scheme may require n transitions. In the limit of a low fluence, the order (n) of the ionization process is easily determined by measuring the change in the log of the ion-signal with a change in the log of the laser fluence:

$$n = \frac{d \log(N_{ION})}{d \log(\varphi)} \quad (2.11)$$

where N_{ION} represents the ion signal. However, as the fluence is increased, the situation becomes more complex. For example, when the laser fluence ϕ approaches $1/\sigma$ for a particular transition the initial and final state populations are equal, and the transition is said to be saturated, i.e. no further absorption is possible for that transition. As a result, the ionization order is decreased, because the saturated transition is independent of laser intensity.⁵ While spectroscopy in this regime increases the efficiency of photoionization,¹⁶ spectroscopic information may be lost or difficult to extract. Furthermore, the increase in fluence increases the chances of absorption past ionization, leading to possible fragmentation. Consequently, photoionization spectra are acquired in a regime where the signal depends heavily on laser fluence.

2.1.2 Fragmentation

Photoionization can lead to diverse collection of products. As more photons are absorbed, higher potential energy surfaces are accessed. Thus, the extent of fragmentation depends largely on laser fluence and the system's capacity to absorb. In the soft ionization regime, where the only the minimum number of photons necessary to ionize the system are absorbed, the molecular parent ion is expected to be produced almost exclusively.¹⁰ Alternatively, very high laser fluences can completely reduce a molecule to atomic ions. Photofragmentation can significantly alter the information available from the ion signal, so determining the conditions under which fragmentation occurs is important.

Two common mechanisms that contribute to photofragmentation are depicted in Figure 2.3. The first mechanism (Figure 2.3a) is parent ion fragmentation corresponding

to dissociation when the parent ion absorbs further.^{18,19} In multiphoton ionization experiments of polyatomic molecules, the mass spectra of photoions are rather complicated. The high radiation intensities necessary for two or three photon transitions make it near impossible to prevent absorption past the initial ionization, in which case fragmentation via mechanism one is expected to occur.

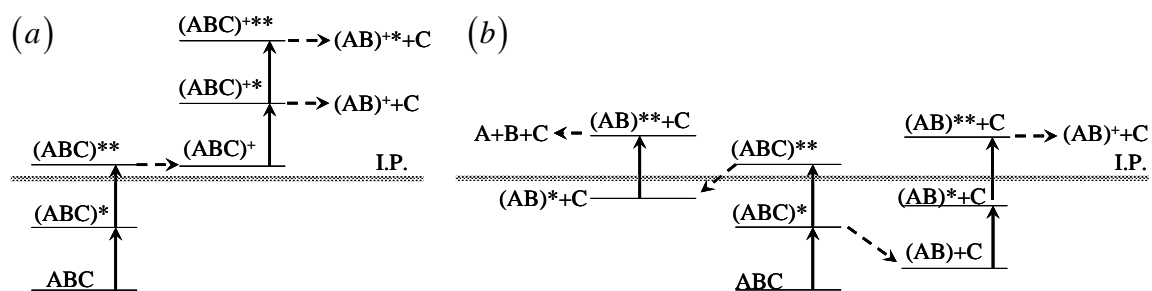


Figure 2.3. Depiction of two fragmentation schemes of multistep ionization. (a) Continued absorption by the parent ion opens up a variety of dissociation channels, which can eventually lead to atomization. (b) Dissociation of the intermediate state will lead to neutral fragments that can be ionized and/or dissociate further.¹⁴

The second mechanism deals with neutral fragments that can be produced very efficiently after absorption.²⁰ Although using a stepwise photoionization technique allows for better control of the conditions by which the ionization continuum is reached, fragmentation is still a possibility. Furthermore, if the produced photofragments are neutral, they must be ionized in order to be detected by a mass spectrometer. Consequently, complementary experiments must be used to fully understand the nature of the neutral fragmentation.

2.2 Time-of-flight mass spectrometry

Time-of-flight (TOF) mass spectrometry separates ions of different masses by exploiting the importance of mass and velocity in an atom/molecule's kinetic energy. A thorough description of this technique can be found in the pioneering work of Wiley and McLaren.²¹ The following discussion highlights a few important aspects of the technique.

2.2.1 Overview

A typical Time-of-Flight (TOF) mass spectrometer consists of an interaction region, a field-free drift region, and a detector (commonly a microchannel plate (MCP) detector). Ions are formed in the interaction region and then accelerated by electric fields produced by a potential gradient. The accelerating electric field can be static or time varying. A system capable of dynamically changing its electric field is more versatile because it can use both pulsed and continuous ionization schemes. Whereas static TOF systems must use a pulsed ionization scheme in order to set time zero.

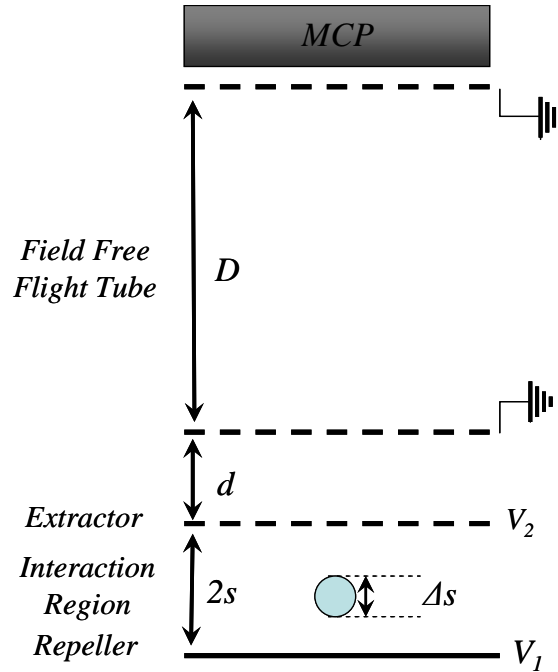


Figure 2.4. Schematic of a basic TOF system. The interaction region has a height of $2s$ and is between the repeller and extractor plates, which hold voltages V_1 and V_2 , respectively. A second acceleration region is above the interaction region and has a height of d . The field free region allows the accelerated ions of different mass time to separate. Ions that collide with the micro-channel plate detector (MCP) cause a cascade of electrons creating a small current, which is detected by an oscilloscope monitoring the MCP.²²

In an ideal case, a positive ion of charge q is initially at rest between the extractor and repeller plates (Figure 2.4). The plates are separated by a distance $2s$. If the plates are charged to voltages V_1 and V_2 (such that $V_1 > V_2$) the ion feels a force equal to $q(V_1 - V_2)/2s$. Once the ion reaches the extractor plate it has accumulated a kinetic energy equal to $q(V_1 - V_2)/2$. The ion then passes through the second acceleration region where it increases its kinetic energy by qV_2 . Thus, the total kinetic energy of the ion, regardless of mass, is

$$U = q \left(\frac{V_1 + V_2}{2} \right) \quad (2.12)$$

Or in terms of the electric fields

$$U = q(sE_1 + dE_2) \quad (2.13)$$

Here, s is the distance the ion travels in the first electric field E_1 , and d is the distance the ion travels in the second electric field E_2 . In the presence of multiple mass species, each ion will have a velocity that depends strictly on its mass m .

$$v = \sqrt{2U/m} \quad (2.14)$$

As the accelerated ions traverse the field-free region, they are separated by mass. The flight times of the different ionic species are given by²¹

$$T(U, s) = 1.02 \left(\frac{m}{2U} \right)^{1/2} \left(2k_0^{1/2}s + \frac{2k_0^{1/2}d}{k_0^{1/2} + 1} + D \right) \quad (2.15)$$

where D is the length of the field free flight tube and k_0 is defined as²¹

$$k_0 = \frac{(sE_1 + dE_2)}{sE_1} \quad (2.16)$$

The factor of 1.02 arises when equation 2.15 is converted to more convenient units, i.e. μs for time, amu for mass, cm for distance, V/cm for electric field, and eV for energy.

According to equation 2.15, the total flight time for each species depends on the square root of their mass. Thus, a mass spectrum may be acquired by recording the ion signal as a function of time and using equation 2.15 to convert flight time to mass. TOF mass spectrometry has several advantages over other common methods. One advantage is it enables an entire mass spectrum to be recorded for every ionizing event, with nearly 100% efficiency.¹⁶ For small to medium sized molecules, individual TOF mass spectra are collected within 50 μs . Thus, data collection is more often limited by the repetition

rate of the ionizer, e.g. the laser. Furthermore, the accuracy of this technique depends more on the response time of the detector and sample rate of the oscilloscope rather than the precise alignment that is required for other types of mass spectrometers.

2.2.2 Resolution

The above discussion presents the principles of TOF mass spectrometry only for ions that start from rest at the center of the ionization region. In actual experiments, ions are initially spread out and possess a range of kinetic energies, which cause ions of the same mass to register at slightly different times. As a result, ion signals have a flight time distribution that limits the mass resolution. The space distribution is due to the finite geometric cross-section of the ionizing source, be it laser or electron gun.

Consider a spherical distribution of ions centered between the repeller and extractor plates with a diameter of Δs , as depicted in Figure 2.4. The ions therefore reside at various distances from the extractor grid ranging from $s - \Delta s/2$ to $s + \Delta s/2$. According to equation 2.13, ions formed further from the extractor grid will gain more kinetic energy than those formed closer to the extractor grid. As a result, ions with the same mass will have different flight times, resulting in a time spread ΔT . However, because the more energetic ions have a longer flight path, there will be a point in space at which the faster ions pass the slower ones – a phenomenon known as space focusing. Ideally ions are spatially focused so that this inflection point occurs at the detector, drastically reducing ΔT . The focusing condition, for which ions of the same mass simultaneously reach the detector, is given by²¹

$$\frac{d}{s} = \left(\frac{k_0 - 3}{k_0} \right) \frac{D}{2s} \quad (2.17)$$

Notice that equation 2.17 is independent of mass. Thus, to satisfy this condition for one mass is to satisfy the condition for all masses. Usually D , s , and d are fixed and k_0 is adjusted to achieve optimal conditions, i.e. by varying V_1 and V_2 .

In addition to the initial spatial distribution, ions in the interaction region will have an initial velocity distribution. Therefore, the ions possess a range of initial kinetic energies that must be considered. [Note that only ions with velocity components towards or away from the detector will affect the resolution]. After acceleration, each ion will have a combined translational energy U_{Tot} of

$$U_{Tot} = U_A + U_0 \quad (2.18)$$

where U_0 is the initial kinetic energy and U_A is the acquired energy from acceleration.

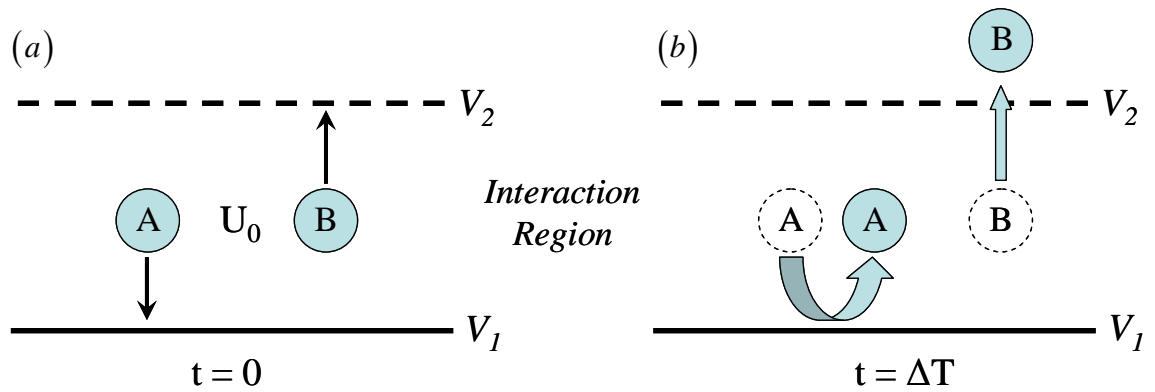


Figure 2.5. Diagram showing the origin of the decreased TOF mass resolution as a result of the initial kinetic energy distribution U_0 . (a) Two identical particles with translational energy U_0 but in opposite directions are shown. A is moving away from the detector, B is moving toward the detector. (b) The applied field must counter the initial kinetic energy of A causing it to reverse direction and return to its initial position with energy U_0 towards the detector, whereas B is simply accelerated toward the detector.²²

Envision two molecules in the interaction region at the same position s that have identical speeds albeit in opposite directions (Figure 2.5). Once ionized, the ion initially moving toward the detector will be accelerated, while the ion moving away from the detector must first decelerate to a stop and then accelerate toward the detector. Although both ions will acquire the same kinetic energy, they will impact the detector at different times. This time spread can be reduced by decreasing the energy ratio (U_0/U_A), e.g. using a supersonically expanded beam³ or increasing the accelerating voltages. In practice both approaches are used. It is also possible to improve the energy resolution by employing energy focusing, i.e. introduce a time delay between ionization and the application of the potential gradient.²¹ However, all attempts to reduce the effect U_0 will adversely affect the spatial resolution. Optimum conditions are most often determined empirically, but these equations are a good start. For a more detailed analysis of mass resolution see reference 21.

2.3 Gas-phase UV-Vis absorption spectroscopy of room temperature solids

Absorption spectroscopy is arguably one of the most widely used analytical tools in physics, chemistry, and industry. Infrared and far-infrared spectroscopy are commonly used for gas analysis and identification of chemical structures,^{23,24} while visible and ultraviolet spectroscopy are extensively used for quantitative analysis of atoms, ions and chemical species in solution.³ Consequently, a great variety of spectrometers are commercially available.

Absorption spectroscopy operates on the principle that electromagnetic radiation is attenuated due to an interaction with matter. In its most common form, the phenomenon of light attenuation by a homogeneous absorber is given by the Beer-Lambert law:¹⁷

$$I = I_0 \times 10^{-\varepsilon(\nu)Cl} \quad (2.19)$$

where I_0 is the intensity of light before interaction, I is the intensity after the interaction, $\varepsilon(\nu)$ is the frequency dependent molar absorption coefficient (units of $\text{L mol}^{-1} \text{cm}^{-1}$), C is the absorber concentration (units of mol L^{-1}), and l is the thickness of the absorbing material (units of cm). Or, by taking the \log of equation 2.19 and defining $\log(I_0/I)$ as the absorbance (A), then:

$$A = \varepsilon(\nu)Cl \quad (2.20)$$

In most UV-Vis absorption experiments, the absorber is dissolved to a known concentration in a solvent that is transparent over the desired spectral range. A quartz cell of 1 cm thickness is filled with the absorbing solution. Continuous white light is then passed through the cell and dispersed with a rotatable grating, allowing each wavelength to be detected separately with a photomultiplier tube. A diagram of a simple absorption spectrometer is shown in Figure 2.6.

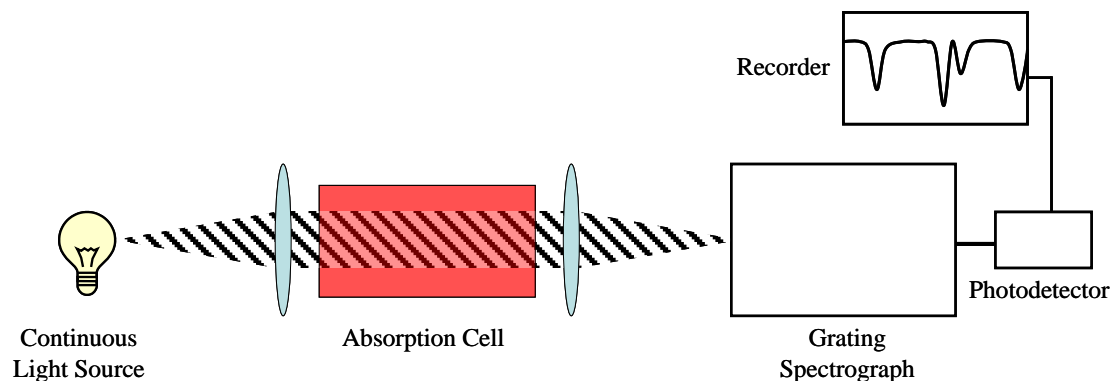


Figure 2.6. Basic operation of a standard spectrophotometer.³ A tungsten lamp generates a continuous white light source that is collimated and passes through the absorbing medium. The transmitted light is then scattered using a rotatable grating and slowly passed over a photodetector. Current generated from the transmitted light striking the detector is sent to a recorder that displays the resultant spectrum.

The absorption spectrum of a particular solute can vary from solvent to solvent. This is because molecules are stabilized by their interaction with a solvent, which induces a shift in their absorption or emission spectrum when compared to that of the gas phase.^{25,26} In light of the spectral shifts that can occur in solution, it is desirable to obtain the gas phase absorption spectrum. Moreover, certain gas phase multiphoton experiments produce spectra that contain information for multiple transitions, including that which produces the absorption spectrum. Thus, obtaining the gas phase absorption spectrum can help deconvolute the multiphoton spectrum. For example, the multistep photoionization of tris(2-phenylpyridine)iridium ($\text{Ir}(\text{ppy})_3$) (Section 3.2.2) involves a one-color two-photon photoionization mechanism. The resultant action spectrum contains spectral features of both the first and second transition. Additionally, the experiment was performed under vacuum, where gaseous $\text{Ir}(\text{ppy})_3$ was prepared by heating the powder to 220°C , thereby imparting a great deal of vibrational energy to the sublimated $\text{Ir}(\text{ppy})_3$.

molecules. Therefore, it is important to try and characterize the first transition under similar experimental conditions.

Before embarking on this task, several factors must be considered. First, it is advantageous to use a commercial spectrophotometer that can accommodate this type of measurement because it reduces the amount of time required to build specialized experimental setups. However, this usually imposes a limitation on the length of the cell. In this case, a maximum cell length of 7.5 cm could be used. Next, equation 2.20 shows that the magnitude of the absorption is dependent on the extinction coefficient, the concentration, and the cell length. The gas phase extinction coefficient can usually be estimated from a solution phase absorption spectrum. For Ir(ppy)₃, the extinction coefficient is relatively large, and between 40000 and 48000 L mol⁻¹ cm⁻¹ for the desired spectral range. Concentration depends on vapor pressure, which in turn depends on temperature. Fortunately, the vapor pressure of Ir(ppy)₃ has been characterized by Deaton et al.²⁷ A plot of Ir(ppy)₃'s vapor pressure vs. temperature is shown in Figure 2.7. Using a 7.5 cm cell length, an extinction of 45000, and an absorption of 0.1, which should be sufficient for a modern spectrophotometer, corresponds to a vapor pressure of 10⁻³ Torr. This requires heating the cell to a temperature of ~270 °C. The above specifications dictated that a new absorption cell be designed.

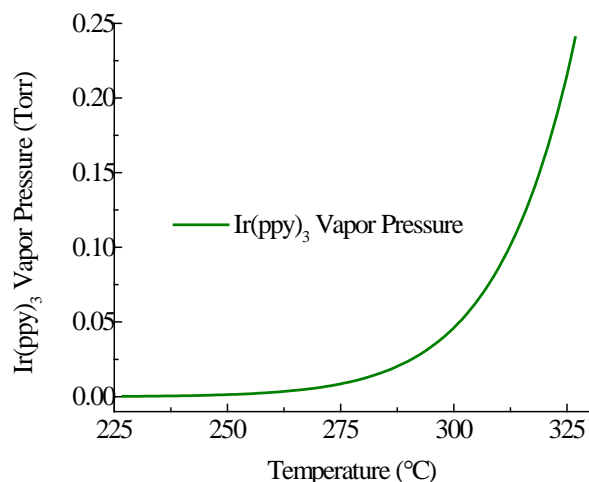


Figure 2.7. A plot of the Ir(ppy)₃ vapor pressure vs. temperature.⁷¹

A quartz tube with a 1 inch outside diameter (OD) was cut to a length of 3 inches. Two quartz windows were then soldered to the tube ends, taking care to ensure that the windows were perpendicular to the centerline of the glass tube, and thus perpendicular to the incoming light. A side port was installed to allow the Ir(ppy)₃ powder to be inserted and the cell to be evacuated. An illustration of this vacuum cell is given in Figure 2.8(a). After the powder was added, the cell was then pumped to a base pressure of $\sim 10^{-6}$ torr and sealed by fusing together the side port while the cell was under vacuum. Heating the cell in its current state caused Ir(ppy)₃ vapor to condense on the windows. Therefore, the cell needed to be shielded and heated such that the windows were the hottest part of the cell. This was achieved by machining a copper sleeve to fit snugly around the cell (Figure 2.8b). The sleeve was made with a 1 inch inner diameter (ID)/1.25 inch OD copper pipe that was cut to a length of just under 5 inches. Two cuts, roughly 90 degrees apart, down the length of the cell created a detachable side panel. A small section at the center of the side panel was removed to accommodate the side port of the vacuum cell. To ensure that

the cell windows were not cooled by air currents or radiative cooling, two identical end caps were constructed out of copper. Each end cap is slightly thicker than the copper tube to better retain heat, and contains a hole in the center with a diameter of 0.3 inches. The cell was inserted using the procedure indication in Figure 2.8(c).

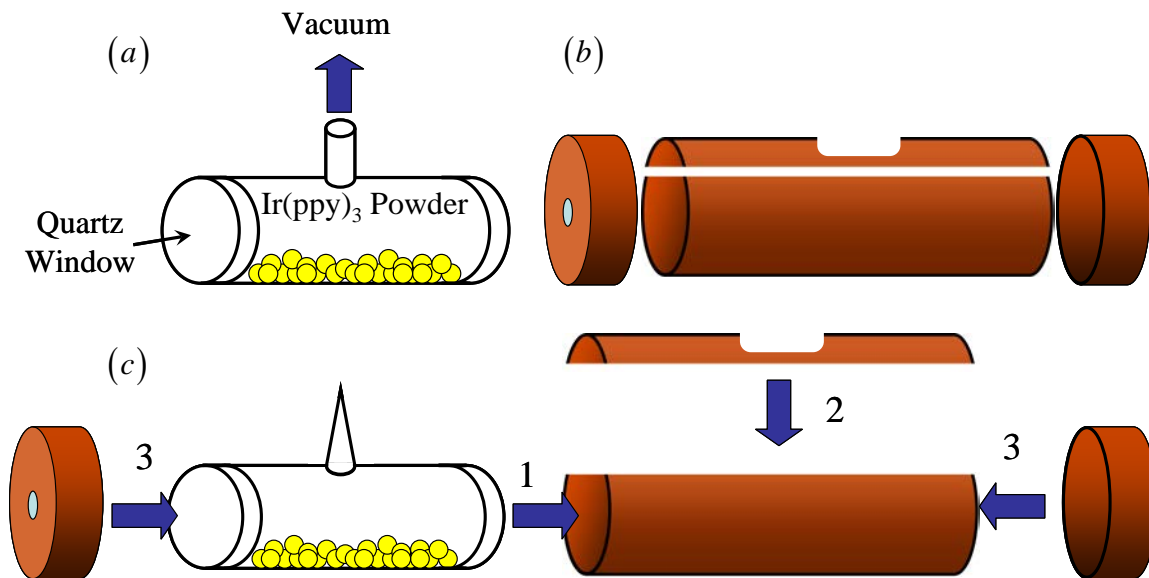


Figure 2.8. Depiction of the (a) UV-Vis vacuum cell, (b) and copper sleeve with end caps. The Ir(ppy)₃ must be added to the cell prior to evacuation. After the cell has been thoroughly pumped, the side port is sealed and the cell is inserted into the sleeve in the order indicated in (c).

To heat the cell, two individual strands of resistive wire were wrapped around the end caps. The wires were attached to separate power supplies, and the temperature was monitored using two thermocouples, one at each end, in order to prevent a temperature gradient from one end of the cell to the other. When acquiring the absorption spectrum, great care was taken to shield the spectrophotometer from the heating elements. Many commercial spectrophotometers have plastic interiors that will melt if exposed to high

temperature. The resultant gas phase absorption spectrum of Ir(ppy)₃ at 270°C is shown in Figure 2.9.

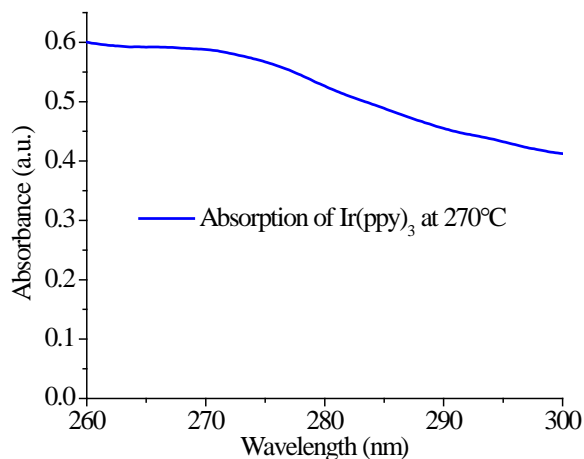


Figure 2.9. Plot of the gas phase Ir(ppy)₃ absorption spectrum at 270 °C.

Although the gas-phase absorption spectrum of Ir(ppy)₃ is rather dull, the technique used to acquire it was effective. Thus, it can be applied a variety of systems where sublimation is required in order to obtain gas phase spectra.

2.4 Helium droplet matrix isolation

Of all atoms that compose the periodic table, helium seems one of the least likely to be the focus of modern chemistry. At everyday temperatures and pressures, helium behaves as one expects of a chemically inert noble gas. However, helium is the only element that does not solidify at normal pressures, even when cooled to nearly zero Kelvin.²⁸ Additionally, below a critical temperature of 2.2 K ⁴He transforms into a superfluid state (³He experiences a similar transition at 3 mK).²⁹ Of the many fascinating

phenomena observed in this quantum liquid, its vanishingly small viscosity and high heat conductivity are most relevant for its use as a spectroscopic matrix.³⁰

Introduction of foreign species into superfluid helium poses unique opportunities to study the imbedded species. The high heat conductivity of the helium rapidly cools the impurity to superfluid helium temperature. ^4He , a boson, is quantum mechanically delocalized at very low temperatures, which enables the helium to gently accommodate the imbedded species with minimal interference. What is more, helium is transparent from the far IR to vacuum UV.³¹ However, quantum delocalization also permits impurities to move nearly unhindered, leading to unwanted aggregation and adherence to the container walls.³²

With the advent of helium droplet molecular beams it has become possible to confine foreign species in helium while avoiding undesired aggregation. Numerous spectroscopic experiments have shown that ^4He droplets also exhibit superfluid behavior.³³⁻³⁸ Although ^3He droplets can be formed through expansion, their ultimate temperature of 0.15 K is above the superfluid transition for this isotope. Consequently, ^4He is primarily used for spectroscopic studies. Additional information on helium droplets can be found in a variety of review articles.^{31,32,39-43}

2.4.1 Helium droplet production and characteristics

Helium droplets are produced by expanding pre-cooled helium through a small orifice.³¹ In general, there are two major expansion regimes.³² The most common mode of operation, known as subcritical, adiabatically expands gaseous helium which causes

extensive cooling resulting from collisions converting enthalpy into translational energy (Figure 2.10).^{2,44,45} As the helium cools, the collisions become less violent, which enables helium to cluster. These clusters, or droplets, cool further via evaporation until they reach an ultimate temperature that is determined solely by the droplet vapor pressure (0.37 K for ^4He and 0.15 K for ^3He).⁴⁶

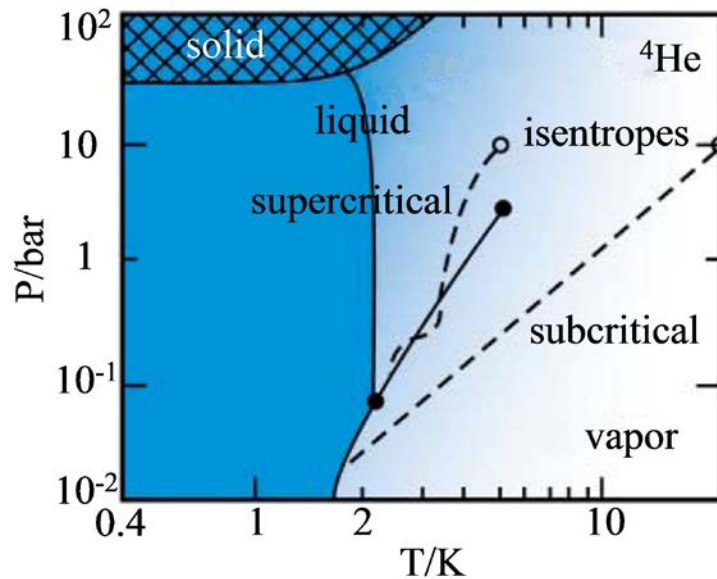


Figure 2.10. The pressure-temperature phase diagram for ^4He . Dashed lines show typical trajectories for supercritical (upper) and subcritical (lower) expansion isentropes.³¹

In contrast, supercritical expansions involve helium that is already liquid when it passes through the nozzle. Fragmentation of the liquid followed by evaporation generates the droplets. Although the final droplet temperature is the same in both regimes, the beam properties, i.e. droplet velocity, size, and distribution, depends on the nozzle parameters and type of expansion.

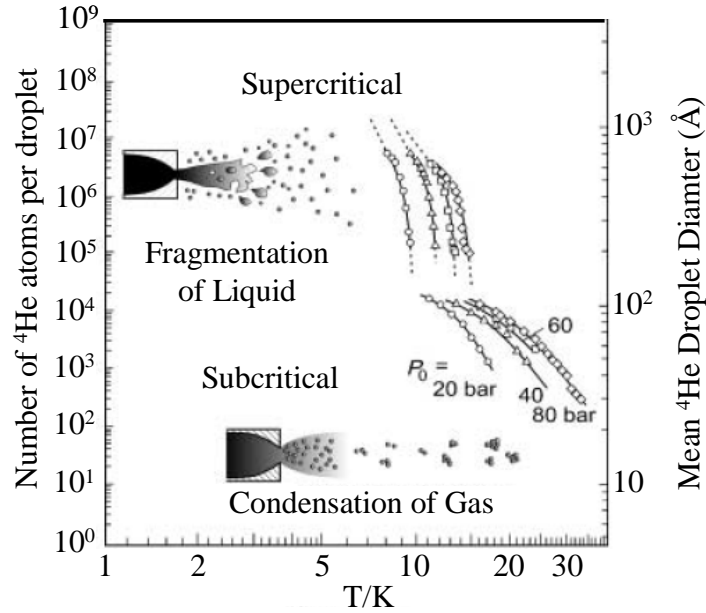


Figure 2.11. Average number of helium atoms per droplet for various backing pressure and nozzle temperatures. The right axis corresponds to the average droplet diameter under the same expansion conditions. Images of the subcritical (lower) and supercritical (upper) expansions are shown.³¹

Droplet velocities lie in the range of 150 – 450 m/s, depending on the nozzle temperature, with a narrow velocity distribution ($\Delta v/v \approx 0.01 - 0.03$).^{32,47} Likewise, the average droplet size is determined by the source conditions. Droplets containing between $10^3 - 10^{11}$ helium atoms are produced by adjusting the nozzle temperature and stagnation pressure, as seen in Figure 2.11. For droplets composed of $\sim 10^4$ helium atoms or more, the binding energy between an atom and the droplet approaches the bulk value of $\sim 5 \text{ cm}^{-1}$. In a continuous subcritical expansion, the size distribution is log-normal, with a half-width comparable to the average droplet size.⁴⁸ Assuming a spherical droplet, the radius, and consequently the droplet cross-section, may be inferred from the density following the liquid drop model, i.e. a sharp cutoff in helium density at the droplet edge. Using the above approximations, a droplet containing N helium atoms has a radius of

$$R = \left(\frac{3N}{4\pi\rho_{bulk}} \right)^{1/3} \quad (2.21)$$

The cross-sectional area, often referred to as the geometrical cross-section, is then

$$\sigma = \pi \left(\frac{3N}{4\pi\rho_{bulk}} \right)^{2/3} \quad (2.22)$$

The importance of the cross-section is emphasized in later sections.

2.4.2 Pulsed helium droplet production

The helium droplet apparatus used in chapter 5 employs a pulsed nozzle. The use of pulsed nozzles as helium droplet sources is a relatively new technique.⁴⁰ In general, a pulsed droplet beam is far less characterized than one created by continuous expansions; this is partly because of the additional parameters involved (e.g. pulse width, repetition rate), and partly because of the inherent difficulty in predicting expansions conditions when mechanical components, such as the poppet, behave differently from pulse to pulse. As a result, the underlying physics involved in droplet production by pulsed nozzles are not fully understood; however, there exist a number of advantages to using pulses droplet sources rather than continuous ones.

A major advantage to using a pulsed vs. continuous nozzle is the significantly higher beam density that is achieved while maintaining appropriate vacuum conditions. Two immediate benefits arise from the improved density: better signal to noise ratio (due to a higher concentration of species in the interaction region), and more efficient use of

material. The latter is particularly important for species that are present in low concentration. A pulsed nozzle is also better suited for use with pulsed lasers.

2.4.3 The pick-up process

Helium droplets are capable of encapsulating a motley collection of atomic and molecular species upon collision. In most cases, the collision cross-section is equivalent to the geometrical cross-section given by equation 2.22, with an average impact parameter of $2/3R$. Any deviation between the collision and geometric cross-sections is attributed to a small percentage of particles being transmitted when impact occurs near the droplet edge.⁴⁹ Collisions between the droplets and foreign species take place in a pick-up cell, located downstream from the droplet source, where — because of the relatively large pick-up cross-sections — low partial pressures of the impurity ($10^{-6} - 10^{-7}$ torr) are sufficient for capture.³¹

It has been experimentally observed that the pick-up process is well described by Poisson statistics.^{49,50} The probability of capturing k particles is given by

$$P = \frac{(n\sigma L\gamma)^k}{k!} \exp(-n\sigma L\gamma) \quad (2.23)$$

where σ is the capture cross-section, L is the length of the pick-up cell, n is the number density of the dopant in the pick-up cell, and γ accounts for the relative velocities of the colliding species.⁴⁹

When an atom or molecule is captured by a droplet, the impurity's internal energy, collision energy, and helium-impurity binding energy are all transferred to the

droplet.⁴⁹ The transferred energy is quickly dissipated by the helium through evaporation (within 10^{-11} seconds), returning the droplet to its quiescent state.⁵¹ By this mechanism, the droplet acts as a nano-cryostat, efficiently cooling molecules to sub-Kelvin temperatures. Consequently, evaporation dictates the size of droplets that should be used for a particular experiment because the evaporative loss must be far less than the number of helium atoms in the pre-collision droplet. While a great many details are known about the pick-up process, the actual dynamics of impurity capture remains an open issue.⁴²

2.5 Electron impact ionization

Electron-matter collisions that produce ions constitute one of the most fundamental processes in collision physics. In gas phase collisions, the ionization efficiency is described by the absolute total electron-impact ionization cross-section, σ .⁵² At low electron energies, σ is found to rise from zero once the energy of the colliding electron exceeds the ionization energy of the atom/molecule. Immediately above the ionization energy, σ exhibits an electron energy dependence of $E^{0.127}$.⁵³ Further increase in the impinging electron's energy corresponds to a sharp increase in σ until a maximum is achieved, σ_{\max} . For polyatomic species, σ_{\max} typically occurs between 70 – 80 eV and is the reason 70 eV is the standard in analytical mass spectrometry. Beyond this maximum, σ decreases and eventually tapers off.

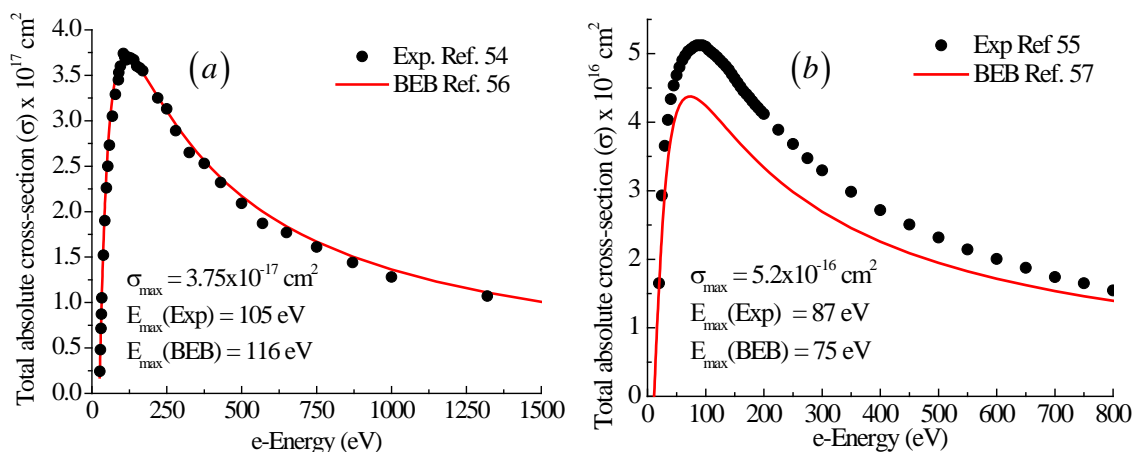


Figure 2.12. The total absolute cross-sections for (a) helium⁵⁴ and (b) acetylene⁵⁵ along with their corresponding theoretical fit calculated using the BEB method.^{56,57} The electron energy at the point of maximum cross-section is displayed for both experiment and BEB.

A direct measurement of absolute cross-sections is challenging, and in most cases relative cross-sections are measured instead. A calibration is then required to convert the measured values into absolute cross-sections. As a consequence, there is considerable variation between reported values of σ , especially when measured with different experimental setups.⁵² To remove the uncertainty, considerable effort has gone into measuring cross-sections for a large selection of molecules using a single apparatus.⁵⁸⁻⁶¹ While this approach has produced consistent results, every apparatus has its limitations. Thus, it is desirable to find an experimental approach that will yield consistent results.

An alternative approach is to determine σ theoretically. Unfortunately, electron impact ionization is a many-body problem, and rigorous quantum mechanical calculation of σ is only feasible for atoms and atomic ions.⁶² However, several semi-empirical and semiclassical models have been developed to circumvent this restriction.^{63,64} One common approach is the so-called additivity model.⁶⁵ This model relies on summing

individual contributions of bonds and functional groups to determine σ_{\max} . The additivity method has been shown to reproduce experimental values of σ_{\max} for alcohols and halocarbons with good accuracy.⁶⁷⁻⁶⁸ Another popular method is the point-like Binary-Encounter-Bethe (BEB) model. BEB uses a weighted combination of modified Mott theory for small-impact parameter collisions, and Bethe cross-section theory for large-impact parameter collisions.^{56,69,70} When combined with a sufficiently high level of *ab initio* calculations, BEB yields cross-sections that are in excellent agreement with experiment.⁵² Moreover, BEB is not limited to calculation of just σ_{\max} . Examples of σ for atoms and molecules are represented in Figure 2.12 by the measured electron impact ionization cross-sections as well as BEB fits for (a) Helium and (b) acetylene. For helium, σ_{\max} is approximately $3.75 \times 10^{-17} \text{ cm}^2$ and occurs when the electron kinetic energy is 105 eV. The maximum total electron impact ionization cross-section for acetylene is $5.2 \times 10^{-16} \text{ cm}^2$ and occurs at an electron energy of 87 eV.

2.5.1 Interpretation of σ_{\max}

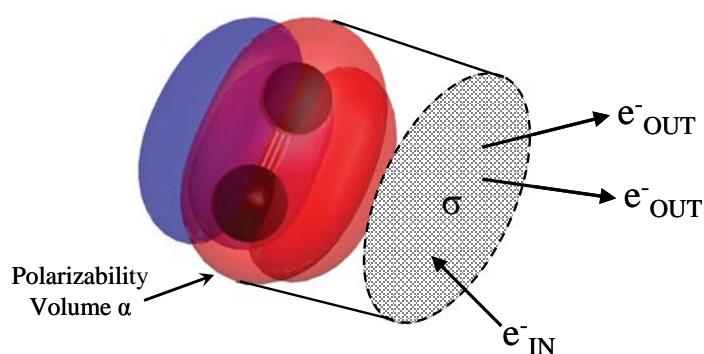


Figure 2.13. Image showing how the polarizability volume acts as an effective cross-section for the process of an incoming electron ejecting a bound electron from a target species.⁵²

The observed shape of an absolute cross-section curve is often explained in terms of a resonance between the de Broglie wavelength of the incoming electron and the size of the atom/molecule's electron cloud. This correlation between σ and the polarizability volume (α) was first observed by Lampe et al.⁷¹ If we envision the electrons that comprise α as a sphere surrounding the target species, then the effective radius of the electron cloud is given by:⁶⁴

$$r_{\alpha} = (3\alpha / 4\pi)^{1/3} \quad (2.24)$$

Combining this radius with the root mean square (rms) radius of the electron density, $(3/5)^{1/2}r_a$, yields a corresponding rms diameter of the molecule:

$$d_{rms} = 2(3/5)^{1/2} (3\alpha / 4\pi)^{1/3} \quad (2.25)$$

The only size-related quantity for the incident electron is its de Broglie wavelength.

$$\lambda = \frac{h}{p} = \left(\frac{h^2}{2mqE} \right)^{1/2} \quad (2.26)$$

where h is Plank's constant, p is the momentum, m is the mass, q is the charge, and E is the kinetic energy of the incoming electron. This suggests that the peak in the ionization efficiency curve may be due to a resonance condition when the incident electron wavelength matches the effective molecular diameter.⁶⁴ This argument is strengthened by using the resonance condition to solve for the electron energy at which σ_{\max} occurs. Setting equations 2.25 and 2.26 equal and solving for E shows:

$$E_{\max} = \left(\frac{5h^2}{24mq} \right) \left(\frac{4\pi}{3\alpha} \right)^{2/3} \quad (2.27)$$

Equation 2.27 correctly predicts the energy of σ_{\max} for most atomic and molecular species. In the molecular case, a rough metric for a local polarizability diameter is the bond length. Consequently, resonance is when the de Broglie wavelength of the incident electron is comparable to various bond lengths of the target molecule. Typical bond lengths in organic molecules lie between 1.3 and 1.5 Å, which correspond to electron energies of 89 and 67 eV, respectively, in good agreement with experiment.

2.6 Production and detection of the ethynyl radical

A number of experimental studies of the ethynyl radical (C_2H) have been carried out in the last thirty years. Many studies have measured the rate coefficients for reactions of C_2H with a variety of neutral molecules.⁷²⁻⁷⁹ Several spectroscopic studies have aimed to understand the vibrationally cold ground state,⁸⁰⁻⁸² vibrational levels of the X state,⁸³⁻⁸⁹ and the electronically excited A state,⁹⁰⁻⁹² while others have used laser induced fluorescence (LIF), UV absorption, and fluorescence detection to examine higher C_2H excited states and C_2 internal excitations.⁹³⁻¹⁰⁴ Although C_2H is a seemingly simple molecule, experimental and theoretical results demonstrate the complexity of this system, and the need for further work.⁹⁷

In many experiments, C_2H is prepared via 193.3 nm photolysis of the C–H bond during supersonic expansion of acetylene (C_2H_2).⁹³⁻¹⁰⁶ [Note that the energy of a 193.3 nm photon (~6.4 eV) is greater than the $D_0(HCC-H)$ of 5.7 eV].¹⁰⁷ Dissociation of acetylene to form vibrationally excited ethynyl radical (C_2H^*) occurs via the mechanisms outlined in Figure 2.14. Briefly, the absorption of a 193.3 nm photon promotes acetylene

to its $1^1A''$ state. This state is diradical-like with a trans-bent geometry, and a C–C bond order of 2.¹⁰⁵ A barrier of $\sim 560\text{ cm}^{-1}$ ¹⁰⁸ inhibits immediate dissociation and arises from an avoided crossing between the $1^1A''$ and the $2^1A''$. Instead, the bottle neck created by the barrier slows the direct production of C_2H^* enough to allow internal conversion (IC) to compete with tunneling through the barrier. IC of the $1^1A''$ state to the dissociative $2^1A'$ state allows acetylene to form C_2H^* . However, dissociation is not instantaneous, and diabatic surface hopping to the $1^1A'$ state at the $2^1A'/1^1A'$ avoided crossing readily occurs.¹⁰⁶ Although, IC to the $1^1A'$ state is possible, it is not considered to be an important reaction pathway.¹⁰⁵ In total, vibrationally excited C_2H is produced primarily in its ground state.¹⁰⁶

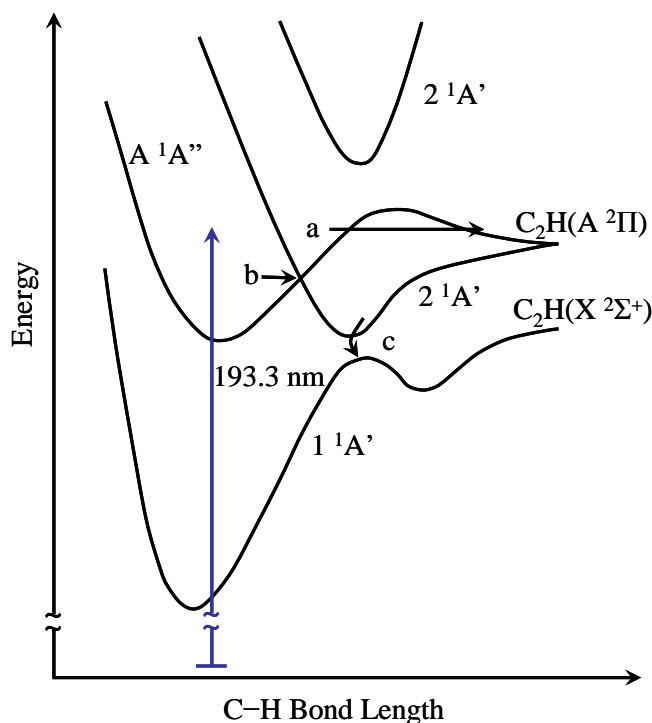


Figure 2.14. Schematic representation of the potential energy surfaces involved in the 193.3 nm photodissociation of acetylene. Formation of excited $C_2H(A^2\Pi)$ occurs via two possible routes: (a) tunneling to the continuum through the potential barrier on the A^1A'' curve and/or (b) through internal conversion to the dissociative $2^1A'$ state. Formation of vibrationally excited $C_2H(X^2\Sigma^+)$ occurs by (c) internal conversion to the $2^1A'$ state followed by subsequent diabatic surface hopping to the $1^1A'$ state at the $2^1A'/1^1A'$ avoided crossing.^{97,105}

The C_2H ground state is linear with $^2\Sigma^+$ symmetry,¹⁰⁹ followed by the electronic A state, which is also linear, but of $^2\Pi$ symmetry. The A state is only $\sim 3600\text{ cm}^{-1}$ above the ground state,⁹¹ where it is speculated that there exist strong couplings between the two states.¹¹⁰ Next is the non-linear B state, which has a CCH angle of $\sim 108^\circ$ and a C-C bond distance that is $\sim 15\%$ longer than the ground state.¹⁰² LIF spectra of the B state ($2^2\Sigma^+$) has been recorded and examined by the Hsu group.⁹⁹⁻¹⁰⁴ They observed that non-radiative processes quickly dominate B state decay when the system is excited to vibrational states that are only a few quanta above the initial transition.¹⁰³ These results,

and the results of Jackson and coworkers,⁹³⁻¹⁰⁴ show that excitation of the ethynyl radical at this energy or higher ultimately leads to dissociation into C₂ and H. This conclusion is in agreement with the theoretical work of Duflot et al.¹¹¹ The calculated potential energy surface of the *B* state shows a shallow well along the C–H coordinate that eventually leads to C₂ and H products (Figure 2.15).

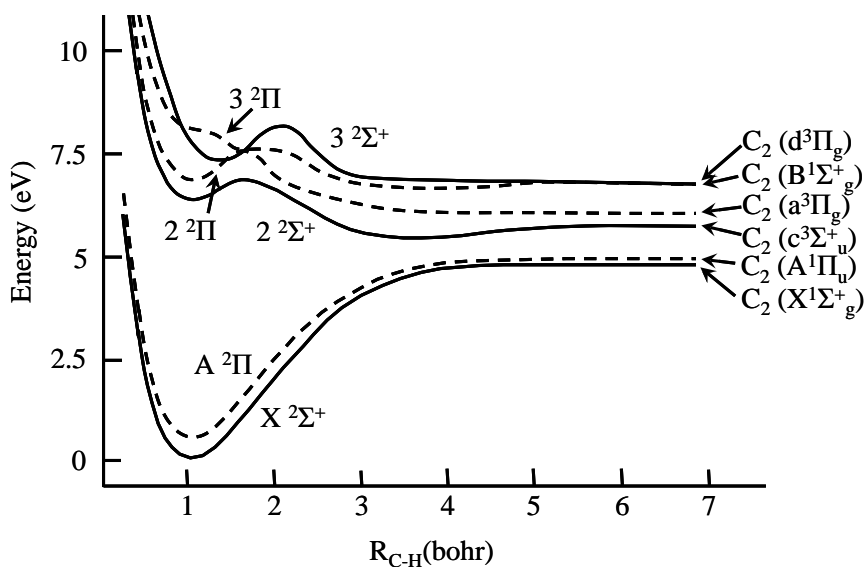


Figure 2.15. Calculated adiabatic potential energy curves for the lowest $^2\Sigma^+$ and $^2\Pi$ states of C₂H as functions of the C–H bond length. Full lines represent Σ^+ symmetry, and dashed lines Π symmetry.¹¹¹

Despite the extensive work that has been carried out on C₂H, a number of important questions remain. For example, what is the $D_0(\text{CC–H})$? Hsu and coworkers reported an upper bound of 39,388 cm⁻¹,¹⁰³ while theoretical estimates place D_0 at 37,422 cm⁻¹.¹¹² To address this, several high-*n* Rydberg time-of-flight¹¹³ experiments were planned that would yield D_0 to a few tens of cm⁻¹. A summary of the work prerequisite to these experiments is given below.

2.6.1 Experiments and results

Several preliminary experiments were performed to try and determine optimal conditions under which to prepare C₂H using supersonic expansion and 193.3 nm photolysis. This involved the setup and alignment of a 780 μm pulsed nozzle (Parker), installation and calibration of a pulsed electron impact ionization TOF mass spectrometer (Jordan TOF products Inc.), and the modification of a vacuum apparatus to allow 193.3 nm light to pass through the expansion chamber. A diagram of the apparatus is shown in Figure 2.16, and useful quantities for acetylene and C₂H are displayed in Table 2.1.

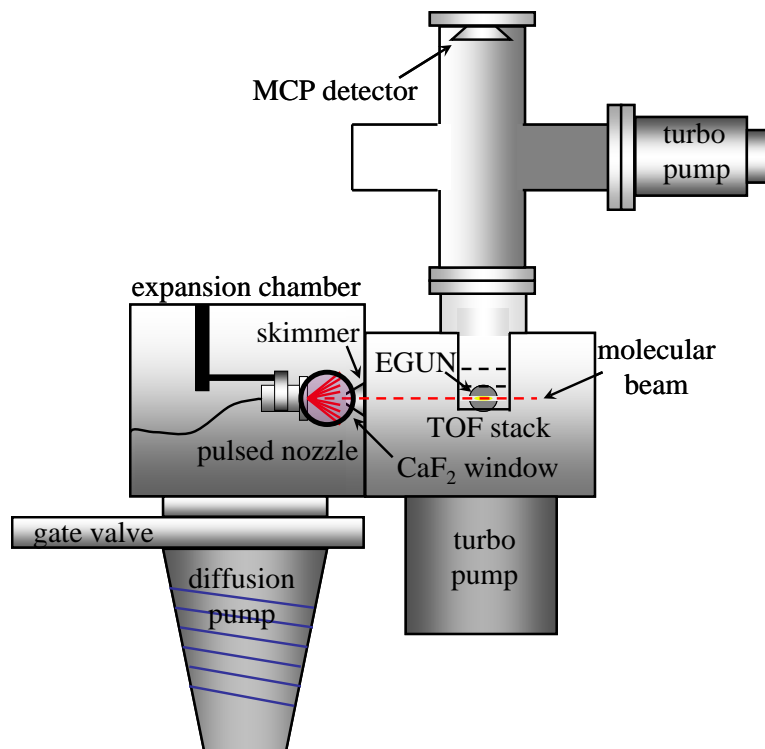


Figure 2.16. Experimental apparatus used for acetylene photolysis. The base pressures were, 2×10^{-6} (torr) in the expansion chamber, 10^{-7} (torr) in the interaction chamber (where the gas was ionized), and 10^{-8} (torr) at the MCP detector. The total length of the TOF was 1 m and voltages of 1500, 1350, and -3500 were used for the repeller, extractor and MCP bias, respectively. The nozzle was set approximately 2 cm away from a 1 mm diameter skimmer and ~ 15 cm away from the interaction region of the TOF.

Molecule	I. P. (eV)	$D_0(\text{C-H})$ (eV)	193.3 nm absorption cross-section (cm^2)
C_2H_2	$11.46 \pm 0.01^{\text{a}}$	$5.712 \pm 0.001^{\text{c}}$	$1.34 \times 10^{-19}^{\text{e}}$
C_2H	$11.6 \pm 0.5^{\text{b}}$	$\sim 4.85^{\text{d}}$	—

References (a) 114, b) 115, (c) 107, (d) 112, (e) 116

Table 2.1. Ionization potential and C–H bond energy for acetylene and the ethynyl radical. The 193.3 nm absorption cross-section of acetylene is for room temperature.

After installation of the TOF, the emission current was set to the manufacturer recommend settings of 1 mA. Focus energy was set to yield optimum signal for each experiment. Several background spectra were acquired at various electron energies in

order to test the performance of the spectrometer. These test spectra were used to determine the operating voltages of the spectrometer. Setting the repeller and extractor plates to 1500 and 1350 volts, respectively, yielded a full width half max (FWHM) of 0.28 amu for argon. The spectra also indicated that the electron energy display on the control panel was not the true electron energy. Therefore, a calibration of the electron energy control was performed. Several gases with known ionization and appearance potentials were leaked into the chamber. The electron energy was then decreased until the mass peak of the respective gas vanished. The energy at which the peak vanished was assumed to be either the ionization or appearance potential and was compared to its accepted literature value. The resultant calibration plot of the actual electron energy vs. the control panel electron energy is shown in Figure 2.17. The data set fits well to a linear regression line, which served as the electron energy calibration for all experiments.

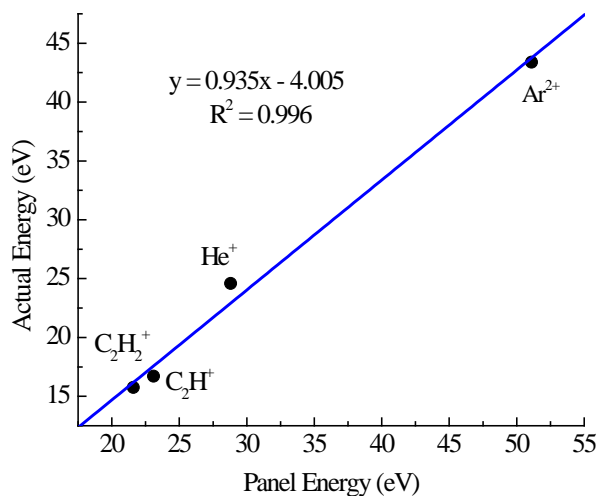


Figure 2.17. Calibration line for the actual electron energy as a function of the electron gun control panel electron energy. The ionization potentials for acetylene and helium as well as appearance potentials of doubly ionized argon and the C_2H ion were used as references for the actual electron energy.

The next experiments were designed to characterize the gas pulse and nozzle operation. Argon was used as the expanding gas. The nozzle was operated at 10 Hz with a backing pressure of 10-15 psig and an open time of 250 μ s. The TOF was run at 50 kHz so that multiple TOF spectra from a single gas pulse could be acquired. A density profile of the gas pulse vs. time is shown in Figure 2.18. It is clear from Figure 2.18 that the expansion is not ideal. The pulse has a fast rise in density until it peaks after \sim 200 μ s then begins to decrease. Yet, it does not drop to zero. Instead, the pulse tapers off and maintains a low signal until completely disappearing almost 2 ms later. The taper indicates that the poppet does not fully close, or possibly bounces, once the nozzle is switched OFF. It was determined that there was also a 115 μ s delay between when the valve was switched ON and when the valve opened. Both behaviors correspond to some form of mechanical delay that will likely vary from one pulse to the next. However, in most experiments the gas pulse is probed at its empirically determined peak. Doing this avoids such inconsistencies because any deviation in the arrival time of the gas pulse at the probing region will likely be small relative to the \sim 100 μ s width of the gas pulse. Moreover, the gas that comprises the tail does not interfere with the gas in the more dense portions of the beam. Thus, the pulse can be treated as if it is of ideal Gaussian shape.

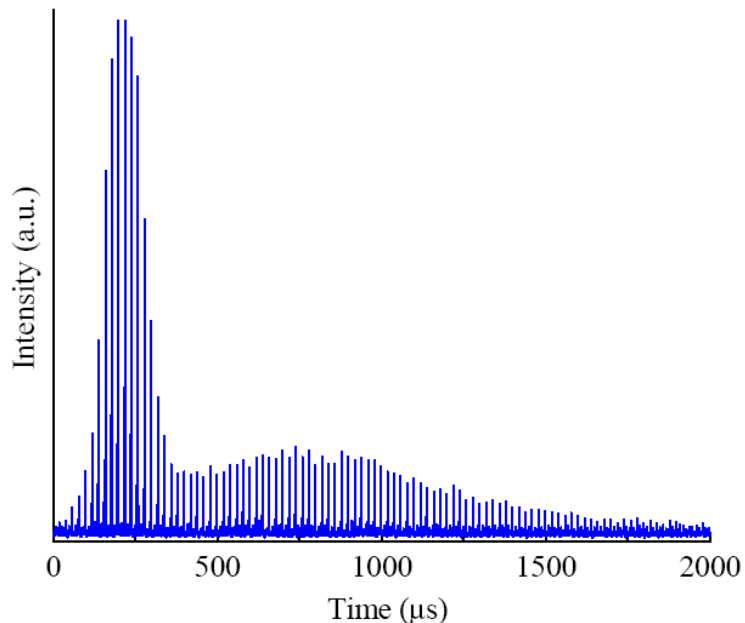


Figure 2.18. Pulsed valve expansion profile using argon. The initial part of the profile is consistent with the 250 μs open time. The long tail is attributed to a mechanical delay in the nozzle's closing.

With the nozzle and TOF characterized and calibrated, a 15% acetylene/argon mixture was prepared. 99.6% pure acetylene was passed through a Matheson gas purifier (Model 450B) and combined with research grade argon. The tank was left overnight to allow for complete mixing. The mixture was expanded using exactly the same conditions as the pure argon expansion. An image of the TOF spectrum for the gas mixture is shown in Figure 2.19a. To better observe any C_2H that may be produced, the electron energy was decreased below the appearance potential of C_2H such that only the C_2H_2 peak was visible in the TOF spectrum (Figure 2.19b). A 193.3 nm beam from an ArF laser was then introduced. Two CaF_2 windows were added to the expansion chamber using custom window mounts, so that the 193.3 nm beam could pass near the nozzle or skimmer (Figure 2.16).

Initially the 193.3 nm beam was directed in front of the nozzle (position 1 of Figure 2.20a). The laser was focused approximately 5 cm after the nozzle with a 100 cm focal length lens at a fluence of 285 mJ cm^{-2} . The relatively high fluence was used to compensate for the low absorption cross-section of acetylene (Table 2.1). Once the light and expanding gas intersected, a faint blue-green glow appeared. It was determined that the glow was the well-known Swan band from C_2 fluorescence.¹¹⁷ The fluorescence indicated that photolysis was indeed occurring. This was also reflected by a depletion of the C_2H_2 peak in the TOF spectrum (Figure 2.19c). Unfortunately, the depletion of the C_2H_2 peak did not correspond to an increase in either C_2H or C_2 signal. Whether the nascent radicals reacted, were ejected from the beam, or were in too little in number was unclear at this time. However, the width and magnitude of the C_2H_2 depletion indicated that the photolysis was interfering with the expansion. As a test, the 193.3 nm beam was aligned just before the skimmer (position 2 of Figure 2.20a). Identical expansion and focusing conditions were used for this experiment. Again, a depletion of C_2H_2 was observed (Figure 2.20d), with no increase in C_2H or C_2 signal. In this case, the depletion was nearly 1/3 in magnitude and narrower in time, confirming that the photolysis in front of the nozzle interfered with the expansion.

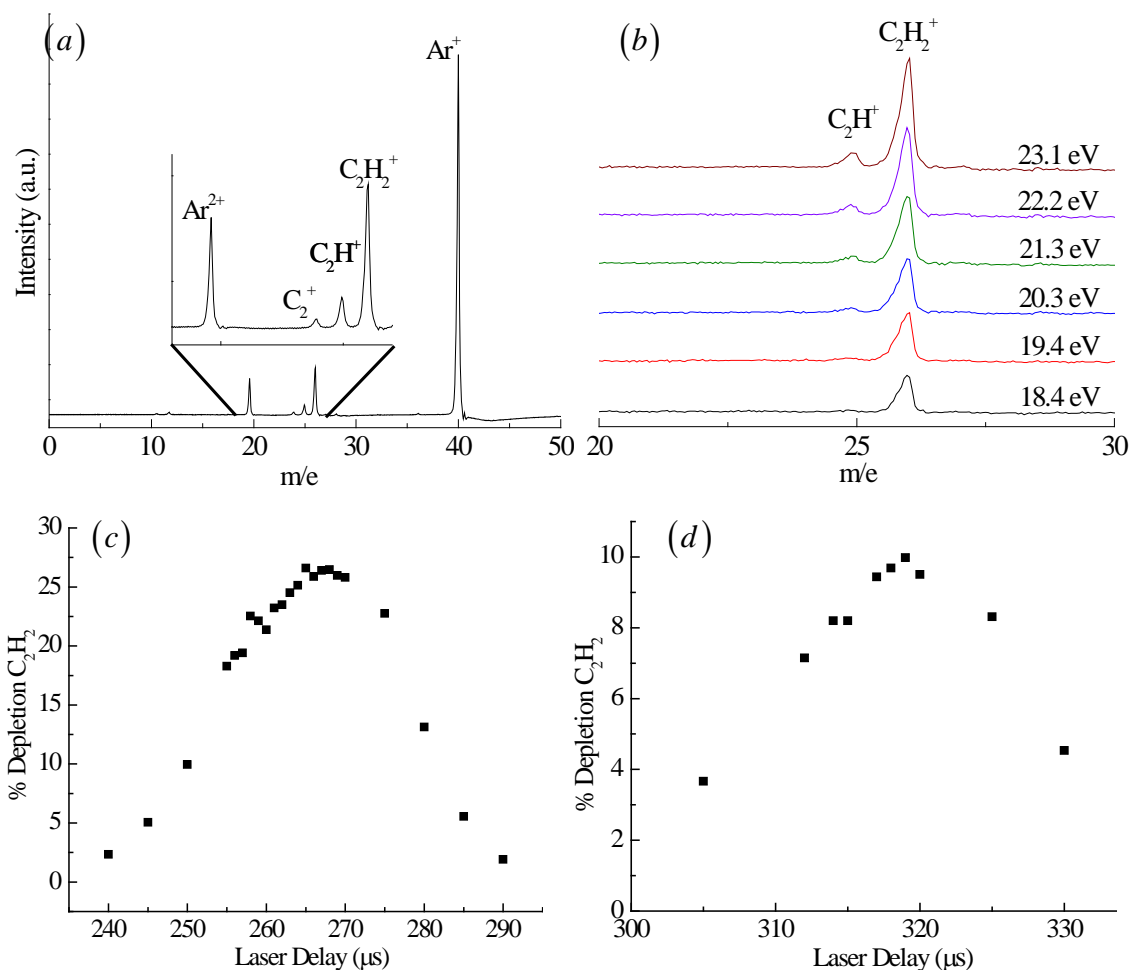


Figure 2.19. (a) TOF mass spectrum of acetylene seeded in argon, taken with an electron energy of 60 eV. The inset in (a) is magnified by 4x to better show the acetylene cracking pattern. (b) TOF spectra at several electron impact energies demonstrate the disappearance of the C₂H peak at sufficiently low electron energy. An electron energy of ~18.4 eV was used in all subsequent experiments to better discern photolyzed C₂H signal from that of fragmented acetylene. (c) The acetylene depletion signal when photolysing directly in front of the nozzle, as opposed to (d), which is the depletion when photolysing in front of the skimmer ~1.5 cm downstream. The FWHM of (c) is roughly 30 μs while that of (d) is only 15 μs, indicating that photolysing in front of the nozzle disturbs the supersonic expansion.

In light of the previous results, or lack thereof, it was decided that acetylene be photolyzed prior to expansion using a technique this is often employed to initiate photochemical reactions.¹¹⁸ To achieve this, the nozzle was first modified by creating a cylindrical cavity centered on the nozzle orifice that was approximately 500 micrometers

deep, but did not affect the orifice. A Suprasil tube, with a 1 mm inner diameter was set into the cavity and glued to the nozzle (Figure 2.20b). The tube was then illuminated with 193.3 nm light during expansion. Again, depletion of the acetylene peak was observed, with no corresponding increase in C_2H . When pure acetylene was expanded during illumination, black soot began to build up inside the tube. This indicated that photolysis and subsequent secondary reactions were occurring, but still no photoproducts were detected. Additionally, Suprasil absorbs a small amount of 193.3 nm and caused the tube to become an opaque milky white over time. Using high fluences, like those needed to compensate for the low acetylene cross-section, caused this to occur quickly, which meant that the tube had to be changed often.

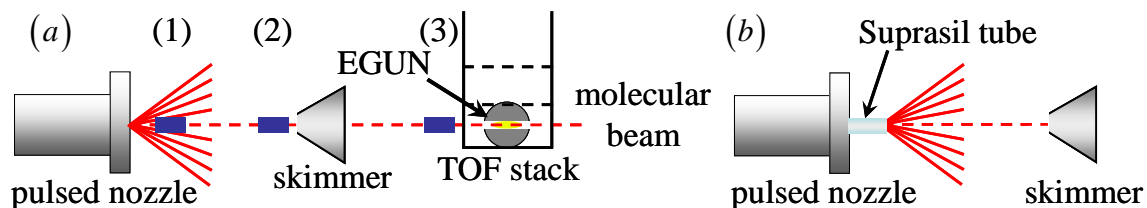


Figure 2.20. (a) Schematic showing the three regions where photolysis of acetylene was attempted. (b) Representation of the suprasil tube attached to the nozzle.

In a final attempt to detect C_2H , acetylene was photolyzed in front of the TOF stack (position 3 in Figure 2.20a). Ideally, photolysing at the ionization region would provide the largest concentration of C_2H that could then be ionized and detected. However, the EGUN physically blocked the laser beam from passing through this region. In light of this, the next best position to photolyze acetylene was in front of the TOF stack. Considering the molecular beam concentration decreases as the inverse of the

distance traveled squared, i.e. $1/d^2$,¹ photolysing as close to the ionization region as possible minimized this loss. Additionally, isotropic recoil velocities generated by photolysis cause the photoproducts to expand in a Newton sphere,¹¹⁹ thereby decreasing the concentration. Thus, photolysing in front of the TOF stack would also minimize the decrease in C_2H concentration associated with the expanding sphere. The radius of the sphere was also reduced by switching the carrier gas from argon to helium. Expanding a dilute concentration of seeder molecules in a light carrier gas increases the beam velocity of the seeder molecule.² The increased beam velocity caused the photolyzed molecules to arrive at the ionization region sooner, and therefore reduced the amount of time in which the Newton sphere could expand.

In light of these changes the laser timing and spatial overlap needed to be determined. This was achieved by first attempting to detect photolysis using 8% hydrogen sulfide (H_2S) in helium. H_2S was chosen because its absorption cross-section at 193.3 nm is ~ 15 x larger than that of acetylene ($6.5 \times 10^{-18} \text{ cm}^{-1}$).¹²⁰ Once optimized, H_2S signal showed a depletion of nearly 50 percent at modest fluences (80 mJ cm^{-2}) and indicated the optimal timing and laser position for photolysis.

Immediately after the optimization, the H_2S mixture was replaced with a similar acetylene mixture and the experiment was run. In this case, no significant depletion was observed, even when expanding pure acetylene and using extremely high laser fluence ($\sim 4.9 \text{ J cm}^{-2}$). However, a difference spectrum (laser on minus laser off) revealed a very small increase in C_2H (inset of Figure 2.21b). While this last approach did produce C_2H , it did not produce an amount that could be effectively studied with the current setup.

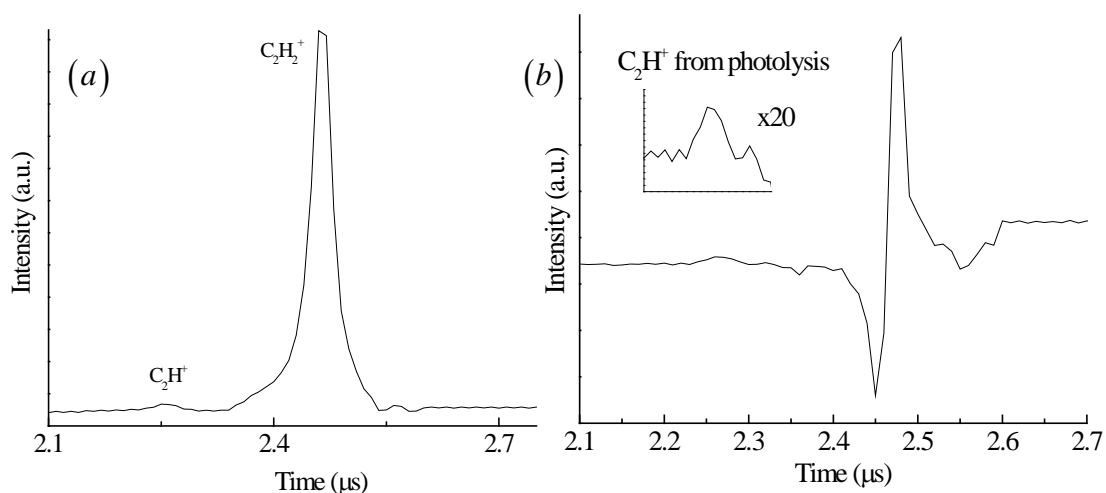


Figure 2.21. (a) Acetylene and ethynyl peaks recorded with 193.3 nm beam directly in front of ionization region of TOF. Pure acetylene and a laser power was $\sim 4.9 \text{ J cm}^{-2}$ was used for this measurement. (b) Difference spectrum for laser on minus laser off. The inset in (b) is the region of the difference spectrum corresponding to C_2H^+ , between 2.2 and 2.35 μs , and shows that a very small amount of photolyzed C_2H is present.

2.6.2 Discussion

Two important results are derived from the above experiments. First, the absence of appreciable radical signal, even when significant depletion was observed, suggests that the radicals either react, are ejected from the beam, absorb further and dissociate, or are too low in concentration to be measured by the current electron gun. Reaction of the nascent C_2H is not expected to be a major factor. The C_2H concentration was kept relatively low to avoid such issues and only when pure acetylene was photolyzed in the Suprasil tube did any type of soot become visible. Ejection of C_2H from the molecular beam was most important after the skimmer where collisions from supersonic expansion have ceased. Without the collisions to oppose the recoil generated from photolysis, the Newton sphere could expand freely. However, this effect was minimized by photolysing

directly in front of the ionization region and using a lighter carrier gas. Absorption beyond the initial photolysis was a concern, especially considering strong C₂ fluorescence was observed when photolysing immediately after the nozzle. The question as to whether all C₂H is quickly photolyzed after creation is further complicated by the absence of the C₂H 193.3 nm absorption cross-section in the literature. However, a range of fluences were used during each attempt at photolysis. And even when the strong glow of C₂ fluorescence was observed, no C₂ was detected. The most likely culprit for the lack of C₂H signal is low electron impact ionization efficiency. The calculation below shows that the probability of ionizing trace amounts of C₂H using electron impact ionization is very low.

The challenge in detecting trace elements using electron impact ionization is producing enough electron current at the desired electron energy to generate a reasonable amount of target ions. For instance, consider an isolated ethynyl radical in the ionizing region of a TOF. Analogous to the saturation condition in optical spectroscopy,³ the probability of ionizing the radical approaches 100% when the electron fluence (ϕ) is comparable to the inverse of the total electron impact ionization cross-section, σ (Section 2.5), i.e. $\phi \approx 1/\sigma$. Thus, if we take the σ of acetylene to be comparable to that of the ethynyl radical, then from Figure 8 $\sigma(\text{ethynyl radical at 20 eV}) \approx 10^{-16} \text{ cm}^2$, which corresponds to an electron fluence of 10^{16} cm^{-2} . For the current setup, the ionizing region has a cross-sectional area (A) of 0.127 cm^2 , and the duration of bombardment (τ) was 5 microseconds. Thus, the required current to achieve ‘saturation’ is:

$$i = \frac{\phi A Q}{\tau} = \frac{10^{16} * 0.127 * 1.602 \times 10^{-19}}{5 \times 10^{-6}} \text{ C/s} = 40.6 \text{ A} \quad (2.28)$$

where Q is the electron charge in Coulombs. Equation 2.28 shows that an electron current of 40.6 amps is needed to produce a flux of 10^{16} cm^{-2} . Unfortunately, the electron gun can only produce a maximum current of 1 mA at 20 eV, which corresponds to a fluence that is $\sim 10^5$ times smaller than what is needed.

The second important result stems from the absence of a C_2H_2 depletion signal when photodissociating in front of the ionization region. This suggests that the absorption cross-section of acetylene at 193.3 nm under these conditions is smaller than the room temperature cross-section reported by Seki et al.¹¹⁶ In fact, all reported cross-sections for C_2H_2 are reported at room temperature. Thus, if thermal population contributes to the room temperature cross-section then cooling the acetylene would cause the cross-section to decrease. Further measurements should be performed to clarify this issue.

2.6.3 Conclusion

Preliminary experiments show that C_2H is not produced in sufficient quantity by 193.3 nm photolysis to be easily detected using the current experimental setup. A significant increase in C_2H concentration or electron current is needed to compensate for the relatively low ionization probability by electron impact ionization. Additionally, a possible drop in the 193.3 nm absorption cross-section of acetylene after supersonic expansion demonstrates the need for absorption cross-section measurements under similar conditions.

2.7 References

1. Ramsey, N. F. *Molecular Beams*; Oxford University Press: New York, NY, **1985**.
2. Miller, D. R. *Atomic and Molecular Beams Methods*; Scoles, G. Ed.; Oxford University Press: New York, NY, **1988**; Vol. I; pp. 14 – 53.
3. Paisner, J. A.; Solarz, R. W.; Chen, H.; *Laser Spectroscopy and Its Applications*; Radziemski L. J.; Solarz R. W.; Paisner, J. A. Ed.; Marcel Dekker: New York, NY, **1987**; pp. 175 – 350.
4. Abramczyk, H. *Introduction to Laser Spectroscopy*; Elsevier: Amsterdam, **2005**.
5. Levenson, M. D. *Introduction to Nonlinear Laser Spectroscopy*; Academic Press: New York, NY, **1982**.
6. Hollas, M. *High Resolution Spectroscopy*; John Wiley & Sons: New York, NY, **1998**.
7. Demtroder, W. *Laser Spectroscopy: Basic Concepts and Instrumentation*, 2nd ed.; Springer: New York, NY, **1998**.
8. McHale, J. L. *Molecular Spectroscopy*. Prentice Hall: Upper Saddle River, NJ, **1999**.
9. Weissler, G. L. *Sci. Light*. **1972**, 21, 89.
10. Schlag, E. W.; Neusser, H. J. *Acc. Chem. Res.* **1983**, 16, 355.
11. Petty, G; Tai, C.; Dalby, F. W. *Phys. Rev. Lett.* **1975**, 34, 1207.
12. Johnson, P. M. *J. Chem Phys.* **1975**, 62, 4562.
13. Ashfold, M. N. R.; Howe, J. D. *Annu. Rev. Phys. Chem.* **1994**, 45, 57.
14. Antonov, V. S.; Letokov, V. S. *Appl. Phys.* **1981**, 24, 89.
15. Johnson, P. M. *Acc. Chem. Res.* **1980**, 13, 20.
16. Letokhov, V. S. *Laser Photoionization Spectroscopy*; Academic Press, Inc.: Orlando, FL, **1987**.

17. Ashfold, M. N. R.; Ledingham, K. W. D. *An Introduction to Laser Spectroscopy*; Andrews, D. L.; Demidov, A. A. Ed.; Plenum Press: New York, NY, **1995**, pp. 35 – 62; pp. 199 – 228
18. Boesl, U.; Neusser, H. J.; Schlag, E. W. *J. Chem. Phys.* **1980**, *72*, 4327.
19. Reilly, J. P.; Kompa, K. L. *J. Chem. Phys.* **1980**, *73*, 5468.
20. Reilly, J. P.; Kompa, K. L. *Adv. Mass. Spectrom.* **1980**, *9*.
21. Wiley, W. C.; McLaren, I. H. *Rev. Sci. Instru.* **1955**, *26*, 1150.
22. Nemirow, C. *Multiphoton Investigation of tris(2-phenylpyridine)iridium*. Ph. D. Dissertation, University of Southern California, Los Angeles, CA, **2011**.
23. McMurry, J. *Organic Chemistry*, 6th ed.; Thomas Learning: Belmont, CA, **2004**.
24. Levine, I. N. *Physical Chemistry*, 5th ed.; McGraw-Hill: New York, NY, **2002**.
25. Onsager, L. *J. Am. Chem. Soc.* **1936**, *58*, 1486.
26. Mataga, N.; Kubota, T. *Molecular Interactions and Electronic Spectra*; Marcel Dekker: New York, NY, **1970**; pp. 371 – 410.
27. Deaton, J. C.; Switalski, S. C.; Kondakov, D. Y.; Young, R. H.; Pawlik, T. D.; Giesen, D. J.; Harkins, S. B.; Miller, A. J. M.; Mickenberg, S. F.; Peters, J. C. *J. Am. Chem. Soc.* **2010**, *132*, 9499.
28. Wilks, J.; Betts, D. S. *An Introduction to Liquid Helium*; Oxford University Press: New York, NY, **1987**.
29. Wheatley, J. *Phys. Today.* **1976**, *29*, 32.
30. Tilley, R. D.; Tilley, J. *Superfluidity and Superconductivity*, 3rd ed.; Institute of Physics Publishing: Bristol, UK, **1990**.
31. Toennies, J. P.; Vilesov, A. F. *Angew. Chem. Int. Ed.* **2004**, *43*, 2622.
32. Toennies, J. P.; Vilesov, A. F. *Annu. Rev. Phys. Chem.* **1998**, *49*, 1.
33. Goyal, S.; Schutt, D. L.; Scoles, G. *Phys. Rev. Lett.* **1992**, *69*, 933.

34. Goyal, S.; Schutt, D. L.; Scoles, G.; Robinson, G. N. *Chem. Phys. Lett.* **1992**, *196*, 123.
35. Harms, J.; Hartmann, M.; Toennies, J. P.; Vilesov, A. F.; Sartakov, B. *J. Mol. Spectrosc.* **1997**, *185*, 204.
36. Harms, J.; Hartmann, M.; Sartakov, B.; Toennies, J. P.; Vilesov, A. F.; *J. Chem. Phys.* **1999**, *110*, 5124.
37. Grebenev, S.; Hartmann, M.; Havenith, M.; Sartakov, B.; Toennies, J. P.; Vilesov, A. F.; *J. Chem. Phys.* **2000**, *112*, 4485.
38. Grebenev, S.; Havenith, M.; Madeja, F.; Toennies, J. P.; Vilesov, A. F.; *J. Chem. Phys.* **2000**, *113*, 9060.
39. Stienkemeier, F.; Vilesov, A. F. *J. Chem. Phys.* **2001**, *115*, 10119.
40. Slipchenko, M. N.; Kuma, S.; Momose, T.; Vilesov, A. F. *Rev. Sci. Instrum.* **2002**, *73*, 1.
41. Northby, J. A. *J. Chem. Phys.* **2001**, *115*, 10065.
42. Barranco, M.; Guardiola, R.; Hernandez, S.; Mayol, R.; Navarro, J.; Pi, M. *J. Low Temp. Phys.* **2006**, *142*, 1.
43. Stienkemeier, F.; Lehmann, K. K. *J. Phys. B* **2006**, *39*, R127.
44. Buchenau, H.; Knuth, E. L.; Northby, J. A.; Toennies, J. P.; Winkler, C. *J. Chem. Phys.* **1990**, *92*, 6875.
45. Buchenau, H.; Toennies, J. P.; Northby, J. A. *J. Chem. Phys.* **1991**, *95*, 8134.
46. Close, J. D.; Federmann, F.; Hoffmann, K.; Quaas, N. *Chem. Phys. Lett.* **1997**, *276*, 393.
47. Gomez, L. F.; Loginov, E.; Sliter, R.; Vilesov, A. F. *J. Chem. Phys.* **2011**, *135*, 154201.
48. Lewerenz, M.; Schilling, B.; Toennies, J. P. *Chem. Phys. Lett.* **1993**, *206*, 381.
49. Lewerenz, M.; Schilling, B.; Toennies, J. P. *J. Chem. Phys.* **1995**, *102*, 8191.

50. Hartmann, M.; Miller, R.; Toennies, J. P.; Vilesov, A. F. *Science*. **1996**, *272*, 1631.
51. Polyakova, E.; Stolyarov, D.; Zhang, X.; Kresin, V. V.; Wittig, C. *Chem. Phys. Lett.* **2003**, *375*, 253.
52. Bull, J. N.; Harland, P. W.; Vallance, C. *J. Phys. Chem. A*. **2012**, *116*, 767.
53. Wannier, G. H. *Phys. Rev.* **1953**, *90*, 817.
54. Shah, M. B.; Elliot, D. S.; McCallion, P.; Gilbody, H. B. *J. Phys. B*. **1988**, *21*, 2751.
55. Zheng, S. H.; Srivastava, S. K. *J. Phys. B*. **1996**, *29*, 3235.
56. Kim, Y. K.; Rudd, M. E. *Phys. Rev. A*. **1994**, *50*, 3954.
57. Kim, Y. K.; Ali, M. A.; Rudd, M. E. *J. Res. Natl. Inst. Stand. Technol.* **1997**, *102*, 693.
58. Bart, M.; Harland, P. W.; Vallance, J. E. *Phys. Chem. Chem. Phys.* **2001**, *3*, 800.
59. Hudson, J. E.; Hamilton, M. L.; Vallance, J. E.; Harland, P. W. *Phys. Chem. Chem. Phys.* **2003**, *5*, 3162.
60. Hudson, J. E.; Weng, Z. F.; Vallance, J. E.; Harland, P. W. *Int. J. Mass Spectrom.* **2006**, *248*, 42.
61. Bull, J. N.; Harland, P. W. *Int. J. Mass Spectrom.* **2008**, *273*, 53.
62. Mark, T. D.; Dunn, G. H. *Electron Impact Ionization*; Springer-Verlag / Wien: New York, NY, **1985**.
63. Deutsch, H.; Becker, K.; Matt, S.; Mark, T. D. *Int. J. Mass. Spectrom.* **2000**, *197*, 37.
64. Harland, P. W.; Vallance, C. *Advances in Gas Phase Ion Chemistry*; Adams, N. G.; Babcock, L. M. Ed.; Jai Press: Greenwich, CT, **1998**; Vol. III; pp. 319 – 358.
65. Otvos, J. W.; Stevenson, D. P. *J. Am. Chem. Soc.* **1956**, *78*, 546.

66. Bart, M.; Harland, P. W.; Hudson, J. E.; Vallance, C. *Phys. Chem. Chem. Phys.* **2001**, *3*, 800.
67. Hudson, J. E.; Hamilton, M. L.; Vallance, C.; Harland, P. W. *Phys. Chem. Chem. Phys.* **2003**, *5*, 3162.
68. Fitch, W. L.; Sauter, A. D. *Anal. Chem.* **1983**, *55*, 832.
69. Hwang, W.; Kim, Y. K.; Rudd, M. E. *J. Chem. Phys.* **1996**, *104*, 2956.
70. Irikura, K. K.; Kim, Y. K.; Ali, M. A. *J. Res. Natl. Inst. Stand. Technol.* **2002**, *107*, 63.
71. Lampe, F. W.; Franklin, J. L.; Field, F. H. *J. Am. Chem. Soc.* **1957**, *79*, 6129.
72. Renlund, A. M.; Shokoohi, F.; Reisler, H.; Wittig, C. *Chem. Phys. Lett.* **1981**, *84*, 293.
73. Laufer, A. H.; Fahr, A. *Chem. Rev.* **2004**, *104*, 2813.
74. Stephens, J. W.; Hall, J. L.; Solka, H.; Yan, W.; Curl, R. F.; Glass, G. P. *J. Phys. Chem.* **1990**, *91*, 5740.
75. Lander, D. R.; Unfried, K. G.; Glass, G. P.; Curl, R. F. *J. Phys. Chem.* **1990**, *94*, 7759.
76. Opansky, B. J.; Seakins, P. W.; Pedersen, J. O. P.; Leone, S. R. *J. Phys. Chem.* **1993**, *97*, 8583.
77. Look, H. V.; Peeters, J. *J. Phys. Chem.* **1995**, *99*, 16284.
78. Lee, S.; Samuels, D. A.; Hoobler, R. J.; Leone, S. R. *J. Geophys. Res.* **2000**, *105*, 15085.
79. Nizamov, B.; Leone, S. R. *J. Phys. Chem. A* **2004**, *108*, 1746.
80. Saykally, R. J.; Veseth, L. *J. Chem. Phys.* **1983**, *80*, 2247.
81. Gottlieb, C. A.; Gottlieb, E. W.; Thaddeus, P. *Astrophys. J.* **1983**, *264*, 740.
82. Padovani, M.; Walmsley, C. M.; Tafalla, M.; Galli, D.; Muller, J. S. P. *Astron. Astrophys.* **2009**, *505*, 1199.

83. Killian, T. C.; Gottlieb, C. A.; Thaddeus, P. *J. Chem. Phys.* **2007**, *127*, 114320.
84. Kanamori, H.; Seki, K.; Hirota, E. *J. Chem. Phys.* **1987**, *87*, 73.
85. Kanamori, H.; Hirota, E. *J. Chem. Phys.* **1988**, *89*, 3962.
86. Kawaguchi, K.; Amano, T.; Hirota, E. *J. Mol. Spectrosc.* **1988**, *131*, 58.
87. Stephens, J. W.; Yan, W.; Richnow, M.; Solka, H.; Curl, R. F. *J. Mol. Struct.* **1988**, *190*, 41.
88. Ervin, K. M.; Lineberger, W. C. *J. Phys. Chem.* **1991**, *95*, 1167.
89. Yan, W.; Amano, T. *J. Chem. Phys.* **1993**, *99*, 4312.
90. Yan, W.; Hall, J. L.; Stephens, J. W.; Richnow, M. L.; Curl, R. F. *J. Chem. Phys.* **1987**, *86*, 1657.
91. Yan, W.; Dane, C. B.; Zeitz, D.; Hall, J. L.; Curl, R. F. *J. Mol. Spectrosc.* **1987**, *123*, 486.
92. Pfelzer, C.; Havenith, M.; Peric, M.; Murtz, P.; Urban, W. *J. Mol. Spectrosc.* **1996**, *176*, 28.
93. Urdahl, R. S.; Bao, Y.; Jackson, W. M. *Chem. Phys. Lett.* **1991**, *178*, 425.
94. Blunt, V. M.; Lin, H.; Sorkhabi, O.; Jackson, W. M. *Chem. Phys. Lett.* **1996**, *257*, 347.
95. Sorkhabi, O.; Blunt, V. M.; Lin, H.; Xu, D.; Wrobel, J.; Price, R.; Jackson, W. M. *J. Chem. Phys.* **1997**, *107*, 9842.
96. Sorkhabi, O.; Blunt, V. M.; Lin, H.; A'Hearn, M. F.; Weaver, H. A.; Arpigny, C.; Jackson, W. M. *Sci.* **1997**, *45*, 721.
97. Mebel, A. M.; Hayashi, M.; Jackson, W. M.; Wrobel, J.; Green, M.; Xu, D.; Lin, S. H. *J. Chem. Phys.* **2001**, *114*, 9821.
98. Apaydin, G.; Fink, W. H.; Jackson, W. M. *J. Chem. Phys.* **2004**, *121*, 9368.
99. Hsu, Y.; Wang, P.; Yang, M.; Papousek, D.; Chen, Y.; Chiang, W. *Chem. Phys. Lett.* **1992**, *190*, 507.

100. Hsu, Y.; Lin, J. J.; Papousek, D.; Tsai, J. *J. Chem. Phys.* **1993**, *98*, 6690.
101. Hsu, Y.; Shiu, Y.; Lin, C. *J. Chem. Phys.* **1995**, *103*, 5919.
102. Chiang, W.; Hsu, Y. *J. Chem. Phys.* **1999**, *111*, 1454.
103. Chiang, W.; Hsu, Y. *J. Chem. Phys.* **2000**, *112*, 7394.
104. Wang, J.; Hsu, Y.; Lin, K. *J. Phys. Chem. A* **1997**, *101*, 6593.
105. Wodtke, A. M.; Lee, Y. T. *J. Phys. Chem.* **1985**, *89*, 4744.
106. Zhang, J.; Reihn, C. W.; Dulligan, M.; Wittig, C. *J. Chem. Phys.* **1995**, *103*, 6815.
107. Mordaunt, D. H.; Ashfold, M. N. R. *J. Chem. Phys.* **1994**, *101*, 2630.
108. Hashimoto, N.; Yonekura, N.; Suzuki, T. *Chem. Phys. Lett.* **1997**, *264*, 545.
109. Gottlieb, C. A.; Gottlieb, E. W.; Thaddeus, P. *Astrophys. J.* **1983**, *264*, 740.
110. Sharp-Williams, E. N.; Roberts, M. A.; Nesbitt, D. J. *J. Chem. Phys.* **2011**, *134*, 064314.
111. Duflot, D.; Robbe, J., Flament, J. *J. Chem. Phys.* **1994**, *100*, 1236.
112. Cui, Q.; Morokuma, K. *J. Phys. Chem.* **1998**, *108*, 626.
113. Schneider, L.; Meier, W.; Welge, K. H.; Ashfold, M. N. R.; Western, C. *J. Chem. Phys.* **1990**, *92*, 6578.
114. Franklin, J. L.; Field, F. H. *J. Amer. Chem. Soc.* **1954**, *76*, 1994.
115. Wyatt, J. R.; Stafford, F. E. *J. Phys. Chem.* **1972**, *59*, 1913.
116. Seki, K.; Okabe, H. *J. Phys. Chem.* **1993**, *97*, 5284.
117. Smith, G. P.; Park, C.; Schneiderman, J.; Luque, J. *Comb. and Flame* **2005**, *141*, 66.
118. Loomis, R. A.; Schwartz, R. L.; Lester, M. I. *J. Chem. Phys.* **1996**, *104*, 6984.

119. Ashfold, M. N. R.; Nahler, N. H.; Orr-Ewing, A. J.; Vieuxmaire, O. P. J.; Toomes, R. L.; Kitsopoulos, T. N.; Garcia, I. A.; Chestakov, D. A.; Wu, S.; Parker, D. H. *Phys. Chem. Chem. Phys.* **2006**, *8*, 26.
120. Watanabe, K.; Jursa, A. S. *J. Chem. Phys.* **1964**, *41*, 1650.

Chapter 3

Photoionization of tris(2-phenylpyridine)iridium

3.1 Introduction

Electroluminescent diodes that use organic and organometallic materials are referred to as organic (organometallic) light emitting diodes (OLED's). Such devices and the materials that comprise them have been the subject of intense research in recent years due to potential applications, most notably in display technologies.¹⁻⁵ The optimization of a given device architecture requires attention to the many interactions that transpire within and among the constituents. In this paper the photoionization of an important OLED species: tris(2-phenylpyridine)iridium, hereafter referred to as Ir(ppy)₃, is examined. Introductory comments are given below to provide context for what follows. A recent review¹ and book² by Yersin (especially the chapter by Yersin and Finkenzeller) provide excellent overviews of the state-of-the-art of OLED research, including a number of fundamental electronic structure considerations.

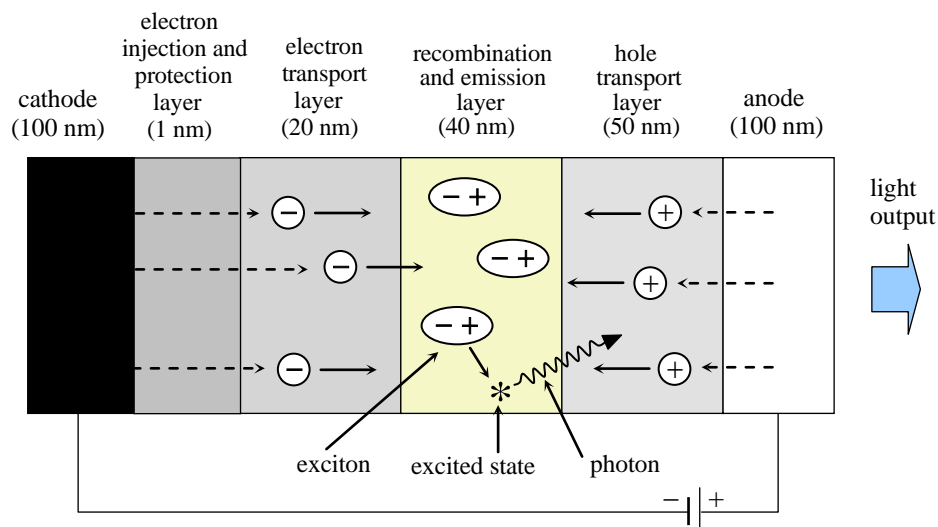


Figure 3.1. This schematic indicates important features of an OLED (not to scale, typical dimensions are given in parentheses). Electrons are injected from the cathode through a thin protection layer into the electron transport layer, which typically consists of an amorphous organic material. Holes are injected into the hole transport layer from an optically transparent anode (typically an $\text{In}_2\text{O}_3 / \text{SnO}_2$ composite) that permits light to exit the device. In the recombination and emission layer, electron-hole pairs form excitons that relax to the dopant excited states (indicated by an asterisk *) that emit photons. Adapted from reference 2.

A typical device consists of layers of compounds sandwiched between electrodes that inject electrons and holes into layers.¹⁻⁵ Figure 3.1 illustrates the most important features. A number of additional layers that further enhance device performance have been omitted to facilitate focusing on the most important processes. When a voltage is applied across the electrodes, electrons are injected from the cathode through a thin (typically ≤ 1 nm) electron injection and protection layer into the lowest unoccupied molecular orbitals (LUMO's) of molecules in the electron transport layer, which typically consists of an amorphous material such as Alq_3 ($q = 8\text{-quinolinolato-O,N}$).^{6,7} The injected electrons migrate slowly by directed site-to-site (polaron) hopping driven by the applied field.

The anode injects holes by removing electrons from the highest occupied molecular orbitals (HOMO's) of molecules in the hole-transport layer. The electrons and holes move toward each other under the influence of the field and form excitons in an emitter-doped recombination layer. Ideally, the excitons are highly excited states of the emitter molecules, rather than of the organic host, though the latter also can also result (ultimately) in the desired excitation.⁸ Electronic excitation cascades down to the molecular excited states (indicated by an asterisk *) that emit photons. The photons exit via the optically transparent anode, which typically consists of a mixture of In₂O₃ and SnO₂, *i.e.*, indium tin oxide (ITO).^{4,5}

Each charge carrier has spin. In the case of a hole, the spin is that of the residual electron. Because the spins of a combining electron and hole are uncorrelated, both singlet and triplet excitons are formed. Specifically, the spins combine to give one singlet and three triplets. It is generally accepted that each of the four states is formed with equal probability. In other words, three triplets are created for each singlet.^{1-3,9}

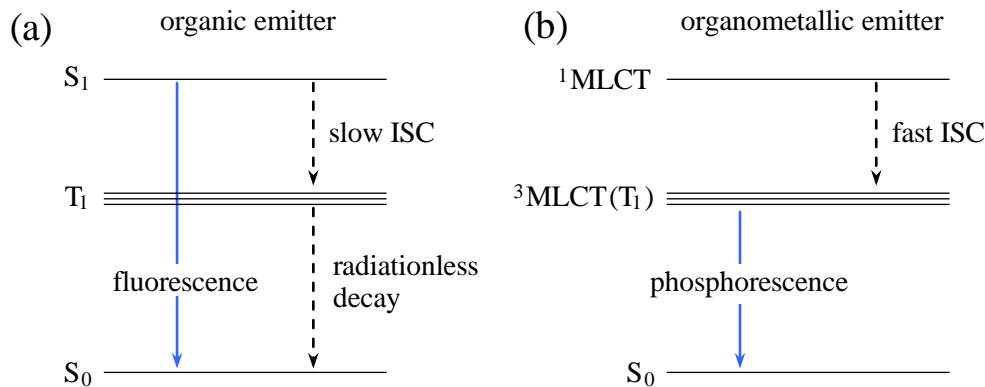


Figure 3.2. (a) Organic molecules (negligible spin-orbit coupling) emit only from the lowest excited singlet S_1 . Because $T_1 \rightarrow S_0$ emission is extremely weak, triplet excitation is lost through radiationless decay rather than photon emission, and consequently the maximum quantum yield is 25%. (b) In triplet harvesting, electron-hole recombination leads to excitons having a triplet-to-singlet population ratio of 3:1. Excitation cascades down the triplet and singlet manifolds, with internal conversion (IC) and intersystem crossing (ISC) resulting in excitation ultimately residing in the lowest triplet, ${}^3\text{MLCT}(T_1)$, which emits photons. An organometallic compound (in which spin-orbit coupling (SOC) is strong) such as $\text{Ir}(\text{ppy})_3$ experiences relatively fast ISC and efficient $T_1 \rightarrow S_0$ phosphorescence. This can result in quantum yield approaching 100%.

Referring to Figure 3.2(a), following the cascade from the initially formed excitons to lower energies, organic emitters, *e.g.*, polyfluorenes,¹⁰ undergo fluorescence from the excited singlet S_1 . Phosphorescence from the lowest triplet (whose sublevels are shown separated from one another for clarity) is, for all practical purposes, eliminated because of the long triplet spontaneous emission lifetimes that are characteristic of the weak spin-orbit coupling (SOC) regime. Because of these long spontaneous emission lifetimes, T_1 decays non-radiatively. As a result, organic emitters have low electroluminescent quantum yield.¹¹ In the limit of negligible $T_1 \rightarrow S_0$ emission, the maximum quantum yield is 25%.

Certain metal-ligand complexes undergo efficient phosphorescence following photoexcitation and / or the passage of electric current through solid hosts that contain

these complexes.^{4-7,12} As mentioned earlier, the latter means of excitation is attractive from the point of view of display technologies. Among the most promising of these complexes is Ir(ppy)₃ and similar species.³ Seminal and extensive contributions by the groups of Thompson,^{4,12,14,15} Forrest,^{4,12,13,15} and Yersin^{16,17} have demonstrated the high potential of this system, and promising paths to device fabrication have been identified.^{1,2,4-7,12,15} Related materials can be used to obtain different emission wavelengths such that the primary colors (red, green, and blue) are obtained. For example, this tuning can be achieved by using electron withdrawing and donating groups substituted at the ppy (2-phenylpyridine) ligand.^{15,18}

Referring to Figure 3.2(b), the triplet states can be made to do useful work by employing a transition metal complex in which the transition-metal atom is responsible for strong SOC.¹⁻³ In such cases, the intersystem crossing (ISC) rate from ¹MLCT to ³MLCT (T₁) is sufficiently fast to inhibit fluorescence from the lowest excited singlet.¹⁹⁻²² The acronym MLCT stands for metal-to-ligand charge transfer. This label can be somewhat misleading, as the situation can be more complicated.²³⁻²⁵ For the sake of brevity, hereafter we shall use the label T₁ instead of ³MLCT, with the understanding that this T₁ bears no resemblance to the one in Figure 3.2(a), in the sense that it contains enough singlet character to ensure high phosphorescence quantum yields. As a result of efficient energy transfer processes, both singlet and triplet excitons populate the T₁ substates, which decay predominantly via phosphorescence.

This is referred to as triplet harvesting.¹⁻³ Strong SOC significantly increases the phosphorescence rate, enabling it to compete favorably with radiationless decay, and

quantum yields therefore can approach 100%.^{6,12} A number of organometallic (specifically, organo-transition-metal) complexes have been used as phosphor dopants in OLED's to overcome the efficiency limit imposed by the absence of sufficient spin-orbit interaction.^{1-3,26}

Internal conversion (IC) and ISC mechanisms are enlisted frequently. Though understood separately, these are unruly in systems that consist of many potential energy surfaces (PES's), unknown coupling parameters, and condensed phase host environments, leaving open important issues: (i) electronic structure of low-lying singlets and triplets including the role of spin-orbit interaction; (ii) vibrational relaxation, *e.g.*, from the regime of quantum chaos to that of good quantum numbers; (iii) interactions with host environments; (iv) electron-hole recombination and transport; and so on.

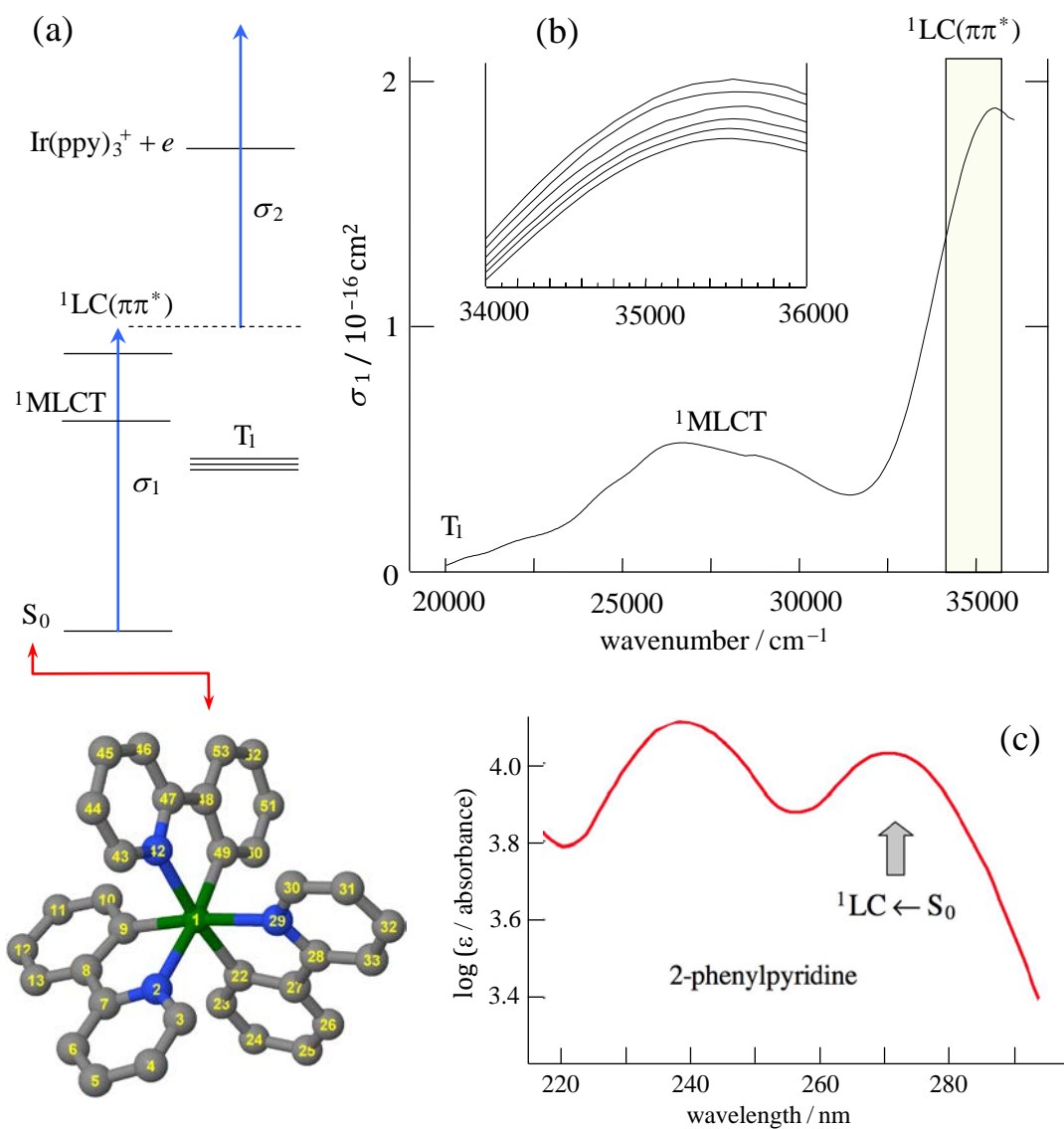


Figure 3.3. (a) Photoexcitation of ligand-centered ${}^1\text{LC}(\pi\pi^*)$ is accompanied by rapid radiationless decay: IC to ${}^1\text{MLCT}$ followed by ISC to the levels labeled T_1 (energies are not to scale).²⁸ (b) Absorption spectrum of $\text{Ir}(\text{ppy})_3$ in dimethylformamide at 414 K. Note the large s_1 absorption cross-sections (*i.e.*, units of 10^{-16} cm^2).²⁹ The yellow boxed region, $34\,150\text{--}35\,775 \text{ cm}^{-1}$ ($4.234\text{--}4.435 \text{ eV}$), corresponds to the portion of the ${}^1\text{LC} \leftarrow S_0$ system examined in this work. Inset: changing the temperature over the range 295–414 K has a minimal effect on the absorption spectrum in the energy range of interest; only slight broadening is observed. In order, from the top trace, the temperatures are: 295, 333, 353, 383, 408, and 414 K. The vertical axis in the inset is not labeled, as the curves are offset from one another for clarity. They are nearly identical over the indicated range. (c) Absorption spectrum of solution phase 2-phenylpyridine, adapted from reference 30. The ${}^1\text{LC} \leftarrow S_0$ feature is analogous to the one in $\text{Ir}(\text{ppy})_3$.

Not surprisingly, many singlets and triplets in the energy region of interest need to be taken into consideration. SOC is effective because of near resonances among singlets and triplets, as well as approximate symmetries. Crossings and near crossings of PES's facilitate couplings, and this likely plays an important role. For Ir(ppy)₃, the papers of Nozaki and Nozaki and coworkers do a good job of combining SOC with time dependent density functional theory (TDDFT) calculations of low-lying singlets and triplets.^{25,27} For example, Table 6 in reference 25 lists energy, singlet fraction, and oscillator strength for 140 low-lying excited states. It is seen that spin-orbit interaction plays an important role in coupling the triplet and singlet manifolds.

To understand what happens in OLED devices, our understanding of an isolated entity such as Ir(ppy)₃ must evolve to one of the larger system of Ir(ppy)₃ plus its host. In principle we would like to refine the theory of an isolated molecule such as Ir(ppy)₃ as much as possible before addressing the challenge presented by the environment. To this end, one of the most important and fundamental properties of a molecule is its ionization: vertical and adiabatic ionization energies, associated orbital and structural changes, etc. Yet, little is known about the ionization of Ir(ppy)₃. This is one of the factors that motivated the present study, in which the photoionization of gaseous Ir(ppy)₃ has been examined using a 2-photon photoionization scheme in which the ligand-centered ¹LC($\pi\pi^*$) state, hereafter referred to as ¹LC, serves as the intermediate (Figure 3.3). The ¹LC state is, however, an interesting intermediate in that radiationless processes (IC and ISC) rapidly transfer excitation to T₁, from which photoionization takes place. A 1-

photon photoionization experiment (*i.e.*, using 193.3 nm radiation from an ArF excimer laser) was carried out as well.

Referring to Figure 3.3, it proved possible to isolate 2-photon photoionization and characterize it over the portion of the ${}^1\text{LC} \leftarrow \text{S}_0$ system indicated by the yellow box. It turned out that photoionization could be achieved with no discernible ion fragmentation. In other words, at sufficiently low fluence, the parent ion, $\text{Ir}(\text{ppy})_3^+$, dominates the mass spectrum. Large molecules such as $\text{Ir}(\text{ppy})_3$ have high densities of electronic states at energies near and above ionization threshold, and it is not always feasible to eliminate the absorption of photons beyond the ionizing transition. In the present case, however, the very large σ_1 values (*i.e.*, $> 10^{-16} \text{ cm}^2$, reference 29, see Figure 3.3) and, following absorption of the second photon, rapid radiationless decay in competition with ionization (discussed later) help make this possible.

From these 2-photon photoionization experiments, an upper bound to the vertical ionization energy (VIE) was obtained subject to a reasonable assumption about the disposition of $\text{Ir}(\text{ppy})_3$ vibrational energy in the $\text{Ir}(\text{ppy})_3^+$ ion, namely, that T_1 vibrational excitation is transferred more-or-less intact to the cation.³¹ As mentioned above, 1-photon photoionization at 193.3 nm ($51\,730 \text{ cm}^{-1}$, 6.414 eV) was also achieved. Again using the assumption that parent vibrational excitation is carried over to the cation yields an approximate upper bound of 6.4 eV. This value agrees with calculations carried out in our group, which places both the VIE and the adiabatic ionization energy (AIE) at approximately 5.9 eV, as well as a previous calculation that places the VIE at approximately 5.94 eV.³²

It is concluded that the ionization energy (both VIE and AIE) of gaseous Ir(ppy)₃ is in the vicinity of 6 eV. This is at odds with a value of 7.2 eV surmised from energy loss spectra, indicating the need to reinterpret the peak at 7.2 eV in the energy loss spectra.³³ It is also shown that the absorption spectrum can be reproduced rather well using vertical excitation from the S₀ equilibrium geometry. This supports the assumption that vibrational excitation is carried more-or-less intact to the cation.

In the context of applications that involve organic photovoltaics (OPV's) and OLED's,¹ a molecule's ionization energy (IE) is one of its key properties, as it quantifies a system's electron-donating ability and it is related to the reduction potential. For optimal performance of materials used in OLED devices, the IE's and electron affinities (EA's) (commonly referred to as HOMO and LUMO energies, respectively) of molecules in the active (*i.e.*, light-generating in OLED's and exciton-generating in OPV's) layer needs to be matched to the energy levels of the electrodes. The fact that the IE of Ir(ppy)₃ is low augurs well for its use in OLED devices. Indeed, it is significantly lower than those of either 2-phenylpyridine (8.0 eV)³⁴ or a bare iridium atom (8.967 eV).³⁵

3.2 Experimental methods and results

The absorption spectra of Ir(ppy)₃ shown in Figure 3.3 were recorded using a Varian Cary 300 spectrophotometer. Solutions were prepared by dissolving 6 mg of Ir(ppy)₃ (provided by the Thompson group at USC) in 125 mL of dimethylformamide (DMF). This solvent was chosen because its high boiling point (426 K)³⁶ enabled spectra to be collected at temperatures up to 414 K. Spectra were also recorded using the solvent

dichloromethane (DCM). Though its UV transmission is superior to that of DMF, it cannot be used at the higher temperatures because its boiling point is 313 K.³⁶ No significant spectral differences were observed with these solvents. Heating was achieved by wrapping the cuvettes in resistive wire and passing current through the wire. Temperature was monitored with a thermocouple.

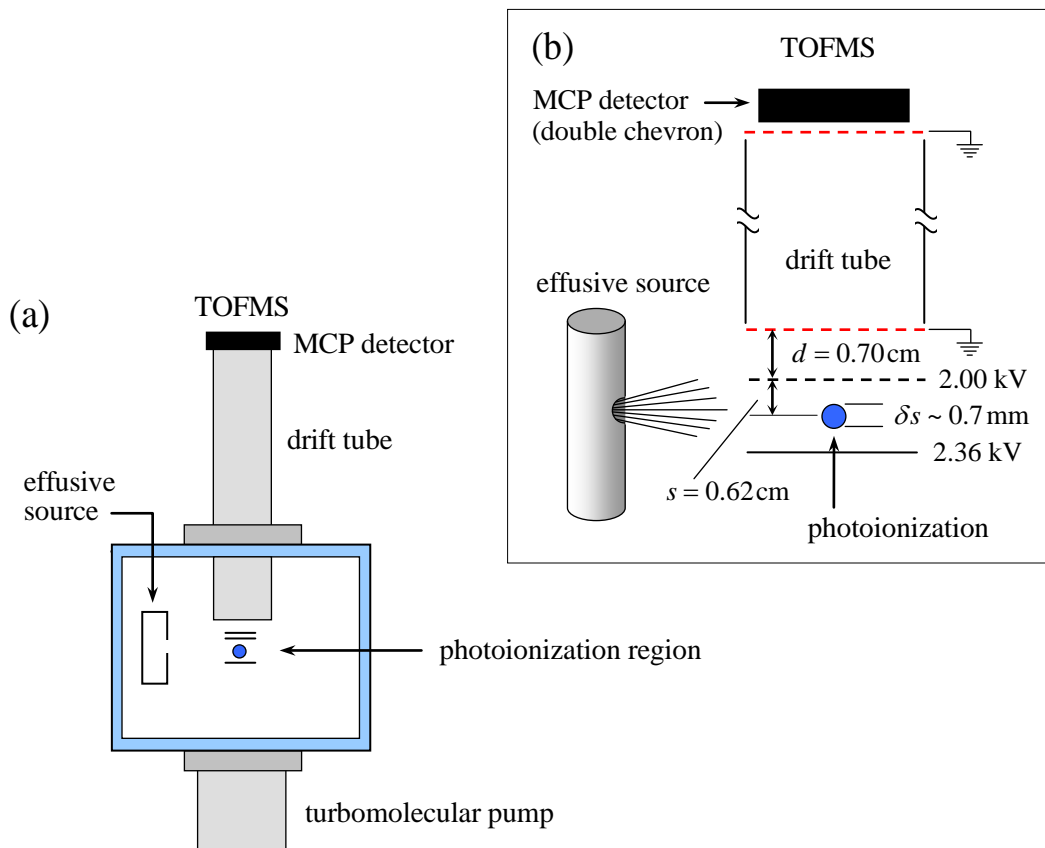


Figure 3.4. Schematic of the experimental arrangement: (a) The main vacuum chamber has a base pressure of 2×10^{-9} Torr. (b) Details of the time-of-flight mass spectrometer (TOFMS): Typical mass resolution was $m/\Delta m \sim 200$.

Laser photoionization was carried out in a chamber that was evacuated using a turbomolecular pump (Leybold Turbovac 1000C), as indicated in Figure 3.4(a). The base pressure was 2×10^{-9} Torr. Solid $\text{Ir}(\text{ppy})_3$ was loaded into a stainless steel cylinder and a

0.5 cm diameter aperture allowed Ir(ppy)₃ vapor to effuse into the chamber. The cylinder was heated using resistive wire. During operation, the cylinder temperature was maintained at approximately 500 K, and the chamber pressure was 5×10^{-9} Torr. At 500 K there was no thermal decomposition of the Ir(ppy)₃ sample.

Referring to Figure 3.4, mass spectra were recorded using a time-of-flight mass spectrometer (TOFMS). Photoions were produced between two electrodes: a repeller plate and an extractor that consists of a metal ring with a fine nickel mesh in the center. Ions receive an additional 2 kV of kinetic energy after passing through the extractor. They then drift for 51.3 cm before arriving at the double-chevron microchannel plate (MCP) detector. The two meshes indicated with red provide a ground shield, ensuring a field-free drift region. Calibration was carried out using NO photoionization with a variety of voltages applied to the electrodes. The NO⁺ flight times, in combination with the distances indicated in Figure 3.4 (*i.e.*, $d = 0.7$ cm, $s = 0.62$ cm, and $\Delta s \sim 0.7$ mm), enabled the length of the drift region to be determined accurately.

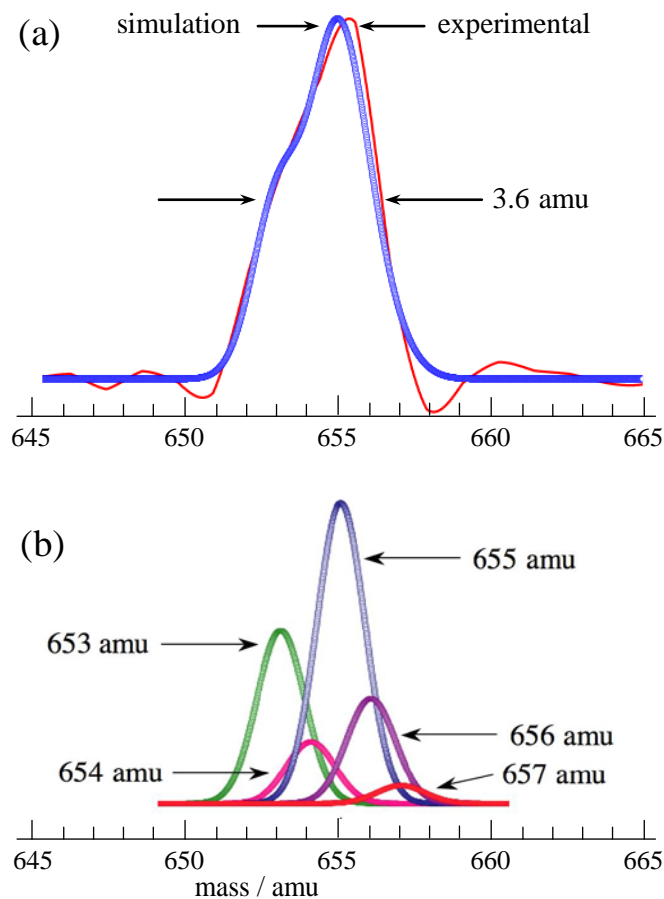


Figure 3.5. With 415 mJ cm^{-2} of 35673 cm^{-1} (4.423 eV) radiation, only the Ir(ppy)_3^+ parent ion is observed (*vide infra* Figure 3.8). The Ir(ppy)_3^+ peak consists of contributions from the major isotopologues (see text for details). (a) The experimental curve (red) is the average of several traces, each of which is comprised of ~ 1000 individual spectra. The blue curve is obtained using the natural isotope abundances and assigning a 2.35 amu FWHM to each mass, as indicated in (b). This fits the experimental trace [red curve in (a)] rather well.

Resolution was optimized at the parent ion mass by adjusting the experimental parameters to make the Ir(ppy)_3^+ peak as narrow as possible. Voltages of 2.36 and 2.00 kV were applied to the repeller and extractor electrodes, respectively. A voltage of approximately -1.9 kV was applied to the MCP detector. The magnitude of this voltage was increased over time to counteract degradation of the detector. Signal acquisition was

carried out using a dual channel Gage Compuscope CS-8012A. The sample rate was 100 MS / s, providing 10 ns bin widths. The repetition rates were those of the lasers, 20 Hz for the 2-photon studies and 10 Hz for the 1-photon study. Typically, ~ 1000 individual spectra were summed. The TOF spectra were processed using custom Labview 8.5.1 programs to yield the mass spectra.

Under these conditions, the Ir(ppy)_3^+ signal shown in Figure 3.5(a) (solid red line) was recorded using $35\,673\text{ cm}^{-1}$ (4.423 eV) radiation and a fluence of $415\text{ }\mu\text{J cm}^{-2}$. The trace shown is the average of several traces. The peak has a full width at half maximum (FWHM) of approximately 3.6 amu. A significant percentage of this width is due to the isotopic composition of the Ir(ppy)_3 sample. Though the natural abundance of ^{13}C is only 1.07%, Ir(ppy)_3^+ contains 33 carbon atoms. Consequently, (rounded to the nearest tenth of a percent) 70.1% of the Ir(ppy)_3 molecules contain only ^{12}C atoms, 25.0% contain one ^{13}C atom, 4.3% contain two ^{13}C atoms, 0.5% contain three ^{13}C atoms, and a negligible percentage contain more than three ^{13}C atoms. Thus, ^{13}C plays a significant role in the mass spectra. Including the natural abundances of the two iridium isotopes (*i.e.*, 62.7% and 37.3% for 193 and 191 amu, respectively) yields the following isotopologues, where the subscript on C denotes the number of ^{13}C atoms in Ir(ppy)_3 :

$^{191}\text{Ir}/^{13}\text{C}_0$ 653 amu 26.2%	$^{193}\text{Ir}/^{13}\text{C}_0$ 655 amu 44.0%
$^{191}\text{Ir}/^{13}\text{C}_1$ 654 amu 9.3%	$^{193}\text{Ir}/^{13}\text{C}_1$ 656 amu 15.7%
$^{191}\text{Ir}/^{13}\text{C}_2$ 655 amu 1.6%	$^{193}\text{Ir}/^{13}\text{C}_2$ 657 amu 2.7%

The percentages of the relevant masses are: 653 (26.2%); 654 (9.3%); 655 (45.6%); 656 (15.9%); 657 (2.7%); and 658 (0.3%). All but the last of these (which is negligible for the purpose of fitting the curve) are represented by the Gaussian curves indicated in Figure 3.5(b) that were used to fit the peak in Figure 3.5(a). In other words, the peak heights of the contributions in Figure 3.5(b) are proportional to their respective abundances. Each of the constituent peaks was assigned a FWHM of 2.35 amu. This choice is *ad hoc*. If one wishes, it can be interpreted as a rough measure of the instrumental resolution at 655 amu. Summing the curves in (b) yields the blue curve in (a), which fits the experimental data (red curve).

3.2.1 Multiphoton ionization

Photoionization was carried out using a tunable dye laser and a variety of dye mixtures to cover a reasonable portion of the ${}^1\text{LC} \leftarrow \text{S}_0$ system. The dye laser (Continuum HD 6000) was pumped with the second harmonic of a 10 ns, 20 Hz Nd:YAG laser (Continuum Powerlite 9020). Mixtures of rhodamine 590 and 610 (Exciton) were used. The use of these dye mixtures enabled different tuning ranges to be achieved with the kind of stable, long-term operation that is needed to obtain quantitative 2-photon spectra. The dye laser output was doubled using a KDP crystal in a UV frequency extender (Continuum UVT-3), yielding radiation in the region 279 – 292 nm.

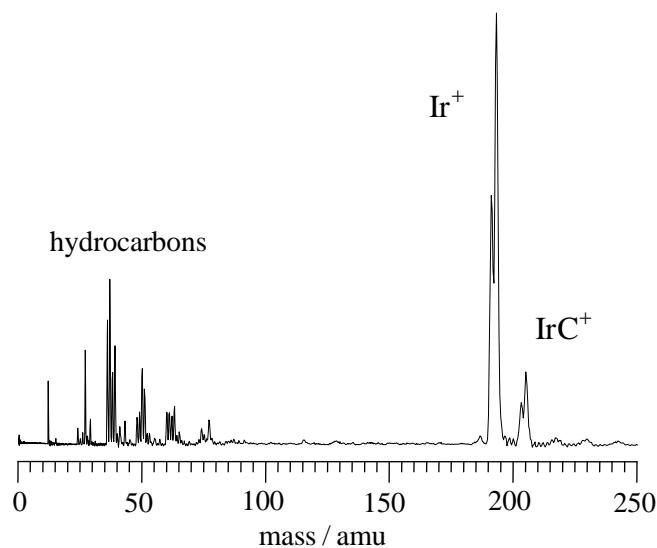


Figure 3.6. At a fluence of 1500 mJ cm^{-2} and photon energy of $35\,774 \text{ cm}^{-1}$ (4.435 eV), the mass spectrum is dominated by Ir^+ , albeit with an IrC^+ contribution that is $\sim 15\%$ as large as that of Ir^+ . Contributions from $\text{Ir}(\text{ppy})_2^+$ and $\text{Ir}(\text{ppy})_3^+$ (not shown) are smaller by an order of magnitude. The hydrocarbon peaks are due to impurity.

The laser radiation was focused using a 60 cm lens to a diameter of approximately 0.7 mm, resulting in a maximum fluence of approximately 1500 mJ cm^{-2} . The TOF spectrum obtained using this fluence and a photon energy of $35\,774 \text{ cm}^{-1}$ (4.435 eV) is shown in Figure 3.6. The most intense peak (*i.e.*, the doublet centered at 192 amu) is split according to the natural isotopes of iridium. The less intense doublet centered at 204 amu is due to $^{191}\text{IrC}^+$ and $^{193}\text{IrC}^+$. Signals due to $\text{Ir}(\text{ppy})_2^+$ and $\text{Ir}(\text{ppy})_3^+$ (not shown) are an order of magnitude smaller than the Ir^+ peak. The cluster of peaks at lower mass is unaffected by source temperature and it is present in the absence of $\text{Ir}(\text{ppy})_3$. Therefore, these peaks are attributed to hydrocarbon contamination.

Figure 3.7(a) shows the intensity of the Ir^+ signal as a function of photon energy in the range $34\,900 - 35\,800 \text{ cm}^{-1}$ (4.327 – 4.438 eV). Fluence of approximately 1400 mJ

cm^{-2} was used. The spectrum consists of a number of sharp peaks superimposed on a weak continuum. The only significant effect observed upon increasing the fluence is to increase the amount of underlying continuum. The boxed area in Figure 3.7(a) is expanded in (b). The vertical dashed lines correspond to transitions of neutral atomic iridium. The agreement between the measured spectrum and the dashed lines indicates that the sharp features are due to multiphoton ionization of atomic iridium,³⁷ itself arising from multiple photon processes. In such high fluence cases, amusing spectra can be recorded, but obtaining detailed information about the low-lying excited states of $\text{Ir}(\text{ppy})_3$ is not feasible.³⁸

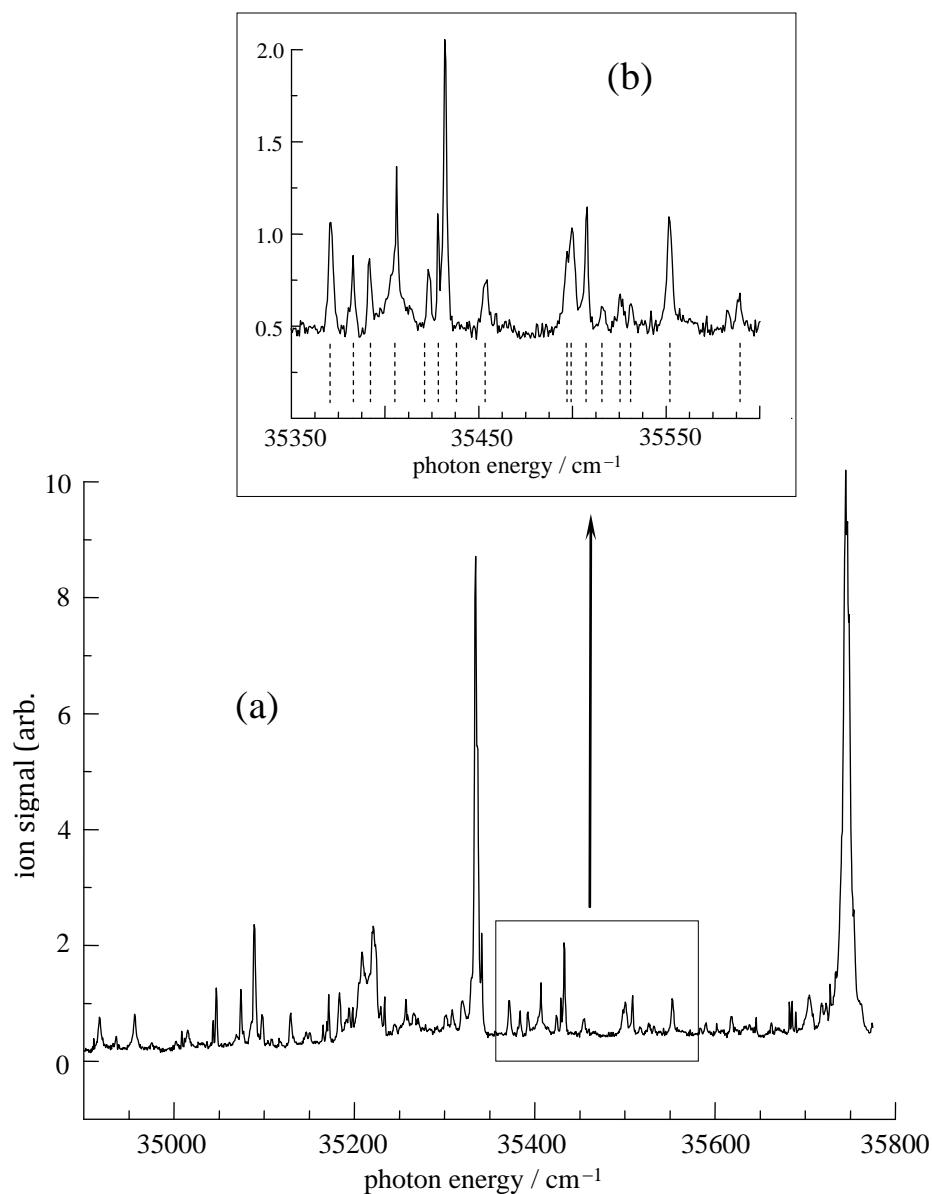


Figure 3.7. (a) Action spectrum obtained by monitoring Ir⁺ while varying the photon energy. Laser fluence was approximately 1400 mJ cm⁻². (b) Expanded view: The vertical dashed lines indicate transitions of (neutral) atomic iridium.³⁷ Note that the spectra are not offset from zero, *i.e.*, there is an underlying broad continuum.

At the same time, an important fact follows from atomic iridium spectra such as those shown in Figure 3.7. They indicate that, at least under high fluence conditions,

photofragmentation is so severe as to yield significant quantities of iridium atoms that then undergo multiphoton ionization. In fact, neutral photofragmentation dominates. Were neutral iridium atoms produced via photodissociation of an ion precursor, there would have to be an ion partner. There is no evidence whatsoever of $\text{Ir}(\text{ppy})^+$, and only a small ppy^+ signal appears at high fluence. The dominance of neutral fragmentation channels is not surprising, given that previous studies have shown that photolysis is a common, often dominant, pathway for photoexcited organometallic compounds.³⁹⁻⁴⁵ The important conclusion is that the ionization and neutral fragmentation channels are in competition with one another. This bears on interpretation of the ion yield spectra (*vide infra* Figure 3.10), as discussed later.

3.2.2 Two-photon ionization

An attenuator consisting of a half-wave plate and a Glan-Thompson polarizer was inserted into the beam path. This allowed the laser fluence to be varied over a broad range with good accuracy, with the caveat that this fluence is an average over the near-Gaussian beam shape. First, the polarizer is set for maximum transmission. Then the half-wave plate is inserted between the light source and the polarizer. Fluence is easily adjusted by turning the half-wave plate. Because focusing limits the lowest fluence that can be obtained using this procedure, the focusing lens was removed to examine the low fluence regime. In this case, the radiation passed through a 1 mm diameter aperture. This enabled fluence as low as $50 \mu\text{J cm}^{-2}$ to be achieved with good accuracy. Diffraction over the aperture-sample distance was minimal.

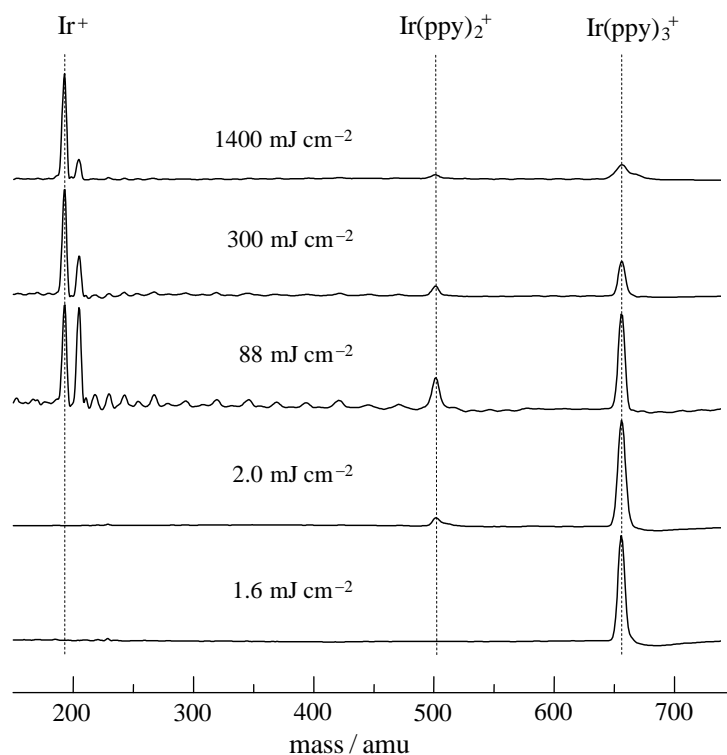


Figure 3.8. Mass spectra recorded at different fluences: The laser frequency is 35357 cm^{-1} (4.383 eV). At low fluence (bottom trace), photoionization produces the Ir(ppy)_3^+ ion exclusively. As the fluence is increased, fragmentation results in the appearance of the Ir(ppy)_2^+ ion. At high fluence (top trace), the Ir^+ peak dominates, indicating severe fragmentation of Ir(ppy)_3 and its photofragments.

Figure 3.8 shows how changing the fluence affects the mass spectra. The highest fluence (top trace) yields a mass spectrum that is similar to the one presented in Figure 3.6. The Ir^+ peak dominates. Signals corresponding to Ir(ppy)_2^+ and Ir(ppy)_3^+ gain intensity as the fluence is decreased. At 88 mJ cm^{-2} , the Ir^+ and Ir(ppy)_3^+ peaks have approximately equal height, and an $\text{IrC}_n^+ / \text{IrN}_n^+$ progression has emerged. When the fluence is below $\sim 1.6\text{ mJ cm}^{-2}$, the Ir(ppy)_3^+ parent ion is isolated, *i.e.*, the mass

spectrum, for all practical purposes, contains no other peaks. No signal corresponding to Ir(ppy)_3^+ has been observed in any of the experiments.

Generally, the parent ion is most useful for acquiring information about the molecule and therefore this signal was the main focus of the present study. It should be noted that it was not obvious *a priori* that it would be possible to isolate the parent ion, particularly in light of the large amount of parent vibrational energy that is present at 500 K. Thus, it was pleasing to find that Ir(ppy)_3^+ was the only ion peak in the mass spectrum over a wide range of experimental conditions.

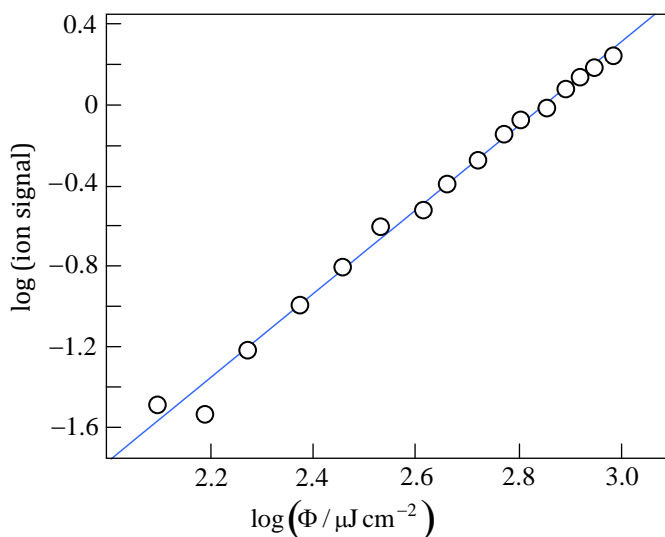


Figure 3.9. Ir(ppy)_3^+ signal versus fluence, F , recorded with a photon energy of $35\,420\text{ cm}^{-1}$ (4.391 eV) The straight line has a slope of 2, in accord with 2-photon ionization.

The fluence dependence of the Ir(ppy)_3^+ signal revealed that it is proportional to the second power of the laser fluence, as long as the fluence is less than $\sim 1.6\text{ mJ cm}^{-2}$ (see Figure 3.8). To be on the safe side, we shall take the low-fluence regime to be less

than 1 mJ cm^{-2} . Figure 3.9 shows a log-log plot of the Ir(ppy)_3^+ signal versus fluence, Φ , obtained with a photon energy of $35\,420 \text{ cm}^{-1}$ (4.391 eV). Similar results were obtained using a number of photon energies in the range $34\,207 - 35\,930 \text{ cm}^{-1}$ (4.241 – 4.455 eV). At slightly higher fluence, but below the regime where significant fragmentation occurs, the Ir(ppy)_3^+ signal is no longer proportional to Φ^n with $n = 2$. For example, the range 2-15 mJ cm^{-2} is characterized by $n = 1.5$. This is consistent with some degree of saturation of one or both transitions, as well as a contribution from parent ion fragmentation.

The term saturation is most often used to describe the near equality of two state populations that is brought about through the application of an intense, resonant electromagnetic field. In the system under consideration here, the electronically excited states are unstable because of radiationless decay. Therefore, the term saturation is used advisedly, *i.e.*, to describe the regime where the figure-of-merit $\sigma\Phi$ assumes values of a few tenths or larger.⁴⁶

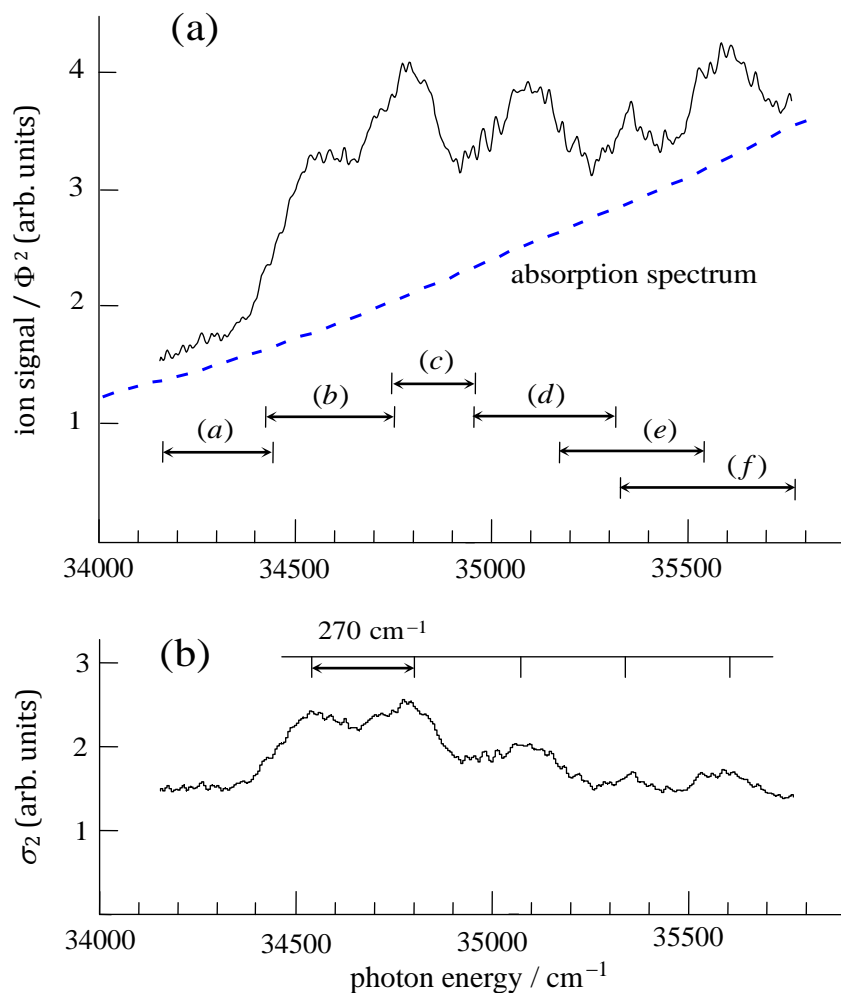


Figure 3.10. (a) The black trace is the Ir(ppy)_3^+ signal, divided by fluence squared, versus photon energy. The blue dashed trace is the absorption cross-section s_1 of gas phase Ir(ppy)_3 at ~ 500 K (arb. units). Different ratios of rhodamine 590 and 610 and the corresponding energy regions are designated by horizontal double-sided arrows: (a) 100% 590 (279.5–283.1 nm); (b) 590:610 = 9:1 (281.5–284.3 nm); (c) 590:610 = 4:1 (283.2–286.8 nm); (d) 590:610 = 7:3 (286.2–288.1 nm); (e) 590:610 = 3:2 (287.8–290.5 nm); (f) 100% 610 (290.2–292.8 nm). (b) The ion signal (scaled by F^2) in (a) has been divided by the (blue dashed) absorption spectrum of ~ 500 K gas phase Ir(ppy)_3 also shown in (a). This indicates that the undulation with ~ 270 cm^{-1} spacing is due to s_2 .

Figure 3.10(a) shows the "fluence-corrected" Ir(ppy)_3^+ signal versus photon energy in the range $34\,150 - 35\,775$ cm^{-1} (4.234 – 4.435 eV). Because the Ir(ppy)_3^+ signal varies as the second power of the laser fluence (Φ^2) in these experiments, care was

taken to ensure that the fluence did not deviate more than 5% from $450 \mu\text{J cm}^{-2}$. To this end, the spectrum in Figure 3.10(a) is composed of six separate spectra recorded using different rhodamine 590 and 610 dye mixtures. The photon energy regions covered by the different dye mixtures are indicated using horizontal double-sided arrows. In addition, the laser fluence was recorded along with the ion signal, enabling the ion signal to be corrected for the modest change of fluence using the Φ^2 dependence. This is the above-mentioned "fluence corrected" signal.

The trace in (b) is the black trace in (a) divided by the absorption spectrum shown as the dashed blue line in (a). An ultraviolet absorption spectrum of gaseous Ir(ppy)_3 was obtained by inserting a heated, sealed 10 cm cell containing Ir(ppy)_3 vapor into a commercial spectrophotometer. The cell was heated more at the ends than in the middle to eliminate condensation on the windows. It was wrapped in insulation and inserted into a split copper cylinder having end plates with holes just large enough to permit the radiation to enter and exit. There was no sample degradation at temperatures in excess of 550 K. Reliable ultraviolet spectra were recorded. A portion of one of them is shown in Figure 3.10(a). Division of the black trace in (a) by the absorption spectrum yields a spectrum (in arbitrary units) for the dependence of the ion signal on the ionizing photon energy. This is discussed in Section 3.3. The upper horizontal scale in (b) indicates that the undulation has spacing of roughly 270 cm^{-1} (33 meV).

The undulation seen in Figure 3.10(b) was unanticipated. If anything, a smooth variation of σ_2 versus photon energy was expected.^{47,48} Therefore, the photoionization

spectrum shown in Figure 3.10 was examined thoroughly to ensure that it is not an artifact. The data were recorded with great care over several months, using six different dye solutions, ensuring that the laser fluence is safely within the 2-photon regime, and taking care to not mistake a variation of laser fluence for a variation of σ_2 . There was no relationship between the undulation and the tuning ranges used with the various dye mixtures. The undulation was repeatable. Possible explanations are discussed in Section 3.3.

3.2.3 One-photon ionization

It also proved straightforward to photoionize Ir(ppy)_3 using a single 193.3 nm (6.414 eV) photon. The output from an ArF excimer laser (Lambda Physik Compex 201) was passed through a 0.7 mm x 12.7 mm aperture. Less than 1 mJ cm^{-2} ($< 10^{15}$ photons cm^{-2}) provided adequate signal. No significant changes to the experimental arrangement indicated in Figure 3.4 were required, *i.e.*, only optics and triggering. The sole ion present in the mass spectrum was Ir(ppy)_3^+ . The photon energy provides an additional estimate of an upper bound for the ionization energy, subject to a reasonable assumption about the role played by parent vibrational energy in photoionization, as discussed in the next section.

3.3 Discussion

Referring to Figure 3.10, single-frequency 2-photon ionization was carried out using photon energies throughout the range $34\,150 - 35\,775 \text{ cm}^{-1}$ (4.234 – 4.435 eV).

The 2-photon nature of Ir(ppy)_3^+ production in this range was verified at a number of photon energies by recording data of similar quality to those shown in Figure 3.9. With photon energies smaller than $34\,150\text{ cm}^{-1}$ (4.234 eV) it was not possible to obtain such high quality fluence dependence data because the absorption cross-section σ_1 diminishes toward smaller photon energy and our ultraviolet radiation source (doubled dye laser) is less stable.

It is noteworthy that with the convenient (and significantly smaller) photon energy $28\,170\text{ cm}^{-1}$ (3.492 eV, corresponding to 355 nm) it was not possible to identify a regime where the Ir(ppy)_3^+ signal varies as the square of the fluence. Even though the 355 nm radiation is quite user-friendly (being the YAG third harmonic), the photoionization fluence dependence changed erratically from one experiment to the next. For example, nine fluence dependence plots were recorded under what we considered similar conditions. In each case, the Ir(ppy)_3^+ signal could be fitted to a Φ^n variation. However, the n values spanned a broad range: 1.5 – 3.3. This was surprising because the 355 nm fluence was more stable than the radiation used throughout the range indicated in Figure 3.10.

As mentioned above, one of the problems is that the cross-section for absorption of the first photon (σ_1) diminishes on the low energy side of the $^1\text{LC} \leftarrow \text{S}_0$ peak indicated in Figure 3.3. Consequently, increasing the fluence to overcome smaller σ_1 values raises the possibility of beginning to saturate the σ_2 transition. Of course, the major unknown with 355 nm radiation is the participation of 3-photon processes, as

28 170 cm^{-1} (3.492 eV) is quite a bit smaller than 34 150 cm^{-1} (4.234 eV). For example, might 355 nm photoionization be, at least in part, a 3-photon process with some degree of saturation (at times) of the σ_2 and σ_3 transitions? As pointed out by one of the reviewers, competition between 2- and 3-photon processes can be exacerbated by the mode hopping that occurs in YAG lasers that are not injection seeded.

In consideration of the above issues, to be on the safe side, all of the spectral scans were limited to the range shown in Figure 3.10. Thus, 34 150 cm^{-1} (4.234 eV) was used to estimate a *very conservative* upper bound for the ionization threshold obtained via single-frequency 2-photon ionization, as discussed below.

3.3.1 Low-lying electronically excited states

Insight into energy transfer and photophysical properties of low-lying electronically excited states of $\text{Ir}(\text{ppy})_3$ is provided by previous experimental studies. The ones most germane to the present study are reviewed here.

It is well known that $\text{Ir}(\text{ppy})_3$ exhibits intense (*i.e.*, high quantum yield) phosphorescence from T_1 with an apparent radiative (spontaneous emission) lifetime of approximately 1.6 μs at room temperature.^{16,17,20,24,28} This lifetime is phenomenological in the sense that the three T_1 sublevels separately have quite different radiative lifetimes: 116, 6.4, and 0.2 μs , as indicated in Figure 3.11.¹⁷ It is interesting that the term phosphorescence is used with a radiative lifetime as short as 0.2 μs . Specifically, 0.2 μs is comparable to the spontaneous emission lifetimes of a large number of allowed singlet-singlet transitions in small molecules. Keep in mind, however, that so short a lifetime

does not, by itself, imply dominant singlet character of the excited state. Specifically, a lifetime of 0.2 μs can arise through the introduction of even modest amounts of ^1LC and / or $^1\text{MLCT}$ character into T_1 via SOC.

Because of the short $^1\text{LC} \rightarrow S_0$ and $^1\text{MLCT} \rightarrow S_0$ spontaneous emission lifetimes (recall the large absorption cross-sections indicated in Figure 3.3), only a modest percentage of ^1LC and / or $^1\text{MLCT}$ character is needed to account for the 0.2 μs lifetime. For example, an estimate of ~ 6 ns was obtained for the $^1\text{MLCT} \rightarrow S_0$ radiative lifetime. This was achieved through application of a Strickler-Berg analysis^{49,50} to several molecules having similar spectral properties in the region of interest,^{30,51-53} and then scaling these lifetimes to the absorption spectrum shown in Figure 3.3.²⁹ This confirmed that only a few percent of $^1\text{MLCT}$ character mixed into the T_1 state is needed to account for the short lifetime of 0.2 μs .

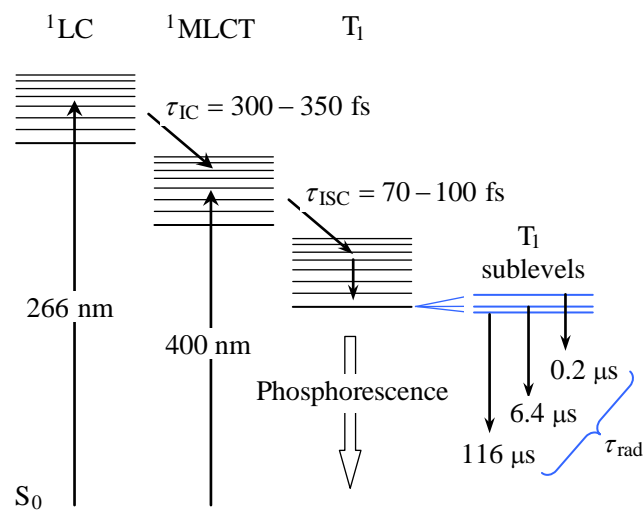


Figure 3.11. Some important properties and processes of low-lying electronic states are indicated schematically (not to scale). Rapid radiationless decay processes (IC and ISC, with respective lifetimes τ_{IC} and τ_{ISC}) ensure efficient T_1 production.²⁸ Spontaneous emission lifetimes (τ_{rad}) for the T_1 sublevels indicated on the far right differ considerably, despite the fact that these levels are close in energy, *i.e.*, 116, 6.4, and 0.2 μs for 19 693, 19 712, and 19 863 cm^{-1} , respectively, in CH_2Cl_2 solvent.¹⁷ At room temperature, an observed phosphorescence lifetime of 1.6 μs reflects the complex interplay that exists between the T_1 levels. The horizontal lines (above the electronic origins) whose spacing decreases with energy indicate (schematically) vibrational levels. Adapted from references 17 and 28.

The radiative and energy transfer processes that transpire among the three T_1 sublevels are subtle. For example, the different spontaneous emission rates participate in proportion to the respective sublevel populations, which in turn depend on both the temperature and the energy transfer rates among the sublevels. This has been examined assiduously by Yersin and coworkers,^{16,17} who have established, through numerous and sophisticated experiments and modeling, the various energy transfer and radiative properties.^{16,17} Specifically, in their experiments, emission spectra and decay rates (for T_1 sublevels) were recorded at temperatures as low as 1.5 K and with applied magnetic fields as high as 12 T. Suffice it to say that, leaving aside for the moment a detailed

assignment of the electronic character of all low-lying singlets and triplets, the radiative and energy transfer processes of the T_1 sublevels are well understood compared to other $\text{Ir}(\text{ppy})_3$ photophysical and energy transfer processes.

It must be kept in mind that non-radiative relaxation processes such as $^1\text{LC} \rightarrow ^1\text{MLCT}$ and $^1\text{MLCT} \rightarrow T_1$, which appear commonly in the literature, are highly simplified (in a sense phenomenological) models. For example, in reality there are several triplets whose energies lie below that of ^1LC , as well as surface crossings. Details of the electronic structure are discussed at length in Chapter 4.

With the above caveat in mind, at energies above the T_1 origin region (Figure 3.11), the femtosecond resolution transient absorption measurements of Tang et al. have revealed ultrafast dynamics among the ^1LC , $^1\text{MLCT}$, and T_1 states.²⁸ Referring to Figures. 3.3 and 3.11, ultrafast (100 fs) photoexcitation at 400 nm was used to access $^1\text{MLCT}$. It was found that absorptions at 520 and 580 nm appeared with time constants of 100 fs and 70 fs, respectively. These 520 and 580 nm absorptions remained constant up to the maximum achievable delay (for the given experimental arrangement) of 1.5 ns. The long-lived absorbing state was assigned to phosphorescent T_1 , implicating rapid ISC (*i.e.*, τ_{ISC} values of 100 fs and 70 fs), as indicated in Figure 3.11. This result is consistent with the essentially complete absence of $^1\text{MLCT} \rightarrow S_0$ fluorescence that has been noted,^{17,20} even at low temperatures.¹⁷

Next, ^1LC was excited at 266 nm, and the transient absorptions at 520 and 580 nm, each originating from T_1 , were fit using a bi-exponential function.²⁸ With the shorter

time constants fixed at the τ_{ISC} values (100 fs and 70 fs, respectively), the other time constants were found to be 300 fs and 350 fs, respectively (Figure 3.11). These longer time constants were assigned to IC from ^1LC to $^1\text{MLCT}$, *i.e.*, τ_{IC} in Figure 3.11. The bottom line is that this study demonstrated that photoexcited $\text{Ir}(\text{ppy})_3$ relaxes via $^1\text{MLCT}$ to phosphorescent T_1 on a sub-picosecond timescale. Complementary experiments by Hedley et al. used ultrafast methods to probe directly the short-lived $^1\text{MLCT}$ spontaneous emission that follows photoexcitation at 400 nm with 100 fs pulses.²⁰ These challenging experiments confirmed the results of Tang et al.,²⁸ and also revealed rapid vibrational energy transfer processes, including intramolecular vibrational redistribution. Again, as impressive as these measurements are, one must keep in mind that the electronic structure is more complex than the simplified scheme indicated in Figure 3.11.

In the gas phase environments of the experiments reported herein, an $\text{Ir}(\text{ppy})_3$ molecule's energy is conserved (until it emits a photon) following its absorption of a single ultraviolet photon. Therefore, intramolecular processes take place at, for all practical purposes, fixed energies, *i.e.*, the photon energy plus a given molecule's (considerable) internal, that arises from 490 K thermal equilibrium. This differs from the condensed phase environments that have been used in previous studies of laser-initiated dynamics in the $\text{Ir}(\text{ppy})_3$ system. In these latter cases, intramolecular processes take place simultaneously with $\text{Ir}(\text{ppy})_3$ – host interactions. It is safe to assume that processes that take place on time scales of 70-100 fs are completely in the intramolecular regime, and processes that transpire on time scales of 300-350 fs are predominantly intramolecular. In the picosecond regime, however, it is hard to justify the assumption of solely

intramolecular mechanisms, as dopant-host vibrational energy transfer processes can be competitive with intramolecular processes. When normal modes are accurate descriptors, dopant-host vibrational energy transfer will likely be slower than intramolecular processes. On the other hand, in the higher-energy regime of vibrational (vibronic) quantum chaos, dopant-host vibrational energy transfer can be rapid.⁵⁴ This regime can be accessed through IC and ISC processes.

Rapid ISC and the resulting efficient quenching of singlet-singlet fluorescence are consequences of strong (or at least efficient) SOC. Several theoretical studies have addressed this issue.^{23-25,27} Of particular note are those of Nozaki²⁵ and Nozaki and coworkers,²⁷ who examined effects due to SOC in Ir(ppy)₃ and analogous systems. The Nozaki results on Ir(ppy)₃²⁵ are in qualitative accord with the experimental results.²⁸

As a result of significant singlet-triplet mixing, it has been suggested that an appropriate picture might be one in which photoexcitation produces the strongly spin-mixed phosphorescent states directly, in which case the term ISC has little meaning.²⁵ In other words, in a regime where ISC has little or no meaning, the lifetime τ_{ISC} would not be observed. Instead, photoexcitation would access states of mixed ¹MLCT/T₁ character, and each of these states would emit in proportion to its percentage ¹MLCT character. This scenario differs from the case in which a temporally short pulse excites the system, with the pulse's spectral width exceeding significantly the mean energy spacing between adjacent eigenstates. A coherent superposition of eigenstates is created whose short time character is that of the "bright state." In the Tang et al. experiments (400 nm), the bright state given by this coherent superposition is ¹MLCT. This enabled τ_{ISC} to be determined.

Indeed, calculations indicate that the emitting states are of predominantly triplet character,²³⁻²⁵ with only modest percentages of singlet character. This is in agreement with the dilution of the very short singlet-singlet spontaneous emission rates mentioned earlier, in which T_1 acquires a small percentage of singlet character due to SOC. As a testament to the reliability of the calculations, the radiative lifetimes were reproduced, at least qualitatively, when SOC was taken into account.²⁴ In any event, on the basis of all of the above work,²³⁻²⁵ it follows that sub-picosecond ISC dynamics are not at all surprising.

3.3.2 Photoionization

Less is known about the ionization of $\text{Ir}(\text{ppy})_3$. This is an important fundamental process that enters the world of OLED's through the electron-hole recombination (exciton formation) that initiates the cascade down the energy "ladder" that terminates at T_1 . Yet, only one experimental value for gas phase $\text{Ir}(\text{ppy})_3$ appears in the literature (7.2 eV),³³ and this is based on indirect evidence, as discussed later. Properties such as the adiabatic and vertical ionization energies (AIE and VIE's) are accessible through studies of gas phase $\text{Ir}(\text{ppy})_3$. Ideally, one would like to prepare samples in which the $\text{Ir}(\text{ppy})_3$ molecules have as little internal excitation as possible. However, to maintain a steady-state of gas phase $\text{Ir}(\text{ppy})_3$ requires elevated temperature, and removing the large amount of vibrational energy imparted to the molecule at such temperatures is challenging. Even if $\text{Ir}(\text{ppy})_3$ were somehow cooled vibrationally, considerable vibrational energy would still be implanted through the IC and ISC processes that follow and/or accompany

photoexcitation. Clearly, the role played by Ir(ppy)₃ vibrational excitation must be taken into account.

There are two sources of vibrational excitation in the present experiments. First, consider the vibrational energy of a gas phase Ir(ppy)₃ molecule at thermal equilibrium. To obtain sufficient Ir(ppy)₃ density in the region where photoionization takes place (Figure 3.6) required maintaining the oven temperature at approximately 490 K. The effusing Ir(ppy)₃ molecules contain considerable vibrational energy (discussed below) as well as, on average, $3kT/2 = 510 \text{ cm}^{-1}$ of rotational energy. As mentioned above, a second source of vibrational energy arises through the first photoexcitation step, say at $34\,150 \text{ cm}^{-1}$ (4.234 eV). The implanted ¹LC excitation undergoes rapid IC to ¹MLCT, which in turn decays rapidly via ISC to T₁, whose origin lies at approximately $19\,700 \text{ cm}^{-1}$ (2.442 eV).¹⁷ Fortunately for OLED applications, T₁ does not undergo ISC to S₀ on any relevant time scale.

The amount of vibrational energy imparted via ¹LC ← S₀ photoexcitation is taken as the difference between the photon energy and the T₁ electronic energy, *i.e.*, $34\,150 - 19\,700 = 14\,450 \text{ cm}^{-1}$ (1.791 eV). Of course, vestiges of ¹LC and ¹MLCT electronic excitations remain because a gas phase Ir(ppy)₃ molecule in a collision-free environment has no way other than photon emission to lower its energy. However, these contributions are minor because of the high density of T₁ vibrational states relative to the densities of vibrational states in the ¹LC and ¹MLCT manifolds at the $34\,150 \text{ cm}^{-1}$ (4.234 eV) photon energy.

It is now assumed that vibrational excitation plays a spectator role in photoionization, *i.e.*, all vibrational excitation in Ir(ppy)₃, regardless of how it got there, or the specific form it might have, appears as vibrational excitation of the Ir(ppy)₃⁺ cation. In other words, all Franck-Condon factors between T₁ and the cation are taken as diagonal, *i.e.*, $\langle m v_j | n v_k' \rangle = \delta_{mn} \delta_{ik}$, where *i* and *k* denote vibrational degrees of freedom such as normal modes, *m* and *n* denote numbers of quanta, and the prime denotes the ion. Note that the equilibrium geometry of the cation is quite close to that of T₁ (*vide infra* Table 3.1), which supports this assumption. Thus, the resulting *very conservative* upper bound to the ionization energy obtained through single-frequency 2-photon ionization is estimated to be the photon energy plus the T₁ electronic energy, *i.e.*, 34 150 + 19 700 = 53 850 cm⁻¹ = 6.67 eV.

Let us now turn to 1-photon photoionization. As discussed in Section 2, it was possible to photoionize 490 K Ir(ppy)₃ vapor using 193.3 nm (6.414 eV) radiation. Again, if it is assumed that all vibrational excitation is transferred intact, this time from S₀ to the cation, a rough upper bound of 6.4 eV is obtained for the VIE. We shall take this to be the experimentally determined upper bound to the VIE, again subject to the assumption that parent vibrational energy is transferred more-or-less intact to the cation. Not surprisingly, it turns out that the AIE and VIE's from S₀ and T₁ geometries do not differ much from one another, as discussed below.

3.3.3 Ion yield spectrum

The 2-photon $\text{Ir}(\text{ppy})_3^+$ yield spectrum shown in Figure 3.10 displays an undulation whose peak-to-peak spacing is $\sim 270 \text{ cm}^{-1}$ (33 meV). As mentioned earlier, these data were recorded over several months, using six different dye solutions, ensuring that the laser fluence is safely within the 2-photon regime, and taking care to not mistake a variation of laser fluence for structure in the ion yield spectrum. Possible origins of this undulation are now discussed.

Large IC rates, such as the one determined experimentally for $^1\text{LC} \rightarrow ^1\text{MLCT}$,²⁸ are consistent with nonadiabatic transitions between potential surfaces taking place via one or more conical intersections. In large systems like $\text{Ir}(\text{ppy})_3$, the search for such intersections presents a daunting computational challenge, so much so that it is not clear that the benefit merits the effort. Nonetheless, it is well known that this is a common and efficient mechanism for the IC of electronically excited states that can leave a fingerprint in the form of selective vibrational excitation in one or more modes. In general, this could be manifest in the first and/or second photoexcitation steps, accounting for the observed structure, as discussed below.

When the 2-photon ion yield spectrum shown in Figure 3.10 was recorded, we could not, at that time, rule out the possibility that the energy dependence of the cross-section for absorption of the first photon, $\sigma_1(E)$, is responsible for the structure. There was no report in the literature of an ultraviolet absorption spectrum of either gaseous $\text{Ir}(\text{ppy})_3$ or even gaseous 2-phenylpyridine. Though spectra of these species in solvent display no hint of structure in the region of interest (Figure 3.3), this does not guarantee

that the corresponding gas phase spectra are also smooth. This led to the experiments described in Section 2, in which $\sigma_1(E)$ was measured for gas phase Ir(ppy)₃ at temperatures > 500 K. No undulation resembling that in Figure 3.10 was discernible in $\sigma_1(E)$. This confirmed that $\sigma_1(E)$ is not responsible for the undulation in the 2-photon ion yield spectrum.

A likely origin of the undulation is competition between the ionization and radiationless decay pathways. In light of the fact that $^1\text{LC} \leftarrow \text{S}_0$ photoexcitation leads (via the $^1\text{MLCT}$ intermediate) to T_1 on a sub-picosecond timescale, the absorption of the second photon can take place via one or more predominantly triplet-triplet transitions, with T_1 being the lower state. It is unlikely that the excited state thus produced fluoresces to any significant extent. Rather, it is expected to either ionize or undergo IC and / or ISC. As mentioned above, a signature of IC via conical intersection is selective vibrational excitation, and it is likely that efficient ISC behaves similarly. Even if the photoionization cross-section has no such structure, such a mechanism — radiationless decay in competition with ionization — can account for the spectrum in Figure 3.10.

Given such possibilities, including combinations thereof and other scenarios, we are remiss to speculate further on the origin of the undulation indicated in Figure 3.10.

3.3.4 Disposition of vibrational energy

We have seen that the photoexcitation step: $^1\text{LC} \leftarrow \text{S}_0$, is accompanied by IC to $^1\text{MLCT}$. At a rigorous level of theory, in the absence of molecular rotation, all molecular

eigenstates in this regime are eigenfunctions of vibronic symmetry, which survives breakdown of the Born-Oppenheimer approximation.⁵⁵ However, each of these eigenstates contains only a modest amount of ¹LC electronic character, because the latter is diluted through the large density of vibrational states of the lower electronic manifold(s). Thus, as a practical matter, it is safe to assume that the system evolves to one of ¹MLCT vibrational excitation. Likewise, the ¹MLCT → T₁ transition that takes place via ISC also leads to mainly vibrational excitation within the T₁ manifold. Thus, the ¹LC ← S₀ photon energy minus the energy of the T₁ electronic origin is taken as vibrational energy. Adding this to the photoexcited molecule's S₀ vibrational energy gives its total vibrational energy.

Turning now to the vibrational energy present in ground electronic state molecules, this is due to thermal population of vibrational levels at 490 K. In light of the fact that there are 177 vibrational degrees of freedom, there is considerable S₀ vibrational energy. An accurate determination of this vibrational energy distribution is challenging. The distribution function for the total amount of vibrational energy consists of (roughly) a delta function (at an energy equal to the photon energy minus the T₁ electronic energy) added to the vibrational energy distribution given by a convolution involving the 177 vibrational degrees of freedom at 490 K. This convolution yields the probability density, $P(E_{vib})$, where E_{vib} is the total vibrational energy. In plain language, the delta function accounts for the energy difference between $h\nu$ and E_{T_1} , with the assumption that the

amounts of ^1LC and $^1\text{MLCT}$ character are small relative to that of T_1 vibrations. This distribution function is determined and discussed in Chapter 4.

The important point here is that essentially all of this vibrational energy is transported from T_1 to the ion, regardless of the details of its distribution. It is in this sense that vibrational excitation is said to act as a spectator in the ionization step.

3.3.5 Comparison with electronic structure theory and previous work

In Chapter 4, a detailed theoretical study of the electronic structure of the $\text{Ir}(\text{ppy})_3$ system, including several low-lying states of the cation $\text{Ir}(\text{ppy})_3^+$, is presented. Here, a few of these results are compared to the experimental findings to establish registry between the experimental and computational results.

	S ₀ (theory)			S ₀ (expt)			T ₁ (theory)		D ₀ (theory)
	(a)	(b)	(c)	(d)	(e)	(f)	(a)	(b)	(a)
Ir–N ₂	2.168	2.153	2.167	2.088	2.071	2.132	2.196	2.176	2.149
Ir–N ₂₉	2.169	2.154	2.167	2.088	2.071	2.132	2.175	2.169	2.184
Ir–N ₄₂	2.165	2.151	2.167	2.088	2.071	2.132	2.139	2.116	2.213
Ir–C ₉	2.025	2.035	2.035	2.006	2.060	2.024	2.025	2.030	2.028
Ir–C ₂₂	2.023	2.035	2.035	2.006	2.060	2.024	2.036	2.048	1.975
Ir–C ₄₉	2.022	2.035	2.035	2.006	2.060	2.024	1.961	2.000	2.035
N ₂ –C ₃ , N ₂₉ –C ₃₀	1.34	1.36	–	1.345	1.361	1.331	1.34	1.36	1.34
N ₄₂ –C ₄₃	1.34	1.36	–	1.345	1.361	1.331	1.33	1.36	1.34
N ₂ –C ₇ , N ₂₉ –C ₂₈	1.35	1.38	–	1.358	1.385	1.371	1.35	1.38	1.355, 1.35
N ₄₂ –C ₄₇	1.35	1.38	–	1.358	1.385	1.371	1.40	1.439	1.35
C ₉ –C ₁₀ , C ₂₂ –C ₂₃	1.405	1.42	–	1.405	1.374	1.401	1.40	1.42	1.395, 1.41
C ₄₉ –C ₅₀	1.405	1.42	–	1.405	1.374	1.401	1.41	1.42	1.40
C ₈ –C ₉ , C ₂₂ –C ₂₇	1.415	1.44	–	1.423	1.396	1.409	1.41	1.43	1.41, 1.407
C ₄₈ –C ₄₉	1.415	1.436	–	1.423	1.396	1.409	1.49	1.485	1.426
C ₇ –C ₈ , C ₂₇ –C ₂₈	1.47	1.47	–	–	–	1.487	1.47	1.47	1.47, 1.476
C ₄₇ –C ₄₈	1.47	1.467	–	–	–	1.487	1.40	1.419	1.473

(a) current work, references (b) 24, (c) 32, (d) 56, (e) 57, (f) 14

Table 3.1. Bond lengths (Å) for S₀, T₁, and D₀ states of Ir(ppy)₃.

Calculations were carried out for the AIE and for VIE's at the S₀ and T₁ geometries, yielding respective values of 5.86, 5.87, and 5.88 eV. The fact that there is little difference among these is not surprising, given the similar geometries of the S₀ and T₁ states of Ir(ppy)₃ and the Ir(ppy)₃⁺ ground state, D₀, (Table 3.1) and the delocalized nature of the orbitals, *i.e.*, the more delocalized the involved orbitals, the less likely it is that there will be a geometry change in going between the equilibrium structures of the electronic states. As mentioned earlier, Franck-Condon factors are expected to be nearly diagonal, where, in the present context, diagonal means $\langle m v_i | n v_k' \rangle = \delta_{mn} \delta_{ik}$, where *i* and *k* denote vibrational degrees of freedom such as normal modes, *m* and *n* denote

numbers of quanta, and the prime denotes the ion. This presupposes that the normal modes of the neutral and the ion can be paired such that a given normal mode applies to both the neutral and the ion. In other words, for a given normal mode, were one to look at the classical motions of the neutral and ion they would be essentially indistinguishable. This is a good assumption in the present system. Thus, our calculations place both the AIE and the VIE's (at the S_0 and T_1 equilibrium geometries) in the vicinity of 5.9 eV. This is in accord with the experimental upper limit of 6.4 eV, and with the calculation of Hay that places the VIE at 5.94 eV.³²

To examine the assumption that vibrational energy is transferred more-or-less intact upon photoexcitation of this system, the $^1LC \leftarrow S_0$ absorption spectrum was calculated with all S_0 vibrational excitation suppressed. Excitation is vertical from the S_0 equilibrium geometry. In this calculation, 130 excited electronic states were included. Details are given in Chapter 4. Figure 3.12 shows the correspondence between the calculated and experimental spectra. The shape of the experimental spectrum is reproduced, albeit with energy offset that is within the anticipated error bars of the methods employed.

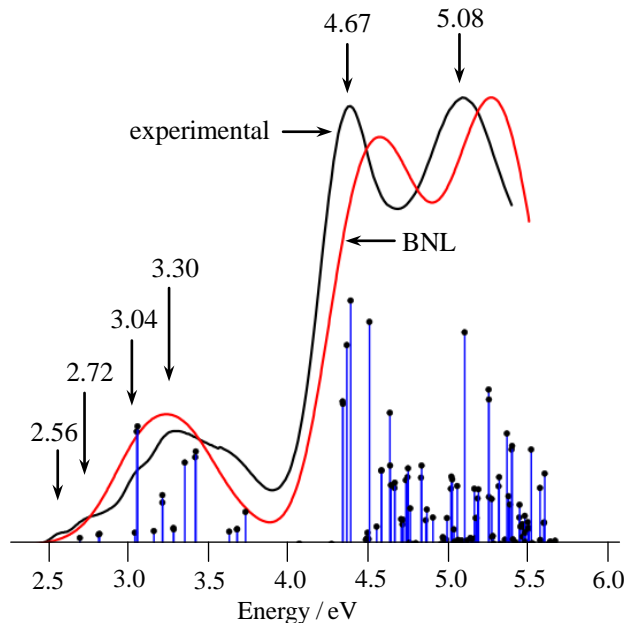


Figure 3.12. Ultraviolet absorption spectra of *fac*-Ir(ppy)₃. The calculated spectrum (red) was obtained from the stick spectrum by assigning to each stick a Gaussian FWHM of 0.43 eV. The experimental spectrum (black) was recorded at room temperature in dichloromethane. Peak and shoulder positions (vertical arrows) are in eV. All stick heights have been increased by the same constant factor for viewing convenience, and curve height has been adjusted such that the maximum absorptions are equal. The low-energy, low-intensity wing due to $T_1 \leftarrow S_0$ (2.56 eV) is absent in the calculated spectrum because SOC was not included.

It was pointed out in Section 2 that we were unable to establish that 355 nm photoionization is a 2-photon process. Adding the 355 nm photon energy to the T_1 electronic energy yields 5.94 eV, which lies below the experimental upper bound of 6.4 eV, is close to our theoretical VIE and AIE values of approximately 5.9 eV, and is equal to the value calculated by Hay.³² It may well be that our inability to establish the 355 nm photoionization fluence dependence is a reflection of this near coincidence. Thus, we conclude that the AIE is less than 6.4 eV and is most likely ~ 6 eV. The only other experimentally based ionization energy for this species places the VIE at 7.2 eV,³³ which is incorrect. In defense of these authors, however, is the fact that their measurement was

not direct, but an inference. Specifically, it was assumed that a peak at 7.2 eV in energy loss spectra (using incident electron energies of 14, 20, 30, and 50 eV) was due to ionization. Apparently this assumption needs to be reconsidered.

3.4 Summary

- A regime of single-frequency 2-photon photoionization has been established (*i.e.*, below $\sim 1 \text{ mJ cm}^{-2}$, see Figure 3.9), and it has been shown that the Ir(ppy)_3^+ parent ion is, for all practical purposes, the only ion product throughout this regime, despite the fact that the cation is formed with considerable vibrational energy. This is examined computationally in Chapter 4. Photoionization was also achieved using a single 193.3 nm (6.41 eV) photon, again yielding Ir(ppy)_3^+ with no discernible fragmentation.
- An upper bound for the ionization threshold for gas phase Ir(ppy)_3 has been estimated on the basis of complementary experiments. Central to interpretation of the experimental results is the reasonable assumption that Ir(ppy)_3 vibrational energy is carried over, essentially intact, to its ion. The 2-photon experiments give a *very conservative* upper bound of 6.67 eV, while the 1-photon experiment gives an upper bound of 6.4 eV. The upper bound of 6.4 eV is consistent with the theoretical values obtained by our group of approximately 5.9 eV (Chapter 4) and by Hay of 5.94 eV.³² Thus, the AIE is estimated to be ~ 6 eV. The VIE's at the S_0 and T_1 equilibrium geometries are essentially the same as the AIE. A calculation of the Ir(ppy)_3 absorption spectrum, in which vertical excitation from the S_0 equilibrium geometry is

assumed, supports the assumption that vibrational excitation is transferred essentially intact upon photoexcitation.

- The electrical efficiency of an OLED depends on the embedded molecule's T_1 energy relative to its ionization energy in the solid host. For example the IE's and electron affinities (EA's) (HOMO and LUMO energies, respectively) of molecules in the light-emitting layer needs to be matched to the energy levels of the electrodes. The low value of ~ 6 eV for the ionization energy of isolated Ir(ppy)_3 augurs well for this species and its close relatives.
- An undulation with spacing of $\sim 270 \text{ cm}^{-1}$ (33 meV) was observed in the Ir(ppy)_3^+ 2-photon yield spectrum. It was shown that this is not due to such structure in the energy dependence of the absorption cross-section for the first photoexcitation step, $\sigma_1(E)$. Specifically, there is no such structure in the ultraviolet absorption spectrum of 500 K gas phase Ir(ppy)_3 . The most likely origin of this undulation is structure in the energy dependence of $\sigma_2(E)$. Competition between radiationless decay and ionization can play a role. Resolution of the mechanism awaits further experimental work.

3.5 References

1. Yersin, H.; Rausch, A. F.; Czerwieńiec, R.; Hofbeck, T.; Fischer, T. *Coordin. Chem. Rev.* **2011**, *255*, 2622.
2. Yersin, H.; Finkenzeller, W. Editor, *Highly Efficient OLEDs with Phosphorescent Materials*; Yersin, H. Ed.; Wiley-VCH Verlag: Weinheim, Germany, **2008**; pp. 1-97.
3. Yersin, H. *Top. Curr. Chem.* **2004**, *241*, 1.
4. Baldo, M. A.; Lamansky, S.; Burrows, P.E.; Thompson, M. E.; Forrest, S. R. *Appl. Phys. Lett.* **1999**, *75*, 4.
5. Baldo, M. A.; Thompson, M. E.; Forrest, S. R. *Nature* **2000**, *403*, 750.
6. Adachi, C.; Baldo, M. A.; Thompson, M. E.; Forrest, S. R. *J. Appl. Phys.* **2001**, *90*, 5048.
7. Adachi, C.; Thompson, M. E.; Forrest, S. R. *IEEE* **2002**, *8*, 372.
8. Adachi, C.; Kwong, R. C.; Djurovich, P.; Adamovich, V.; Baldo, M. A.; Thompson, M. E.; Forrest, S. R. *Appl. Phys. Lett.* **2001**, *79*, 2082.
9. Baldo, M. A.; O'Brien, D. F.; Thompson, M. E.; Forrest, S. R. *Phys. Rev. B* **1999**, *60*, 14422.
10. Leclerc, M. *J. Polym. Sci A: Polym. Chem.* **2001**, *39*, 2867.
11. Cleave, V.; Yahioglu, G.; Le Barny, P.; Friend, R.H.; Tessler, N. *Adv. Mater.* **1999**, *11*, 285.
12. Adachi, C.; Baldo, M. A.; Forrest, S. R.; Thompson, M. E. *Appl. Phys. Lett.* **2000**, *77*, 904.
13. Baldo, M. A.; Forrest, S. R. *Phys. Rev. B* **2000**, *62*, 10958.
14. Tamayo, A. B.; Alleyne, B. D.; Djurovich, P.; Lamansky, S.; Tsyba, I.; Ho, N. N.; Bau, R.; Thompson, M. E. *J. Am. Chem. Soc.* **2003**, *125*, 7377.
15. Lamansky, S.; Djurovich, P.; Murphy, D.; Abdel-Razzaq, F.; Lee, H.; Adachi, C.; Burrows, P.; Forrest, S. R.; Thompson, M. E. *J. Am. Chem. Soc.* **2001**, *123*, 4304.
16. Finkenzeller, W.; Yersin, H. *Chem. Phys. Lett.* **2003**, *377*, 299.

17. Hofbeck, T.; Yersin, H. *Inorg. Chem.* **2010**, *49*, 9290.
18. Liu, X.; Feng, J.; Ren, A.; Yang, L.; Yang, B.; Ma, Y. *Opt. Mater.* **2006**, *29*, 231.
19. Hedley, G. J.; Ruseckas, A.; Samuel, I. D. W. *J. Phys. Chem. A Lett.* **2008**, *113*, 2.
20. Hedley, G. J.; Ruseckas, A.; Samuel, I. D. W. *Chem. Phys. Lett.* **2008**, *450*, 292.
21. Hedley, G. J.; Ruseckas, A.; Liu, Z.; Lo, S. C.; Bum, P. L.; Samuel, I. D. W. *J. Am. Chem. Soc.* **2008**, *130*, 11842.
22. Tsuboi, T. *J. Lumin.* **2006**, *119/120*, 288.
23. Matsushita, T.; Asada, T.; Koseki, S. *J. Phys. Chem. C* **2007**, *111*, 6897.
24. Jansson, E.; Minaev, B.; Schrader, S.; Ågren, H. *Chem. Phys.* **2007**, *333*, 157.
25. Nozaki, K. *J. Chin. Chem. Soc.* **2006**, *53*, 101.
26. Rausch, A. F.; Homeier, H. H. H.; Yersin, H. *Top. Organomet. Chem.* **2010**, *29*, 193.
27. Nozaki, K.; Takamori, K.; Nakatsugawa, Y.; Ohno, T. *Inorg. Chem.* **2006**, *45*, 6161.
28. Tang, K.; Liu, K. L.; Chen, I. *Chem. Phys. Lett.* **2004**, *386*, 437.
29. Holzer, W.; Penzkofer, A.; Tsuboi, T. *Chem. Phys. Lett.* **2005**, *308*, 93.
30. Krumholz, P. *J. Am. Chem. Soc.* **1951**, *73*, 3487.
31. Johnson, P. M.; Otis, C. E. *Ann. Rev. Phys. Chem.* **1981**, *32*, 139.
32. Hay, P. J. *J. Phys. Chem. A* **2002**, *106*, 1634.
33. Kukhta, A. V.; Kukhta, I. N.; Bagnich, S. A.; Kazakov, S. M.; Andreev, V. A.; Neyra, O. L.; Meza, E. *Chem. Phys. Lett.* **2007**, *434*, 11.
34. Dobbs, K. D.; Sohlberg, K. *J. Chem. Theory Comput.* **2006**, *2*, 1530.
35. Periodic Table of the Elements: <http://www.periodni.com/ir.html>.
36. *CRC Handbook of Chemistry and Physics*, 92nd ed; **2011-2012**.

37. Van Kleef, T. A. M. *Physica* **1957**, *23*, 843.
38. Ow, F. P.; Djurovich, P.; Thompson, M. E.; Zink, J. I. *Inorg. Chem.* **2008**, *47*, 2389.
39. Ketkov, S. Y.; Selzle, H. L.; Schlag, E. W.; Domrachev, G. *J. Phys. Chem. A* **2003**, *107*, 4041.
40. Ketkov, S. Y.; Selzle, H. L.; Schlag, E. W.; Titova, S. N. *Chem. Phys.* **2003**, *293*, 91.
41. Leutwyler, S.; Even, U.; Jortner, J. *J. Phys. Chem.* **1981**, *85*, 3026.
42. Leutwyler, S.; Even, U.; Jortner, J. *Chem. Phys. Lett.* **1980**, *74*, 11.
43. Engelking, P. C. *Chem. Phys. Lett.* **1980**, *74*, 207.
44. Braun, J. E.; Neusser, H. J.; Harter, P.; Stockl, M. *J. Phys. Chem. A* **2000**, *104*, 2013.
45. Banares, L.; Baumet, T.; Bergt, M.; Kiefer, B.; Gerber, G. *J. Chem. Phys.* **1998**, *108*, 5799.
46. Letokhov, V. S. *Laser Photoionization Spectroscopy*; Academic Press, Inc.: Orlando, FL, **1987**.
47. Antonov, V. S.; Letokhov, V. S. *Appl. Phys.* **1981**, *24*, 89.
48. Ashfold, M. N. R.; Howe, J. D. *Annu. Rev. Phys. Chem.* **1994**, *56*, 57.
49. Strickler, S. J.; Berg, R. A. *J. Chem. Phys.* **1962**, *37*, 814.
50. Birks, J. B.; Dyson, D. J. *Proc. R. Soc. Lond. Ser. A* **1963**, *275*, 135.
51. Du, H.; Fuh, R. C. A.; Li, J. Z.; Corkan, L. A.; Lindsey, J. S. *Photochem. Photobiol.* **1998**, *68*, 141.
52. Hale, G. M.; Querry, M. R. *Appl. Opt.* **1973**, *12*, 555.
53. Kubin, J.; Testa, A. *J. Photochem. Photobiol. A: Chem.* **1994**, *83*, 91.
54. Polyakova, E.; Stolyarov, D.; Zhang, X.; Kresin, V. V.; Wittig, C. *Chem. Phys. Lett.* **2003**, *375*, 253.
55. Ionov, S.; Davis, H. F.; Mikhaylichenko, K.; Valachovic, L.; Beaudet, R. A.; Wittig, C. *J. Chem. Phys.* **1994**, *101*, 4809.

56. Allen, F. H.; Kennard, O. *Chem. Des. Auto. News* **1993**, 8, 31.
57. Breu, J.; Stossel, P.; Schrader, S.; Starukhin, A.; Finkenzeller, W.; Yersin, H. *Chem. Mater.* **2005**, 17, 1745.

Chapter 4

Electronic structure of tris(2-phenylpyridine)iridium: electronically excited and ionized states

4.1 Introduction

The use of organo-transition-metal complexes as phosphorescent species in light-emitting diodes (OLED's) enables quantum yields approaching 100% to be achieved through a mechanism referred to as triplet harvesting.¹⁻⁵ In triplet harvesting, spin-orbit coupling (SOC) enables electronic excitation that originates with electron-hole recombination (*i.e.*, both singlet and triplet excitons) to relax non-radiatively to the lowest triplet, T_1 . In turn, T_1 undergoes $T_1 \rightarrow S_0$ phosphorescence with near 100% quantum efficiency. This high quantum efficiency is also a consequence of SOC.¹⁻⁷ Namely, SOC results in short enough $T_1 \rightarrow S_0$ phosphorescence lifetimes to render T_1 non-radiative decay ineffective.

Such OLED's offer great advantage over purely organic counterparts, whose maximum quantum yield is 25%, *i.e.*, the singlet exciton fraction that results from electron-hole recombination with a statistical distribution of spin states.¹⁻⁷ In other words, phosphorescence is not a viable means of obtaining photons in organics because SOC is negligible, and consequently triplet excitation is lost rather than harvested.

As the light-emitting ingredient in OLED devices, organo-transition-metal complexes play a central role in the rapidly evolving research area of display

technologies. With billions of euros at stake, motivation from the high-tech commercial sector has never been higher. At the same time, these complexes are amenable to exacting and symbiotic experimental and theoretical studies. To wit, they are small enough to accommodate rigor, yet large enough to support bulk phenomena in a range of host materials. The OLED systems that are based on organo-transition-metal complexes are both technologically important and scientifically interesting, and their study benefits from, and is well suited to, mix-and-match interdisciplinary approaches.

An overview of OLED's as they relate to the experiments and calculations carried out in our groups is presented in the Introduction of Chapter 3. The reader is encouraged to read, at the very least, the Introduction in Chapter 3, as none of this is repeated below. In Chapter 3, several experimental results are presented and discussed, and possible interpretations are considered, in some cases enlisting comparisons with the calculated results presented herein.

In the present Chapter, tris(2-phenylpyridine)iridium, hereafter referred to as Ir(ppy)₃, is examined using time dependent density functional theory; details concerning its use in the present study are given in the next section. The goal is to obtain qualitative — and to the extent possible quantitative — understanding of low-lying singlets and triplets of Ir(ppy)₃, and of low-lying doublets of the cation Ir(ppy)₃⁺. This includes structural properties, spectral properties, molecular orbital (MO) descriptions, and ionization energies. The latter is germane to OLED devices because the ionization energies and electron affinities (commonly referred to as the HOMO and LUMO

energies, respectively) of the light-emitting molecules in the active layer need to be matched to the energy levels of the electrodes.

There are two low-energy Ir(ppy)₃ isomers: *facial* and *meridional*, hereafter referred to as *fac*-Ir(ppy)₃ and *mer*-Ir(ppy)₃, respectively. As discussed later, the energy difference between them is $\sim 1800 \text{ cm}^{-1}$ ($\sim 220 \text{ meV}$),^{8,9} with the *fac* isomer the more stable of the two. This is sufficient to rule out the participation of *mer*-Ir(ppy)₃ in most environments. Consequently, though some calculations were carried out on the *mer*-Ir(ppy)₃ system, the main focus of the present study is *fac*-Ir(ppy)₃.

The work reported herein builds on and complements earlier theoretical studies,⁸⁻¹² and it assists in the interpretation of experimental results,¹³⁻¹⁶ including, but not limited to, those presented in Chapter 3. Organization of the Chapter is as follows. Computational strategies and procedures are presented and discussed in Section 4.2. This is followed (in Section 4.3) by the results, and discussions of their relevance to experimental data and practical applications. These results include: equilibrium structures; vertical and adiabatic ionization energies; MO descriptions obtained at the equilibrium structures of the ground state (S_0), lowest triplet (T_1), and lowest ionized state (D_0); the ultraviolet absorption spectrum; comparison to experimental T_1 phosphorescence parameters ($T_1 - S_0$ energy gap, spontaneous emission lifetimes, and Franck-Condon factors); and an interesting point regarding the probability density for T_1 vibrational energy following photoexcitation of gaseous Ir(ppy)₃ at 500 K, *i.e.*, the temperature at which the experiments presented in Chapter 3 were carried out. The Chapter concludes with a brief summary.

4.2 Computational details

Two long-range-corrected (LRC) functionals were used: ω B97X and BNL.¹⁷⁻²⁰ Each treats the long-range Coulomb interaction exactly (*i.e.*, 100% Hartree-Fock exchange), thus ensuring proper asymptotic behavior and mitigating the notorious self-interaction errors.²¹ Specifically, these functionals reduce the unphysical charge delocalization that is often observed when using standard functionals such as B3LYP. They also eliminate contamination of time dependent density functional theory (TDDFT) results by an artificially low-lying Rydberg manifold that converges to the Koopmans ionization energy (IE), which is underestimated when using non-LRC functionals. A brief introduction to density functional theory (DFT) is provided in Appendix A.

Our choice is based on the following considerations. The ω B97X functional has been carefully parameterized and benchmarked.^{17,18} It consistently gives more accurate structures and standard thermochemical quantities than, for example, B3LYP. Thus, structures calculated using ω B97X are taken as our best estimates. The BNL functional has been developed for excited states. Its range-separation parameter ω is system-dependent, and it is chosen such that the Koopmans IE is equal to the vertical ionization energy (VIE), a condition that should be satisfied for the exact exchange-correlation functional. BNL performs well for excited and ionized states, including ionization from lower orbitals.^{19,20} Thus, we expect its IE's and excited state energies to be of higher quality than the ω B97X ones.

Structures of *fac*-Ir(ppy)₃ and *mer*-Ir(ppy)₃ in the S₀, T₁, and D₀ states were optimized using the ω B97X functional.^{18,19} For the iridium atom, the lanl2dz basis was employed, whereas 6-311G++(d,p) was used for all other atoms.^{22,23} The range-separation parameter ω in the BNL functional was optimized such that the VIE that was computed using the energy differences method (Δ SCF) matched the HOMO energy (Koopmans IE) at the S₀ equilibrium geometry. This yielded $\omega = 0.17 a_0^{-1}$.¹⁷ The default ω value for BNL is $0.50 a_0^{-1}$, and the ω value in ω B97X is fixed at $0.3 a_0^{-1}$.^{19,24,25} (as mentioned above, BNL ω values are system specific).

The IE's were calculated using Koopmans theorem, which has been shown to yield accurate results for the BNL functional, owing to its LRC character and a system-specific choice of ω . Moreover, the BNL orbitals provide a reasonable representation of the ionized state, which is not the case for B3LYP. The shape of the hole in the ionized state can be verified by calculating the spin density: $\rho(\alpha) - \rho(\beta)$, for each MO. This accounts for non-Koopmans character, *i.e.*, orbital relaxation. This analysis was carried out for D₀ at selected geometries.

Excited states were calculated at the S₀ and T₁ geometries using TDDFT with ω B97X and BNL functionals and lanl2dz and 6-311+G(d,p) bases. At the S₀ geometry, 50 singlet and 50 triplet states were calculated using ω B97X, spanning the energy range 2.86 – 6.31 eV. With BNL at the S₀ geometry, 130 singlets and 130 triplets were calculated, spanning the energy range 2.56 – 5.66 eV. With BNL at the T₁ geometry, only the 10 lowest singlet and 10 lowest triplet states were calculated.

The TDDFT excited state energies and oscillator strengths were used to calculate absorption spectra. Gaussian shaped spectral densities, $g_i(E)$, were assigned to each of the transitions in a given theoretical "stick spectrum." Specifically, the absorption spectrum was simulated as a sum of Gaussian spectral densities, $g_i(E)$, each having the same width parameter σ :

$$g_i(E) = f_i (2\pi\sigma^2)^{-1/2} \exp\left(-\frac{(E-E_i)^2}{2\sigma^2}\right) \quad (4.1)$$

The factor f_i is the oscillator strength of the electric dipole transition from the S_0 ground state to the i^{th} electronic state. Each Gaussian spectral density is centered at its excited state energy, E_i . The width parameter σ is related to the full width at half maximum (FWHM) of the Gaussian distribution according to: $\text{FWHM} = 2(2\ln 2)^{1/2}\sigma = 2.35\sigma$. All calculations were carried out using the QChem electronic structure package.²⁶

4.3 Results and discussion

In this section, the strategies and procedures described in Section 4.2 are applied to calculations of properties of Ir(ppy)_3 and Ir(ppy)_3^+ . A number of technical details and data sets that are omitted from the text for the sake of brevity are included in Appendix B (AB). Reference to AB is made whenever appropriate. Energies and frequencies are given in wavenumbers (cm^{-1}), with eV counterparts in parentheses. On occasion, kcal mol^{-1} is used, *i.e.*, when comparing to literature values given in these units.

4.3.1 Equilibrium structures

The ground electronic state structures of *fac*-Ir(ppy)₃ and *mer*-Ir(ppy)₃ are indicated in Figure 4.1. As discussed below, their energies differ by $\sim 1800\text{ cm}^{-1}$ ($\sim 220\text{ meV}$) with *fac*-Ir(ppy)₃ the more stable of the two. Table 4.1 lists selected bond lengths for *fac*-Ir(ppy)₃ at its S₀ and T₁ equilibrium geometries, and for Ir(ppy)₃⁺ at the equilibrium geometry of the lowest energy cation state, D₀. Table 4.2 lists selected bond lengths for the S₀ and D₀ equilibrium geometries of *mer*-Ir(ppy)₃. The z -matrices and relevant energies are provided in AB.

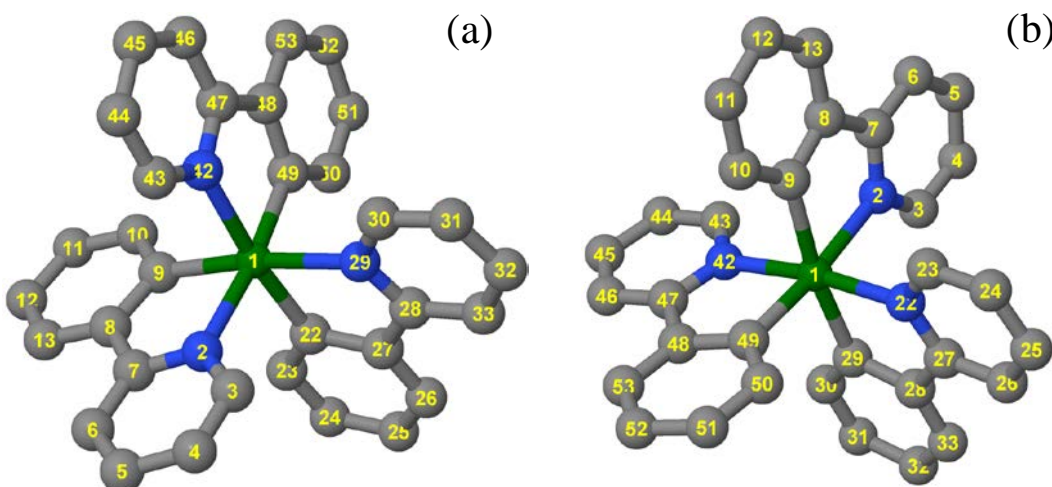


Figure 4.1. Ground electronic state structures and atom numbering for (a) *fac*-Ir(ppy)₃ and (b) *mer*-Ir(ppy)₃. H atoms are omitted. Color scheme: green = Ir; blue = N; gray = C. Tables 4.1 and 4.2 list geometrical parameters.

	S ₀ (theory)			S ₀ (expt)			T ₁ (theory)		D ₀ (theory)
	(a)	(b)	(c)	(d)	(e)	(f)	(a)	(b)	(a)
Ir–N ₂	2.168	2.153	2.167	2.088	2.071	2.132	2.196	2.176	2.149
Ir–N ₂₉	2.169	2.154	2.167	2.088	2.071	2.132	2.175	2.169	2.184
Ir–N ₄₂	2.165	2.151	2.167	2.088	2.071	2.132	2.139	2.116	2.213
Ir–C ₉	2.025	2.035	2.035	2.006	2.060	2.024	2.025	2.030	2.028
Ir–C ₂₂	2.023	2.035	2.035	2.006	2.060	2.024	2.036	2.048	1.975
Ir–C ₄₉	2.022	2.035	2.035	2.006	2.060	2.024	1.961	2.000	2.035
N ₂ –C ₃ , N ₂₉ –C ₃₀	1.34	1.36	–	1.345	1.361	1.331	1.34	1.36	1.34
N ₄₂ –C ₄₃	1.34	1.36	–	1.345	1.361	1.331	1.33	1.36	1.34
N ₂ –C ₇ , N ₂₉ –C ₂₈	1.35	1.38	–	1.358	1.385	1.371	1.35	1.38	1.355, 1.35
N ₄₂ –C ₄₇	1.35	1.38	–	1.358	1.385	1.371	1.40	1.439	1.35
C ₉ –C ₁₀ , C ₂₂ –C ₂₃	1.405	1.42	–	1.405	1.374	1.401	1.40	1.42	1.395, 1.41
C ₄₉ –C ₅₀	1.405	1.42	–	1.405	1.374	1.401	1.41	1.42	1.40
C ₈ –C ₉ , C ₂₂ –C ₂₇	1.415	1.44	–	1.423	1.396	1.409	1.41	1.43	1.41, 1.407
C ₄₈ –C ₄₉	1.415	1.436	–	1.423	1.396	1.409	1.49	1.485	1.426
C ₇ –C ₈ , C ₂₇ –C ₂₈	1.47	1.47	–	–	–	1.487	1.47	1.47	1.47, 1.476
C ₄₇ –C ₄₈	1.47	1.467	–	–	–	1.487	1.40	1.419	1.473

(a) current work, references (b) 10, (c) 9, (d) 27, (e) 28, (f) 29

Table 4.1. Bond lengths (Å) for S₀, T₁, and D₀ states of Ir(ppy)₃.

Referring to Table 4.1, the equilibrium bond lengths of ground state *fac*-Ir(ppy)₃ are compared with results of *x*-ray diffraction measurements of *fac*-Ir(ppy)₃^{27,28} and of its tolylpyridine analog *fac*-Ir(tpy)₃,²⁹ as well as with previous theoretical estimates.^{9,10} The T₁ equilibrium structure is compared to the calculations of Jansson *et al.*¹⁰ Referring to Table 4.2, the calculated *mer*-Ir(ppy)₃ structure is compared with the crystallographic structure of its tolylpyridine analog: *mer*-Ir(tpy)₃.¹⁶

Variations in the experimentally determined bond lengths arise, at least in part, because of different experimental conditions. For example, the high pressure

crystallographic structure reported by Breu *et al.*²⁸ showed that the *fac*-Ir(ppy)₃ crystal has a racemic unit cell (three Δ and three Λ complexes in the $P\bar{3}$ point group). Thus, though isolated ground state *fac*-Ir(ppy)₃ molecules are of C₃ symmetry, they can develop different equilibrium bond lengths when exposed to local environments.

Table 4.1 includes entries from one of the three data sets reported in reference 28. Specifically, the set chosen for comparison with our calculated values is the one that displays the *largest* differences with our values. Differences in bond lengths among the data sets reported in reference 28 are within 0.03 Å of one another. Differences between all reported experimental values are slightly larger, *i.e.*, approximately 0.04 and 0.05 Å for Ir–N and Ir–C bond lengths, respectively, but less than 0.02 Å for all other bond lengths. All crystallographic structures are of similar quality, with a reported bond length uncertainty of < 1%.

	<u>S₀ (theory)</u>	<u>S₀ (expt)</u>	<u>D₀ (theory)</u>
	(a)	(b)	(a)
Ir-N ₂	2.193	2.151	2.275
Ir-N ₂₂	2.079	2.044	2.083
Ir-N ₄₂	2.068	2.065	2.077
Ir-C ₉	2.101	2.086	2.094
Ir-C ₂₉	2.078	2.076	2.070
Ir-C ₄₉	2.006	2.020	1.973
N ₂ -C ₃ , N ₂₂ -C ₂₃	1.34		1.34
N ₄₂ -C ₄₃	1.34		1.34
N ₂ -C ₇ , N ₂₂ -C ₂₇	1.35, 1.36		1.35, 1.354
N ₄₂ -C ₄₇	1.355		1.353
C ₉ -C ₁₀ , C ₂₉ -C ₃₀	1.404, 1.40		1.40, 1.394
C ₄₉ -C ₅₀	1.404		1.404
C ₈ -C ₉ , C ₂₈ -C ₂₉	1.414, 1.41		1.40, 1.406
C ₄₈ -C ₄₉	1.413		1.42
C ₇ -C ₈ , C ₂₇ -C ₂₈	1.48, 1.47		1.47, 1.47
C ₄₇ -C ₄₈	1.464		1.47

(a) current work, (b) reference 16.

Table 4.2. Bond lengths (Å) for S₀ and D₀ *mer*-Ir(ppy)₃.

The *fac*-Ir(ppy)₃ ground state structure was optimized with no symmetry constraints. It deviates slightly from C₃ symmetry due to numerical thresholds used in optimization, and the inability of Cartesian integration grids to support groups like C₃. Our calculated structure is similar to the one reported by Jansson *et al.*,¹⁰ and it is in reasonable agreement with other theoretical values,⁹ despite the fact that they were obtained at a lower level of theory. The computed Ir–C and Ir–N bond lengths are closest to the experimental values reported in reference 29. The deviations are 0.001 and 0.04 Å for Ir–C and Ir–N, respectively. The N–C and C–C bond lengths are within 0.01 Å of the values reported in reference 27, while deviations from the values reported in reference 28 are about 0.03 Å.

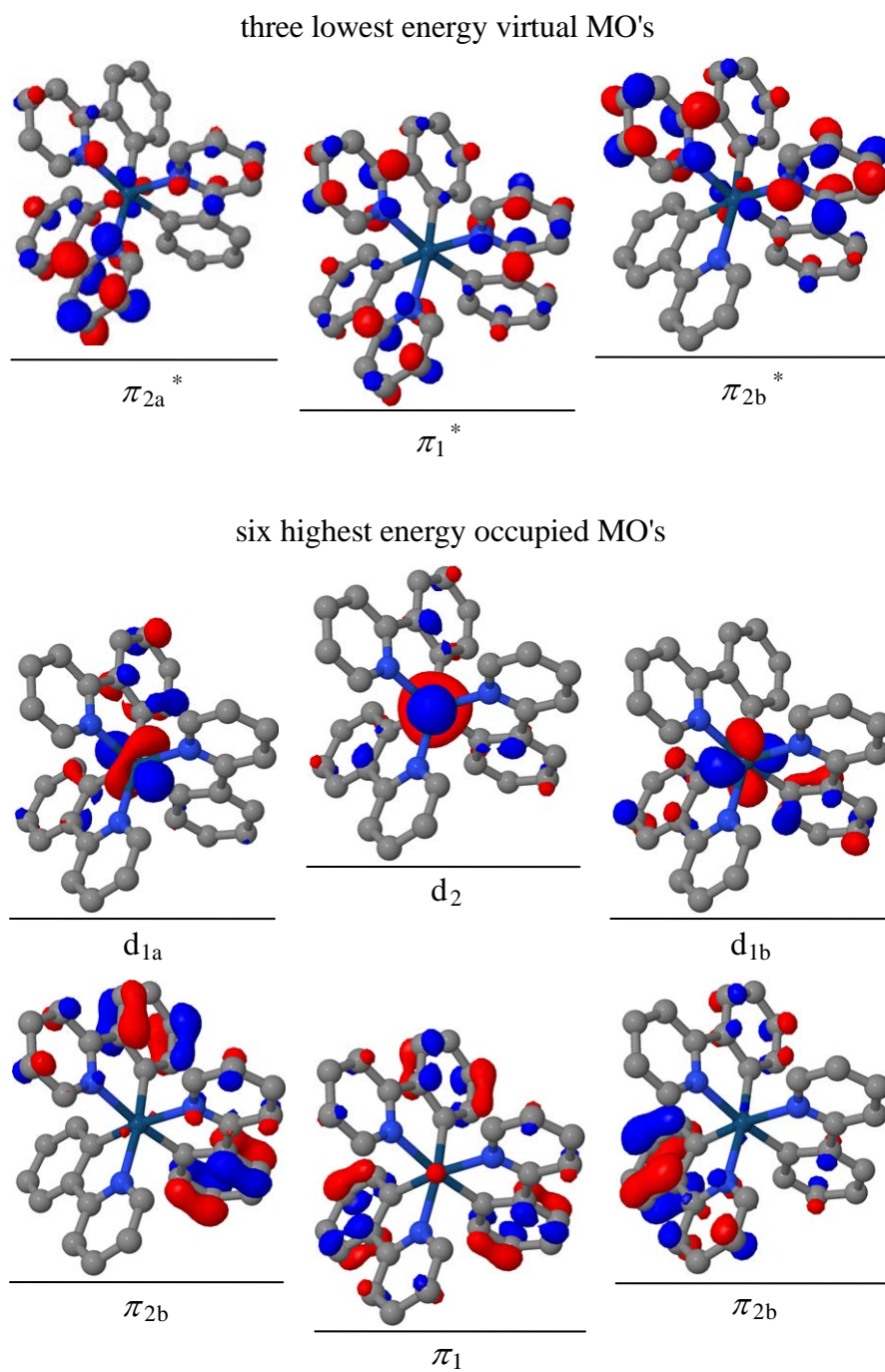


Figure 4.2. Six highest occupied MO's and three lowest virtual MO's for fac-Ir(ppy)₃ at S₀ geometry using BNL: Orbital labeling follows Hay.¹⁰ Energies of occupied orbitals (Koopmans IE's) are given in Table 4.3.

Referring to Figure 4.2, π_{2a}^* and π_{2b}^* are components of a doubly degenerate e orbital. Consequently, T_1 and D_0 each exhibit Jahn-Teller distortion that breaks C_3 symmetry. In T_1 , relative to the S_0 values, two ligands move away from the iridium atom and one is drawn closer to the iridium atom. Specifically, the closer ligand corresponds to Ir-C₄₉ and Ir-N₄₂ our calculations (see Figure 4.1 for numbering of atoms). The D_0 structure follows a similar pattern. The Ir-C₂₂ and Ir-N₂ bonds contract, whereas the other metal-ligand bonds lengthen relative to their S_0 values. An interesting difference between T_1 and D_0 is that the contracted bonds in D_0 are not part of the same ligand. These structural changes are consistent with the MO shapes, as discussed later.

Calculations were also carried out for the *mer*-Ir(ppy)₃ isomer whose structure is indicated in Figure 4.1(b). The results are summarized in Table 4.2. When using ω B97X and BNL, the *mer* isomer is calculated to be less stable than the *fac* isomer by 280 and 220 meV (2270 and 1760 cm⁻¹, 6.5 and 5.0 kcal mol⁻¹), respectively. These values are total electronic energy differences, Δ SCF. This is consistent with previous theoretical^{8,9} and experimental¹⁶ results.

Despite the apparent similarity between the *fac* and *mer* isomers seen in Figure 4.1, bonding is different. In the *mer* isomer, the three nitrogen atoms lie in a plane that contains the iridium atom (with two nitrogen atoms lying on a straight N-Ir-N line), whereas in the *fac* isomer the nitrogen atoms form an equilateral triangle with the iridium atom out of the plane on the C_3 axis. This difference, in which the *mer* isomer is obtained

from the *fac* isomer by rotating a single ligand 180° about its $\angle\text{C-Ir-N}$ bisection line, places two phenyl groups, and consequently two pyridyl groups, *trans* to one another.

As shown in Table 4.2, and referring to the *mer* isomer indicated in Figure 4.1(b), its *trans* Ir–C bonds (*i.e.*, Ir–C₉ and Ir–C₂₉) are longer than the Ir–C bonds in *fac*-Ir(ppy)₃, while the remaining *mer* Ir–C₄₉ bond length is nearly equal to the *fac* Ir–C bond length. Also note that the remaining Ir–C₄₉ bond has an environment that is similar to that of the *fac* Ir–C bonds, in the sense that it is perpendicular to two Ir–N bonds (*i.e.*, Ir–C₂₄ and Ir–C₄₂). Thus, it is not surprising that their lengths are similar. On the other hand, the *trans* Ir–C bonds do not share the same environment as the Ir–C bonds in the *fac* isomer, in the sense that they are perpendicular to all three Ir–N bonds.

The extended Ir–C bond lengths are consistent with the weaker structural *trans*-effect, often called the *trans* influence,^{30,31} of a pyridyl group relative to a phenyl group. A similar analysis of the *mer* Ir–N bonds shows that the *trans* N–Ir–N bonds are noticeably shorter than in the *fac* isomer. This is again consistent with the weaker structural *trans*-effect of the pyridyl group. Our predicted *mer* structure is in reasonable agreement with the *x*-ray data for *mer*-Ir(tpy)₃, *i.e.*, bond lengths are within 0.04 Å of the experimental values.¹⁶

In making comparisons to the experimental work presented in Chapter 3, it is possible to rule out significant participation of the *mer*-Ir(ppy)₃ isomer. Specifically, the energy gap between the *fac* and *mer* isomers, say 220 meV (*i.e.*, the BNL value), is large enough that at 500 K the *mer*-Ir(ppy)₃ population is only $\exp(-E_{mer}/kT) = \exp(-5.12) \approx$

0.6% of that of *fac*-Ir(ppy)₃. Thus, hereafter only the *fac*-Ir(ppy)₃ isomer will be considered.

4.3.2 Molecular orbitals

The molecular orbitals (MO's) of *fac*-Ir(ppy)₃ that are most relevant to the present study are shown in Figure 4.2, and the orbital energies (Koopmans IE's) for the six highest energy occupied MO's are listed in Table 4.3. As mentioned earlier, the use of an LRC functional reduces artificial delocalization caused by self-interaction error. Consequently, the LRC functionals used here yield MO's that represent the character of the excited and ionized states better, for example, than does B3LYP. In addition, the Koopmans IE's with BNL are more reliable.³²

MO	BNL	ω B97X
d ₂	-5.87	-7.42
d _{1a} , d _{1b}	-6.06	-7.49
π_{2a} , π_{2b}	-7.15	-8.45
π_1	-7.27	-8.59

Table 4.3. Koopmans IE's (eV) for the six highest energy occupied MO's of *fac*-Ir(ppy)₃.

Referring to Figure 4.2, the three highest occupied molecular orbitals at the S₀ equilibrium geometry are of mixed 5d – π character. They are labeled: d_{1a}, d_{1b}, and d₂, and they will also be referred to as HOMO-1, HOMO-2, and HOMO, respectively. The d₂ HOMO is dominated by the iridium 5dz² orbital, but with a π contribution that arises almost entirely from the phenyl groups. The d_{1a} and d_{1b} orbitals, which are components of

a doubly degenerate e orbital, consist of combinations of d-orbitals, with a somewhat larger contribution from the phenyl groups than in the case of d_2 .

The three lowest energy MO's in Figure 4.2 are primarily of π character, with most of the electron density residing on the phenyl groups. They have less than 4% iridium character. The lowest energy virtual orbitals are primarily of π^* character in the pyridyl group. These lowest virtual orbitals are of e and a symmetries, with π_{2a}^* and π_{2b}^* being components of a doubly degenerate e orbital. From the Jahn-Teller theorem, single occupancy of e orbitals will lead to symmetry lowering in excited and ionized states. This is consistent with orbital localization in which the HOMO becomes asymmetrically distributed among the ligands. It is also consistent with the results reported by Jansson *et al.*¹⁰

Mulliken spin density of hole				
	Ir	C ₁	C ₂	C ₃
S ₀	67	~4 ^a	~4 ^a	~4 ^a
T ₁	58	12	11	6
D ₀	61	10	13	10

^a For S₀ there are 3 identical sets of carbon atoms (C₁, C₂, C₃), so the listed percentages (~4) need to be multiplied 3 to account for the 9 main participating carbon atoms.

Table 4.4. BNL percent spin density for *fac*-Ir(ppy)₃ at the S₀, T₁, and D₀ equilibrium geometries. For T₁ and D₀, only the main contributions are listed.

This above picture is consistent qualitatively with previous findings.⁹⁻¹¹ However, relative to previous calculations, our orbitals are more localized, owing to the use of LRC functionals. This was confirmed by a shell population analysis of S₀ (details are given in

AB). Iridium comprised 58% of the HOMO character, but only 48% of the HOMO-1 and HOMO-2 character.

The shape of the hole in the cation has been verified by spin density calculations that account for non-Koopmans character, *i.e.*, orbital relaxation. The spin density analysis is in qualitative agreement with a Koopmans description of the electron hole (Figure 4.3). A summary of Mulliken spin densities of the cation at S_0 , T_1 , and D_0 geometries is given in Table 4.4, and the HOMO's from which an electron is removed are shown in Figure 4.3. It is seen that structural relaxation causes the amount of iridium character in the electron hole to increase from 58% to 65%. The complete list of Mulliken spin densities for all three geometries is provided in AB.

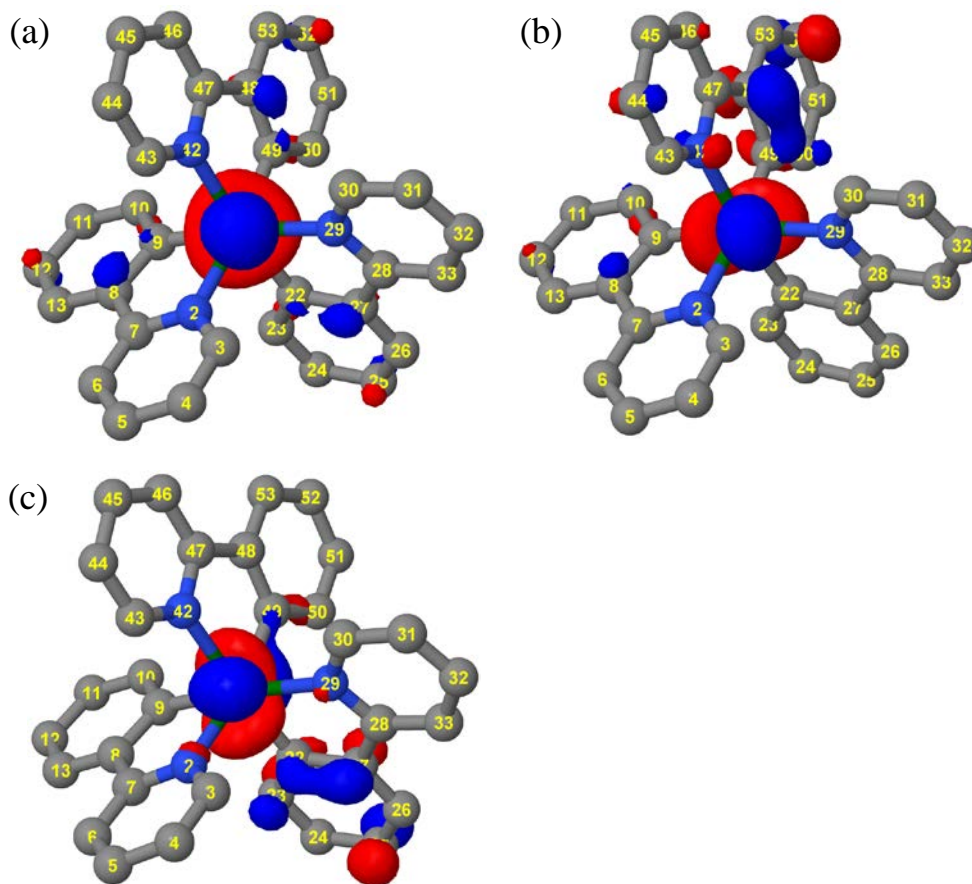


Figure 4.3. Shapes of the electron hole wave functions obtained from Koopmans analyses for cations at the (a) S_0 , (b) T_1 , and (c) D_0 equilibrium geometries.

Referring to Figure 4.3(a) and Table 4.4, the HOMO at the S_0 geometry, and therefore the character of the cation hole of S_0 , is the d_2 orbital indicated in Figure 4.2. [Note that the orbital shown in Figure 4.3(a) is identical to the d_2 orbital in Figure 4.2.] Therefore, the hole is symmetric with the iridium atom hosting most of the hole spin density. The remaining $\approx 35\%$ is distributed over the three phenyl groups. In each phenyl group (see Figure 4.4), carbons C1, C2, and C3 account for most of the spin density.

At the D_0 and T_1 equilibrium geometries, the HOMO differs considerably from that of the S_0 equilibrium geometry. First, the HOMO at the D_0 equilibrium geometry has a large percentage of its density on the phenyl group drawn closest to iridium. It resembles the d_{1a} orbital in Figure 4.2. Much of the hole spin density in the cation resides on the carbons C1, C2, and C3 indicated in Figure 4.4.

Now consider T_1 at its equilibrium geometry. The ligand closest to the iridium atom contains nearly all of the ligand portions of the HOMO and LUMO that describe T_1 , as indicated in Figure 4.5. Note that the HOMO in Figure 4.5(d) is identical to the electron hole wave function (at the T_1 equilibrium geometry) in Figure 4.3(b). In contrast to the D_0 hole in Figure 4.3(c), the T_1 hole in Figure 4.3(b) has more amplitude over the pyridyl group of the closest ligand. The pyridyl atoms hosting most of the spin density are those labeled N42, C44, and C46 in Figure 4.1(a).

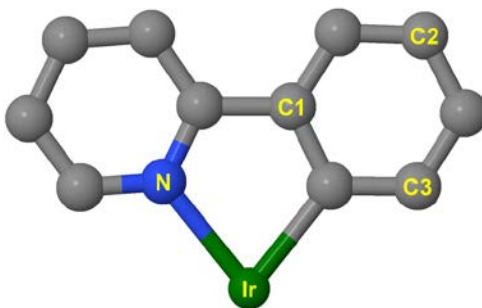


Figure 4.4. Ir(ppy) corresponding to Table 4.4: For the T_1 equilibrium geometry, C1, C2, and C3 correspond to carbons labeled 48, 52, and 50 in Figure 4.1(a) [see also Figure 4.3(b)]. For the D_0 equilibrium geometry C1, C2, and C3 correspond to carbons labeled 23, 25, and 27 in Figure 4.1(a) [see also Figure 4.3(c)].

Furthermore, because the character of the HOMO changes from d_2 at the S_0 geometry to d_{1a} at the D_0 and T_1 geometries, the electronic character of the cation ground state changes upon these displacements. In other words, the d_2 and d_{1a}/d_{1b} orbitals (and consequently the respective diabatic states of the cation) change their relative order. This is not surprising in view of the small energy gap between them (0.19 eV) at the S_0 geometry.

The Koopmans IE's for the six highest-energy occupied MO's are listed in Table 4.3. Due to small deviations from C_3 symmetry, the energies of degenerate e orbitals are slightly different (< 0.01 eV), so we report the average of the two values. As seen in Table 4.3, the density of electronic states in the cation is rather high, *i.e.*, there are 6 cation states in the range: 5.87 – 7.27 eV. The difference between the BNL and ω B97X values is due to different values of ω . Based on the previous benchmarks and reported VIE values, the BNL results are expected to be more reliable.

Adiabatic and vertical IE's calculated as a total energy difference are presented in Table 4.5 for S_0 and T_1 geometries. The small difference between the BNL VIE and AIE values (≤ 0.02 eV) for S_0 and T_1 suggests that structural relaxation caused by the removal of a single electron is small, possibly because of the delocalized character of the orbitals. The use of ω B97X results in a larger difference between VIE and AIE than BNL for both S_0 and T_1 (0.09 eV for S_0 and 0.46 eV for T_1).

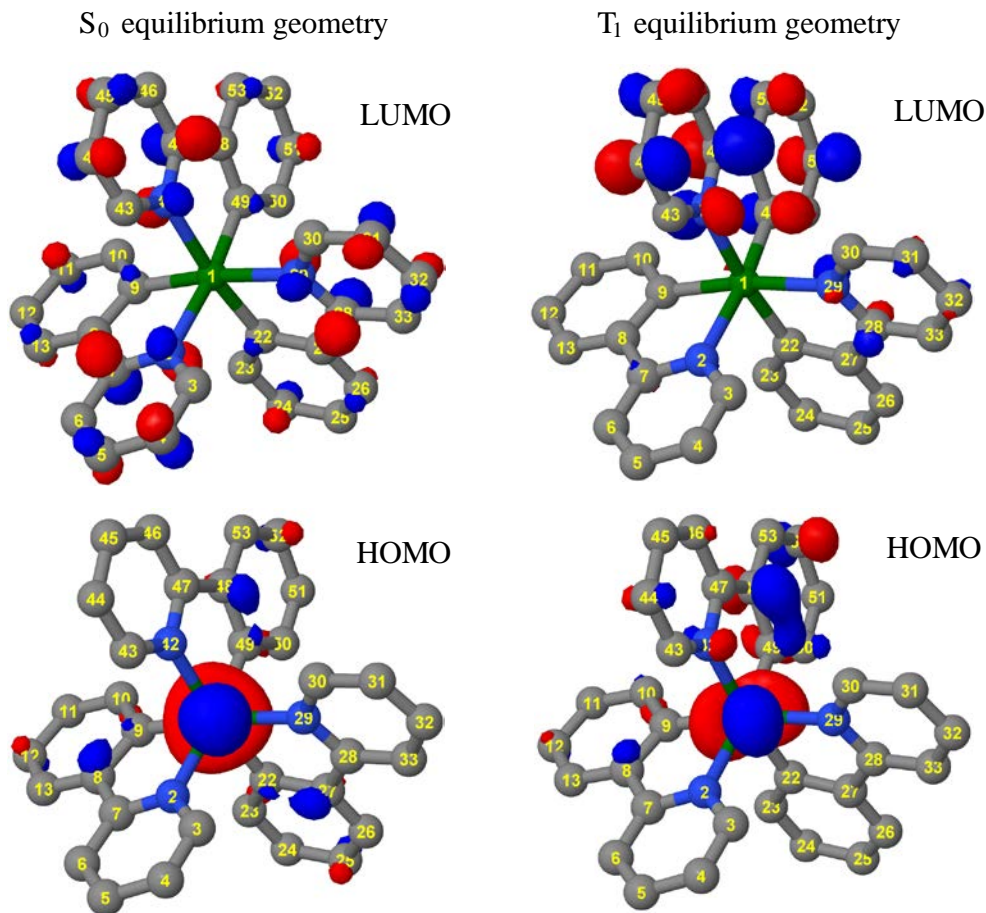


Figure 4.5. Orbitals giving rise to T_1 excitation (HOMO and LUMO of S_0): left and right columns correspond, respectively, to S_0 and T_1 equilibrium geometries.

	BNL		ω B97X	
	VIE	AIE	VIE	AIE
S_0	5.87	5.86	6.42	6.33
T_1	3.40	3.38	3.98	3.52

Table 4.5. Vertical and adiabatic IE's (eV) for *fac*-Ir(ppy)₃ from S_0 and T_1 states at their equilibrium geometries.

The only previously reported theoretical estimate of the VIE from S_0 is 5.94 eV,⁹ while the only previously reported experimental value is an indirect inference of 7.2 eV.¹⁵

Our experimental study (Chapter 3) provides a conservative VIE upper bound of 6.4 eV.

Both BNL and ω_{B97X} values (5.87 and 6.42 eV, respectively) agree with this experimentally derived upper bound. However, the BNL value is the more accurate estimate for the reasons given in Section 4.2.

4.3.3 Ultraviolet absorption spectrum

Figure 4.6 shows experimental and calculated ultraviolet absorption spectra. All excited state energies and oscillator strengths were evaluated at the ground state equilibrium geometry. As discussed in Section 4.2, BNL gives the most reliable excited states. Therefore, it is the BNL spectrum that is compared to the experimental spectrum.

Though ω_{B97X} yielded good values for ground state equilibrium structures (Figure 4.1, Tables 4.1 and 4.2), it is inferior insofar as excited states are concerned, *e.g.*, see the comparison in the inset in Figure 4.6. The ω_{B97X} spectrum was computed using the first 50 singlets, whereas for the BNL spectrum, 130 singlets were necessary to achieve convergence. Selected BNL excitation energies are given in Tables 4.6 and 4.7. A complete list of the calculated excited states and oscillator strengths that were used to construct the theoretical spectra is given in AB.

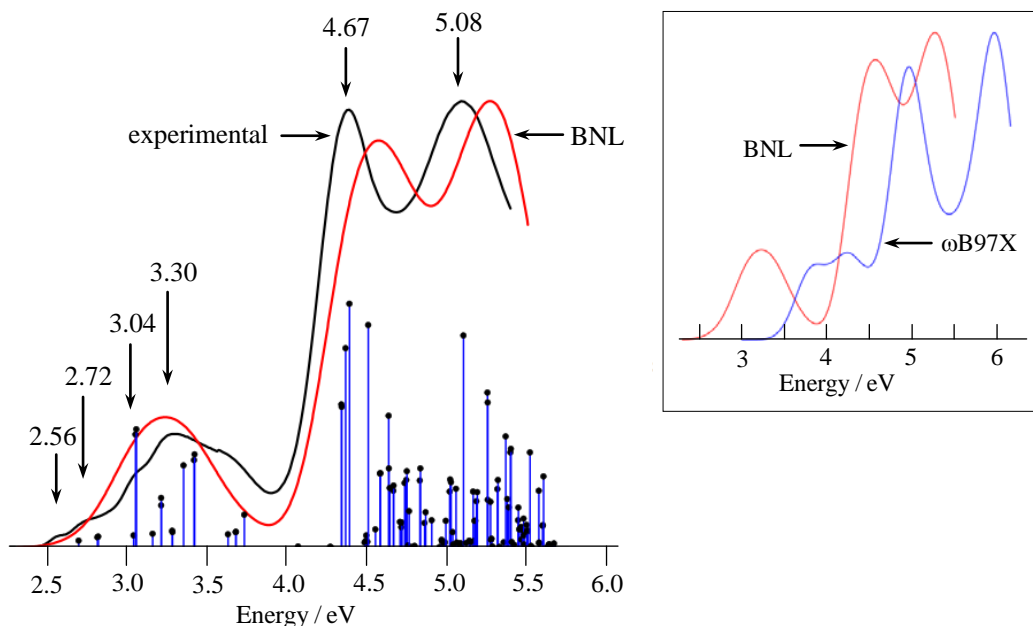


Figure 4.6. Ultraviolet absorption spectra of *fac*-Ir(ppy)₃. The calculated spectrum (red) was obtained from the stick spectrum by assigning to each stick a Gaussian FWHM of 0.43 eV. The experimental spectrum (black) was recorded at room temperature in dichloromethane. Peak and shoulder positions (vertical arrows) are in eV. All stick heights have been increased by the same constant factor for viewing convenience, and curve height has been adjusted such that the maximum absorptions are equal. The low-energy, low-intensity wing due to $T_1 \leftarrow S_0$ (2.56 eV) is absent in the calculated spectrum because SOC was not included. Inset: The BNL (red) and ω B97X (blue) spectra differ considerably, the latter being far out of registry with the experimental spectrum.

state	S_0 geometry			T_1 geometry		
	energy	leading character	amplitude	energy	leading character	amplitude
T_1	2.56	$d_2 \rightarrow \pi_{1}^*$	0.89	2.30	$d_2 \rightarrow \pi_{1}^*$	0.87
T_2	2.61	$d_2 \rightarrow \pi_{2a}^*$	0.59	2.74	$d_{1a} \rightarrow \pi_{1}^*$	0.71
		$d_2 \rightarrow \pi_{2b}^*$	-0.54			
T_3	2.62	$d_2 \rightarrow \pi_{2a}^*$	0.59	2.78	$d_2 \rightarrow \pi_{2b}^*$	0.47
		$d_2 \rightarrow \pi_{2b}^*$	0.53		$d_{1b} \rightarrow \pi_{1}^*$	
T_4	2.83	$d_{1b} \rightarrow \pi_{2a}^*$	0.67	2.82	$d_2 \rightarrow \pi_{2a}^*$	-0.46
					$d_2 \rightarrow \pi_{2b}^*$	0.51

Table 4.6. Orbital character and leading amplitude for the four lowest energy triplet states at the S_0 and T_1 equilibrium geometries: Energies are relative to that of S_0 at its equilibrium geometry.

Referring to equation 4.1, a width parameter of $\sigma = 0.185$ eV (corresponding to Gaussian FWHM of 0.43 eV) was obtained from a least-squares fit of the BNL spectrum to the experimental spectrum. No attempt was made to calculate absolute intensities. Thus, the vertical axis in Figure 4.6 is not labeled. The BNL curve was scaled such that its maximum is the same height as the maximum of the experimental spectrum. These calculations do not include contributions from triplets due to SOC. The low-energy part of the experimental spectrum has been assigned to singlet-triplet transitions,¹⁴ where it is understood that the "triplets" contain modest amounts of singlet character. The shoulder at 2.56 eV in the experimental spectrum is the same as our T_1 value (Table 4.6). Note that T_2 and T_3 , though close in energy to T_1 at the S_0 equilibrium geometry, are much higher in energy than T_1 at the T_1 equilibrium geometry (Figure 4.7).

state	S_0 geometry			T_1 geometry		
	energy	character	amplitude	energy	character	amplitude
S_1	2.69	$d_2 \rightarrow \pi_1^*$	0.94	2.62	$d_2 \rightarrow \pi_1^*$	0.95
S_2	2.80	$d_2 \rightarrow \pi_{2a}^*$	0.90	2.91	$d_2 \rightarrow \pi_{2a}^*$	0.82
S_3	2.81	$d_{1b} \rightarrow \pi_{2a}^*$	0.90	2.96	$d_2 \rightarrow \pi_{2b}^*$	0.84

Table 4.7. Orbital character and leading amplitude for the three lowest energy singlet excited states at the S_0 and T_1 equilibrium geometries. Energies are relative to that of S_0 at its equilibrium geometry.

The two intense bands at energies higher than 4 eV have been assigned to ligand-centered transitions (${}^1LC \leftarrow S_0$). The broad absorbance below 4 eV is due primarily to spin-allowed transitions that terminate on metal-to-ligand charge transfer states (1MLCT).

The shoulder at 2.56 eV in the experimental spectrum is attributed to $^3\text{MLCT}$ by analogy with organic compounds. These assignments are qualitative because configuration interaction and spin-orbit coupling result in mixed state character.¹²

The label MLCT is correct in the sense that metal-to-ligand electron transfer dominates. However, orbital analyses show that, in addition, a significant amount of charge is transferred from the phenyl to the pyridyl groups. Intra-ligand charge transfer also participates in ligand-centered transitions that involve asymmetric orbitals, *e.g.*, $\pi_{2a}^* \leftarrow d_{1a}$.

The BNL and experimental spectra are in agreement in terms of locations of maxima and overall shape. The ωB97X spectrum (Figure 4.6, inset) is blue-shifted by almost 1 eV, and relative intensities of the three major bands match the experimental spectrum significantly less well. It is clearly of inferior quality and will not be considered further insofar as excited states are concerned. In assigning line shapes, the same FWHM (0.43 eV) was used for each transition. The high density of electronic states gives rise to broad bands. Because of the delocalized nature of the orbitals involved in the transitions, it is expected that the Franck-Condon factors are near diagonal, *i.e.*, $\Delta v_i = 0$. Thus, transitions were taken as vertical from the S_0 equilibrium geometry, *i.e.*, the nuclear degrees of freedom are treated classically. It would be unreasonable to expect a better match between experiment and theory.

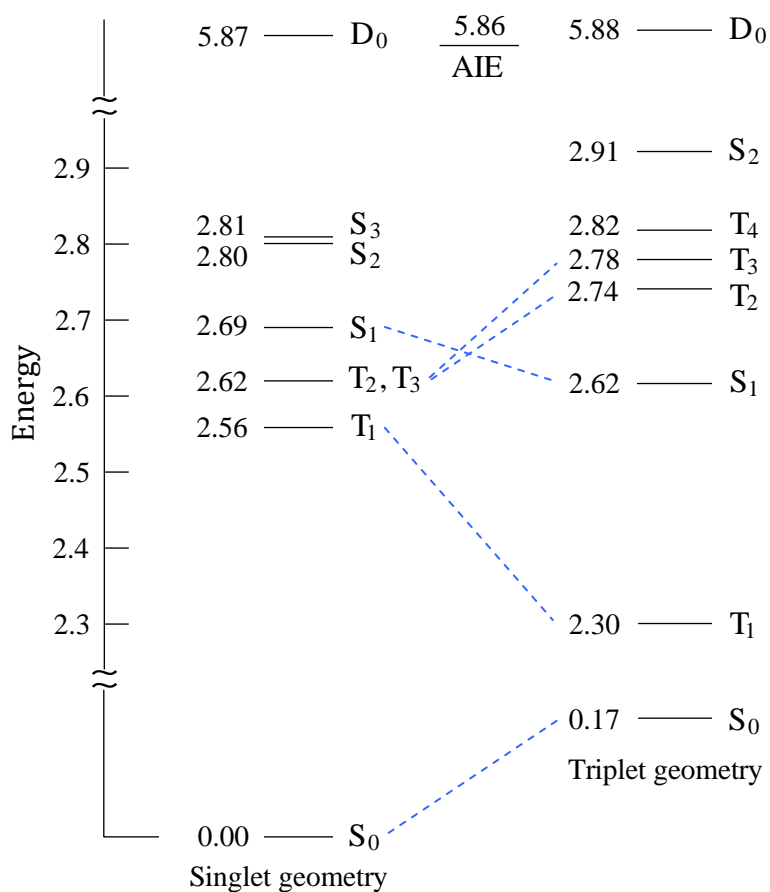


Figure 4.7. The first six BNL excited states at S_0 and T_1 geometries (in eV). Note that the adiabatic ionization energy (AIE) is 5.86 eV.

At the T_1 equilibrium geometry, the 10 lowest singlets and 10 lowest triplets were calculated. Figure 4.7 and Tables 4.6 and 4.7 compare energies of excited states at the S_0 and T_1 equilibrium geometries. There are significant changes in the excited states between the S_0 and T_1 equilibrium geometries. For example, singlet and triplet potential surfaces cross (Figure 4.7).

4.3.4 Phosphorescence from T_1

Phosphorescence originates from T_1 vibrational levels, and in condensed phases it is assumed that vibrational relaxation takes place rapidly on the phosphorescence timescale. In other words, it is assumed, and rightly so, that the T_1 vibrational level populations are in thermal equilibrium during phosphorescence. Though the lowest frequency $\text{Ir}(\text{ppy})_3$ vibrational modes most likely couple well to the host, the picture of intramolecular vibrations remains nonetheless useful.

According to our calculations, at its equilibrium geometry the electronic energy of T_1 is 0.44 eV less than that of the next highest triplet, T_2 , whose energy is 0.04 eV below that of T_3 and 0.08 eV below that of T_4 . From the right hand column in Figure 4.7, one might consider subtracting 0.17 eV from 2.30 eV to obtain a $T_1 \rightarrow S_0$ emission origin of 2.13 eV. However, Yersin and coworkers have demonstrated, through detailed experimental studies carried out at temperatures as low as 1.5 K and with external magnetic fields as high as 12 Tesla, that the energy of the $T_1 \rightarrow S_0$ origin is 2.44 eV, and that this value depends little on the detailed nature of the host material.¹⁴

Of course, the calculations do not include zero-point energy whereas the experiments do. More importantly, it is not the case that a calculation of the vertical electronic energy difference at the T_1 equilibrium geometry corresponds to the phosphorescence origin. The $\text{Ir}(\text{ppy})_3$ molecule has 177 vibrational degrees of freedom, so an even-handed apportionment of 0.17 eV over these degrees of freedom results in each oscillator acquiring, on average, only 7.7 cm^{-1} . Also, if one calculates the average

magnitude of the differences between the S_0 and T_1 equilibrium bond lengths listed in Table 4.1, this yields just 0.018 Å. Moreover, of the 21 bond lengths listed in Table 4.1, three of the differences are a bit larger than the rest: Ir–C₄₉, C₄₈–C₄₉, and C₄₇–C₄₈. For the remaining 18, the average magnitude of the difference between the S_0 and T_1 equilibrium bond lengths is only 0.0088 Å. Thus, most of the bond lengths differ little in going between S_0 and T_1 equilibrium geometries.

The picture this presents is one in which Franck-Condon factors for transitions that originate from the T_1 zero-point level are dominated by (0, 0) contributions. Thus, the origin observed by Yersin and coworkers corresponds to our calculation of the energy of T_1 at its equilibrium geometry (2.30 eV) minus the energy of S_0 at its equilibrium geometry (0.00 eV). This agrees with the experimental value of 2.44 eV. Again, the calculations do not include vibrational zero-point energy nor do they include spin-orbit interaction, which results in additional shifts.⁹ Note that the zero-field splitting of the three T_1 sublevels examined by Yersin and coworkers are minuscule on the energy scale of Figure 4.8, *e.g.*, 19 693, 19 712, and 19 863 cm⁻¹ in dichloromethane.¹⁴ It is concluded that the theoretical and experimental values of the phosphorescence origin are in quite reasonable agreement.

4.3.5 Vibrational energy distribution

As mentioned earlier, at 500 K a significant amount of energy is present in the 177 vibrational degrees of freedom of ground electronic state gas phase Ir(ppy)₃. This

energy is of course above and beyond the zero-point energy. The probability density for this "thermal" vibrational energy, E_{vib} , shall be referred to as $P(E_{vib})$. The molecule's rotational energy, whose average value at 500 K is 520 cm^{-1} , shall be left aside. It is modest relative to E_{vib} , and for the most part it is unavailable in gas phase intramolecular processes because of angular momentum conservation.

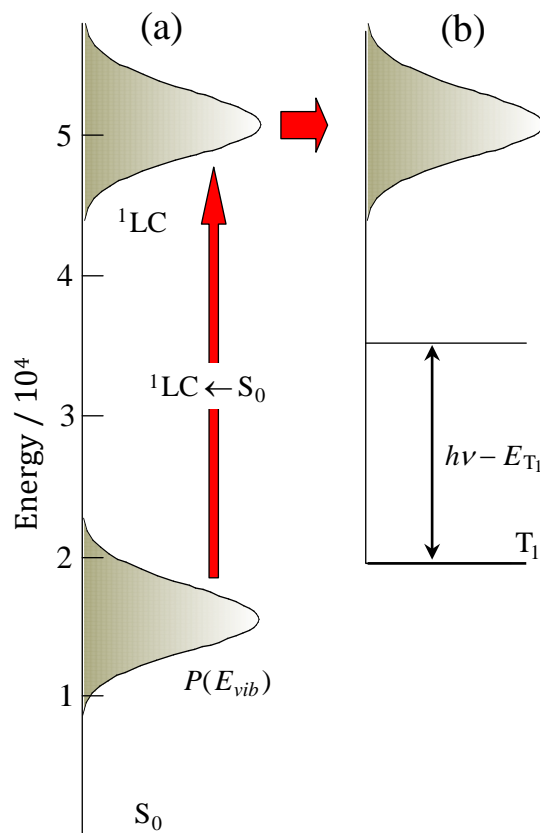


Figure 4.8. (a) Photoexcitation transports populated S_0 vibrational levels to 1LC , which undergoes radiationless decay on a subpicosecond timescale, resulting ultimately in T_1 electronic excitation. This maps $P(E_{vib})$ to T_1 with additional T_1 vibrational energy given by $h\nu - E_{T_1}$, as indicated in (b) and in Figure 4.9.

In addition, radiationless decay transforms 1LC electronic excitation to T_1 electronic excitation, with mere vestiges of 1LC and 1MLCT electronic character

distributed throughout the T_1 vibronic levels. Thus, the amount of vibrational energy imparted to T_1 via ${}^1\text{LC} \leftarrow S_0$ photoexcitation is approximately equal to $h\nu - E_{T_1}$ (see Figure 4.8), where E_{T_1} is the T_1 electronic energy. This energy is taken to be approximately $19\,700\text{ cm}^{-1}$, as the sublevel energies are $19\,693$, $19\,712$, and $19\,863\text{ cm}^{-1}$ in dichloromethane.¹⁴

Adding $h\nu - E_{T_1}$ to the vibrational energy due to 500 K thermal equilibrium, E_{vib} , gives the total amount of T_1 vibrational energy. Once again, it is assumed that this is transformed essentially intact to vibrational excitation of the $\text{Ir}(\text{ppy})_3^+$ cation. However, whereas $h\nu - E_{T_1}$ is simply a number, the vibrational energy due to 500 K thermal equilibrium is distributed according to $P(E_{vib})$, and it is important to have at least a qualitative picture of how $P(E_{vib})$ varies with E_{vib} . For example, this variation gives the spread of vibrational energies carried over to the cation.

The main idea is illustrated schematically in Figure 4.8. Figure 4.8(a) indicates how ${}^1\text{LC} \leftarrow S_0$ photoexcitation transfers vibrational energy from S_0 to ${}^1\text{LC}$, which in turn undergoes rapid radiationless decay (horizontal red arrow). In other words, a given S_0 molecule has a probability density $P(E_{vib})$ for being found in a small energy range centered at E_{vib} . Therefore photoexcitation maps $P(E_{vib})$ to essentially the same probability density in ${}^1\text{LC}$, which in turn transfers it to T_1 , as indicated in Figure 4.8.

Pursuant to the above, a calculation of the 177 normal mode frequencies of $\text{Ir}(\text{ppy})_3$ was carried out using B3LYP with lanl2dz and 6-31+G* at the optimized geometry. The level of electronic structure theory that used in this calculation is

adequate, as the goal is a qualitative understanding of the shape of $P(E_{vib})$ versus E_{vib} . It is worth noting that $P(E_{vib})$ is not a strong function of vibrational frequency values, as discussed below and illustrated in Figure 4.9.

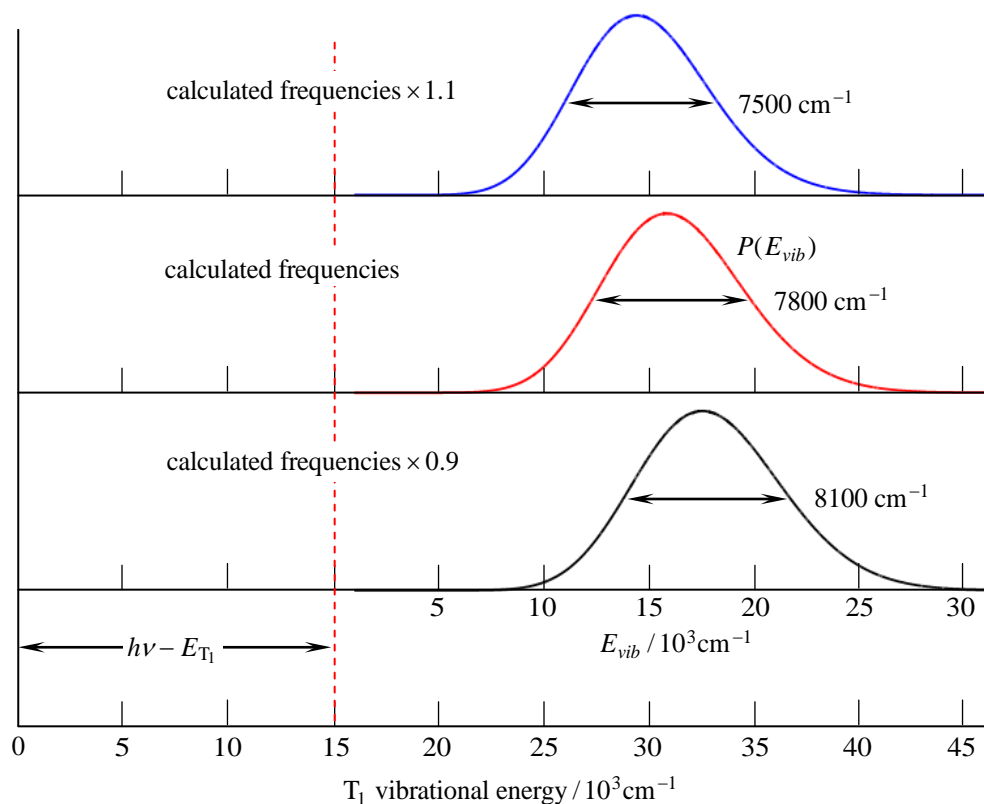


Figure 4.9. The red curve is a plot of equation 4.2 with $T = 500$ K; see text for details. Following photoexcitation, the total vibrational energy in T_1 is given by $h\nu - E_{T1} + E_{vib}$. The probability density for E_{vib} is $P(E_{vib})$, and $h\nu - E_{T1} = 15\,000\text{ cm}^{-1}$ is chosen as a representative value. When all frequencies are changed by $\pm 10\%$, the $P(E_{vib})$ plots change accordingly (blue and black curves). However, the main qualitative feature is preserved. Namely, a considerable amount of T_1 vibrational energy is distributed with a FWHM that is modest relative to the energy of maximum $P(E_{vib})$, e.g., 7800 versus 31 000 cm^{-1} , respectively, for the red curve.

Carrying out calculations at the S_0 equilibrium geometry given in Table 4.1 resulted in five small-curvature saddle points, which are likely to be artifacts of numerical integration on a grid. When calculating density of states, the imaginary frequencies

associated with these saddle points were replaced *ad hoc* with real frequencies of the same magnitudes: 45.7, 45.5, 31.6, 15.6, and 12.7 cm⁻¹. As long as these frequencies are significantly smaller than kT , the calculated $P(E_{vib})$ probability density is insensitive to their values. For example, increasing or decreasing these five frequencies by a factor of two causes the shapes of curves such as those in Figure 4.9 to change by no more than the thickness of the traces. Likewise, horizontal displacements are small, *e.g.*, decreasing these five frequencies by a factor of two shifts the peak by + 25 cm⁻¹, which is minuscule on the scale of Figure 4.9. All of the frequencies are given in AB.

With the vibrational frequencies in hand, the vibrational density of states $\rho(E_{vib})$ was calculated by using the MultiWell Program Suite, specifically, the Densum program, which employs the Beyer-Swinehart algorithm for harmonic oscillators.³³⁻³⁶ This $\rho(E_{vib})$ was then multiplied by $e^{-E_{vib}/kT}$ (with $T = 500$ K) to obtain $P(E_{vib})$:

$$P(E_{vib}) = Z^{-1} \rho(E_{vib}) e^{-E_{vib}/kT} \quad (4.2)$$

where Z is the partition function. Plots of $P(E_{vib})$ are given in Figure 4.9.

Figure 4.9 illustrates the fact that altering the frequencies by a modest amount has a modest affect on the total T₁ vibrational energy. Specifically, combining $P(E_{vib})$ and $h\nu - E_{T_1}$ gives the probability density for vibrational energy within T₁ following ¹LC ← S₀ photoexcitation (Figure 4.8). Referring to Figure 4.9, for an assumed value of $h\nu - E_{T_1} = 15\,000$ cm⁻¹, the total T₁ vibrational energy peaks at ~ 31 000 cm⁻¹ with a FWHM of ~ 7800 cm⁻¹. From the plots in Figure 4.9, it follows that the main (qualitative) result would not change were a higher level of theory enlisted.

On the one hand, the use of a 500 K sample results in vibrational energy that we would rather were not present. On the other hand, the amount of vibrational energy imparted via photoexcitation is considerable and inevitable in experiments with gaseous $\text{Ir}(\text{ppy})_3$.

4.4 Summary

Electronic structure theory has been used to examine a number of excited singlet and triplet states of $\text{Ir}(\text{ppy})_3$ and a few low-lying states of $\text{Ir}(\text{ppy})_3^+$. Specifically, time-dependent density functional theory (TDDFT) calculations were carried out using long-range-corrected (LRC) ωB97X and BNL functionals. There is good agreement with several previous experimental and theoretical results,^{8-14,16} as well as with the experimental results presented in Chapter 3. The main conclusions are listed below.

- Yersin and coworkers have carried out detailed experimental studies of $T_1 \rightarrow S_0$ phosphorescence.¹⁴ They report a 2.44 eV electronic origin and phosphorescence lifetimes of 0.2, 6.4, and 116 μs for the T_1 sublevels in dichloromethane.¹⁴ The present calculations yield 2.30 eV, in agreement with the 2.44 eV experimental value. It was pointed out in Chapter 3 that just a few percent of $^1\text{LC} / ^1\text{MLCT}$ character is sufficient to reconcile the short phosphorescence lifetime of 0.2 μs because of the large oscillator strengths of the singlet-singlet transitions: $^1\text{LC} \leftarrow S_0$ and $^1\text{MLCT} \leftarrow S_0$. This degree of singlet-triplet mixing is in qualitative agreement with calculations of Nozaki that include SOC.¹²

- The ${}^1\text{LC} \leftarrow \text{S}_0$ transition is accompanied by rapid radiationless decay of ${}^1\text{LC}$, resulting ultimately in population of the phosphorescent state, T_1 . The number of electronically excited states having energy less than or equal to the photon energy is larger than the trio of states (${}^1\text{LC}$, ${}^1\text{MLCT}$, and T_1) used in phenomenological models aimed at reconciling experimental results. In addition, potential surfaces cross, *e.g.*, as seen in going between the S_0 and T_1 equilibrium geometries (Figure 4.7).
- A calculation of the ultraviolet absorption spectrum was carried out using 130 excited singlets obtained with the BNL functional. Oscillator strengths were calculated for vertical excitation from the S_0 equilibrium geometry. The resulting stick spectrum was assigned a Gaussian shape with FWHM of 3470 cm^{-1} (0.43 eV) for each transition. This calculated spectrum is in agreement with the experimental room temperature absorption spectrum. This agreement is consistent with Franck-Condon factors dominated by $\Delta v_i = 0$, as expected for the delocalized nature of the orbitals involved.
- The calculated adiabatic and vertical (S_0 and T_1 equilibrium geometries) ionization energies are 5.86, 5.87, and 5.88 eV, respectively. These values agree with the calculated result of 5.94 eV reported by Hay,⁹ as well as with the conservative experimental upper bound of 6.4 eV reported in Chapter 3. It is concluded that the ionization energy is in the vicinity of 6 eV. This low ionization energy is advantageous for OLED applications.
- The probability density for finding a gas phase $\text{Ir}(\text{ppy})_3$ molecule with "thermal" vibrational energy E_{vib} at temperature T is: $P(E_{\text{vib}}) = Z^{-1} \rho(E_{\text{vib}}) \exp(-E_{\text{vib}} / kT)$, where

Z is the partition function. This can be combined with the vibrational energy imparted through photoexcitation, $h\nu - E_{T_1}$, to obtain the probability density as a function of total vibrational energy. In rough terms, for 500 K this probability density peaks at $\sim 31\,000\text{ cm}^{-1}$ (3.84 eV) with a FWHM spread of $\sim 7800\text{ cm}^{-1}$ (0.97 eV) (Figure 4.9). It is interesting that, despite this large amount of vibrational energy, 2-photon ionization is dominated by the parent cation $\text{Ir}(\text{ppy})_3^+$, with no discernible fragmentation over a significant frequency range (Chapter 3).

- Qualitative understanding of the photophysics of this system is assisted greatly by the MO's obtained at the S_0 , T_1 , and D_0 equilibrium geometries.

4.5 References

1. Yersin, H.; Finkenzeller, W. Ed; *Highly Efficient OLEDs with Phosphorescent Materials*; Yersin, H. Ed.; Wiley-VCH Verlag: Weinheim, Germany, **2008**.
2. Yersin, H.; Finkenzeller, W. Editor, *Highly Efficient OLEDs with Phosphorescent Materials*; Yersin, H. Ed.; Wiley-VCH Verlag: Weinheim, Germany, **2008**; pp. 1-97.
3. Yersin, H. *Top. Curr. Chem.* **2004**, *241*, 1.
4. Rausch, A. F.; Homeier, H. H. H.; Yersin, H. *Top. Organomet. Chem.* **2010**, *29*, 193.
5. Yersin, H.; Rausch, A. F.; Czerwieniec, R.; Hofbeck, T.; Fischer, T. *Coord. Chem. Rev.* **2011**, *255*, 2622.
6. Baldo, M. A.; Thompson, M. E.; Forrest, S. R. *Nature* **2000**, *403*, 750.
7. Cleave, V.; Yahioğlu, G.; Le Barny, P.; Friend, R. H.; Tessler, N. *Adv. Mater.* **1999**, *11*, 285.
8. Matsushita, T.; Asada, T.; Koseki, S. *J. Phys. Chem. C* **2007**, *111*, 6897.
9. Hay, P. J. *J. Phys. Chem. A* **2002**, *106*, 1634.
10. Jansson, E.; Minaev, B.; Schrader, S.; Ågren, H. *Chem. Phys.* **2007**, *333*, 157.
11. Liu, X. D.; Feng, J. K.; Ren, A. M.; Yang, L.; Yang, B.; Ma, Y. G. *Opt. Mater.* **2006**, *29*, 231.
12. Nozaki, K. *J. Chin. Chem. Soc.* **2006**, *53*, 101.
13. Finkenzeller, W. J.; Yersin, H. *Chem. Phys. Lett.* **2003**, *377*, 299.
14. Hofbeck, T.; Yersin, H. *Inorg. Chem.* **2010**, *49*, 9290.
15. Kukhta, A. V.; Kukhta, I. N.; Bagnich, S. A.; Kazakov, S. M.; Andreev, V. A.; Neyra, O. L.; Meza, E. *Chem. Phys. Lett.* **2007**, *434*, 11.

16. Tamayo, A. B.; Alleyne, B. D.; Djurovich, P.; Lamansky, S.; Tsyba, I.; Ho, N. N.; Bau, R. Thompson, M. E. *J. Am. Chem. Soc.* **2003**, *125*, 7377.
17. Chai, J. D.; Head-Gordon, M. *J. Chem. Phys.* **2008**, *128*, 084106.
18. Chai, J. D.; Head-Gordon, M. *Phys. Chem. Chem. Phys.* **2008**, *10*, 6615.
19. Baer, R.; Neuhauser, D. *Phys. Rev. Lett.* **2005**, *94*, 043002.
20. Livshits, E.; Baer, R. *Phys. Chem. Chem. Phys.* **2007**, *9*, 2932.
21. Lange, A.; Herbert, J. M. *J. Chem. Theory Comp.* **2007**, *3*, 1680.
22. Hay, P. J.; Wadt, W. R. *J. Chem. Phys.* **1985**, *82*, 299.
23. Hehre, W. J.; Stewart, R. F.; Pople, J. A. *J. Chem. Phys.* **1969**, *51*, 2657.
24. Baer, R.; Livshits, E.; Salzner, U. *Ann. Rev. Phys. Chem.* **2010**, *61*, 85.
25. QChem User's Manual, version 3.2, **2011**.
26. Shao, Y.; Molnar, L. F.; Jung, Y.; Kussmann, J.; Ochsenfeld, C.; Brown, S. T.; Gilbert, A. T. B.; Slipchenko, L. V.; Levchenko, S. V.; O'Neill, D. P.; DiStasio, R. A.; Lochan, R. C.; Wang, T.; Beran, G. J. O.; Besley, N. A.; Herbert, J. M.; Lin, C. Y.; Van Voorhis, T.; Chien, S. H.; Sodt, A.; Steele, R. P.; Rassolov, V. A.; Maslen, P. E.; Korambath, P. P.; Adamson, R. D.; Austin, B.; Baker, J.; Byrd, E. F. C.; Dachsel, H.; Doerksen, R. J.; Dreuw, A.; Dunietz, B. D.; Dutoi, A. D.; Furlani, T. R.; Gwaltney, S. R.; Heyden, A.; Hirata, S.; Hsu, C. P.; Kedziora, G.; Khalliulin, R. Z.; Klunzinger, P.; Lee, A. M.; Lee, M. S.; Liang, W.; Lotan, I.; Nair, N.; Peters, B.; Proynov, E. I.; Pieniazek, P. A.; Rhee, Y. M.; Ritchie, J.; Rosta, E.; Sherrill, C. D.; Simmonett, A. C.; Subotnik, J. E.; Woodcock, H. L.; Zhang, W.; Bell, A. T.; Chakraborty, A. K.; Chipman, D. M.; Keil, F. J.; Warshel, A.; Hehre, W. J.; Schaefer, H. F.; Kong, J.; Krylov, A. I.; Gill, P. M. W.; Head-Gordon, M. *Phys. Chem. Chem. Phys.* **2006**, *8*, 3172.
27. Allen, F. H.; Kennard, O.; Galloy, J. J.; Johnson, O.; Watson, D. G. *Chem. Structures* **1993**, *2*, 343.

28. Breu, J.; Stossel, P.; Schrader, S.; Starukhin, A.; Finkenzeller, W. J.; Yersin, H. *Chem. Mater.* **2005**, *17*, 1745.
29. Garces, F. O.; Dedeian, K.; Keder, N. L.; Watts, R. J. *Acta Cryst. C* **1993**, *49*, 1117.
30. Coe, B. J.; Glenwright, S. J. *Coord. Chem. Rev.* **2000**, *203*, 5.
31. Hartley, F. R.; *Chem. Soc. Rev.* **1973**, *2*, 163.
32. Salzner, U.; Baer, R. *J. Chem. Phys.* **2009**, *131*, 23110.
33. Barker, J. R.; Ortiz, N. F.; Preses, J. M.; Lohr, L. L.; Maranzana, A.; Stimac, P. J.; Nguyen, T. L.; Dhilip Kumar, T. J. MultiWell-2011.3 Software, <http://aoss.engin.umich.edu/multiwell>
34. Beyer, T.; Swinehart, D. *Comm. ACM* **1973**, *16*, 379.
35. Barker, J. R. *Int. J. Chem. Kin.* **2001**, *33*, 232.
36. Barker, J. R. *Int. J. Chem. Kin.* **2009**, *41*, 748.

Chapter 5

Investigation of He_4^+ formation via electron impact and the photoionization of tris(2-phenylpyridine)iridium in helium droplets

5.1 Introduction

In recent years, studies involving superfluid helium nanodroplets have evolved into a rich field of research.¹⁻⁴ Helium droplets provide an ultracold matrix in which to perform a variety of spectroscopic studies on embedded species.⁵ In this matrix isolation technique, a well-known number of molecules are embedded inside helium droplets via gas phase collisions. These experiments were predated by studies of SF_6 molecules attached to heavier gas clusters where the utility of the nanocluster technique was demonstrated.⁶ In the spectroscopy that follows, helium plays a predominantly spectator role due its optical transparency over a large frequency range and vanishingly low viscosity.

Experiments involving helium nanoclusters typically use free jet expansion to force cold (9 - 20 K) helium at 20-80 bar out of a 5 μm (continuous) or ~ 1 mm (pulsed) nozzle to produce the clusters. In this so called subcritical regime, the initial state of the helium is well within the gaseous region of the phase diagram.⁷ The expanding helium cools because of an adiabatic change in state along isentropes in the phase diagram to temperatures and pressures well below the critical point.⁵ As a result, condensation of the helium occurs to form “hot” clusters. The droplets then undergo rapid evaporative

cooling to dissipate residual energy until they reach an equilibrium temperature of about 0.4K.⁸

The average size of He droplets is an important parameter, which dictates the size and number of species that can be embedded and the required pickup pressure for this process. The size distribution of droplets between $10^3 - 10^7$ atoms has been determined in continuous He droplet beams via scattering of the neutral droplet beam⁹ or deflection of charged droplets.¹⁰ More recently, attenuation of He droplet beams, caused by collisions with He gas, have extended droplet size measurements up to 10^{11} He atoms.¹¹

In this work, a pulsed He droplet beam is used.¹² The work of Gomez et al.¹¹ has shown that quadrupole mass spectra obtained via electron impact ionization of a He droplet beam are sensitive to the average droplet size. In particular, they observed a nearly 10 fold increase in the intensity ratio of the signal due to splitter ions He_4^+ to He_2^+ (i.e. mass 16 to mass 8, I_{16}/I_8) upon increase of the average droplet size from $\sim 10^4$ to $\sim 10^9$ atoms.¹¹ Here we study the utility of this approach using a pulsed He droplet beam in conjunction with time-of-flight (TOF) and quadrupole mass spectrometry.

5.2 Experimental

The pulsed He droplet apparatus has been described previously (Figure 5.1).¹² Briefly, helium is expanded through a General Valve series 99 solenoid type nozzle with an orifice diameter of 1 mm. The orifice was specially modified by machining a conical 90° opening as described in reference 12. A Parker Iota One controller operates the nozzle. The valve is attached to the second stage of a Sumitomo RDK 408 close cycle

cryo-cooler, and its temperature is measured by solid state temperature sensors and controlled via resistive heating. The lowest expansion temperature achievable by this setup is ~ 9 K at a repetition rate of 1 Hz.

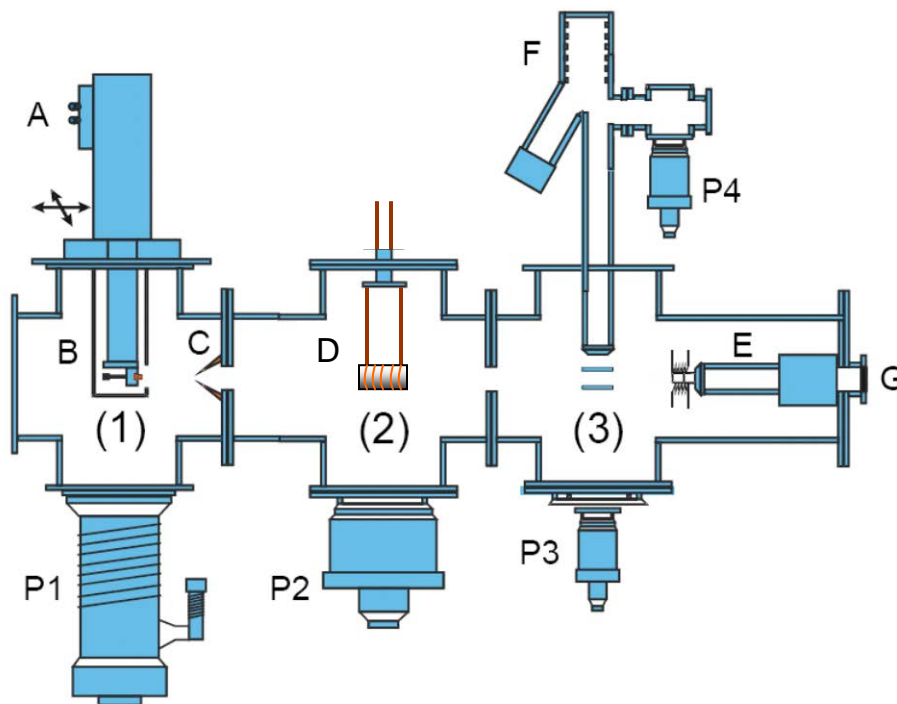


Figure 5.1. Schematic of the pulsed droplet apparatus. The machine consists of 3 vacuum chambers (1 - 3). Chamber (1) contains the pulsed helium droplet source (B) mounted on a closed cycle cryostat (A) with beam skimmer (C). The source chamber is pumped by a 3000 L/s diffusion pump (P1) backed in series by a roots blower followed by a rotary pump. Chamber (2) houses a ceramic pickup cell (D) wrapped in a tungsten filament. Chamber (2) is pumped by a 1000 L/s turbo-molecular pump (P2). Chamber (3) contains a combination reflectron / linear time-of-flight (TOF) spectrometer (F) as well as an axial quadrupole mass spectrometer (E) followed by a BaF₂ window (G). This UHV chamber is pumped by two 170 L/s turbo molecular pumps (P3 & P4).

In the majority of experiments described below, He was expanded at two nozzle temperatures, $T_0 = 10.3$ and 18 Kelvin, both at a stagnation pressure of $P_0 = 20$ bar and repetition rate of 10 Hz. Mass spectra were recorded using a Jordan TOF Products time-

of-flight mass spectrometer placed perpendicular to the droplet beam, and an axial quadrupole mass spectrometer (Extranuclear Laboratories), both equipped with electron impact ionization source. The TOF and quadrupole ionizers are placed ~ 104 and ~ 113 cm downstream from the nozzle, respectively. The default ionization settings for the TOF were 3 mA current, 2 microsecond (μs) ionizer pulse duration, and 95 eV electron energy. Any adjustment to these parameters is either noted or it is the parameter being varied. The quadrupole ionizer was set at 2 mA current, and 99 eV electron energy.

5.3 Results and discussion

A variety of measurements on helium droplets produced by a pulsed nozzle were performed using electron impact ionization. Initially, quadrupole time-of-flight (TOF) measurements were used to determine the average droplet size for the two expansion regimes based upon work by Gomez et al.¹¹ (section 5.3.1). Quadrupole measurements are consistent with the results in reference 11 and show a sharp increase in I_{16}/I_8 with decreasing T_0 indicating a corresponding rise in droplet size. The quadrupole results are compared to those of a TOF mass spectrometer using similar electron impact ionization parameters and show that the quadrupole I_{16}/I_8 is $\sim 5x$ larger than that of the TOF. This discrepancy arises from the dramatically different time scales used by each type of spectrometer. Additional TOF measurements of the droplet beam were used to characterize the droplets produced by the pulsed nozzle (section 5.3.2 – 5.3.4). The origin of the increased I_{16}/I_8 ratio for large droplets is due to the increased probability of forming two exciplex He_2^* molecules within the same droplet. The He_2^* formation

mechanism is addressed in section 5.3.5. Finally, this chapter closes with the experiments on doping and photoionization of gaseous tris(2-phenylpyridine)iridium ($\text{Ir}(\text{ppy})_3$) in helium droplets. Low fluence photoionization at 266 nm exclusively produced $\text{Ir}(\text{ppy})_3^+$ indicating that it follows the two-photon mechanism described in Chapter 3. This suggests that the photoionization experiments discussed in section 3.2.2 are possible using helium droplets.

5.3.1 Droplet sizes

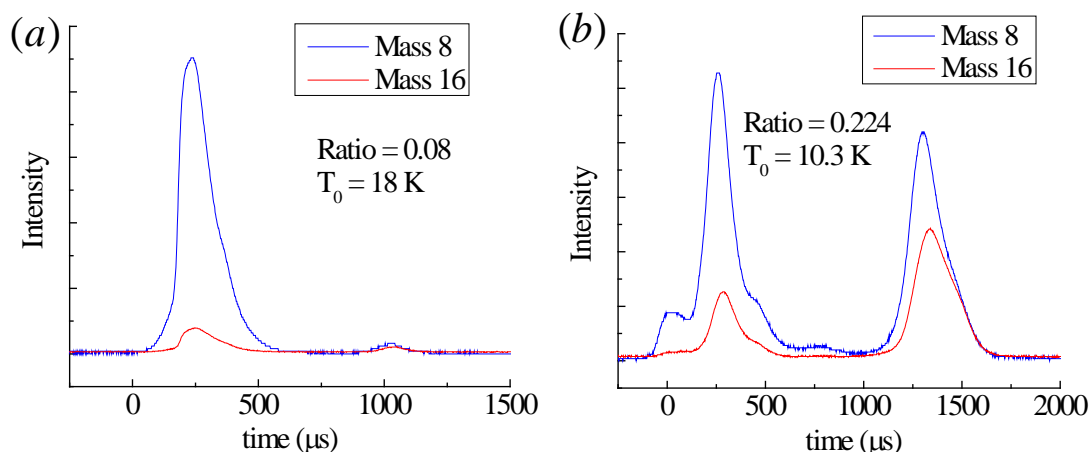


Figure 5.2. Time dependence of the quadrupole mass spectrometer signal set at $M = 8$ and $M = 16$, as indicated, and measured at nozzle temperatures of 18 K (a) and 10.3 K (b). The duration of the nozzle pulse was chosen to be 220 μs in order to give the most intense signal with the shortest open duration. Time zero corresponds to a delay with respect to the nozzle trigger of 2.99 ms and 3.96 ms in panels (a) and (b), respectively.

Figure 5.2(a) and (b) shows the time dependence of the quadrupole mass spectrometer signal at nozzle temperatures of 10.3 K and 18 K respectively. In each case two measurements were performed using a quadrupole mass filter set at $M = 8$ and $M = 16$ (as indicated) and recorded by a digital oscilloscope. Time zero in (a) and (b)

corresponds to a delay with respect to the leading edge of the nozzle trigger pulse of 2.99 ms, and 3.96 ms, respectively. The delays are consistent with the mechanical delay of the pulsed valve (i.e. roughly 350 μ s),¹³ and the time of flight of the droplets from the nozzle to the ionizer separated by ~ 1.13 m. The velocity of the droplets in (a) and (b) were obtained via TOF measurements and were found to be ~ 297 m/s and ~ 411 m/s respectively.

Each of the time profiles in Figure 5.2 consists of two peaks. The peak at earlier arrival times corresponds to He_2^+ and He_4^+ ions that are ejected from the droplets upon electron beam ionization. These ions are accelerated by ~ 20 V and detected after a flight time (after ionization) of about ~ 300 μ s. The peaks at later arrival times correspond to ionized droplets with masses larger than $\sim 10^4$. The mass of these droplets exceeds the 300 amu range of the present mass filter. Due to their large mass, the clusters are not deflected by the mass filter and therefore proceed with normal flight along the axis, which is the origin of the delay with respect to the small fast ions. The relative intensity of the second peak is larger at lower nozzle temperature. This is ascribed to larger sizes of the droplets obtained at lower T_0 .

The intensity ratio of mass 16 to mass 8 (I_{16}/I_8) of the fast peaks can be used to determine the average size of the droplets. Similar ratios have been determined for continuous droplet beams where the average droplet size is well known.¹¹ Here we obtained $I_{16}/I_8 = 0.08$, and 0.224 at nozzle temperatures 18 K and 10.3 K respectively. A comparison of our ratios with those of Gomez et al.¹¹ indicates the average number of atoms per droplet ($\langle N_{\text{He}} \rangle$) is approximately 5×10^4 and 3×10^5 for 18 K and 10.3 K,

respectively. Hereafter we shall refer to droplets obtained at 18 K and 10.3 K as small and large droplets, respectively.

Previous measurements indicate that $\langle N_{\text{He}} \rangle$ of droplets produced by a pulsed nozzle are comparable to those produced by a continuous nozzle, but at nozzle temperatures that are several degrees higher than that of the continuous nozzle;¹¹ The proximate cause of which is the larger orifice diameter that is used with the pulsed nozzle.¹² Due to a larger orifice diameter the gas spends more time in the expansion, which apparently facilitates formation of larger droplets.

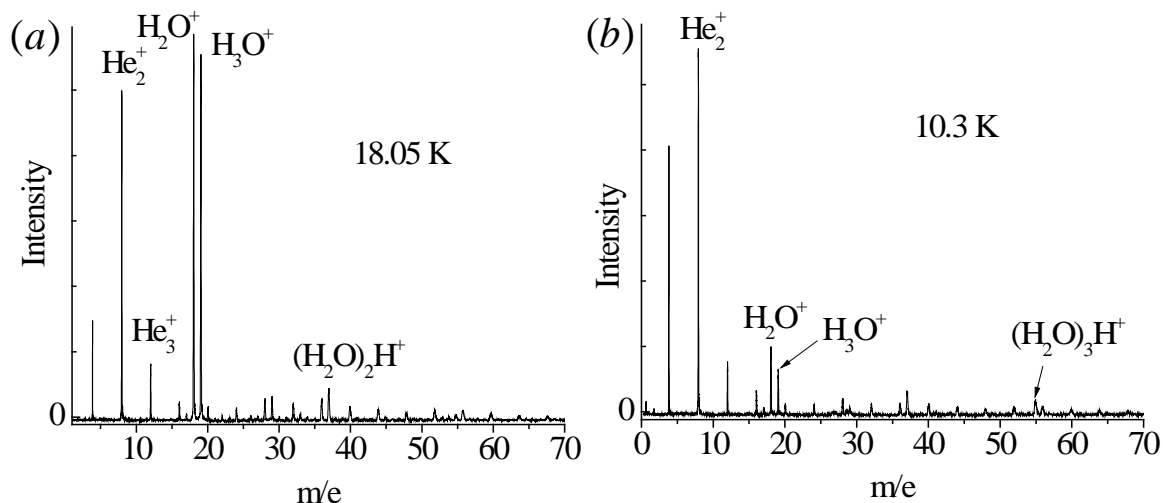


Figure 5.3. Typical TOF mass spectra at 18K (a) and 10.3K (b) with important peaks labeled. The considerable water ($M = 18$) and protonated water cluster peaks ($M = n \cdot 18 + 1$) indicates pickup of multiple water molecules, due to the relatively high background pressure (10^{-6} mbar) in our pick up chamber during the experiments.

Figure 5.3 shows two typical TOF spectra at 18K and 10.3K. The strong He₂⁺ peak followed by a succession of small He_n⁺ peaks is the telltale sign of helium droplet production.¹⁴ Water greatly contributes to the spectra, which is particularly noticeable in small droplets, and is caused by the relatively high base pressure in our interaction

chamber (10^{-6} mbar). There are also various peaks that correspond to water clusters; most notably mass 19 (H_3O^+). The strong H_3O^+ signal, but weak $(\text{H}_2\text{O})_n\cdot\text{H}^+$ signal in small droplets suggests that large water clusters are not formed in the small droplets. However, large droplets possess a greater capture cross-section. Thus, effective capture of up to 9 water molecules is observed ($M = 145$, not shown in Figure 5.3). In large droplets the H_3O^+ signal is weaker with respect to the strong He_2^+ signal, which is likely due to an abundance of larger clusters, and presumably their inefficient fragmentation upon ionization. The ionization branching ratio also shifts towards He_n^+ ions in larger droplets. Regardless of the differences, it is clear that there is good droplet production at both temperatures.

Figure 5.4 shows a comparison of I_{16}/I_8 measured with quadrupole and TOF mass spectrometers at various temperatures – nozzle repetition rates are indicated. For quadrupole measurements the maxima of the corresponding peaks were used to obtain the ratios. With TOF, mass peak areas were used to calculate the intensity ratio. In both measurements an increase of I_{16}/I_8 with decreasing nozzle temperature is observed. However, at low nozzle temperatures I_{16}/I_8 is about a factor of 5 smaller in the TOF measurements, whereas at higher temperatures the values are comparable. This incongruity is surprising, considering both techniques use electron impact ionization. Therefore, the discrepancy between the two methods indicates some difference in the extraction of ions. Below a general description of the two mass spectrometric techniques is provided to point out crucial differences.

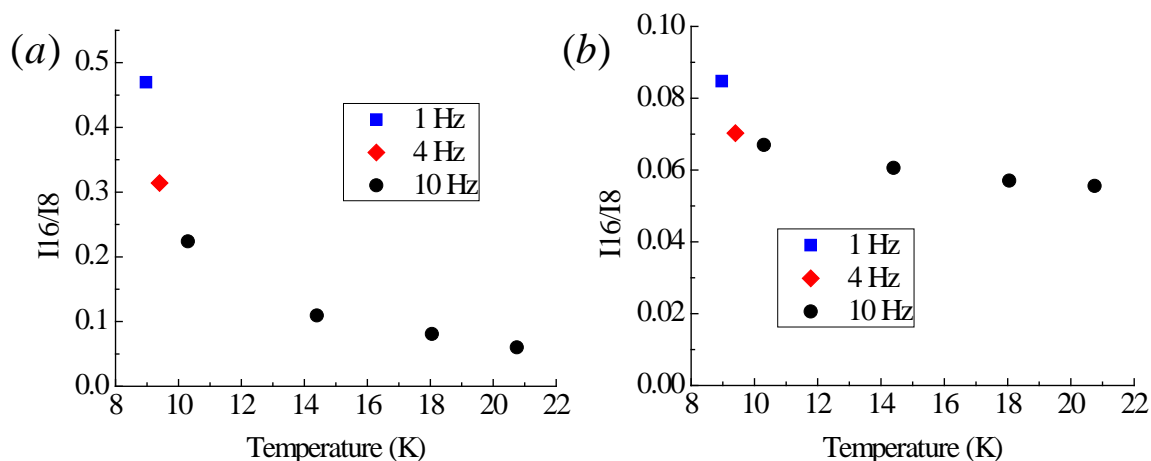


Figure 5.4. Comparison of I_{16}/I_8 measured with quadrupole (a) and TOF (b) mass spectrometers at various nozzle temperatures with repetition rates indicated. Both plots exhibit a sharp initial decrease followed by a moderate leveling when moving from low to high temperature albeit with different absolute ratios. The TOF ratios here were measured with 1 mA current, 2 μ s pulse duration, and 95 eV e-energy.

The extraction technique employed by the TOF system uses a voltage pulse to create an equipotential between repeller and extractor plates. Without a potential gradient the ionizing electrons are free collide with droplets passing between these plates, thereby creating positive ions. As described earlier the default ionization pulse lasts for 2 μ s. When the pulse is switched off, and the potential gradient restored, ionized atoms and clusters are accelerated to ~ 1800 eV down a 1 meter tube toward a micro channel plate (MCP) where their collision with the MCP is detected. The entire process from ionization to detection occurs in less than 30 μ s for masses up to ~ 200 amu when using standard voltages.

In comparison, the quadrupole mass spectrometer employs a continuous extraction method, where the ionizing electrons constantly bombard droplets as they pass through the ionizing region. With a droplet flight velocity of ~ 350 m/s, and a 1 cm path through the ionizing region, droplets spend about 30 μ s in the ionizing region. After

exiting the ionizing region positive ions are mildly accelerated (~ 20 V) toward a detector followed by mass selection in the quadrupole. The time lapse from ionization to detection in the quadrupole occurs within ~ 300 μs .

The above comparison shows that the time droplets spend in the ionizer region before extraction seems to be the most obvious difference between the two methods. If the creation of positive ions were instantaneous, there should be no difference in the observed relative intensities. Thus, any disparity in measured intensities may indicate that the mechanism leading to ionization (in particular the formation of He_4^+ ions) is not instantaneous and may include some intermediate steps.

5.3.2 Pulse profile

In order to elucidate the origin of the differences in the quadrupole and TOF intensities, several additional measurements were performed. Figure 5.5 shows the time profile of the He_2^+ and He_4^+ signals vs. delay between the nozzle trigger and ionizing pulse trigger of the TOF mass spectrometer, measured at high (a) and low (b) nozzle temperatures. As mention above, the ionizing pulse width was 2 μs .

The pulse profile in Figure 5.5(a) exhibits a spike at the beginning of the profile followed by broad shoulder of lower intensity. These features are reproduced in both mass signals. The spike is attributed to the mechanical inconsistency of the nozzle. The He_2^+ peak has a full width at half maximum (FWHM) of ~ 180 μs , which is close to the 220 μs pulse driving the nozzle. Figure 5.5(b) He_2^+ signal shows a broad pulse profile

with no sharp peak in the beginning and has a FWHM of $\sim 200 \mu\text{s}$ again consistent with the $220 \mu\text{s}$ driving pulse.

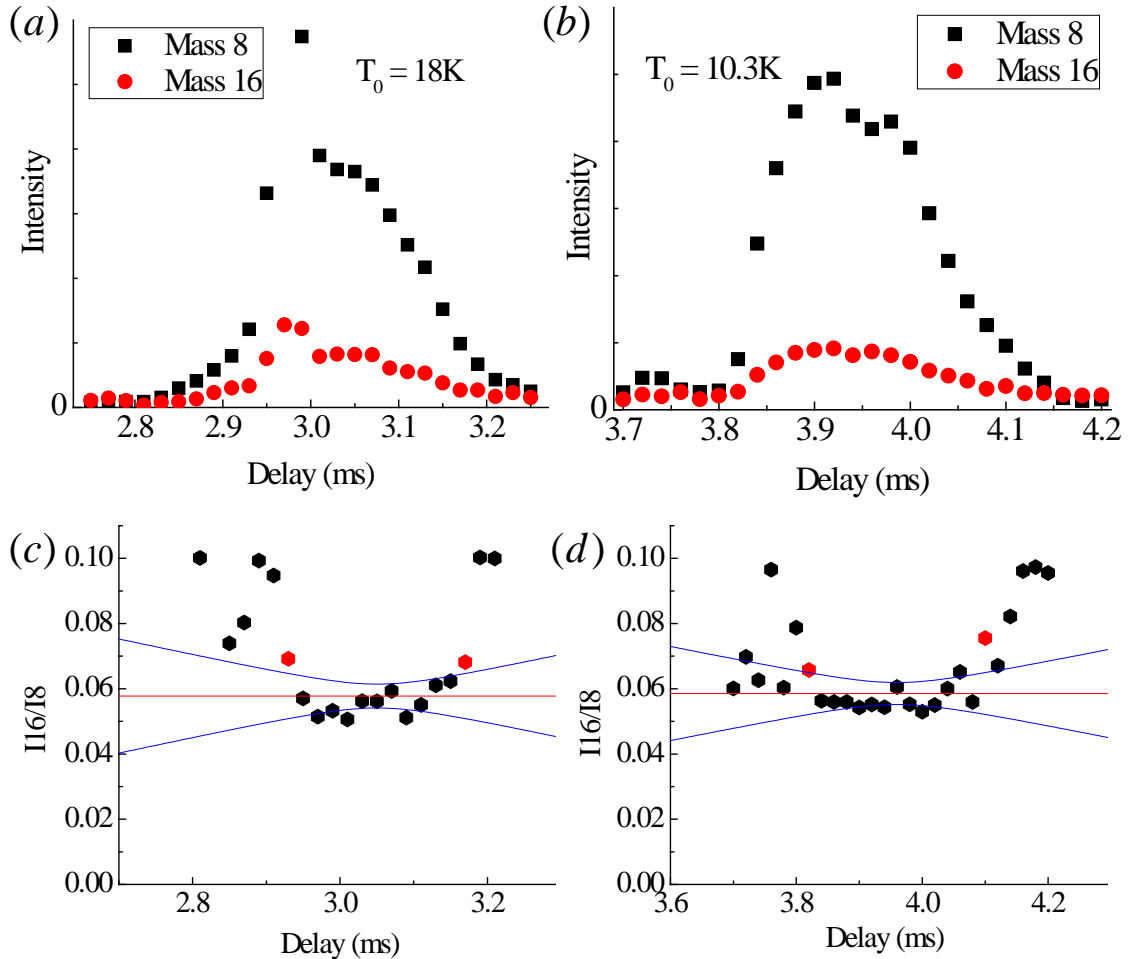


Figure 5.5. TOF pulse intensity profile vs. delay for small (a) and large (b) droplets as measured with TOF. In (a) and (b), signal for mass 16 was multiplied by 4 and 3 for small and large droplets respectively. (c) and (d) show the delay dependence of I_{16}/I_8 throughout the pulse profiles for small and large droplets, respectively. The average value (red line) of each ratio taken over their respective profile (endpoints indicated in red and 95% confidence curves in blue) was 0.058 ± 0.004 and 0.059 ± 0.0035 for small and large droplets respectively.

At $T_0 = 18 \text{ K}$ the gas pulse arrived at the ionization region at a median value of 2.99 ms after the nozzle was triggered, but at 3.96 ms when $T_0 = 10.3 \text{ K}$, which

corresponds to droplet beam velocities of ~ 411 and ~ 297 m/s, respectively. In a continuous expansion, droplet speeds obtained between $T_0 = 18$ K and 10 K were found to be 400 and 240 m/s, respectively.¹⁵ The agreement is considered satisfactory, considering the use of a different nozzle sources and that the actual pulsed nozzle temperature is expected to be higher than measured by our sensor, which was mounted a short distance from the nozzle, due to heat release associated with motion of the piston.

Figure 5.5(c) and (d) shows that I_{16}/I_8 remains approximately constant during the most intense part of the pulse, with values of 0.058 ± 0.004 and 0.059 ± 0.0035 for small and large droplets, respectively. The slight disagreement between ratio values for Figure 5.5(c) and (d) and those of Figure 5.4(b) is primarily due to the different currents used (section 5.3.3). On the wings of each pulse the ratio increases, however, mass 8 decreases to zero, while mass 16 reverts to the O^+ background signal. Thus, the increased ratio at the pulse edges (when the signal drops to less than 10% from its maximum) does not reflect the droplet size. It appears that the average cluster size is relatively constant throughout the pulses, and the ratio at the center of the pulse, gives the most reliable value of I_{16}/I_8 .

5.3.3 Current Dependence

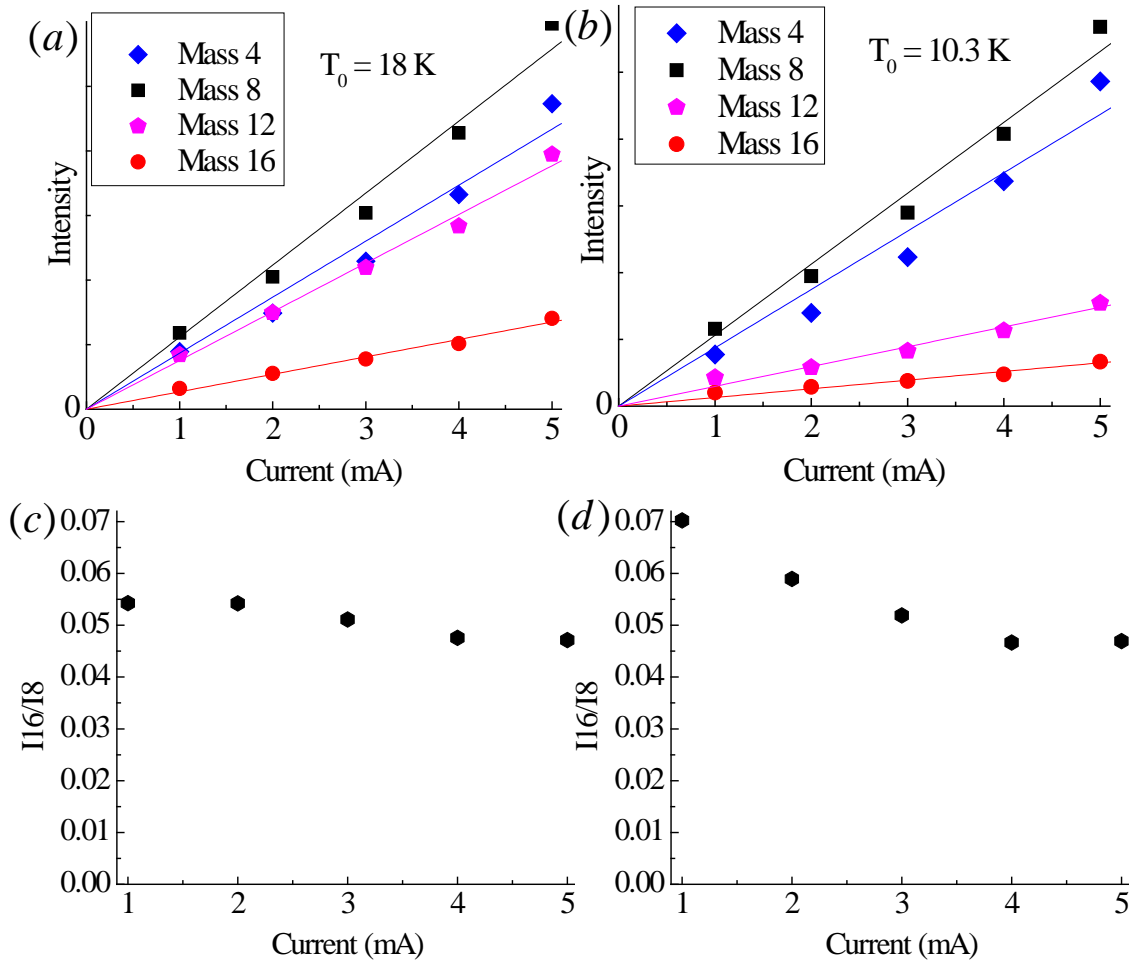


Figure 5.6. Current dependence of the TOF mass spectrometer peak intensities at $M = 4, 8, 12,$ and 16 for small (a) and large droplets (b), as well as I_{16}/I_8 for small (c) and large (d) droplets measured at ionization currents ranging from 1 to 5 mA. Intensities for mass 4, 12, and 16 are multiplied by 5 and by 2.5 in (a) and (b), respectively.

The current dependence of the mass signals and I_{16}/I_8 are shown in Figure 5.6(a) – (d). To facilitate data comparison, signals for masses 4, 12, and 16 were multiplied by factors of 5 and 2.5 for small and large droplets, respectively. It is seen that the intensity of all peaks scale approximately linearly with ionizing current. Consequently, I_{16}/I_8 is approximately constant with current for small and large droplets. However, a very small

initial decrease in I_{16}/I_8 is observed with increasing current. An effect that is more pronounced in large droplets. The difference in I_{16}/I_8 at 1 and 3 mA for both large and small droplets mostly accounts for the different observed ratio values between Figures 5.5(c), (d) and those of Figure 5.4(b). Any small difference that remains is likely due to uncertainty in the measurement.

Buchenau et al.¹⁶ previously examined the effect of electron current on droplet ionization using a quadrupole mass spectrometer. Their work focused on lower electron current (between 0 and 1 mA), but they observed, via log-log plots, a roughly linear dependence on He^+ signal vs. electron current. The agreement between this work and that of reference 16 indicates there is no change in mechanism of the ionization at the higher electron currents.

5.3.4 Electron Energy Dependence

Figure 5.7(a) and (b) plots mass signals vs. electron energy. It is seen that all mass signals increase as the electron energy is increased from 40 to 90 eV. The fast initial rise from 40 – 65 eV followed by the slower increase from 65 – 90 eV is consistent with a changing electron impact ionization cross-section (section 2.5). The very low He_4^+ signal at $E = 40$ eV is consistent with its appearance potential of 37.5 eV as found previously.¹⁶

Interestingly, I_{16}/I_8 show similar increase with electron energy in both large and small droplets - reflecting a faster rise of the $M = 16$ signal than that of $M = 8$. Therefore, we concluded that the electron energy of higher than about 40 eV is essential for the

preferential formation of He_4^+ , and that at least one formation mechanism of He_4^+ is likely similar in large and small droplets.

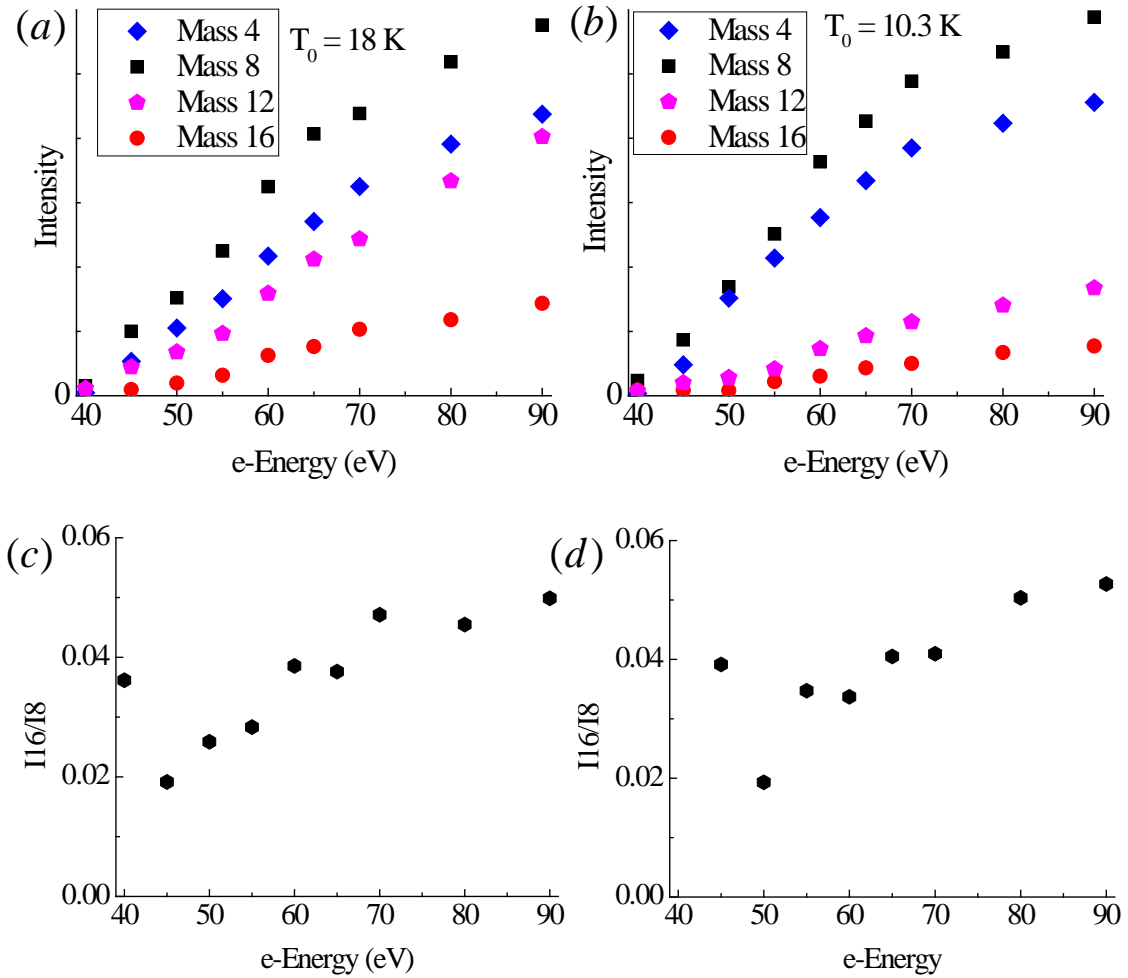


Figure 5.7. Intensity of the TOF mass 4, 8, 12, and 16 peaks vs. electron energy are shown for small (a) and large (b) droplets as well as I_{16}/I_8 for small (c) and large (d) droplets, respectively. In (a) and (b) masses 4, 12, and 16 are multiplied by factors of 5 and 2.5, respectively.

5.3.5 Pulse Duration Dependence

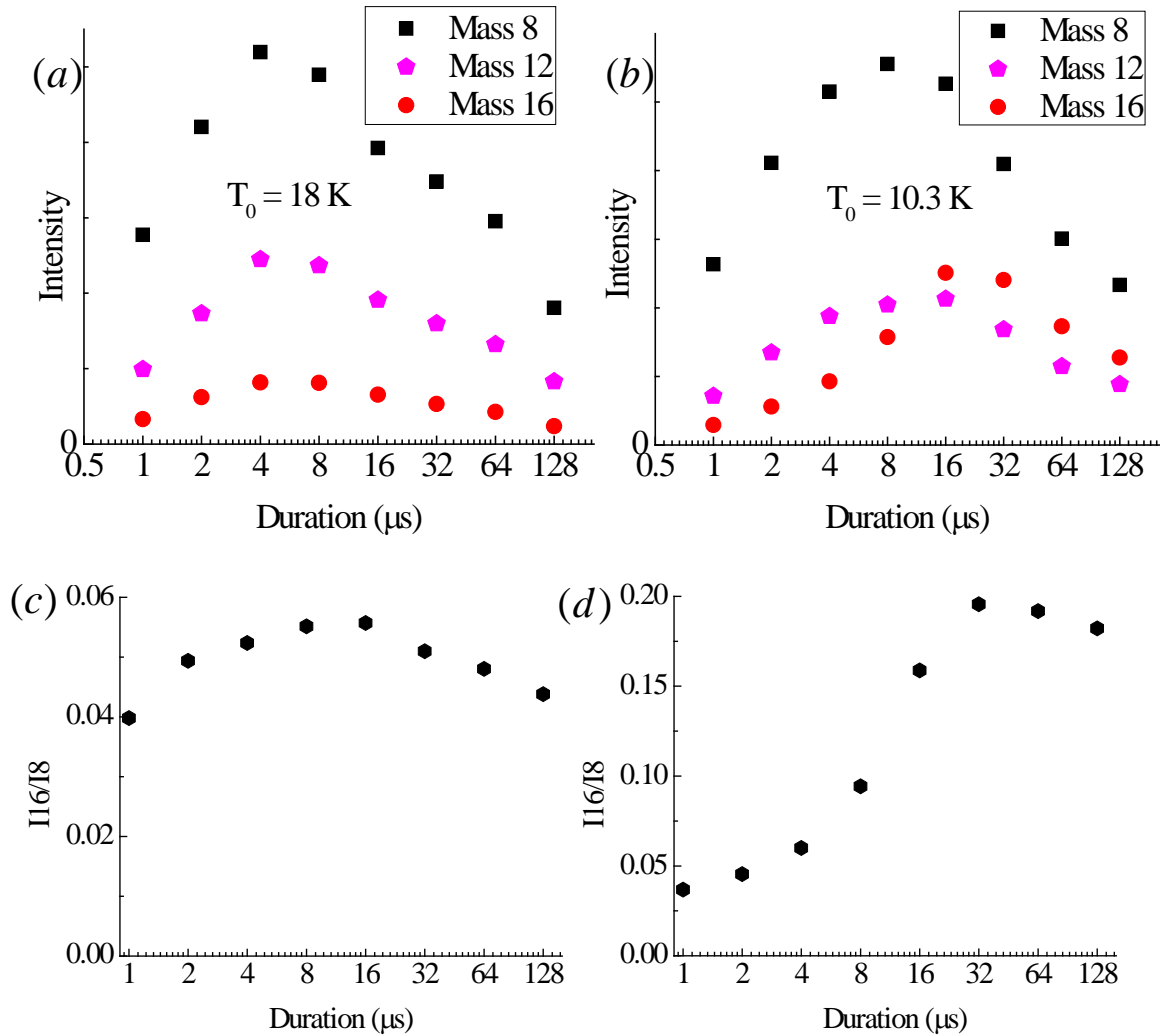


Figure 5.8. TOF peak intensity vs. duration of the ionization pulse for small (a) and large (b) droplets followed by I_{16}/I_8 for small (c) and large (d) droplets. All ionization pulses were initiated at the maximum intensity of their respective droplet pulse, see Figure 5.5. In (a) and (b) intensities of mass 12 and 16 peaks were multiplied by a factor of 3.

The dependence of the intensity of the TOF mass peaks vs. ionization duration (Δt) is shown in Figure 5.8(a) and (b) for small and large droplets, respectively. In both cases the ionization pulses were initiated ($t = 0$) at the maximum of the $M = 8$ signal, i.e. 2.99 and 3.96 ms after the nozzle trigger pulse, for small and large droplets, respectively

(see Figure 5.5). At $T_0 = 18\text{K}$ the signal levels initially increase with the duration of the ionization pulse, reach a maximum at approximately $\Delta t = 4 \mu\text{s}$ and then decrease. In small droplets, the signals at mass 8, 12 and 16 show a very similar dependence, resulting in a nearly constant I_{16}/I_8 ratio. The decrease at longer times is due to the decrease in droplet number density at the end of the droplet pulse (see Figure 5.5). Because ionization is triggered during the most intense portion of the droplet beam, any signal, especially that originating from the creation of ions at longer times, is in competition with the decreasing droplet density. For short Δt , this effect is small, but at $\Delta t > \sim 30 \mu\text{s}$ the droplet density begins to decrease rapidly, which significantly affects signal intensity.

In large droplets, mass 8 and 12 behave similar to those in the small droplet measurements, but mass 16 reaches maximum at $\Delta t \sim 16 \mu\text{s}$, where the He_4^+ signal becomes larger than He_3^+ (see Figure 5.8b). This delayed rise in mass 16 signal results in a considerable increase of I_{16}/I_8 from ~ 0.04 at $\Delta t = 1 \mu\text{s}$ to nearly 0.2 at $\Delta t = 16 \mu\text{s}$. This shows that He_4^+ signal behaves differently in large droplets than mass He_2^+ or He_3^+ , which suggests a different or an additional mechanism of He_4^+ formation in large droplets.

At this point we note that there is an optimal duration of the ionization pulse, beyond which no significant signal increase is observed. Figure 5.9 shows the intensity of background H_2O^+ signal vs. Δt at 1, 3, and 5 mA electron current. Clearly, the greatest increase in signal is acquired within the first $\sim 4 \mu\text{s}$ of irradiation. The signal then saturates upon longer irradiation. Therefore, the majority of signal at any duration must be due to ions created in the $4 \mu\text{s}$ preceding extraction. This behavior is likely related to

the finite lifetime of ions inside the ionization region. For example, the root mean squared velocity of gaseous water at room temperature is ~ 640 m/s. Thus, a water molecule at the center of the ionization volume, which must travel ~ 6 mm to escape extraction, vacates the region in less than $9 \mu\text{s}$.

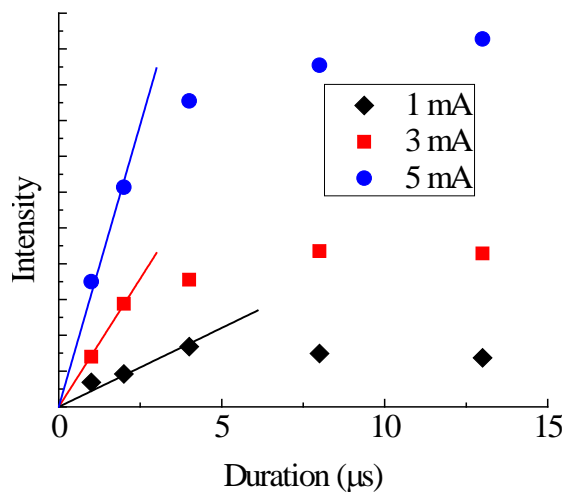


Figure 5.9. The effect of the ionizing pulse duration on background H_2O^+ TOF intensity at various electron currents.

I_{16}/I_8 vs. duration levels at $t \approx 30 \mu\text{s}$ for large droplets, where it reaches a value similar to that obtained with the quadrupole mass spectrometer (Figure 5.8d). It is important to note that the time of $\sim 30 \mu\text{s}$ is very similar to the time droplets spend passing through the ionization region of the quadrupole mass spectrometer.

As noted above, the signal behavior in small droplets appears to be the same for mass 8, 12, and 16. Therefore we propose that these clusters are formed in small droplets via a nearly instantaneous ejection of He_n^+ ions from the droplets (mechanism 1). The decrease in peak intensity with increasing n suggests that mass 8 is the favored cluster in

this formation mechanism. The deviation in mass 16 from this trend in large droplets suggests that an additional mechanism is involved.

Buchaneau et al. have proposed that in addition to direct formation, mass 16 arises from the reaction of two He_2^* exciplex molecules that combine on the surface of a droplet to form He_4^+ , which is then ejected (mechanism 2).¹⁶ Accordingly, two excited helium atoms (He^*) are first created by a single energetic electron passing through the droplet. Both He^* quickly form bubbles and migrate to the surface of the droplet where they become trapped.¹⁷ From bulk helium studies¹⁸ it is known that He^* decays with a time constant of $\sim 15 \mu\text{s}$ to produce metastable ($\text{He}_2^*(v=16) \text{ a}^3\Sigma_u^+$) excimers. Here we assume that same formation time is applicable to He^* on the surface of the droplet. The two He_2^* on the surface finally combine and produce He_4^+ , which is then ejected. An estimate of the time “roaming” on the surface before reaction occurs is given by:

$$\tau_{\text{roaming}} \sim \frac{A_s}{d_{\text{He}_2^*} v_{\text{He}_2^*}(0.4\text{K})} = \frac{4\pi(2.2 \text{ \AA})^2 N^{2/3}}{5 \text{ \AA} * 30 * 10^{10} \text{ \AA/s}} = 0.2 \mu\text{s} \quad (5.1)$$

where A_s is the surface area of the droplet, N is the number of atoms in the droplet taken to be 3×10^5 atoms, $v_{\text{He}_2^*}(0.4\text{K})$ is the velocity of He_2^* at 0.4 Kelvin, and $d_{\text{He}_2^*} = 5 \text{ \AA}$ is a diameter of He_2^* , which replaces the cross-section for 2D kinetics. It is seen that any additional delay due to “roaming” is short, and that the delay in He_4^+ formation via mechanism 2 must be due to the $\sim 15 \mu\text{s}$ formation time of the He_2^* . This is in qualitative agreement with the He_4^+ maximum at $16 \mu\text{s}$. Mechanism 2 is of minor importance in small droplets because of the low probability of creating of two He^* with the same

electron. The low probability is justified because the electron's mean free path is comparable to the small droplet diameter.¹¹

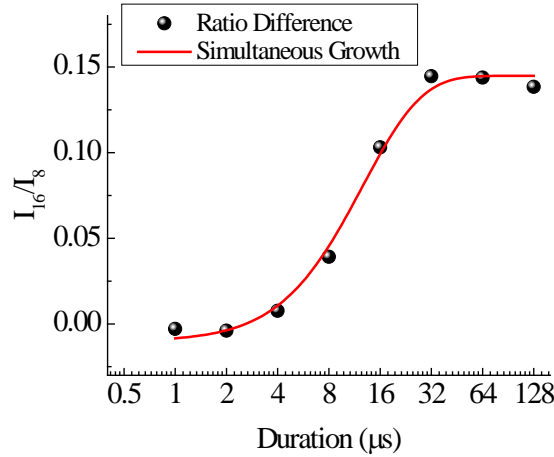


Figure 5.10. Plot of I_{16}/I_8 for large droplet subtracted by I_{16}/I_8 for small droplets. Data is fit the equation $y = a[1 - \exp(-kt)]^2 + b$. Optimized values for a , b , k are 0.1551, -0.0102, and 0.11442, respectively.

To better test the validity of mechanism 2 we subtracted I_{16}/I_8 of large droplets by I_{16}/I_8 of small droplets. This approach is justified as follows: first, small droplets exhibit no trace of the delayed He_4^+ rise observed in large droplets and therefore He_4^+ is expected to be formed via mechanism 1; and second, mechanism 1 is expected to participate regardless of droplets size. Additionally, I_{16}/I_8 better accounts for the decreasing droplet density of the pulse. Thus, the resultant data points, seen in Figure 5.10, eliminate any contribution of mechanism 1 from the I_{16}/I_8 ratio of large droplets. Scharf et al. showed that in bulk helium He_2^* is formed via exponential growth to an equilibrium value using:¹⁸

$$G = G_0 [1 - \exp(-t / \tau)] \quad (5.2)$$

where G is the number of He_2^* at time t , G_0 is the number of He_2^* at equilibrium, and τ is the formation time constant of He_2^* . In helium droplets where only one or two He_2^* species are expected, G becomes the probability of formation, and equation 5.2 becomes:

$$P = [1 - \exp(-t / \tau')] \quad (5.3)$$

Here τ is replaced with τ' in anticipation of a new time constant due to the slightly different environment. In the case of two He_2^* forming simultaneously the total probability is the product of the individual probabilities. Thus:

$$P_{TOT} = [1 - \exp(-t / \tau')]^2 \quad (5.4)$$

Figure 5.10 shows the subtracted ratios fit by the following curve:

$$y = a[1 - \exp(-kt)]^2 + b \quad (5.5)$$

Here b accounts for a deviation from zero baseline and a accounts for the arbitrary amplitude. Thus, the most important parameter k should better represent the true time constant and will be unaffected by an arbitrary baseline or saturation amplitude. Fitted values of a , b , k are 0.1551, -0.0102, and 0.11442, respectively. This yields a value for $\tau' = 1/k = 8.74 \mu\text{s}$. The fit is in very good agreement with the experimental data and provides compelling evidence that mechanism proposed by Buchenau et al. is reasonable. It is unclear why the reaction time in droplets is roughly one half that of bulk helium.

Future work on recombination lifetime would entail setting a delay between electron irradiation and extraction. Varying the delay between irradiation and extraction would help pin down the creation lifetime of He_4^+ and its dependence on droplet size. An alternate approach would be to use a continuous droplet beam. Removing the competition

with decreasing droplet signal would enable the signal to reach saturation / equilibrium. Varying parameters under these conditions, such as duration and droplet size, would facilitate a better understanding of this process.

5.3.6 Photoionization of tris(2-phenylpyridine)iridium in Helium droplets

Great interest in the tris(2-phenylpyridine)iridium ($\text{Ir}(\text{ppy})_3$) molecule stems from its application in OLED displays. One- and two-photon photoionization experiments of gaseous $\text{Ir}(\text{ppy})_3$ are presented in Chapter 3. A major concern in these experiments is the large amount of internal energy imparted to the $\text{Ir}(\text{ppy})_3$ molecules during sublimation. In general, it is desirable to cool molecules to their lowest quantum state prior to probing for spectroscopic information. Unfortunately, attempts to cool the gaseous $\text{Ir}(\text{ppy})_3$ molecules using supersonic expansion and small helium droplets ($\langle N_{\text{He}} \rangle \sim 10^4$) using the apparatus described in Chapter 3 were unsuccessful.¹⁹ However, by increasing the droplet size to $\langle N_{\text{He}} \rangle \approx 5 \times 10^4$ using the pulsed droplet apparatus, it proved possible to embed and photoionize gaseous $\text{Ir}(\text{ppy})_3$ molecules in droplets.

$\text{Ir}(\text{ppy})_3$ molecules were inserted into droplets by heating solid $\text{Ir}(\text{ppy})_3$ in a ceramic oven aligned with the droplet beam axis. This pick-up cell (section 2.4.3) has two orifices for the droplet beam to pass through and is wrapped in resistive tungsten wire (Figure 5.11). The oven is heated by passing current through the tungsten filament with a K-type thermocouple attached below the exit orifice of the oven to monitor the oven temperature.

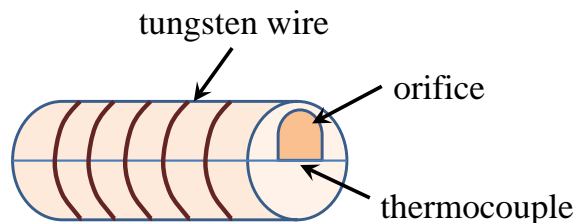


Figure 5.11. Diagram of the crucible pick-up cell used to imbed $\text{Ir}(\text{ppy})_3$ in helium droplets. The droplet beam was aligned through the crucible openings and the solid $\text{Ir}(\text{ppy})_3$ was placed in the lower half of the crucible. Tungsten wire was wrapped around the crucible and heated. The temperature was measured by a thermocouple just below the exit orifice.

As the temperature increased, mass peaks at $M = 655$ and $M = 1310$ amu appeared in the TOF mass spectra (Figure 5.12). Referring to figure 5.12(c), the $\text{Ir}(\text{ppy})_3^+$ and $(\text{Ir}(\text{ppy})_3)_2^+$ signals were a maximum at an oven temperature of 192°C and 202°C , respectively. As seen from Table 5.1, the $\text{Ir}(\text{ppy})_3$ vapor pressure at 192°C and 202°C is $\sim 7 \times 10^{-6}$ Torr and 2×10^{-5} Torr, respectively.²⁰ These pressures are sufficient to produce an effusive beam, which will contribute to the $\text{Ir}(\text{ppy})_3$ TOF signal. Fortunately, measurement of the effusive signal shows a contribution of less than $1/30^{\text{th}}$ of the overall $\text{Ir}(\text{ppy})_3$ signal.

Typically, as the dopant vapor pressure increases, peaks due to dopant clusters, such as dimers, trimers, etc. become more prominent. This is also seen in Figure 5.12(c). As the cell temperature rises from 192°C to 200°C the $M = 1310$ peak due to $\text{Ir}(\text{ppy})_3$ dimers increases. However, at 211°C and beyond all mass signals, including those of the pure droplets, decrease rapidly. The loss of all signal hints that the entire beam is being blocked. We attribute the blockage to a pressure increase inside the pick-up cell as more droplet-impurity collisions occur. Specifically, the energy imparted to the droplet upon capture of the impurity causes rapid evaporation of He atoms from the droplet.

Consequently, this evaporation, and further droplet collisions with the evaporated helium, causes a pressure increase inside the oven, which blocks the remainder of the droplet beam. The local pressure build-up would likely be reduced if the oven orifices were widened. However, the focus of this study was the Ir(ppy)₃ monomer. Thus, the oven temperature was set to 192 °C to maximize the insertion of only one Ir(ppy)₃ molecule in the droplets.

With the doping process characterized, 266 nm light from the YAG fourth harmonic was used to photoionize the embedded Ir(ppy)₃ via multiphoton absorption. The TOF spectra obtained with unfocused 266 nm are shown in Figure 5.13 using 5 mJ cm⁻² and < 1 mJ cm⁻² in (a) and (b), respectively. Referring to Figure 5.13(a), the spectrum obtained at higher fluence shows a pronounced Ir(ppy)₂⁺ fragmentation peak that is not present in the lower fluence spectrum. Fragmentation is not observed at the lower fluence spectrum (5.13b) but the parent peak in 5.13(b) has a much lower intensity. The baseline oscillations in 5.13(b) are due to transient electrical noise. Both spectra show the absence of any He_n⁺ progression, which is consistent with the higher ionization energy of helium (~24.6 eV).

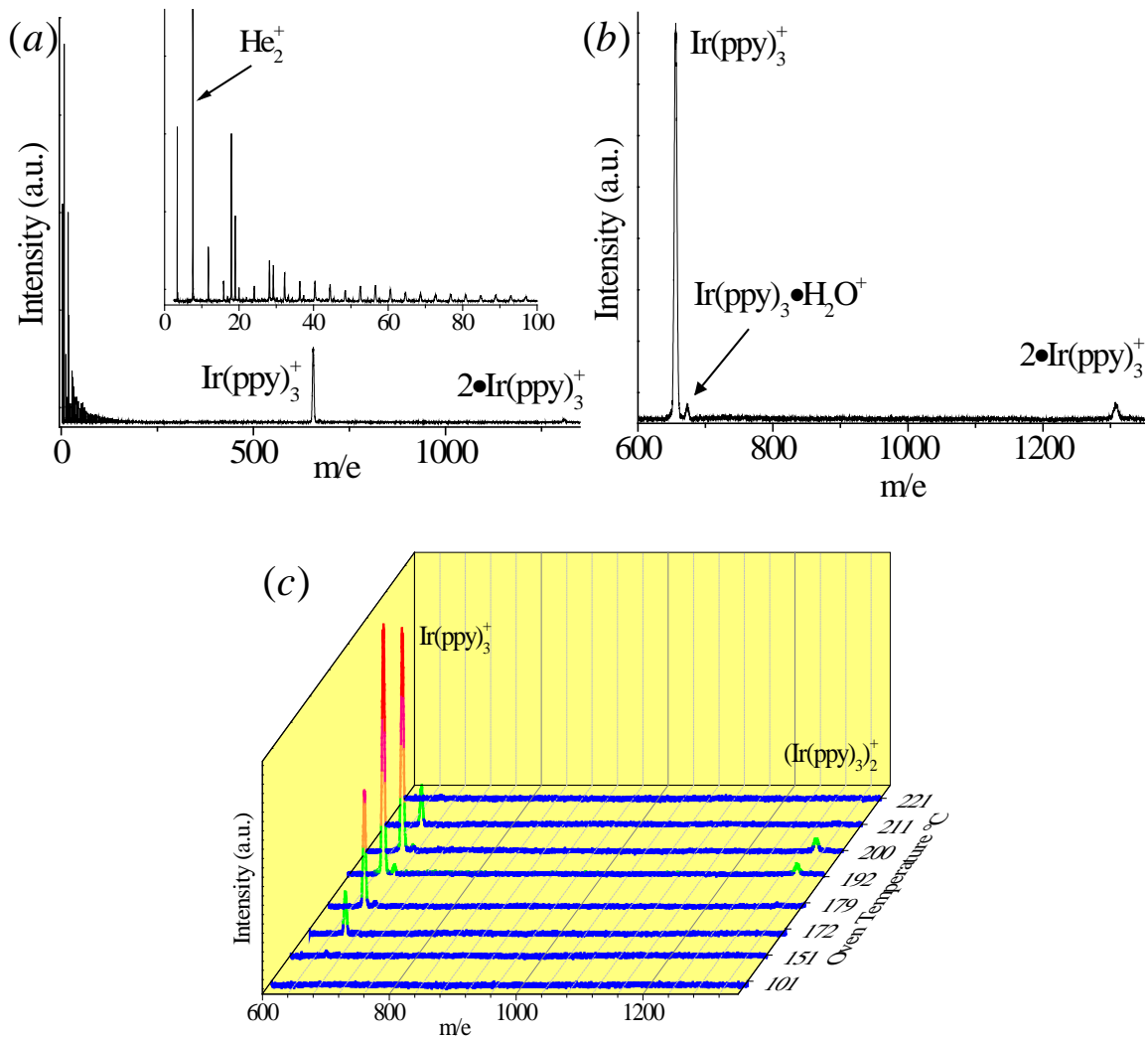


Figure 5.12. Full (a) and zoomed in (b) mass spectra of the droplet beam after pickup of Ir(ppy)_3 . The inset in (a) is an expanded view of the droplet signal. The oven temperature in both (a) and (b) is 192 °C. (c) Ir(ppy)_3^+ and $(\text{Ir(ppy)}_3)_2^+$ progression upon increase of the oven temperature. $M = 655$ and $M = 1310$ signals reach a maximum at 192 °C and 200 °C, respectively.

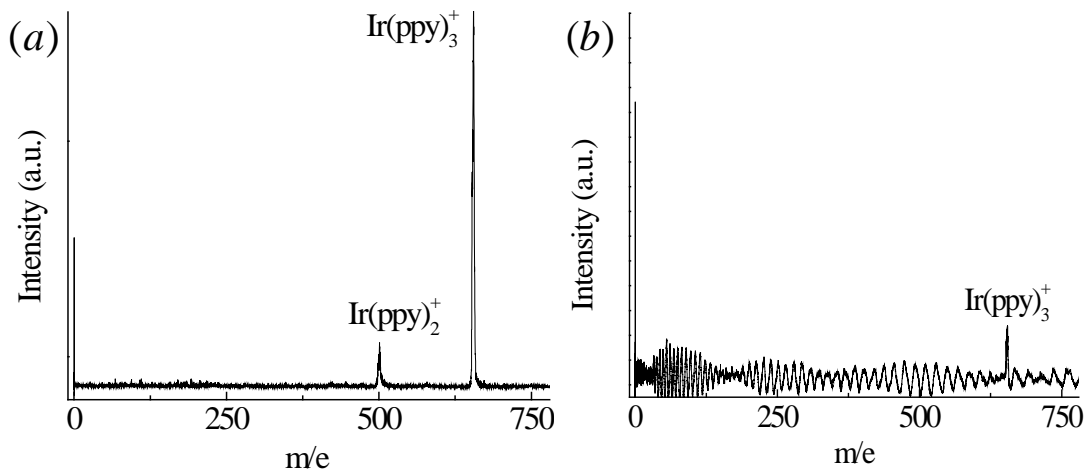


Figure 5.13. Photoionization mass spectra of Ir(ppy)₃ doped helium droplets. The fluences of (a) and (b) were $\sim 5 \text{ mJ cm}^{-2}$ and $< 1 \text{ mJ cm}^{-2}$, respectively. The peak at $M = 0$ in (a) and (b) is scatter from the 266 nm radiation, which served as the $t = 0$ reference.

It was shown in Chapter 3 that photoionization of gaseous Ir(ppy)₃ at photon energies between 4.424 - 4.435 eV and fluences $< 1.6 \text{ mJ cm}^{-2}$ is a two-photon process. Although a fluence study of Ir(ppy)₃ photoionization in helium droplets was not performed, the TOF spectra in Figure 5.13 are consistent with those of Chapter 3. This suggests that at low fluence the photoionization of Ir(ppy)₃ in helium droplets using 266 nm is also a two-photon process.

Temperature (C)	Vapor Pressure (torr)
150	9.47589×10^{-8}
160	3.00606×10^{-7}
170	9.05189×10^{-7}
180	2.59624×10^{-6}
190	7.11514×10^{-6}
200	1.86857×10^{-5}

There are several advantages to employing helium droplets for the photoionization of Ir(ppy)₃. The high heat conductivity and low temperature of the droplets quickly extract and dissipate all energy imparted to Ir(ppy)₃ during sublimation. Moreover, the transfer of internal energy from Ir(ppy)₃ to the droplet occurs quickly, such that, for two-photon photoionization, the first and second transition may occur from the lowest vibrational level of the singlet ground state (S₀) and the lowest triplet state (T₁), respectively.

Another benefit to using helium droplets for this particular experiment is that photoionization in helium droplets requires an additional 1230 cm⁻¹ needed to eject the electron from the droplet.²¹ Loginov et al. observed that the value of 1230 cm⁻¹ was invariant for droplets with radii large than 38 Å,²¹ which is the case in these experiments. This means that only cases where the energy of the photon(s) is greater than the ionization energy by 1230 cm⁻¹ will cations be observed. In cases where the electron is not ejected from the droplet, subsequent electron–cation recombination will occur and no signal will be detected. Thus, successful photoionization of Ir(ppy)₃ using 193.3 nm would correspond to a revised ionization energy (IE) upper bound of 6.26 eV (6.41 – 0.15). However, the actual situation is more complex as the droplet environment is considerably different than that of a vacuum.

Helium abhors electron density, which results in broadened and shifted electronic spectra.^{22,23} The magnitude of such spectral shifts are typically on the order of a few hundred wavenumbers.²³ The electron-helium interaction has also been shown to reduce the ionization potential.²¹ The situation is further complicated by the finite size of the

droplets. In this case, a reasonable approach is to apply a polarizable continuum model.²⁴

In this model, the IE of the embedded molecule varies as:²¹

$$\text{IE}(R) = \text{IE}_\infty - \frac{e^2(1 - \varepsilon^{-1})}{8\pi\varepsilon_0 R} \quad (5.6)$$

where IE_∞ is the vertical ionization threshold in bulk helium, e the electron charge, ε_0 is the permittivity of free space, and ε is the dielectric constant of the cluster. Although the polarizable continuum model provides a way to compensate for the changing IE as a function of droplet size, the IE in bulk helium is still unknown! Thus, the main benefit of using droplets for $\text{Ir}(\text{ppy})_3$ photoionization lies in its ability to remove internal energy. The expected spectral shifts are indicative of the uncertainty in the IE upper bound. Overall, photoionization of $\text{Ir}(\text{ppy})_3$ inside helium droplets would greatly compliment the gas-phase experiments of Chapter 3.

5.4 References

1. Choi, M. Y.; Douberly, G. E.; Falconer, T. M.; Lewis, W. K.; Lindsay, C. M.; Merritt, J. M.; Stiles, P. L.; Miller, R. E. *Int. Rev. Phys. Chem.* **2006**, *25*, 15.
2. Tiggesbaumker, J.; Stienkemeier, F. *Phys. Chem. Chem. Phys.* **2007**, *9*, 4748.
3. Krasnokutski, S. A.; Huisken, F. *J. Phys. Chem. A* **2010**, *114*, 7292.
4. Stienkemeier, F.; Lehmann, K. K. *J. Phys. B* **2006**, *39*, R127 .
5. Toennies, J. P.; Vilesov, A. F. *Angew. Chem. Int. Ed.* **2004**, *43*, 2622.
6. Gough, T. E.; Mengel, M.; Rowntree, P. A.; Scoles, G. *J. Chem. Phys.* **1985**, *83*, 4958.
7. Buchenau, H.; Knuth, E. L.; Northby, J.; Toennies, J. P.; Winkler, C. *J. Chem. Phys.* **1990**, *92*, 6875.
8. Harms, J.; Hartmann, M.; Toennies, J. P.; Vilesov, A. F.; Sartakov, B. *J. Molec. Spec.* **1997**, *185*, 204.
9. Lewerenz, M.; Schilling, B.; Toennies, J. P. *Chem. Phys. Lett.* **1993**, *206*, 381.
10. Knuth, E. L.; Henne, U. *J. Chem. Phys.* **1999**, *110*, 2664.
11. Gomez, L. F.; Loginov, E.; Sliter, R.; Vilesov, A. F. *J. Chem. Phys.* **2011**, *135*, 154201.
12. Slipchenko, M. N.; Kuma, S.; Momose, T.; Vilesov, A. F. *Rev. Sci. Inst.* **2002**, *73*, 3600.
13. Sliter, R. *Infrared and Raman Spectroscopy of Molecules and Molecular Aggregates in Helium Droplets*, Ph. D. Dissertation, University of Southern California, Los Angeles, CA, 2011.
14. Peterka, D. S.; Kim, J. H.; Wang, C. C.; Poisson, L.; Neumark, D. M. *J. Phys. Chem. A* **2007**, *111*, 7449.
15. Schilling, B. Ph. D Dissertation, University of Gottingen, Gottingen, Germany, 1993.
16. Buchenau, H.; Toennies, J. P.; Northby, J. A. *J. Chem. Phys.* **1991**, *95*, 8134.

17. Scharf, D.; Jortner, J.; Landman, U. *J. Chem. Phys.* **1988**, *88*, 4273.
18. Keto, J. W.; Soley, F. J.; Stockton, M.; Fitzsimmons, W. A. *Phys. Rev. A* **1974**, *10*, 872, 887.
19. Nemirow, C. *Multiphoton Investigation of tris(2-phenylpyridine)iridium*. Ph. D. Dissertation, University of Southern California, Los Angeles, CA, **2011**.
20. Deaton, J. C.; Switalski, S. C.; Kondakov, D. Y.; Young, R. H.; Pawlik, T. D.; Giesen, D. J.; Harkins, S. B.; Miller, A. J. M.; Mickenberg, S. F.; Peters, J. C. *J. Am. Chem. Soc.* **2010**, *132*, 9499.
21. Loginov, E.; Rossi, D.; Drabbels, M. *Phys. Rev. Lett.* **2005**, *95*, 163401.
22. Schmied, R.; Carcabal, P.; Dokter, A. M.; Lonij, V. P. A.; Lehmann, K. K.; Scoles, G. *J. Chem. Phys.* **2004**, *121*, 2701.
23. Brauer, N. B.; Smolarek, S.; Zhang, X.; Buma, W. J.; Drabbels, M. *J. Phys. Chem. Lett.* **2011**, *2*, 1563.
24. Jortner, J. *Z. Phys. D* **1992**, *24*, 247.

Chapter 6

Future Work

6.1 Introduction

An open question in this dissertation is whether the ethynyl radical (C_2H , section 2.6) can be produced in sufficient quantity, such that detection with electron impact ionization / time-of-flight (TOF) mass spectrometry is possible. It was shown in section 2.6 that 193.3 nm photolysis of acetylene (C_2H_2) was able to produce C_2 and C_2H molecules. However, detection of these species using electron impact ionization / TOF mass spectrometry was inadequate, because either the concentration and / or the electron impact ionization efficiency was too low to effectively monitor the nascent species.

In light of the previous results, it is proposed that C_2H is more aptly produced by electrical discharge of a supersonically expanding acetylene / carrier gas mixture. Both continuous and pulsed discharge sources have been developed,^{1,2} but a pulsed source is particularly promising due to the large molecular density produced while maintaining reasonable vacuum. Therefore, production of C_2H will be achieved via pulsed electrical discharge. This approach has been used previously to generate OH radicals from a gaseous water / argon mixture.³ Reported measurements of the OH centerline flux using pulsed discharge have been as high as 2.2×10^{17} molecules $sr^{-1} s^{-1}$, which corresponds to a concentration of $\sim 3 \times 10^{12}$ molecules cm^{-3} approximately 1 cm after the nozzle.³ Additionally, the radical species are created prior to expansion, which allows the radicals to cool in the expansion that follows.

6.2 Experimental

The proposed nozzle and discharge setup is similar to that used by McCarthy et al.⁴ A rendering of the nozzle and discharge geometry is depicted in Figure 6.1. A commercially available pulsed valve (R. M. Jordan) with a 500 μm nozzle will be used. The valve operates based on a current loop mechanism, which avoids the inconsistency of poppets and the need to constantly replace them. The valve has a repetition rate 10 Hz and a pulse duration of $\sim 50 \mu\text{s}$. Attached to the nozzle faceplate is a 5 mm Teflon spacer followed by a copper electrode. Both the spacer and electrode are encased in a Teflon housing. The electrode will initially be set between -2.0 and -2.5 kV, with the nozzle faceplate wired to ground. This insures that the electron current flows against the gas stream. Operation with a positively biased electrode is known to cause an unstable discharge with less efficient radical generation.² Discharge initiates by the rise in local pressure when the valve opens. The discharge automatically terminates once the local pressure returns to vacuum. C_2H is generated by collisions between the flowing discharge electrons and the expanding acetylene molecules.

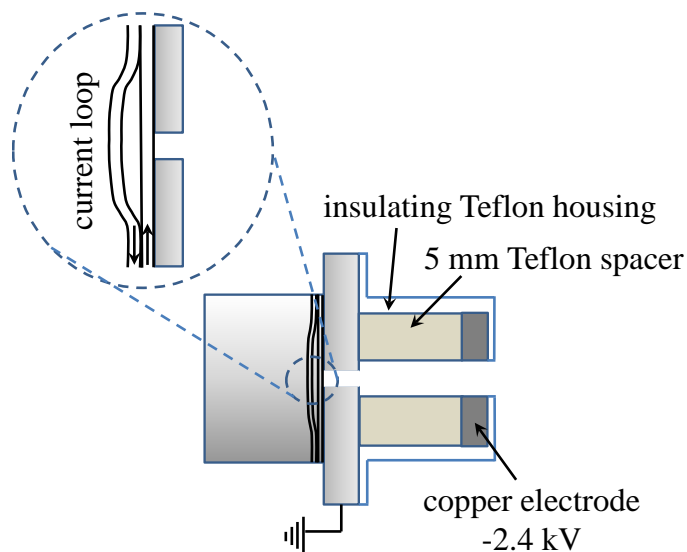


Figure 6.1. Depiction of the nozzle and discharge assembly. The nozzle operates on a current loop mechanism. Attached to the grounded nozzle faceplate is a Teflon spacer followed by a negatively biased copper electrode. Both spacer and electrode are encased in a Teflon shroud.

The acetylene mixture will contain 10% or less acetylene in Argon and expanded using a backing pressure between 1 – 2 psia. Compared to the 3 % mixture and 1 psia backing pressure of reference 3, the proposed conditions should increase the number density by a factor of 5. In fact, under similar expansion conditions a total beam density of 3×10^{13} has been measured approximately 8 cm past the nozzle,⁵ which would correspond to an acetylene concentration of 10^{12} molecules / cm^{-3} at the detection region. The mixture concentration may need to be fine-tuned to prevent reactions among the radicals during expansion. The above conditions allow for source and detection chamber pressures of about $\sim 10^{-5}$ and mid 10^{-7} torr, respectively.

To ensure a stable discharge, several precautions need to be taken. First, a gating circuit will be used to prevent current from flowing 50 us prior to and 50 us after the gas

pulse begins and ends, respectively. This will reduce that probability of gas leaks triggering a discharge. In addition, ballast resistors must be implemented to ensure the current does not rise above a reasonable value. In the absence of such a limitation, arcing may occur due to the negative resistance characteristic of the gas, which will pit the surface of the electrodes. The asymmetry created by a pit in the electrode surface will prevent a stable uniform discharge from occurring and the electrode will need to be replaced. As noted above, after discharge the molecules are left to cool via expansion and travel to the detector.

Detection will again use electron impact ionization coupled with TOF mass spectrometry, albeit with a few changes to the setup described in section 2.6. A new vacuum chamber will be constructed, in which the distance between the nozzle and TOF detection region is minimized (Figure 6.2a). A distance of 10 cm or less is easily achieved. The small separation between source and detector will minimize the loss of signal due to molecular beam propagation. The nozzle will be ~ 2 cm away from a 1 mm skimmer, which were optimal conditions for the experiments described in section 2.6. Additionally, the detection chamber will contain three very different optical paths in anticipation of future experiments on C_2H (Figure 6.2b). Path 1 will cross the source chamber directly in front of the nozzle and skimmer, path 2 will pass diagonally through the center of the TOF stack assembly, and path 3 will pass through the rear of the detection chamber in order to overlap the molecule beam. These paths will insure that all opportunities to optically probe C_2H are explored.

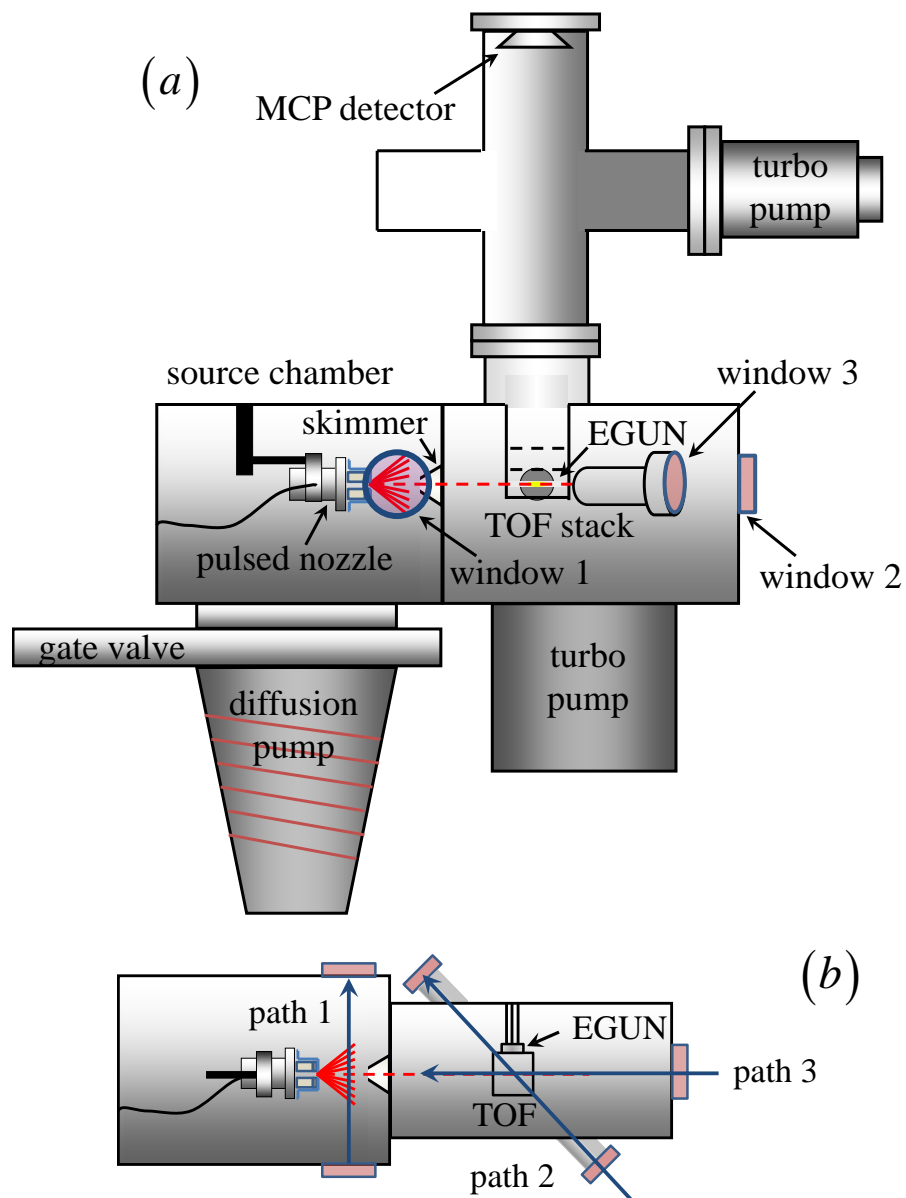


Figure 6.2. (a) side view of the proposed vacuum chamber. The distance between the nozzle and TOF stack is less than 10 cm. Window 1, 2, and 3 correspond to path 1, 2, and 3 in part (b), respectively. The operating pressures in the source and detection regions are expected to be 10^{-5} torr and mid 10^{-7} torr, respectively. (b) shows a top view of the proposed vacuum chamber. Three optical paths are illustrated. Path 1 passes directly in front of the nozzle, path 2 crosses the center of the detection region, and path 3 overlaps the molecular beam with anti-parallel propagation.

Ionization is achieved through electron impact (section 2.5). The electron gun will operate at 80 eV and the highest electron current possible (between 5 – 10 mA). The duration of bombardment will also be increased from 2 to 12.5 μ s. An increased electron energy corresponds to a \sim 5 fold increase in the electron impact cross-section (section 2.5), the 5 – 10 mA current results in a 5 – 10 fold increase in collision probability with respect to the previous experiments (section 2.6), and the increased ionization time contributes a factor of 6. In total, these changes will increase the probability of C₂H ionization to $> 10^{-3}$.

6.3 Discussion

As mentioned above, the radical number density just after leaving the nozzle will be at least 10^{12} molecules cm^{-3} . Seeing as the decrease in concentration scales as the inverse of the distance traveled squared,⁶ approximately 10 cm downstream, a concentration of $\sim 10^{10}$ molecules cm^{-3} is expected. Using the electron impact settings discussed earlier the probability of ionization will be greater than 10^{-3} . Thus, the worst case scenario yields a C₂H⁺ concentration at of 10^7 molecules cm^{-3} , which is easily detected using TOF.

Several radical and ion products are expected from the discharge source. Considering radical / ion generation in electrical discharge follows an electron impact mechanism, it is reasonable to assume that similar “cracking pattern” to that observed in the electron impact / TOF measurements will be present. However, the TOF mass spectrometer only observes ions. Therefore, the discharge voltage will be tuned, most

likely reduced, to maximize radical formation. The radicals can then be ionized and detected with the TOF mass spectrometer.

One difficulty arises with using 80 eV as the electron impact ionization energy. At this energy fragmentation of acetylene creates C_2^+ , C_2H^+ , and $C_2H_2^+$ ions, and a very small amount of CH^+ . This cracking pattern will mask subtle changes in the ion signal. Consequently, a difference between spectra with the discharge on and discharge off will reveal the C_2H signal produced. Once C_2H signal is detected all parameters will be tuned to optimize this signal.

In summation, pulsed electrical discharge of an acetylene/carrier gas mixture shows great promise as a reliable and robust source for C_2H production. A new vacuum chamber and improved electron impact / TOF parameters yield encouraging estimates for C_2H detection. With the ability to monitor the C_2H species, optical probing of this species with one or more of three optical schemes will provide new spectroscopic information on this fundamental molecule.

6.4 References

1. Crabtree, K. N.; Kauffman, C. A.; McCall, B. J. *Rev. Sci. Instrum.* **2010**, *81*, 086103.
2. Anderson, D. T.; Davis, S.; Zwier, T. S.; Nesbitt, D. J. *Chem. Phys. Lett.* **1996**, *258*, 207.
3. Van Beek, M. C.; Ter Meulen, J. J. *Chem. Phys. Lett.* **2010**, *337*, 237.
4. McCarthy, M. C.; Chen, W.; Travers, M. J.; Thaddeus, P. *Astrophys. J. Suppl. Ser.* **2000**, *129*, 611.
5. Irimia, D.; Kortekaas, R.; Janssen, M. H. M. *Phys. Chem. Chem. Phys.* **2009**, *11*, 3958.
6. Ramsey, N. F. *Molecular Beams*; Oxford University Press: New York, NY, **1985**.

Bibliography

- Abramczyk, H. *Introduction to Laser Spectroscopy*; Elsevier: Amsterdam, **2005**.
- Adachi, C.; Baldo, M. A.; Forrest, S. R.; Thompson, M. E. *Appl. Phys. Lett.* **2000**, *77*, 904.
- Adachi, C.; Baldo, M. A.; Thompson, M. E.; Forrest, S. R. *J. Appl. Phys.* **2001**, *90*, 5048.
- Adachi, C.; Kwong, R. C.; Djurovich, P.; Adamovich, V.; Baldo, M. A.; Thompson, M. E.; Forrest, S. R. *Appl. Phys. Lett.* **2001**, *79*, 2082.
- Adachi, C.; Thompson, M. E.; Forrest, S. R. *IEEE* **2002**, *8*, 372.
- Allen, F. H.; Kennard, O. *Chem. Des. Auto. News* **1993**, *8*, 31.
- Allen, F. H.; Kennard, O.; Galloy, J. J.; Johnson, O.; Watson, D. G. *Chem. Structures* **1993**, *2*, 343.
- Anderson, D. T.; Davis, S.; Zwier, T. S.; Nesbitt, D. J. *Chem. Phys. Lett.* **1996**, *258*, 207.
- Antonov, V. S.; Letokhov, V. S. *Appl. Phys.* **1981**, *24*, 89.
- Apaydin, G.; Fink, W. H.; Jackson, W. M. *J. Chem. Phys.* **2004**, *121*, 9368.
- Argaman, N.; Makov, G. *Amer. J. Phys.* **2000**, *68*, 69.
- Ashfold, M. N. R.; Howe, J. D. *Annu. Rev. Phys. Chem.* **1994**, *45*, 57.
- Ashfold, M. N. R.; Ledingham, K. W. D. *An Introduction to Laser Spectroscopy*; Andrews, D. L.; Demidov, A. A. Ed.; Plenum Press: New York, NY, **1995**, pp. 35 – 62; pp. 199 – 228
- Ashfold, M. N. R.; Nahler, N. H.; Orr-Ewing, A. J.; Vieuxmaire, O. P. J.; Toomes, R. L.; Kitsopoulos, T. N.; Garcia, I. A.; Chestakov, D. A.; Wu, S.; Parker, D. H. *Phys. Chem. Chem. Phys.* **2006**, *8*, 26.
- Atkins, P. W.; Friedman, R. S. *Molecular Quantum Mechanics*, 4th ed; Oxford University Press: New York, NY, **2005**.
- Baer, R.; Livshits, E.; Salzner, U. *Ann. Rev. Phys. Chem.* **2010**, *61*, 85.

- Baer, R.; Neuhauser, D. *Phys. Rev. Lett.* **2005**, *94*, 043002.
- Baldo, M. A.; Forrest, S. R. *Phys. Rev. B* **2000**, *62*, 10958.
- Baldo, M. A.; Lamansky, S.; Burrows, P.E.; Thompson, M. E.; Forrest, S. R. *Appl. Phys. Lett.* **1999**, *75*, 4.
- Baldo, M. A.; O'Brien, D. F.; Thompson, M. E.; Forrest, S. R. *Phys. Rev. B* **1999**, *60*, 14422.
- Baldo, M. A.; Thompson, M. E.; Forrest, S. R. *Nature* **2000**, *403*, 750.
- Banares, L.; Baumet, T.; Bergt, M.; Kiefer, B.; Gerber, G. *J. Chem. Phys.* **1998**, *108*, 5799.
- Barker, J. R. *Int. J. Chem. Kin.* **2001**, *33*, 232.
- Barker, J. R. *Int. J. Chem. Kin.* **2009**, *41*, 748.
- Barker, J. R.; Ortiz, N. F.; Preses, J. M.; Lohr, L. L.; Maranzana, A.; Stimac, P. J.; Nguyen, T. L.; Dhilip Kumar, T. J. MultiWell-2011.3 Software,
<http://aoss.engin.umich.edu/multiwell>
- Barranco, M.; Guardiola, R.; Hernandez, S.; Mayol, R.; Navarro, J.; Pi, M. *J. Low Temp. Phys.* **2006**, *142*, 1.
- Bart, M.; Harland, P. W.; Hudson, J. E.; Vallance, C. *Phys. Chem. Chem. Phys.* **2001**, *3*, 800.
- Bart, M.; Harland, P. W.; Vallance, J. E. *Phys. Chem. Chem. Phys.* **2001**, *3*, 800.
- Becke, A. D. *J. Chem. Phys.* **1993**, *98*, 5648.
- Beyer, T.; Swinehart, D. *Comm. ACM* **1973**, *16*, 379.
- Birks, J. B.; Dyson, D. J. *Proc. R. Soc. Lond. Ser. A* **1963**, *275*, 135.
- Blunt, V. M.; Lin, H.; Sorkhabi, O.; Jackson, W. M. *Chem. Phys. Lett.* **1996**, *257*, 347.
- Boesl, U.; Neusser, H. J.; Schlag, E. W. *J. Chem. Phys.* **1980**, *72*, 4327.

Brauer, N. B.; Smolarek, S.; Zhang, X.; Buma, W. J.; Drabbels, M. *J. Phys. Chem. Lett.* **2011**, *2*, 1563.

Braun, J. E.; Neusser, H. J.; Harter, P.; Stockl, M. *J. Phys. Chem. A* **2000**, *104*, 2013.

Breu, J.; Stossel, P.; Schrader, S.; Starukhin, A.; Finkenzeller, W. J.; Yersin, H. *Chem. Mater.* **2005**, *17*, 1745.

Buchenau, H.; Knuth, E. L.; Northby, J. A.; Toennies, J. P.; Winkler, C. *J. Chem. Phys.* **1990**, *92*, 6875.

Buchenau, H.; Toennies, J. P.; Northby, J. A. *J. Chem. Phys.* **1991**, *95*, 8134.

Bull, J. N.; Harland, P. W.; Vallance, C. *J. Phys. Chem. A* **2012**, *116*, 767.

Bull, J. N.; Harland, P. W. *Int. J. Mass Spectrom.* **2008**, *273*, 53.

Car, R. *Quant. Struct.-Act. Relat.* **2002**, *21*, 97.

Chai, J. D.; Head-Gordon, M. *J. Chem. Phys.* **2008**, *128*, 084106.

Chai, J. D.; Head-Gordon, M. *Phys. Chem. Chem. Phys.* **2008**, *10*, 6615.

Chiang, W.; Hsu, Y. *J. Chem. Phys.* **1999**, *111*, 1454.

Chiang, W.; Hsu, Y. *J. Chem. Phys.* **2000**, *112*, 7394.

Choi, M. Y.; Douberly, G. E.; Falconer, T. M.; Lewis, W. K.; Lindsay, C. M.; Merritt, J. M.; Stiles, P. L.; Miller, R. E. *Int. Rev. Phys. Chem.* **2006**, *25*, 15.

Cleave, V.; Yahioglu, G.; Le Barny, P.; Friend, R. H.; Tessler, N. *Adv. Mater.* **1999**, *11*, 285.

Close, J. D.; Federmann, F.; Hoffmann, K.; Quaas, N. *Chem. Phys. Lett.* **1997**, *276*, 393.

Coe, B. J.; Glenwright, S. J. *Coord. Chem. Rev.* **2000**, *203*, 5.

Crabtree, K. N.; Kauffman, C. A.; McCall, B. J. *Rev. Sci. Instrum.* **2010**, *81*, 086103.

CRC Handbook of Chemistry and Physics, 92nd ed; **2011-2012**.

Cui, Q.; Morokuma, K. *J. Phys. Chem.* **1998**, *108*, 626.

Deaton, J. C.; Switalski, S. C.; Kondakov, D. Y.; Young, R. H.; Pawlik, T. D.; Giesen, D. J.; Harkins, S. B.; Miller, A. J. M.; Mickenberg, S. F.; Peters, J. C. *J. Am. Chem. Soc.* **2010**, *132*, 9499.

Demtroder, W. *Laser Spectroscopy: Basic Concepts and Instrumentation*, 2nd ed.; Springer: New York, NY, **1998**.

Deutsch, H.; Becker, K.; Matt, S.; Mark, T. D. *Int. J. Mass. Spectrom.* **2000**, *197*, 37.

Dobbs, K. D.; Sohlberg, K. *J. Chem. Theory Comput.* **2006**, *2*, 1530.

Du, H.; Fuh, R. C. A.; Li, J. Z.; Corkan, L. A.; Lindsey, J. S. *Photochem. Photobio.* **1998**, *68*, 141.

Duflot, D.; Robbe, J., Flament, J. *J. Chem. Phys.* **1994**, *100*, 1236.

Engelking, P. C. *Chem. Phys. Lett.* **1980**, *74*, 207.

Ervin, K. M.; Lineberger, W. C. *J. Phys. Chem.* **1991**, *95*, 1167.

Finkenzeller, W. J.; Yersin, H. *Chem. Phys. Lett.* **2003**, *377*, 299.

Fitch, W. L.; Sauter, A. D. *Anal. Chem.* **1983**, *55*, 832.

Franklin, J. L.; Field, F. H. *J. Amer. Chem. Soc.* **1954**, *76*, 1994.

Garces, F. O.; Dedeian, K.; Keder, N. L.; Watts, R. J. *Acta Cryst. C* **1993**, *49*, 1117.

Gomez, L. F.; Loginov, E.; Sliter, R.; Vilesov, A. F. *J. Chem. Phys.* **2011**, *135*, 154201.

Gottlieb, C. A.; Gottlieb, E. W.; Thaddeus, P. *Astrophys. J.* **1983**, *264*, 740.

Gough, T. E.; Mengel, M.; Rowntree, P. A.; Scoles, G. *J. Chem. Phys.* **1985**, *83*, 4958.

Goyal, S.; Schutt, D. L.; Scoles, G. *Phys. Rev. Lett.* **1992**, *69*, 933.

Goyal, S.; Schutt, D. L.; Scoles, G.; Robinson, G. N. *Chem. Phys. Lett.* **1992**, *196*, 123.

Grebenev, S.; Hartmann, M.; Havenith, M.; Sartakov, B.; Toennies, J. P.; Vilesov, A. F.; *J. Chem. Phys.* **2000**, *112*, 4485.

Grebenev, S.; Havenith, M.; Madeja, F.; Toennies, J. P.; Vilesov, A. F.; *J. Chem. Phys.* **2000**, *113*, 9060.

Hale, G. M.; Querry, M. R. *Appl. Opt.* **1973**, *12*, 555.

Harland, P. W.; Vallance, C. *Advances in Gas Phase Ion Chemistry*; Adams, N. G.; Babcock, L. M. Ed.; Jai Press: Greenwich, CT, **1998**; Vol. III; pp. 319 – 358.

Harms, J.; Hartmann, M.; Sartakov, B.; Toennies, J. P.; Vilesov, A. F.; *J. Chem. Phys.* **1999**, *110*, 5124.

Harms, J.; Hartmann, M.; Toennies, J. P.; Vilesov, A. F.; Sartakov, B. *J. Mol. Spectrosc.* **1997**, *185*, 204.

Hartley, F. R.; *Chem. Soc. Rev.* **1973**, *2*, 163.

Hartmann, M.; Miller, R.; Toennies, J. P.; Vilesov, A. F. *Science.* **1996**, *272*, 1631.

Hashimoto, N.; Yonekura, N.; Suzuki, T. *Chem. Phys. Lett.* **1997**, *264*, 545.

Hay, P. J. *J. Phys. Chem. A* **2002**, *106*, 1634.

Hay, P. J.; Wadt, W. R. *J. Chem. Phys.* **1985**, *82*, 299.

Hedley, G. J.; Ruseckas, A.; Samuel, I. D. W. *Chem. Phys. Lett.* **2008**, *450*, 292.

Hedley, G. J.; Ruseckas, A.; Liu, Z.; Lo, S. C.; Bum, P. L.; Samuel, I. D. W. *J. Am. Chem. Soc.* **2008**, *130*, 11842.

Hedley, G. J.; Ruseckas, A.; Samuel, I. D. W. *J. Phys. Chem. A Lett.* **2008**, *113*, 2.

Hehre, W. J.; Stewart, R. F.; Pople, J. A. *J. Chem. Phys.* **1969**, *51*, 2657.

Hofbeck, T.; Yersin, H. *Inorg. Chem.* **2010**, *49*, 9290.

Hohenberg, P.; Kohn, W. *Phys. Rev.* **1964**, *136*, B864.

Hollas, M. *High Resolution Spectroscopy*; John Wiley & Sons: New York, NY, **1998**.

Holzer, W.; Penzkofer, A.; Tsuboi, T. *Chem. Phys. Lett.* **2005**, *308*, 93.

Hsu, Y.; Lin, J. J.; Papousek, D.; Tsai, J. *J. Chem. Phys.* **1993**, *98*, 6690.

- Hsu, Y.; Shiu, Y.; Lin, C. *J. Chem. Phys.* **1995**, *103*, 5919.
- Hsu, Y.; Wang, P.; Yang, M.; Papousek, D.; Chen, Y.; Chiang, W. *Chem. Phys. Lett.* **1992**, *190*, 507.
- Hudson, J. E.; Hamilton, M. L.; Vallance, J. E.; Harland, P. W. *Phys. Chem. Chem. Phys.* **2003**, *5*, 3162.
- Hudson, J. E.; Weng, Z. F.; Vallance, J. E.; Harland, P. W. *Int. J. Mass Spectrom.* **2006**, *248*, 42.
- Hudson, J. E.; Hamilton, M. L.; Vallance, C.; Harland, P. W. *Phys. Chem. Chem. Phys.* **2003**, *5*, 3162.
- Hwang, W.; Kim, Y. K.; Rudd, M. E. *J. Chem. Phys.* **1996**, *104*, 2956.
- Ionov, S.; Davis, H. F.; Mikhaylichenko, K.; Valachovic, L.; Beudet, R. A.; Wittig, C. *J. Chem. Phys.* **1994**, *101*, 4809.
- Irikura, K. K.; Kim, Y. K.; Ali, M. A. *J. Res. Natl. Inst. Stand. Technol.* **2002**, *107*, 63.
- Irimia, D.; Kortekaas, R.; Janssen, M. H. M. *Phys. Chem. Chem. Phys.* **2009**, *11*, 3958.
- Jansson, E.; Minaev, B.; Schrader, S.; Ågren, H. *Chem. Phys.* **2007**, *333*, 157.
- Johnson, P. M. *Acc. Chem. Res.* **1980**, *13*, 20.
- Johnson, P. M. *J. Chem. Phys.* **1975**, *62*, 4562.
- Johnson, P. M.; Otis, C. E. *Ann. Rev. Phys. Chem.* **1981**, *32*, 139.
- Jortner, J. Z. *Phys. D* **1992**, *24*, 247.
- Kanamori, H.; Hirota, E. *J. Chem. Phys.* **1988**, *89*, 3962.
- Kanamori, H.; Seki, K.; Hirota, E. *J. Chem. Phys.* **1987**, *87*, 73.
- Kawaguchi, K.; Amano, T.; Hirota, E. *J. Mol. Spectrosc.* **1988**, *131*, 58.
- Ketkov, S. Y.; Selzle, H. L.; Schlag, E. W.; Domrachev, G. *J. Phys. Chem. A* **2003**, *107*, 4041.

Ketkov, S. Y.; Selzle, H. L.; Schlag, E. W.; Titova, S. N. *Chem. Phys.* **2003**, *293*, 91.

Keto, J. W.; Soley, F. J.; Stockton, M.; Fitzsimmons, W. A. *Phys. Rev. A* **1974**, *10*, 872, 887.

Killian, T. C.; Gottlieb, C. A.; Thaddeus, P. *J. Chem. Phys.* **2007**, *127*, 114320.

Kim, Y. K.; Ali, M. A.; Rudd, M. E. *J. Res. Natl. Inst. Stand. Technol.* **1997**, *102*, 693.

Kim, Y. K.; Rudd, M. E. *Phys. Rev. A* **1994**, *50*, 3954.

Knuth, E. L.; Henne, U. *J. Chem. Phys.* **1999**, *110*, 2664.

Koch, W.; Holthausen, M. C. *A Chemist's guide to Density Functional Theory*, 2nd ed; Wiley-VHC Verlag: Weinheim, Germany, **2002**.

Kohn, W.; Sham, L. J. *Phys. Rev.* **1965**, *140*, A1133.

Krasnokutski, S. A.; Huisken, F. *J. Phys. Chem. A* **2010**, *114*, 7292.

Krumholz, P. *J. Am. Chem. Soc.* **1951**, *73*, 3487.

Kubin, J.; Testa, A. *J. Photochem. Photobiol. A: Chem.* **1994**, *83*, 91.

Kukhta, A. V.; Kukhta, I. N.; Bagnich, S. A.; Kazakov, S. M.; Andreev, V. A.; Neyra, O. L.; Meza, E. *Chem. Phys. Lett.* **2007**, *434*, 11.

Lamansky, S.; Djurovich, P.; Murphy, D.; Abdel-Razzaq, F.; Lee, H.; Adachi, C.; Burrows, P.; Forrest, S. R.; Thompson, M. E. *J. Am. Chem. Soc.* **2001**, *123*, 4304.

Lampe, F. W.; Franklin, J. L.; Field, F. H. *J. Am. Chem. Soc.* **1957**, *79*, 6129.

Lander, D. R.; Unfried, K. G.; Glass, G. P.; Curl, R. F. *J. Phys. Chem.* **1990**, *94*, 7759.

Lange, A.; Herbert, J. M. *J. Chem. Theory Comp.* **2007**, *3*, 1680.

Laufer, A. H.; Fahr, A. *Chem. Rev.* **2004**, *104*, 2813.

Leclerc, M. *J. Polym. Sci A: Polym. Chem.* **2001**, *39*, 2867.

Lee, S.; Samuels, D. A.; Hoobler, R. J.; Leone, S. R. *J. Geophys. Res.* **2000**, *105*, 15085.

Letokhov, V. S. *Laser Photoionization Spectroscopy*; Academic Press, Inc.: Orlando, FL, **1987**.

Leutwyler, S.; Even, U.; Jortner, J. *Chem. Phys. Lett.* **1980**, *74*, 11.

Leutwyler, S.; Even, U.; Jortner, J. *J. Phys. Chem.* **1981**, *85*, 3026.

Levenson, M. D. *Introduction to Nonlinear Laser Spectroscopy*; Academic Press: New York, NY, **1982**.

Levine, I. N. *Physical Chemistry*, 5th ed.; McGraw-Hill: New York, NY, **2002**.

Lewerenz, M.; Schilling, B.; Toennies, J. P. *Chem. Phys. Lett.* **1993**, *206*, 381.

Lewerenz, M.; Schilling, B.; Toennies, J. P. *J. Chem. Phys.* **1995**, *102*, 8191.

Liu, X. D.; Feng, J. K.; Ren, A. M.; Yang, L.; Yang, B.; Ma, Y. G. *Opt. Mater.* **2006**, *29*, 231.

Livshits, E.; Baer, R. *Phys. Chem. Chem. Phys.* **2007**, *9*, 2932.

Loginov, E.; Rossi, D.; Drabbels, M. *Phys. Rev. Lett.* **2005**, *95*, 163401.

Look, H. V.; Peeters, J. *J. Phys. Chem.* **1995**, *99*, 16284.

Loomis, R. A.; Schwartz, R. L.; Lester, M. I. *J. Chem. Phys.* **1996**, *104*, 6984.

Mark, T. D.; Dunn, G. H. *Electron Impact Ionization*; Springer-Verlag / Wien: New York, NY, **1985**.

Mataga, N.; Kubota, T. *Molecular Interactions and Electronic Spectra*; Marcel Dekker: New York, NY, **1970**; pp. 371 – 410.

Matsushita, T.; Asada, T.; Koseki, S. *J. Phys. Chem. C* **2007**, *111*, 6897.

McCarthy, M. C.; Chen, W.; Travers, M. J.; Thaddeus, P. *Astrophys. J. Suppl. Ser.* **2000**, *129*, 611.

McHale, J. L. *Molecular Spectroscopy*. Prentice Hall: Upper Saddle River, NJ, **1999**.

McMurry, J. *Organic Chemistry*, 6th ed.; Thomas Learning: Belmont, CA, **2004**.

Mebel, A. M.; Hayashi, M.; Jackson, W. M.; Wrobel, J.; Green, M.; Xu, D.; Lin, S. H. *J. Chem. Phys.* **2001**, *114*, 9821.

Miller, D. R. *Atomic and Molecular Beams Methods*; Scoles, G. Ed.; Oxford University Press: New York, NY, **1988**; Vol. I; pp. 14 – 53.

Mordaunt, D. H.; Ashfold, M. N. R. *J. Chem. Phys.* **1994**, *101*, 2630.

Nemirow, C. *Multiphoton Investigation of tris(2-phenylpyridine)iridium*. Ph. D. Dissertation, University of Southern California, Los Angeles, CA, **2011**.

Nizamov, B; Leone, S. R. *J. Phys. Chem. A* **2004**, *108*, 1746.

Northby, J. A. *J. Chem. Phys.* **2001**, *115*, 10065.

Nozaki, K. *J. Chin. Chem. Soc.* **2006**, *53*, 101.

Nozaki, K.; Takamori, K.; Nakatsugawa, Y.; Ohno, T. *Inorg. Chem.* **2006**, *45*, 6161.

Onsager, L. *J. Am. Chem. Soc.* **1936**, *58*, 1486.

Opansky, B. J.; Seakins, P. W.; Pedersen, J. O. P.; Leone, S. R. *J. Phys. Chem.* **1993**, *97*, 8583.

Otvos, J. W.; Stevenson, D. P. *J. Am. Chem. Soc.* **1956**, *78*, 546.

Ow, F. P.; Djurovich, P.; Thompson, M. E.; Zink, J. I. *Inorg. Chem.* **2008**, *47*, 2389.

Padovani, M.; Walmsley, C. M.; Tafalla, M.; Galli, D.; Muller, J. S. P. *Astron. Astrophys.* **2009**, *505*, 1199.

Paisner, J. A.; Solarz, R. W.; Chen, H.; *Laser Spectroscopy and Its Applications*; Radziemski L. J.; Solarz R. W.; Paisner, J. A. Ed.; Marcel Dekker: New York, NY, **1987**; pp. 175 – 350.

Parr, R. G.; Yang, W. *Density Functional Theory of Atoms and Molecules*; Oxford University Press: New York, NY, **1989**.

Periodic Table of the Elements: <http://www.periodni.com/ir.html>.

Peterka, D. S.; Kim, J. H.; Wang, C. C.; Poisson, L.; Neumark, D. M. *J. Phys. Chem. A* **2007**, *111*, 7449.

- Petty, G; Tai, C.; Dalby, F. W. *Phys. Rev. Lett.* **1975**, *34*, 1207.
- Pfelzer, C.; Havenith, M.; Peric, M., Murtz, P., Urban, W. *J. Mol. Spectrosc.* **1996**, *176*, 28.
- Polyakova, E.; Stolyarov, D.; Zhang, X.; Kresin, V. V.; Wittig, C. *Chem. Phys. Lett.* **2003**, *375*, 253.
- QChem User's Manual, version 3.2, **2011**.
- Ramsey, N. F. *Molecular Beams*; Oxford University Press: New York, NY, **1985**.
- Rausch, A. F.; Homeier, H. H. H.; Yersin, H. *Top. Organomet. Chem.* **2010**, *29*, 193.
- Rausch, A. F.; Thompson, M. E.; Yersin, H. J. *Phys. Chem. A* **2009**, *113*, 5927.
- Reilly, J. P.; Kompa, K. L. *Adv. Mass. Spectrom.* **1980**, *9*.
- Reilly, J. P.; Kompa, K. L. *J. Chem. Phys.* **1980**, *73*, 5468.
- Renlund, A. M.; Shokoohi, F.; Reisler, H.; Wittig, C. *Chem. Phys. Lett.* **1981**, *84*, 293.
- Salzner, U.; Baer, R. *J. Chem. Phys.* **2009**, *131*, 23110.
- Saykally, R. J.; Veseth, L. *J. Chem. Phys.* **1983**, *80*, 2247.
- Scharf, D.; Jortner, J.; Landman, U. *J. Chem. Phys.* **1988**, *88*, 4273.
- Schilling, B. Ph. D Dissertation, University of Gottingen, Gottingen, Germany, **1993**.
- Schlag, E. W.; Neusser, H. J. *Acc. Chem. Res.* **1983**, *16*, 355.
- Schmied, R.; Carcabal, P.; Dokter, A. M.; Lonij, V. P. A.; Lehmann, K. K.; Scoles, G. *J. Chem. Phys.* **2004**, *121*, 2701.
- Schneider, L.; Meier, W.; Welge, K. H.; Ashfold, M. N. R.; Western, C. *J. Chem. Phys.* **1990**, *92*, 6578.
- Seki, K.; Okabe, H. *J. Phys. Chem.* **1993**, *97*, 5284.
- Shah, M. B.; Elliot, D. S.; McCallion, P.; Gilbody, H. B. *J. Phys. B.* **1988**, *21*, 2751.

Shao, Y.; Molnar, L. F.; Jung, Y.; Kussmann, J.; Ochsenfeld, C.; Brown, S. T.; Gilbert, A. T. B.; Slipchenko, L. V.; Levchenko, S. V.; O'Neill, D. P.; DiStasio, R. A.; Lochan, R. C.; Wang, T.; Beran, G. J. O.; Besley, N. A.; Herbert, J. M.; Lin, C. Y.; Van Voorhis, T.; Chien, S. H.; Sodt, A.; Steele, R. P.; Rassolov, V. A.; Maslen, P. E.; Korambath, P. P.; Adamson, R. D.; Austin, B.; Baker, J.; Byrd, E. F. C.; Dachsel, H.; Doerksen, R. J.; Dreuw, A.; Dunietz, B. D.; Dutoi, A. D.; Furlani, T. R.; Gwaltney, S. R.; Heyden, A.; Hirata, S.; Hsu, C. P.; Kedziora, G.; Khalliulin, R. Z.; Klunzinger, P.; Lee, A. M.; Lee, M. S.; Liang, W.; Lotan, I.; Nair, N.; Peters, B.; Proynov, E. I.; Pieniazek, P. A.; Rhee, Y. M.; Ritchie, J.; Rosta, E.; Sherrill, C. D.; Simmonett, A. C.; Subotnik, J. E.; Woodcock, H. L.; Zhang, W.; Bell, A. T.; Chakraborty, A. K.; Chipman, D. M.; Keil, F. J.; Warshel, A.; Hehre, W. J.; Schaefer, H. F.; Kong, J.; Krylov, A. I.; Gill, P. M. W.; Head-Gordon, M. *Phys. Chem. Chem. Phys.* **2006**, *8*, 3172.

Sharp-Williams, E. N.; Roberts, M. A.; Nesbitt, D. J. *J. Chem. Phys.* **2011**, *134*, 064314.

Slipchenko, M. N.; Kuma, S.; Momose, T.; Vilesov, A. F. *Rev. Sci. Instrum.* **2002**, *73*, 3600.

Sliter, R. *Infrared and Raman Spectroscopy of Molecules and Molecular Aggregates in Helium Droplets*, Ph. D. Dissertation, University of Southern California, Los Angeles, CA, **2011**.

Smith, G. P.; Park, C.; Schneiderman, J.; Luque, J. *Comb. and Flame* **2005**, *141*, 66.

Sorkhabi, O.; Blunt, V. M.; Lin, H.; A'Hearn, M. F.; Weaver, H. A.; Arpigny, C.; Jackson, W. M. *Sci.* **1997**, *45*, 721.

Sorkhabi, O.; Blunt, V. M.; Lin, H.; Xu, D.; Wrobel, J.; Price, R.; Jackson, W. M. *J. Chem. Phys.* **1997**, *107*, 9842.

Stampor, W.; Mezyk, J.; Kalinowski, J. *Chem. Phys.* **2004**, *300*, 189.

Stephens, J. W.; Hall, J. L.; Solka, H.; Yan, W.; Curl, R. F.; Glass, G. P. *J. Phys. Chem.* **1990**, *91*, 5740.

Stephens, J. W.; Yan, W.; Richnow, M.; Solka, H.; Curl, R. F. *J. Mol. Struct.* **1988**, *190*, 41.

Stephens, P. J.; Devlin, J. F.; Chabalowski, C. F.; Frisch, M. J. *J. Phys. Chem.* **1994**, *98*, 11623.

Stienkemeier, F.; Lehmann, K. K. *J. Phys. B* **2006**, *39*, R127.

Stienkemeier, F.; Vilesov, A. F. *J. Chem. Phys.* **2001**, *115*, 10119.

Strickler, S. J.; Berg, R. A. *J. Chem. Phys.* **1962**, *37*, 814.

Sun, Y. Y.; Lee, K.; Wang, L.; Kim, Y.; Chen, W.; Chen, Z.; Zhang, S. B. *Phys. Rev. B* **2010**, *82*, 073401.

Szabo, A.; Ostlund, N. S. *Modern Quantum Chemistry: Introduction to Advanced Electronic Structure Theory*; Dover Publications: Mineola, NY, **1996**.

Tamayo, A. B.; Alleyne, B. D.; Djurovich, P.; Lamansky, S.; Tsyba, I.; Ho, N. N.; Bau, R.; Thompson, M. E. *J. Am. Chem. Soc.* **2003**, *125*, 7377.

Tang, K.; Liu, K. L.; Chen, I. *Chem. Phys. Lett.* **2004**, *386*, 437.

Tiggesbaumker, J.; Stienkemeier, F. *Phys. Chem. Chem. Phys.* **2007**, *9*, 4748.

Tilley, R. D.; Tilley, J. *Superfluidity and Superconductivity*, 3rd ed.; Institute of Physics Publishing: Bristol, UK, **1990**.

Toennies, J. P.; Vilesov, A. F. *Angew. Chem. Int. Ed.* **2004**, *43*, 2622.

Toennies, J. P.; Vilesov, A. F. *Annu. Rev. Phys. Chem.* **1998**, *49*, 1.

Tsuboi, T. *J. Lumin.* **2006**, *119/120*, 288.

Tsuboi, T.; Alaroudi, N. *Phys. Rev. B* **2005**, *72*, 125109.

Urdahl, R. S.; Bao, Y.; Jackson, W. M. *Chem. Phys. Lett.* **1991**, *178*, 425.

Vacha, M.; Koide, Y.; Kotani, M.; Sato, H. *J. Lumin.* **2004**, *107*, 51.

Van Beek, M. C.; Ter Meulen, J. J. *Chem. Phys. Lett.* **2010**, *337*, 237.

Van Kleef, T. A. M. *Physica* **1957**, *23*, 843.

Wang, J.; Hsu, Y.; Lin, K. *J. Phys. Chem. A* **1997**, *101*, 6593.

Wannier, G. H. *Phys. Rev.* **1953**, *90*, 817.

- Watanabe, K.; Jursa, A. S. *J. Chem. Phys.* **1964**, *41*, 1650.
- Weissler, G. L. *Sci. Light.* **1972**, *21*, 89.
- Wheatley, J. *Phys. Today.* **1976**, *29*, 32.
- Wiley, W. C.; McLaren, I. H. *Rev. Sci. Instru.* **1955**, *26*, 1150.
- Wilks, J.; Betts, D. S. *An Introduction to Liquid Helium*; Oxford University Press: New York, NY, **1987**.
- Wodtke, A. M.; Lee, Y. T. *J. Phys. Chem.* **1985**, *89*, 4744.
- Wyatt, J. R.; Stafford, F. E. *J. Phys. Chem.* **1972**, *59*, 1913.
- Yan, W.; Amano, T. *J. Chem. Phys.* **1993**, *99*, 4312.
- Yan, W.; Dane, C. B.; Zeitz, D.; Hall, J. L.; Curl, R. F. *J. Mol. Spectrosc.* **1987**, *123*, 486.
- Yan, W.; Hall, J. L.; Stephens, J. W.; Richnow, M. L.; Curl, R. F. *J. Chem. Phys.* **1987**, *86*, 1657.
- Yersin, H. Ed.; *Highly Efficient OLEDs with Phosphorescent Materials*; Wiley-VCH Verlag: Weinheim, Germany, **2008**.
- Yersin, H. *Top. Curr. Chem.* **2004**, *241*, 1.
- Yersin, H.; Rausch, A. F.; Czerwieniec, R.; Hofbeck, T.; Fischer, T. *Coordin. Chem. Rev.* **2011**, *255*, 2622.
- Zhang, J.; Reihn, C. W.; Dulligan, M.; Wittig, C. *J. Chem. Phys.* **1995**, *103*, 6815.
- Zheng, S. H.; Srivastava, S. K. *J. Phys. B.* **1996**, *29*, 3235.

Appendix A

A brief introduction to density functional theory

The ultimate goal of most quantum calculations is to find an approximate solution to the time-independent Schrödinger equation:¹

$$H\Psi_i = E_i\Psi_i \quad (\text{A.1})$$

Here, \hat{H} is the Hamiltonian, Ψ_i is the i^{th} state wave function, and E_i is the i^{th} state energy of the system. Most conventional methods, i.e. wave function based methods, build upon the Hartree-Fock (HF) approximation to determine the “best” ground state wave function Ψ_0 .² From Ψ_0 , E_0 and all other system properties may be determined. In contrast, density functional theory (DFT) uses electron density, not wave functions, to describe the system.

The appeal of using electron density over wave functions lies in its simplicity. In general, wave functions are very complicated and depend on $4N$ variables, where N is the number of electrons in the system, while the electron density depends only on three spatial variables.³ Consequently, DFT calculations have a computation cost that is comparable self-consistent field (SCF) single particle calculations⁴ with an accuracy comparable to MP2.⁵ This makes electronic calculations on large and/or complicated systems tractable, and is the reason the use of DFT has increased dramatically over the last 40 years.⁶

The entire field of density functional theory rests on two fundamental theorems proved by Kohn and Hohenberg⁷ and a set of equations derived by Kohn and Sham.⁸ The first theorem states: *The ground-state energy from Schrodinger's equation is a unique functional of the electron density.*

To fully appreciate the above theorem requires understanding the nature of a “functional”. First, consider an arbitrary function of n variables $f(\mathbf{x})$. The function $f(\mathbf{x})$ takes n independent variables as its argument and returns a unique value $f(\mathbf{x})$. Similarly, a functional of the form $F[f(\mathbf{x})]$ returns a number when $f(\mathbf{x})$ is used as the argument. For example:

$$F[f(x)] = \int_{-1}^1 f(x) dx \quad (\text{A.2})$$

is a functional of $f(\mathbf{x})$. Theorem 1 may now be restated as: *The ground state energy from Schrödinger's equation E can be uniquely expressed as $E[\rho(\mathbf{r})]$, where $\rho(\mathbf{r})$ is the electron density of the system.* Once the energy is determined, all other system properties follow.

Although theorem 1 proves the existence of this energy functional, it does not provide further information about the functional. However, the second theorem by Hohenberg and Kohn defines an important property of the functional: *The electron density that minimizes the energy of the overall functional is the true electron density corresponding to the full solution of the Schrödinger equation.* Hence, if the “true” energy functional form were known, varying the electron density until the energy is minimized would reveal the exact solution to the Schrödinger equation.

Both Hohenberg-Kohn theorems may be written as:

$$E_0 = \min_{\rho \rightarrow N} \left(T[\rho(\vec{r})] + J[\rho(\vec{r})] + E_{ncl}[\rho(\vec{r})] + \int \rho(\vec{r}) V_{ncl} d\vec{r} \right) \quad (\text{A.3})$$

where E_0 is the ground state energy, and the four terms on the right are functionals for the electron kinetic energy, coulomb interaction between electrons, coulomb interaction between nuclei, and interaction between electrons and nuclei, respectively. Note that equation A.3 is written in atomic units, as are all equations in this appendix, and employs the Born-Oppenheimer approximation. Of these terms, only $J[\rho(\mathbf{r})]$ and the electron-nuclei interaction term are known. The explicit forms of the other two contributions are unknown.

To address the unknown forms of the kinetic and nuclear functionals, Kohn and Sham concentrated on computing everything that is known exactly and finding approximate forms for everything else. They achieved this by using the kinetic energy of a non-interacting system and combining all other unknown terms into one functional:⁸

$$E[\rho(\vec{r})] = T_s[\Phi_{SD}] + J[\rho(\vec{r})] + \int \rho(\vec{r}) V_{ncl} d\vec{r} + E_{xc}[\rho(\vec{r})] \quad (\text{A.4})$$

where $E[\rho(\mathbf{r})]$ is the energy of the real interacting system, $T_s[\Phi_{SD}]$ is the Hartree-Fock electron kinetic energy, and $E_{xc}[\rho(\mathbf{r})]$ is the *exchange-correlation* energy that accounts for everything unknown. In practice, $E_{xc}[\rho(\mathbf{r})]$ is separated into $E_x[\rho(\mathbf{r})] + E_c[\rho(\mathbf{r})]$. However, we shall keep the form $E_{xc}[\rho(\mathbf{r})]$ for the sake of simplicity. Note that $T_s[\Phi_{SD}]$ uses Slater determinants, which are exact wave functions for a non-

interacting system.³ Applying the variational principle to equation A.4 yields the following self-consistent equations:⁹

$$\left(-\frac{1}{2}\nabla^2 + \int \frac{\rho(\vec{r}_2)}{r_{12}} d\vec{r}_2 + V_{XC}(\vec{r}_1) - \sum_A^M \frac{Z_A}{r_{1A}} \right) \Phi_{SDi} = \varepsilon_i \Phi_{SDi} \quad (\text{A.5})$$

where V_{XC} is the exchange-correlation potential defined as $\delta E_{XC}/\delta\rho$. Analogous to the Hartree-Fock equations, A.5 represents a pseudo-eigenvalue problem than must be solved iteratively.³ It is important to observe that no approximations, aside from Born-Oppenheimer, have been made, i.e. the Kohn-Sham approach is in principle exact. The approximation enters when a derived form of V_{XC} , and consequently E_{XC} , is used. Hence, the perpetual challenge to improving DFT methods is finding better approximations to the exchange-correlation functional.

Virtually all approximate exchange-correlation functionals are based upon the local density approximation (LDA), which treats electron density as a uniform electron gas. In this system, electrons move over a positive charge distribution created by the nuclei such that the total ensemble is electrically neutral. This approximation allows E_{XC} to be written as:⁸

$$E_{XC}^{LDA}[\rho(\vec{r})] = \int \rho(\vec{r}) \varepsilon_{XC}(\rho(\vec{r})) d\vec{r} \quad (\text{A.6})$$

Here, ε_{XC} is the exchange-correlation energy per particle of a uniform electron gas with density $\rho(\mathbf{r})$. Another interpretation to equation A.6 is the term $\rho(\mathbf{r})\varepsilon_{XC}$ is the weighted probability of finding electron density at the point in space \mathbf{r} . In the unrestricted case, the electron density is split into $\rho(\mathbf{r})_\alpha$ and $\rho(\mathbf{r})_\beta$ that extends LDA

to the local spin-density approximation (LSDA).³ For the most part, DFT coupled with LDA/LSDA performs as well as to slightly better than the Hartree-Fock approach.

The next logical step to improve LDA/LSDA was to consider not only the electron density, but also the gradient of the electron density. In other words, LDA/LSDA accounts for only the first term of a Taylor expansion of the density. Thus, incorporating higher order terms should produce more accurate approximations. Unfortunately, simply incorporating gradients in the electron density does not lead to improved accuracy. Blindly introducing higher order terms removes the error cancelation that contributes to the accuracy of LDA/LSDA, and distorts the physical picture that makes LDA/LSDA meaningful. For example, the sum rule no longer applies, i.e. spatial integration of an exchange-correlation hole (the repulsive cavity created by an electron's density) does not yield the charge of an electron.³ However, by forcing these "holes" to obey the appropriate sum constraints we arrive at the workhorses of DFT collectively known as generalized gradient approximations (GGA) functionals. GGA functionals are of a general form:³

$$E_{XC}^{GGA}[\rho_{\alpha}(\vec{r}), \rho_{\beta}(\vec{r})] = \int f[\rho_{\alpha}(\vec{r}), \rho_{\beta}(\vec{r}), \nabla\rho_{\alpha}(\vec{r}), \nabla\rho_{\beta}(\vec{r})] d\vec{r} \quad (\text{A.7})$$

where $f[\rho(\mathbf{r})_{\alpha}, \rho(\mathbf{r})_{\beta}, \nabla\rho(\mathbf{r})_{\alpha}, \nabla\rho(\mathbf{r})_{\beta}]$ is some functional. These functionals are complex mathematical constructs that have been chosen to satisfy the appropriate boundary conditions. In addition, it is often the results and not the underlying physics that govern the choice of these constructs.³ In this sense, it is difficult to

draw a physical picture from the form of the GGA exchange-correlation functional. However, this permits different functionals to be mixed and matched in order to achieve better results. The collection of exchange and correlation functionals is further expanded by combining GGA, LDA, and HF treatments to achieve what are collectively known as hybrid functionals.

Currently, the most popular hybrid functional is B3LYP that was suggested by Stephens et al.¹⁰ B3LYP uses various GGA and LSD functionals weighted by semi-empirical coefficients determined by Becke.¹¹ The success of B3LYP is fueled by its good performance, even with difficult open-shell transition-metal chemistry.³ However, approximate functionals, including B3LYP, are prone to self-interaction errors, i.e. where an electron contributes to a bulk potential that then acts on this electron creating an artificial self-interaction.³ Long-range corrected functionals (LRC), like those used in chapter 4, implement 100% Hartree-Fock exchange for the long-range Coulomb interaction, which mitigates this self-interaction. The impressive results achieved by LRC functionals mean that they will likely replace B3LYP as the front runners of modern density functional theory.

Appendix B

Supplementary Material for Chapter 4

The data used to construct tables and figures in Chapter 4 are given here beginning with the z -matrices and Cartesian coordinates for the S_0 , T_1 , and D_0 equilibrium geometries. Next are the Mulliken charges and spin densities for each cation at its respective geometry. The Mulliken analysis is followed by the ground state "shell populations" of the first six HOMO's (*i.e.*, HOMO, HOMO-1, etc.) to show the atomic contributions to each molecular orbital. How the populations were computed is also given. Next, the results of the BNL and ω B97X TDDFT calculations at the S_0 equilibrium geometry are listed. The table contains only singlets. Without SOC, only excited singlets have oscillator strength with S_0 and therefore were used to construct the absorption spectrum. Finally, the $\text{Ir}(\text{ppy})_3$ S_0 vibrational frequencies are listed.

Z-matrices for equilibrium geometries

The columns for the z -matrices below are labeled as follows: (a) atom number; (b) atom; (c) bond length (\AA); (d) atom to which the current atom is connected; (e) bond angle; (f) center atom of dihedral angle; (g) dihedral angle.

Table B.1. Z-matrix for S₀ equilibrium geometry

a	b	c	d	e	f	g
1	Ir					
2	C1	2.022446				
3	C2	1.404535	1	127.565023		
4	H3	1.086057	2	119.014367	1	-1.067994
5	C3	1.387399	2	121.818939	1	179.561533
6	H5	1.087104	3	119.631649	2	179.855448
7	C5	1.395346	3	120.748027	2	-0.320281
8	H7	1.085402	5	120.698815	3	-179.833071
9	C7	1.383408	5	119.052468	3	0.519936
10	H9	1.086494	7	118.926866	5	179.978896
11	C9	1.40044	7	120.235889	5	-0.185909
12	C11	1.471922	9	122.188246	7	178.02043
13	N12	1.351975	11	114.828365	9	179.151581
14	C13	1.338578	12	119.930566	11	178.007835
15	H14	1.085953	13	115.838605	12	-179.003959
16	C14	1.38071	13	122.866282	12	0.651586
17	H16	1.08346	14	120.14115	13	-179.324622
18	C16	1.392298	14	118.020707	13	-0.249991
19	H18	1.085439	16	120.488133	14	-179.336428
20	C18	1.381226	16	119.329149	14	0.062421
21	H20	1.082865	18	120.266689	16	-179.142522
22	C1	2.023439	2	96.036581	3	-5.444014
23	C22	1.403829	1	127.705969	2	91.780995
24	H23	1.086156	22	119.033759	1	-0.783377
25	C23	1.387452	22	121.840061	1	179.507891
26	H25	1.086935	23	119.705857	22	179.712337
27	C25	1.395262	23	120.690302	22	-0.123281
28	H27	1.085416	25	120.589475	23	-179.727328
29	C27	1.383189	25	119.090049	23	0.218533
30	H29	1.086567	27	118.919163	25	179.829061
31	C29	1.400286	27	120.262687	25	-0.10011
32	C31	1.471926	29	122.155867	27	179.115507
33	N32	1.351564	31	114.734591	29	179.099383
34	C33	1.338089	32	120.057407	31	179.213868
35	H34	1.085925	33	115.557917	32	-179.1191
36	C34	1.380783	33	122.89688	32	0.659773
37	H36	1.083358	34	120.186413	33	-179.950613
38	C36	1.392892	34	117.911438	33	-0.356574

39	H38	1.085431	36	120.558013	34	-179.717481
40	C38	1.381691	36	119.368437	34	-0.043381
41	H40	1.082915	38	120.284676	36	-179.556678
42	C1	2.025406	2	95.836638	3	91.384582
43	C42	1.404896	1	127.962451	2	-6.063495
44	H43	1.086302	42	119.058801	1	-0.730982
45	C43	1.387625	42	121.842466	1	179.720178
46	H45	1.087138	43	119.65475	42	179.869153
47	C45	1.395255	43	120.764884	42	-0.106873
48	H47	1.085067	45	120.748387	43	-179.838192
49	C47	1.383039	45	119.012315	43	0.177612
50	H49	1.086349	47	118.797538	45	179.708626
51	C49	1.399849	47	120.273082	45	-0.074407
52	C51	1.471557	49	121.972814	47	178.717392
53	N52	1.351521	51	114.952042	49	-179.195048
54	C53	1.338537	52	119.878729	51	178.511114
55	H54	1.08596	53	115.815578	52	-178.840661
56	C54	1.381082	53	122.951127	52	1.019915
57	H56	1.083308	54	120.166103	53	179.946922
58	C56	1.392764	54	117.958418	53	-0.210127
59	H58	1.085376	56	120.417102	54	179.825177
60	C58	1.380813	56	119.287692	54	-0.413776
61	H60	1.082728	58	120.26533	56	-179.616612

Table B.2. S₀ Standard Nuclear Orientation (Å)

I	Atom	X	Y	Z
1	Ir	0.009744	-0.002078	-0.021299
2	N	-0.608071	-1.778575	1.056498
3	C	0.019125	-2.317207	2.109200
4	C	-0.434933	-3.450358	2.755102
5	C	-1.596253	-4.052997	2.277660
6	C	-2.239470	-3.508159	1.184011
7	C	-1.727121	-2.359543	0.569866
8	C	-2.308099	-1.697308	-0.608857
9	C	-1.625113	-0.552554	-1.082660
10	C	-2.162288	0.064801	-2.224610
11	C	-3.300666	-0.420671	-2.852233
12	C	-3.958657	-1.549735	-2.363354
13	C	-3.457659	-2.184897	-1.241585
14	H	-3.969969	-3.066483	-0.866752
15	H	-4.850301	-1.927592	-2.852809
16	H	-3.684592	0.083864	-3.735361
17	H	-1.668277	0.942502	-2.631610
18	H	-3.139927	-3.967316	0.795872
19	H	-1.990155	-4.943611	2.756920
20	H	0.108208	-3.847540	3.604102
21	H	0.921935	-1.808004	2.433169
22	C	1.332213	-1.124314	-1.063396
23	C	1.086657	-1.898528	-2.208400
24	C	2.089511	-2.633918	-2.823631
25	C	3.389280	-2.629399	-2.316344
26	C	3.669114	-1.876284	-1.190413
27	C	2.658226	-1.131808	-0.570201
28	C	2.913637	-0.301296	0.617897
29	N	1.827147	0.338185	1.105063
30	C	1.941607	1.134726	2.174130
31	C	3.137347	1.336397	2.834506
32	C	4.267600	0.681232	2.351357
33	C	4.155188	-0.135829	1.242823
34	H	5.025680	-0.646650	0.850378
35	H	5.230500	0.812626	2.834802
36	H	3.180073	1.992021	3.695899
37	H	1.026257	1.623361	2.494446
38	H	4.682869	-1.872554	-0.799371
39	H	4.171579	-3.208797	-2.796381
40	H	1.861737	-3.217830	-3.711658

41	H	0.084369	-1.918190	-2.626453
42	N	-1.230786	1.390032	1.086333
43	C	-2.033819	1.076433	2.110337
44	C	-2.847243	2.000825	2.734999
45	C	-2.826515	3.312066	2.267333
46	C	-2.002309	3.639788	1.208529
47	C	-1.203552	2.656418	0.613723
48	C	-0.316411	2.865866	-0.541988
49	C	0.343853	1.716043	-1.034570
50	C	1.157088	1.899198	-2.164978
51	C	1.308368	3.141572	-2.763725
52	C	0.655398	4.263929	-2.252906
53	C	-0.157674	4.120865	-1.142832
54	H	-0.665404	4.996074	-0.746992
55	H	0.776450	5.236008	-2.720353
56	H	1.945065	3.242408	-3.639079
57	H	1.673257	1.041909	-2.587052
58	H	-1.984488	4.651788	0.823643
59	H	-3.457899	4.068940	2.721947
60	H	-3.488434	1.696114	3.553480
61	H	-2.015386	0.037309	2.425260

Table B.3. Z-matrix for T₁ equilibrium geometry

a	b	c	d	e	fg	
1	Ir					
2	C1	1.960661				
3	C2	1.408154	1	128.96714		
4	H3	1.085789	2	118.243755	1	0.124374
5	C3	1.379839	2	122.370014	1	-179.297635
6	H5	1.084579	3	120.935203	2	179.753881
7	C5	1.429032	3	119.430973	2	-0.088252
8	H7	1.087169	5	118.897993	3	179.848727
9	C7	1.363612	5	122.001244	3	0.006373
10	H9	1.084499	7	119.706094	5	179.960207
11	C9	1.433843	7	120.006217	5	-0.125189
12	C11	1.400328	9	124.021502	7	-179.366043
13	N12	1.400585	11	115.278922	9	179.786797
14	C13	1.330822	12	119.276906	11	179.052245
15	H14	1.087486	13	115.702095	12	-179.087045
16	C14	1.38451	13	123.767747	12	1.150541
17	H16	1.082828	14	120.014681	13	179.700867
18	C16	1.421257	14	118.231809	13	-0.843532
19	H18	1.084981	16	120.42283	14	-179.491423
20	C18	1.362857	16	119.24321	14	0.093647
21	H20	1.084004	18	120.107639	16	-179.37437
22	C1	2.025169	2	95.401004	3	91.310713
23	C22	1.403115	1	127.342268	2	-3.710646
24	H23	1.086312	22	119.071393	1	-1.589484
25	C23	1.387298	22	121.783782	1	178.859141
26	H25	1.086636	23	119.628007	22	-179.711743
27	C25	1.394247	23	120.663747	22	-0.119468
28	H27	1.084953	25	120.722903	23	-179.835254
29	C27	1.382948	25	119.027274	23	0.365129
30	H29	1.086151	27	118.78023	25	-179.763564
31	C29	1.399425	27	120.444523	25	-0.157718
32	C31	1.471801	29	121.948281	27	179.102605
33	N32	1.349496	31	115.066231	29	178.559079
34	C33	1.338077	32	120.036219	31	178.839851
35	H34	1.08598	33	116.020165	32	-179.358325
36	C34	1.380466	33	122.794331	32	0.617333
37	H36	1.083233	34	120.271759	33	-179.819315
38	C36	1.392573	34	117.999069	33	-0.438103
39	H38	1.085314	36	120.427105	34	-179.682301

40	C38	1.38067	36	119.347159	34	0.129568
41	H40	1.082587	38	120.232196	36	-179.263148
42	C1	2.036201	2	95.584561	3	-5.732148
43	C42	1.403042	1	128.605627	2	88.896672
44	H43	1.086882	42	119.272166	1	-0.713106
45	C43	1.388907	42	121.790322	1	179.683617
46	H45	1.086821	43	119.745462	42	179.607431
47	C45	1.394412	43	120.706731	42	-0.133669
48	H47	1.08513	45	120.691654	43	179.914261
49	C47	1.382896	45	119.05978	43	-0.031183
50	H49	1.085933	47	118.814828	45	179.729695
51	C49	1.399237	47	120.283478	45	0.027783
52	C51	1.473492	49	121.576817	47	179.539649
53	N52	1.350621	51	115.493367	49	179.750349
54	C53	1.339431	52	120.333182	51	179.614085
55	H54	1.086279	53	115.626035	52	-179.125507
56	C54	1.381092	53	122.500547	52	0.53632
57	H56	1.083272	54	120.252439	53	179.994659
58	C56	1.392739	54	118.051494	53	-0.217558
59	H58	1.085458	56	120.521957	54	-179.758594
60	C58	1.380581	56	119.449001	54	-0.07276
61	H60	1.082446	58	120.135859	56	-179.805464

Table B.4. T₁ Standard Nuclear Orientation (Å)

I	Atom	X	Y	Z
1	Ir	-0.019227	0.023884	-0.051622
2	N	0.893739	-1.623116	1.077766
3	C	1.755509	-1.503129	2.094331
4	C	2.319714	-2.591681	2.728694
5	C	1.975841	-3.862878	2.275851
6	C	1.091588	-3.989943	1.223140
7	C	0.551501	-2.846790	0.623198
8	C	-0.382256	-2.850687	-0.514466
9	C	-0.770644	-1.588997	-1.018731
10	C	-1.642146	-1.592270	-2.118369
11	C	-2.105927	-2.773139	-2.679663
12	C	-1.717713	-4.007623	-2.160756
13	C	-0.855237	-4.040072	-1.080186
14	H	-0.558498	-5.003857	-0.676715
15	H	-2.081935	-4.931684	-2.597304
16	H	-2.783755	-2.734747	-3.528104
17	H	-1.956184	-0.644248	-2.545815
18	H	0.823514	-4.970885	0.851814
19	H	2.400130	-4.746061	2.742621
20	H	3.015528	-2.447114	3.546212
21	H	1.993133	-0.488575	2.400222
22	C	1.694555	0.166410	-1.141921
23	C	2.065081	-0.552469	-2.288415
24	C	3.283618	-0.343227	-2.921227
25	C	4.188918	0.596728	-2.430004
26	C	3.857921	1.321192	-1.299520
27	C	2.630638	1.111193	-0.661132
28	C	2.244680	1.874037	0.538987
29	N	1.035796	1.568588	1.058100
30	C	0.584950	2.208745	2.144844
31	C	1.318279	3.186781	2.787566
32	C	2.570418	3.511853	2.271626
33	C	3.032642	2.856187	1.148035
34	H	4.002806	3.102245	0.735814
35	H	3.179005	4.277276	2.742760
36	H	0.918107	3.681311	3.664367
37	H	-0.402238	1.913147	2.488474
38	H	4.563995	2.055308	-0.922979
39	H	5.140288	0.760990	-2.925405
40	H	3.534064	-0.914363	-3.811317

41	H	1.379275	-1.289267	-2.698426
42	N	-1.775668	0.120657	1.165225
43	C	-2.049171	-0.558752	2.276390
44	C	-3.232958	-0.433366	2.983353
45	C	-4.221508	0.458744	2.486484
46	C	-3.973856	1.156620	1.342362
47	C	-2.733284	1.002356	0.648294
48	C	-2.366623	1.657422	-0.533808
49	C	-1.020118	1.347815	-1.095470
50	C	-0.640935	2.015056	-2.276108
51	C	-1.466710	2.920048	-2.910965
52	C	-2.755138	3.201201	-2.360476
53	C	-3.200348	2.600818	-1.219966
54	H	-4.185364	2.841419	-0.835267
55	H	-3.399668	3.913803	-2.869118
56	H	-1.152448	3.417911	-3.821835
57	H	0.334609	1.795933	-2.699470
58	H	-4.722003	1.833190	0.945385
59	H	-5.165515	0.578311	3.007771
60	H	-3.389879	-1.013306	3.884221
61	H	-1.271255	-1.237783	2.617547

Table B.5. Z-matrix for D₀ equilibrium geometry

a	b	c	d	e	f	g
1	Ir					
2	C1	1.974711				
3	C2	1.40894	1	126.643255		
4	H3	1.084614	2	119.419379	1	0.218888
5	C3	1.386076	2	121.094457	1	-178.57675
6	H5	1.08502	3	119.963632	2	178.970535
7	C5	1.393602	3	120.165421	2	-0.927248
8	H7	1.084925	5	120.11332	3	-179.885853
9	C7	1.390587	5	120.247837	3	0.045584
10	H9	1.084663	7	118.842088	5	-179.50194
11	C9	1.389786	7	120.07878	5	0.456065
12	C11	1.476088	9	122.595944	7	179.79467
13	N12	1.349129	11	114.647528	9	178.94898
14	C13	1.337913	12	120.041109	11	177.878772
15	H14	1.08571	13	116.149977	12	-178.436872
16	C14	1.382076	13	122.340242	12	0.937388
17	H16	1.082999	14	120.050129	13	-179.473234
18	C16	1.390471	14	118.303661	13	-0.145721
19	H18	1.084686	16	120.540223	14	-179.542025
20	C18	1.383778	16	119.365489	14	-0.323638
21	H20	1.08269	18	120.083887	16	-179.496106
22	C1	2.027768	2	96.494738	3	-1.801654
23	C22	1.395284	1	126.868788	2	90.129443
24	H23	1.085736	22	119.653594	1	0.348033
25	C23	1.389926	22	120.929722	1	-179.341689
26	H25	1.085904	23	119.710962	22	179.685182
27	C25	1.393044	23	120.611962	22	-0.060733
28	H27	1.084666	25	120.352201	23	179.660108
29	C27	1.384611	25	119.568993	23	-0.453817
30	H29	1.085827	27	118.983416	25	-179.985795
31	C29	1.398846	27	120.006861	25	0.295549
32	C31	1.471277	29	122.698297	27	-179.371387
33	N32	1.3543	31	114.904961	29	179.74008
34	C33	1.342619	32	120.700238	31	-179.903085
35	H34	1.085402	33	115.968366	32	-179.434184
36	C34	1.376406	33	122.337289	32	0.682323
37	H36	1.082799	34	120.198209	33	179.925475
38	C36	1.394787	34	117.973166	33	-0.410128
39	H38	1.084961	36	120.172208	34	179.888403

40	C38	1.381617	36	119.751984	34	-0.026752
41	H40	1.082653	38	120.281552	36	-179.775089
42	C1	2.035182	2	99.631309	3	97.266787
43	C42	1.397774	1	125.451998	2	-3.072514
44	H43	1.085207	42	120.115306	1	-1.454419
45	C43	1.389832	42	120.955679	1	179.277084
46	H45	1.085715	43	119.467118	42	179.674354
47	C45	1.39127	43	120.619436	42	-0.309973
48	H47	1.084262	45	120.533648	43	-179.927733
49	C47	1.384233	45	119.307237	43	0.115892
50	H49	1.085181	47	119.000234	45	-179.968059
51	C49	1.397569	47	120.403449	45	0.005916
52	C51	1.472585	49	122.530193	47	179.853375
53	N52	1.350962	51	114.977915	49	178.956408
54	C53	1.340872	52	119.832164	51	178.81841
55	H54	1.084632	53	116.553053	52	-179.026785
56	C54	1.379442	53	122.714935	52	0.992874
57	H56	1.082908	54	119.982881	53	179.907089
58	C56	1.391889	54	118.173559	53	-0.359192
59	H58	1.084846	56	120.597908	54	-179.945839
60	C58	1.38163	56	119.248686	54	-0.214533
61	H60	1.08247	58	120.263845	56	-179.473843

Table B.6. D₀ Standard Nuclear Orientation (Å)

I	Atom	X	Y	Z
1	Ir	0.011572	-0.059961	-0.067414
2	N	-1.322670	-1.231929	1.143560
3	C	-1.000718	-1.806498	2.313535
4	C	-1.901031	-2.552422	3.039845
5	C	-3.186087	-2.712962	2.521875
6	C	-3.516157	-2.129622	1.313722
7	C	-2.562646	-1.378859	0.619154
8	C	-2.777291	-0.694105	-0.665250
9	C	-1.678231	0.021747	-1.185329
10	C	-1.852670	0.703174	-2.390338
11	C	-3.068040	0.664313	-3.063584
12	C	-4.142127	-0.057158	-2.547456
13	C	-3.997706	-0.733202	-1.347767
14	H	-4.841132	-1.292373	-0.954090
15	H	-5.087007	-0.089110	-3.079133
16	H	-3.180385	1.197832	-4.002693
17	H	-1.027153	1.268239	-2.812294
18	H	-4.509980	-2.251732	0.901968
19	H	-3.924750	-3.292442	3.065675
20	H	-1.604495	-2.999502	3.980397
21	H	0.016251	-1.646729	2.657550
22	C	0.770606	-1.667540	-0.927088
23	C	0.212269	-2.390438	-1.999837
24	C	0.861346	-3.491664	-2.535755
25	C	2.077777	-3.915065	-2.003636
26	C	2.648462	-3.235554	-0.932973
27	C	2.011629	-2.123845	-0.394409
28	C	2.569270	-1.359035	0.738259
29	N	1.807825	-0.322950	1.146766
30	C	2.230995	0.469210	2.138442
31	C	3.431010	0.259620	2.791262
32	C	4.219610	-0.814012	2.392724
33	C	3.786671	-1.627709	1.360589
34	H	4.395282	-2.462022	1.035423
35	H	5.171608	-1.007669	2.875156
36	H	3.741479	0.929337	3.583710
37	H	1.580946	1.298996	2.398553
38	H	3.591800	-3.589666	-0.531462
39	H	2.584192	-4.778252	-2.422580
40	H	0.422758	-4.024944	-3.372727

41	H	-0.731704	-2.067900	-2.425597
42	N	-0.678644	1.784838	0.941196
43	C	-1.594851	1.862228	1.917165
44	C	-1.990340	3.060171	2.475180
45	C	-1.413846	4.231773	1.993144
46	C	-0.478051	4.156253	0.979496
47	C	-0.119108	2.913689	0.453635
48	C	0.852706	2.706743	-0.633223
49	C	1.062096	1.379779	-1.050019
50	C	1.980068	1.153395	-2.079508
51	C	2.658517	2.208858	-2.677285
52	C	2.442851	3.517893	-2.258302
53	C	1.540584	3.762640	-1.237462
54	H	1.376597	4.785506	-0.914241
55	H	2.973763	4.340144	-2.724840
56	H	3.362415	2.005850	-3.478592
57	H	2.164311	0.143880	-2.432509
58	H	-0.025611	5.057664	0.586435
59	H	-1.696630	5.195579	2.403024
60	H	-2.733407	3.071115	3.262848
61	H	-2.021149	0.924731	2.257451

Table B.7. Shell populations of first six HOMO's at S_0 equilibrium geometry

			HOMO-5	HOMO-4	HOMO-3	HOMO-2	HOMO-1	HOMO
1	Ir	s	0.00167	0	0	0	0.00001	0.00441
2	Ir	p	0.00113	0.00058	0.00065	0.00644	0.00657	0.00087
3	Ir	d	0.06378	0.04395	0.04375	0.96495	0.95605	1.15212
4	N1	s	0.00037	0.0000 8	0.00007	0.00118	0.00069	0.00152
5	N1	p	0.01643	0.04729	0.001	0.01165	0.01322	0.01347
6	N1	d	0.00051	0.00087	0.00015	0.00226	0.00221	0.00245
7	C1	s	0.00001	0.00002	0.00003	0.0001	0.00091	0.00124
8	C1	p	0.02855	0.03185	0.00173	0.02701	0.00365	0.00508
9	C1	d	0.00203	0.00491	0.00003	0.00059	0.00114	0.00083
10	C2	s	0	0.00001	0	0.0001	0.00024	0.00006
11	C2	p	0.0519	0.10676	0.0001	0.00402	0.01016	0.01062
12	C2	d	0.00061	0.00043	0.0001	0.0016	0.00012	0.00032
13	C3	s	0.00001	0	0	0.00001	0.00001	0.00006
14	C3	p	0.00185	0.00007	0.00152	0.02634	0.00071	0.00644
15	C3	d	0.00295	0.00549	0.00002	0.00042	0.00055	0.00052
16	C4	s	0.00005	0.00001	0	0.00003	0.00001	0.00011
17	C4	p	0.05623	0.09226	0.00089	0.00997	0.00693	0.00592
18	C4	d	0.00018	0.00058	0.00005	0.00147	0.00018	0.00062
19	C5	s	0.0001	0.00001	0	0.00004	0.00026	0.00036
20	C5	p	0.01386	0.03559	0.00079	0.01828	0.00362	0.00988
21	C5	d	0.00415	0.00931	0.00007	0.00154	0.00177	0.00227
22	C6	s	0.00007	0.00002	0.00006	0.00002	0.00132	0.00106
23	C6	p	0.10047	0.21913	0.00066	0.06042	0.04699	0.05043
24	C6	d	0.00198	0.00337	0.00012	0.00092	0.00093	0.00105
25	C7	s	0.00028	0.00007	0.00001	0.00001	0.00164	0.00039
26	C7	p	0.01024	0.02447	0.00178	0.02877	0.03786	0.03299
27	C7	d	0.00446	0.00814	0.00045	0.01064	0.01279	0.01143
28	C8	s	0.00012	0.00003	0.00015	0.00002	0.0008	0.00076
29	C8	p	0.10269	0.14665	0.00512	0.08618	0.03901	0.03369
30	C8	d	0.00243	0.00591	0.00003	0.00053	0.00083	0.0008
31	C9	s	0.0000 8	0.00002	0.00003	0.00001	0.00019	0.00012
32	C9	p	0.13294	0.28442	0.00038	0.00054	0.00715	0.00664
33	C9	d	0.00117	0.00128	0.00018	0.00528	0.00284	0.00256
34	C10	s	0.00001	0	0	0	0.0000 4	0.00001
35	C10	p	0.00055	0.00874	0.00314	0.10862	0.04863	0.05056
36	C10	d	0.0056	0.01091	0.0000	0.00023	0.00007	0.00007

					8			
37	C11	s	0.00001	0.00001	0.00001	0	0.00003	0.00014
38	C11	p	0.10932	0.18833	0.00376	0.02123	0.00209	0.0013
39	C11	d	0.00151	0.00409	0.00007	0.0049	0.00278	0.00291
40	H1	s	0.00002	0.00001	0.00005	0.00004	0.00065	0.00042
41	H1	p	0.00199	0.00347	0.00008	0.00057	0.00007	0.00007
42	H2	s	0.00011	0.00002	0.00002	0	0.00002	0
43	H2	p	0.00001	0.00017	0.00006	0.00251	0.00113	0.0012
44	H3	s	0.00028	0.00009	0.00006	0.00003	0.0019	0.00085
45	H3	p	0.00248	0.00539	0.00001	0.00001	0.00019	0.00018
46	H4	s	0.00012	0.00003	0.00005	0.00008	0.00077	0.00017
47	H4	p	0.00212	0.00239	0.0002	0.00165	0.00104	0.00063
48	H5	s	0.00008	0	0	0.00003	0.00014	0.00038
49	H5	p	0.00104	0.00168	0.00003	0.00028	0.00016	0.00014
50	H6	s	0	0.00002	0.00001	0.00004	0.00014	0.00004
51	H6	p	0.00003	0	0.00003	0.00064	0.00002	0.00018
52	H7	s	0.00001	0.00002	0.00004	0.00008	0.00029	0.00004
53	H7	p	0.00116	0.00245	0	0.00011	0.0003	0.0003
54	H8	s	0.00017	0.00003	0.00013	0.00019	0.00034	0.00057
55	H8	p	0.0007	0.00072	0.00009	0.00065	0.00002	0.00006
56	C12	s	0.00031	0.00002	0.00006	0.00129	0.0004	0.00035
57	C12	p	0.00963	0.01263	0.01457	0.05663	0.00855	0.03544
58	C12	d	0.00444	0.00192	0.00677	0.01682	0.00677	0.01153
59	C13	s	0.00015	0.00017	0.00001	0.00067	0.00027	0.00069
60	C13	p	0.10342	0.02081	0.13206	0.08633	0.03645	0.03752
61	C13	d	0.00235	0.00181	0.00425	0.00124	0.00009	0.00086
62	C14	s	0.0001	0.00004	0	0.00021	0.00003	0.00011
63	C14	p	0.12984	0.07058	0.21865	0.00646	0.0008	0.00697
64	C14	d	0.0012	0.00011	0.00135	0.00585	0.00206	0.00285
65	C15	s	0.00001	0	0	0.00004	0.00001	0.00001
66	C15	p	0.00036	0.00951	0.00285	0.11751	0.03318	0.05844
67	C15	d	0.00553	0.00225	0.00889	0.00007	0.00024	0.00006

68	C16	s	0.00001	0.00001	0	0.00002	0.00002	0.00013
69	C16	p	0.10937	0.02978	0.16408	0.01161	0.01173	0.00169
70	C16	d	0.00143	0.00151	0.00274	0.00584	0.0015	0.0033
71	C17	s	0.00006	0.00005	0.00003	0.00101	0.00045	0.00097
72	C17	p	0.09729	0.06193	0.16181	0.08554	0.0165	0.05634
73	C17	d	0.00199	0.00057	0.00296	0.00133	0.00052	0.0011
74	C18	s	0.00009	0	0.00001	0.00015	0.00014	0.00036
75	C18	p	0.01379	0.00678	0.0294	0.00347	0.01903	0.00933
76	C18	d	0.00402	0.00258	0.00694	0.00264	0.00047	0.00252
77	N2	s	0.00027	0.0001	0.00002	0.00006	0.00166	0.00165
78	N2	p	0.01573	0.00969	0.03879	0.01303	0.01082	0.01465
79	N2	d	0.00051	0.00032	0.00069	0.00152	0.00311	0.00234
80	C19	s	0.00002	0.00003	0.00001	0.0006	0.00051	0.00117
81	C19	p	0.0277	0.01619	0.01809	0.00862	0.0226	0.00452
82	C19	d	0.00196	0.00123	0.00376	0.0009	0.00074	0.00092
83	C20	s	0	0.00001	0	0.00008	0.00027	0.00005
84	C20	p	0.05039	0.0307	0.07721	0.01151	0.0012	0.01195
85	C20	d	0.00059	0.00039	0.00017	0.00035	0.0014	0.00028
86	C21	s	0.00001	0	0	0.00002	0.00001	0.00007
87	C21	p	0.00175	0.00128	0.00043	0.00392	0.02378	0.00599
88	C21	d	0.00287	0.00178	0.0038	0.00078	0.00012	0.0006
89	C22	s	0.00005	0.00001	0	0.00001	0.00004	0.00012
90	C22	p	0.05477	0.03407	0.0608	0.01298	0.00286	0.00695
91	C22	d	0.00018	0.00007	0.00056	0.00031	0.00138	0.00059
92	H9	s	0.00007	0	0	0.00018	0.00001	0.00039
93	H9	p	0.00102	0.00066	0.00108	0.00033	0.00009	0.00017
94	H10	s	0	0.00002	0	0.00005	0.00014	0.00004
95	H10	p	0.00003	0.00002	0.00001	0.00009	0.00059	0.00017
96	H11	s	0.00001	0.00006	0	0.00011	0.00024	0.00003
97	H11	p	0.00113	0.0007	0.00177	0.00031	0.00005	0.00034
98	H12	s	0.00016	0.00008	0.00009	0.00013	0.00044	0.00054
99	H12	p	0.00068	0.00042	0.0004	0.00021	0.00046	0.00006
100	H13	s	0.00002	0.00004	0.00002	0.0004	0.00033	0.00038
101	H13	p	0.002	0.00052	0.00306	0.00034	0.00029	0.00008
102	H14	s	0.00012	0.00004	0.00001	0.00002	0	0

103	H14	p	0.00001	0.00019	0.00005	0.00271	0.00076	0.00139
104	H15	s	0.00027	0.00012	0.00003	0.0014	0.00069	0.00074
105	H15	p	0.00242	0.00134	0.00415	0.00018	0.0000 2	0.00019
106	H16	s	0.00014	0.00006	0.00003	0.00044	0.00036	0.00014
107	H16	p	0.00215	0.00021	0.00239	0.00185	0.00079	0.00069
108	N3	s	0.00028	0.00004	0.0001	0.00154	0.00033	0.00154
109	N3	p	0.01445	0.01638	0.03359	0.01177	0.01287	0.01418
110	N3	d	0.00049	0.00036	0.00068	0.00307	0.00149	0.0023
111	C23	s	0.00002	0.00002	0.00003	0.00091	0.00014	0.00115
112	C23	p	0.02727	0.00369	0.03124	0.01058	0.02043	0.00418
113	C23	d	0.00183	0.00138	0.00374	0.001	0.00069	0.00091
114	C24	s	0	0	0.00001	0.00034	0.00001	0.00006
115	C24	p	0.0475	0.0254	0.08505	0.00413	0.009	0.01206
116	C24	d	0.0006	0.00002	0.00055	0.00065	0.0011	0.00025
117	C25	s	0.00001	0	0	0.00001	0.00001	0.00007
118	C25	p	0.00195	0.00113	0.00049	0.01079	0.01711	0.00536
119	C25	d	0.00273	0.00114	0.00457	0.00016	0.00074	0.00061
120	C26	s	0.00006	0	0.00002	0.00003	0.0000 3	0.0001
121	C26	p	0.05261	0.01628	0.08047	0.00089	0.01512	0.00715
122	C26	d	0.00016	0.0003	0.00035	0.00072	0.00097	0.00056
123	C27	s	0.00011	0	0	0.00024	0.0000 4	0.00037
124	C27	p	0.01267	0.01265	0.02477	0.01159	0.01103	0.00886
125	C27	d	0.00379	0.00243	0.00728	0.00058	0.00263	0.00246
126	C28	s	0.00006	0.00005	0.00003	0.00109	0.00026	0.00106
127	C28	p	0.09154	0.05464	0.17318	0.00927	0.093	0.05691
128	C28	d	0.00189	0.00138	0.00226	0.00051	0.00136	0.0011
129	C29	s	0.00031	0.00001	0.00004	0.00119	0.00052	0.00037
130	C29	p	0.00939	0.00303	0.02334	0.01311	0.05206	0.03586
131	C29	d	0.00418	0.00303	0.00587	0.00768	0.01538	0.01214
132	C30	s	0.00014	0.0000 8	0.00011	0.00066	0.00022	0.00072
133	C30	p	0.0977	0.06432	0.09536	0.01151	0.10948	0.03929
134	C30	d	0.00221	0.00134	0.0048	0.00024	0.00109	0.00085
135	C31	s	0.0000 8	0	0.00004	0.00012	0.00011	0.00012
136	C31	p	0.12214	0.07957	0.21639	0.00423	0.00331	0.00666
137	C31	d	0.00115	0.00084	0.0007	0.00076	0.00706	0.00297
138	C32	s	0	0.00001	0	0.00003	0.0000 2	0.00001

139	C32	p	0.00035	0.00003	0.0117	0.00158	0.14834	0.0596
140	C32	d	0.0052	0.00361	0.00786	0.00016	0.00015	0.00006
141	C33	s	0.00001	0	0.00001	0.00003	0	0.00014
142	C33	p	0.10291	0.07491	0.12658	0.00171	0.02121	0.00193
143	C33	d	0.00134	0.00076	0.00351	0.00038	0.00692	0.00336
144	H17	s	0.00002	0.00005	0.00001	0.00063	0.00007	0.0004
145	H17	p	0.00188	0.00142	0.0023	0.00004	0.00059	0.00009
146	H18	s	0.00012	0	0.00005	0.00001	0.00002	0
147	H18	p	0.00001	0	0.00023	0.00003	0.00342	0.00142
148	H19	s	0.0003	0	0.00011	0.00162	0.0004	0.00083
149	H19	p	0.00228	0.00151	0.0041	0.0001	0.00009	0.00018
150	H20	s	0.00011	0.00005	0.00005	0.00071	0.00012	0.00017
151	H20	p	0.00204	0.00136	0.00137	0.00045	0.00216	0.00073
152	H21	s	0.00007	0	0.00001	0.00006	0.00012	0.00039
153	H21	p	0.00098	0.00027	0.0015	0.00002	0.0004	0.00017
154	H22	s	0	0	0.00003	0.00019	0	0.00004
155	H22	p	0.00003	0.00003	0.00001	0.00028	0.00041	0.00015
156	H23	s	0.00001	0.00002	0.00005	0.00035	0.00001	0.00004
157	H23	p	0.00106	0.00058	0.00195	0.00014	0.00023	0.00034
158	H24	s	0.00018	0.00015	0.00003	0.00051	0.00004	0.00054
159	H24	p	0.00069	0.00012	0.00073	0.00015	0.00051	0.00005

Shell populations

The electron density of a molecule having N electrons is: $\rho(\vec{r}) = 2\sum_a^{N/2} |\psi_a(\vec{r})|^2$.

Expanding $\psi_a(\vec{r})$ in an atomic basis, *i.e.*, $\psi_a(\vec{r}) = c_{a\mu}\phi_\mu$ (implied summation), yields

$$\rho(\vec{r}) = 2\sum_a^{N/2} c_{a\mu}^* c_{a\nu} \phi_\mu^* \phi_\nu = 2\sum_a^{N/2} C_{a\mu\nu} \phi_\mu^* \phi_\nu.$$

The a^{th} MO contains 2 electrons, so integration and minor manipulation yields

$$1 = C_{a\mu\nu} \int d^3\vec{r} \phi_\nu \phi_\mu^* = C_{a\mu\nu} S_{\nu\mu} = (CS)_{a\mu\mu} = \text{Tr}(CS)_a,$$

where $S_{\nu\mu}$ is an overlap matrix element. Thus, $\text{Tr}(CS) = 1$. The distribution of electrons

in the a^{th} MO over the atomic orbitals is given by the diagonal elements.

Table B.8. Mulliken charges and spin density the S_0 equilibrium geometry

	atom	charge	spin density
1	Ir	0.078	0.672
2	N	0.873	0.003
3	C	-0.132	0.020
4	C	-0.402	0.014
5	C	-0.645	0.001
6	C	-0.351	0.003
7	C	-0.273	-0.008
8	C	0.378	0.033
9	C	0.333	-0.020
10	C	-0.149	0.035
11	C	-0.415	-0.005
12	C	-0.564	0.039
13	C	-0.279	-0.019
14	H	0.178	0.000
15	H	0.257	-0.002
16	H	0.260	0.000
17	H	0.266	-0.002
18	H	0.222	0.000
19	H	0.287	0.000
20	H	0.274	0.000
21	H	0.212	0.007
22	C	0.081	-0.020
23	C	-0.133	0.039
24	C	-0.273	-0.006
25	C	-0.543	0.045
26	C	-0.448	-0.022
27	C	0.339	0.038
28	C	-0.097	-0.007
29	N	0.827	0.004
30	C	-0.107	0.020
31	C	-0.394	0.014
32	C	-0.592	0.001
33	C	-0.281	0.004
34	H	0.230	0.000
35	H	0.288	0.000
36	H	0.275	-0.001
37	H	0.198	0.007
38	H	0.164	0.000
39	H	0.260	-0.002

40	H	0.260	0.000
41	H	0.255	-0.002
42	N	0.810	0.005
43	C	-0.089	0.017
44	C	-0.443	0.018
45	C	-0.720	-0.001
46	C	-0.631	-0.002
47	C	0.224	-0.014
48	C	0.467	0.045
49	C	0.147	-0.011
50	C	-0.241	0.037
51	C	-0.314	-0.008
52	C	-0.532	0.047
53	C	-0.319	-0.019
54	H	0.171	0.000
55	H	0.258	-0.002
56	H	0.261	0.001
57	H	0.253	-0.002
58	H	0.219	0.000
59	H	0.287	0.000
60	H	0.273	-0.001
61	H	0.204	0.006

Table B.9. Mulliken charges and spin density the T₁ equilibrium geometry

	atom	charge	spin density
1	Ir	0.205	0.582
2	N	0.909	0.001
3	C	-0.157	0.013
4	C	-0.368	0.013
5	C	-0.786	-0.002
6	C	-0.548	-0.003
7	C	0.305	-0.013
8	C	0.688	0.031
9	C	0.019	0.002
10	C	-0.292	0.040
11	C	-0.182	-0.010
12	C	-0.807	0.033
13	C	-0.340	-0.011
14	H	0.172	0.000
15	H	0.251	-0.001
16	H	0.258	0.001
17	H	0.266	-0.002
18	H	0.213	0.000
19	H	0.285	0.000
20	H	0.270	0.000
21	H	0.215	0.004
22	C	0.361	-0.024
23	C	-0.139	0.011
24	C	-0.380	0.002
25	C	-0.517	0.001
26	C	-0.462	-0.006
27	C	0.276	0.000
28	C	-0.249	0.004
29	N	0.856	0.003
30	C	-0.143	0.016
31	C	-0.373	0.003
32	C	-0.613	0.008
33	C	-0.267	-0.001
34	H	0.224	0.001
35	H	0.288	0.000
36	H	0.272	0.000
37	H	0.227	0.006
38	H	0.164	0.000
39	H	0.252	0.000

40	H	0.256	0.000
41	H	0.247	0.000
42	N	0.776	0.032
43	C	-0.108	0.001
44	C	-0.435	0.050
45	C	-0.659	-0.011
46	C	-0.567	0.027
47	C	0.078	-0.034
48	C	0.441	0.125
49	C	-0.123	0.004
50	C	-0.098	0.059
51	C	-0.221	-0.017
52	C	-0.610	0.113
53	C	-0.302	-0.042
54	H	0.181	0.001
55	H	0.267	-0.005
56	H	0.272	0.000
57	H	0.258	-0.003
58	H	0.220	-0.001
59	H	0.289	0.000
60	H	0.276	-0.002
61	H	0.205	0.005

Table B.10. Mulliken charges and spin density the D_0 equilibrium geometry

	atom	charge	spin density
1	Ir	0.166	0.606
2	N	0.769	0.014
3	C	-0.105	0.016
4	C	-0.430	0.003
5	C	-0.532	0.006
6	C	-0.312	0.000
7	C	-0.284	-0.016
8	C	0.280	0.025
9	C	0.218	-0.027
10	C	-0.073	0.019
11	C	-0.512	-0.004
12	C	-0.482	0.031
13	C	-0.310	-0.016
14	H	0.178	0.000
15	H	0.256	-0.001
16	H	0.258	0.000
17	H	0.233	-0.002
18	H	0.222	0.001
19	H	0.290	0.000
20	H	0.271	0.000
21	H	0.205	0.006
22	C	-0.252	0.015
23	C	-0.308	0.097
24	C	-0.136	-0.031
25	C	-0.722	0.126
26	C	-0.285	-0.026
27	C	0.747	0.095
28	C	0.299	-0.024
29	N	0.784	0.001
30	C	-0.117	0.012
31	C	-0.385	0.020
32	C	-0.649	-0.004
33	C	-0.635	0.009
34	H	0.218	-0.001
35	H	0.286	0.000
36	H	0.274	-0.001
37	H	0.190	0.003
38	H	0.177	0.001
39	H	0.264	-0.005

40	H	0.269	0.001
41	H	0.262	-0.004
42	N	0.938	0.000
43	C	-0.150	0.008
44	C	-0.355	0.007
45	C	-0.663	0.004
46	C	-0.301	-0.001
47	C	-0.325	0.010
48	C	0.543	-0.006
49	C	0.596	0.016
50	C	-0.370	0.019
51	C	-0.350	0.001
52	C	-0.554	-0.001
53	C	-0.492	-0.005
54	H	0.169	0.000
55	H	0.253	0.000
56	H	0.259	0.002
57	H	0.224	-0.001
58	H	0.220	0.001
59	H	0.285	0.000
60	H	0.270	0.000
61	H	0.212	0.004

Table B.11. BNL TDDFT excited states – S_0 equilibrium geometry

S_n	$E(S_n)$	f (oscillator strength)
1	2.69	0.004
2	2.80	0.006
3	2.81	0.006
4	3.03	0.007
5	3.04	0.059
6	3.05	0.061
7	3.15	0.007
8	3.20	0.022
9	3.20	0.026
10	3.27	0.009
11	3.27	0.008
12	3.34	0.043
13	3.41	0.045
14	3.41	0.048
15	3.62	0.007
16	3.67	0.008
17	3.67	0.008
18	3.72	0.017
19	4.06	0.001
20	4.26	0.001
21	4.26	0.001
22	4.33	0.074
23	4.33	0.073
24	4.36	0.103
25	4.38	0.126
26	4.48	0.003
27	4.48	0.004
28	4.49	0.007
29	4.50	0.003
30	4.50	0.115
31	4.55	0.010
32	4.57	0.038
33	4.58	0.039
34	4.63	0.068
35	4.63	0.041
36	4.63	0.031
37	4.66	0.030
38	4.66	0.032

39	4.70	0.014
40	4.71	0.011
41	4.71	0.013
42	4.73	0.034
43	4.74	0.035
44	4.74	0.040
45	4.75	0.001
46	4.76	0.019
47	4.78	0.000
48	4.79	0.001
49	4.79	0.001
50	4.82	0.035
51	4.83	0.041
52	4.85	0.013
53	4.86	0.019
54	4.90	0.014
55	4.95	0.001
56	4.96	0.004
57	4.96	0.004
58	4.97	0.002
59	4.98	0.003
60	4.99	0.014
61	5.01	0.029
62	5.01	0.035
63	5.02	0.034
64	5.03	0.008
65	5.03	0.002
66	5.05	0.031
67	5.05	0.002
68	5.06	0.003
69	5.08	0.001
70	5.08	0.003
71	5.08	0.002
72	5.10	0.110
73	5.11	0.003
74	5.13	0.004
75	5.14	0.003
76	5.15	0.003
77	5.16	0.029
78	5.16	0.004
79	5.17	0.014
80	5.17	0.014

81	5.18	0.024
82	5.18	0.029
83	5.25	0.080
84	5.25	0.025
85	5.25	0.075
86	5.27	0.024
87	5.27	0.004
88	5.27	0.005
89	5.28	0.001
90	5.31	0.030
91	5.31	0.035
92	5.32	0.001
93	5.32	0.000
94	5.35	0.003
95	5.36	0.058
96	5.37	0.025
97	5.38	0.021
98	5.39	0.049
99	5.39	0.051
100	5.40	0.003
101	5.42	0.002
102	5.44	0.014
103	5.44	0.021
104	5.45	0.010
105	5.46	0.011
106	5.46	0.004
107	5.47	0.009
108	5.47	0.015
109	5.47	0.007
110	5.48	0.002
111	5.49	0.012
112	5.49	0.008
113	5.50	0.009
114	5.51	0.049
115	5.52	0.001
116	5.53	0.000
117	5.57	0.030
118	5.57	0.003
119	5.57	0.002
120	5.59	0.012
121	5.59	0.012
122	5.60	0.037

123	5.62	0.001
124	5.62	0.000
125	5.63	0.002
126	5.64	0.002
127	5.64	0.002
128	5.65	0.000
129	5.66	0.002
130	5.66	0.002

Table B.12. ω B97X TDDFT excited states – S_0 equilibrium geometry

S_n	$E(S_n)$	f (oscillator strength)
1	3.80	0.054
2	3.80	0.057
3	3.82	0.091
4	4.21	0.094
5	4.21	0.098
6	4.30	0.007
7	4.34	0.011
8	4.34	0.013
9	4.39	0.016
10	4.50	0.030
11	4.58	0.028
12	4.58	0.029
13	4.86	0.073
14	4.86	0.073
15	4.94	0.353
16	4.98	0.112
17	4.98	0.120
18	5.04	0.071
19	5.21	0.008
20	5.21	0.006
21	5.23	0.074
22	5.35	0.050
23	5.35	0.048
24	5.40	0.071
25	5.51	0.006
26	5.52	0.006
27	5.60	0.001
28	5.62	0.057
29	5.62	0.062
30	5.63	0.047
31	5.64	0.009
32	5.65	0.018
33	5.69	0.018
34	5.90	0.080
35	5.90	0.067
36	5.92	0.104
37	5.93	0.116
38	5.94	0.102

39	5.98	0.119
40	6.00	0.074
41	6.01	0.072
42	6.01	0.030
43	6.08	0.124
44	6.09	0.007
45	6.09	0.005
46	6.19	0.012
47	6.20	0.012
48	6.22	0.019
49	6.31	0.032
50	6.31	0.040

Table B.13. Calculated vibrational frequencies for the S_0 geometry. B3LYP – lanl2dz for Ir, 6-31+G* for all other atoms

Mode	frequency
1	i45.71
2	i45.5
3	i31.62
4	i15.55
5	i12.66
6	13.51
7	51.8
8	53.11
9	55.48
10	95.55
11	96.75
12	104.85
13	147.79
14	162.23
15	166.15
16	178.82
17	195.22
18	197.62
19	227.27
20	229.84
21	257.11
22	266.85
23	269.46
24	273.31
25	279.17
26	301.97
27	303.68
28	376.2
29	378.14
30	386.55
31	421.19
32	421.55
33	425.02
34	440.56
35	441.68
36	448.04
37	485.28

38	488.06
39	489.97
40	512.34
41	512.93
42	513.94
43	568.33
44	568.87
45	571.18
46	645.03
47	645.7
48	647.46
49	652.32
50	655.23
51	656.32
52	679.75
53	680.52
54	686.75
55	742.09
56	744.14
57	746.41
58	750.22
59	751.1
60	751.19
61	759.41
62	761.96
63	765.22
64	779.31
65	780.25
66	782.48
67	815.83
68	817.48
69	820.12
70	884.77
71	887.02
72	890.98
73	891.13
74	892.58
75	895.6
76	952.43
77	956.09
78	959.22
79	966.58

80	975.33
81	977.65
82	997.69
83	999.01
84	1002.07
85	1004.18
86	1007.79
87	1010.39
88	1040.69
89	1041.86
90	1044.05
91	1046.39
92	1047.09
93	1048.33
94	1062.66
95	1063.96
96	1072.63
97	1092.63
98	1095.28
99	1096.01
100	1098.84
101	1102.87
102	1107.81
103	1142.51
104	1144.18
105	1148.8
106	1165.5
107	1166.18
108	1168.43
109	1192.79
110	1194.31
111	1196.58
112	1203.21
113	1203.51
114	1208.13
115	1289.13
116	1294.43
117	1297.6
118	1319.67
119	1321.21
120	1324.51
121	1335.97

122	1338.41
123	1343.4
124	1363.85
125	1364.52
126	1365.71
127	1378.56
128	1378.71
129	1378.96
130	1475.47
131	1476.54
132	1477.56
133	1492.54
134	1494.33
135	1494.51
136	1506.21
137	1507.1
138	1510.26
139	1531.31
140	1534.57
141	1535.97
142	1618.55
143	1619.46
144	1620.15
145	1643.24
146	1644.34
147	1645.29
148	1660.05
149	1661.48
150	1663.72
151	1677.87
152	1679.06
153	1679.9
154	3179.66
155	3180.92
156	3181.78
157	3187.14
158	3188.89
159	3189.55
160	3203.51
161	3203.88
162	3205.65
163	3206.89

164	3207.59
165	3209.33
166	3211.78
167	3212.12
168	3213.43
169	3214.37
170	3215.06
171	3217.6
172	3238.08
173	3238.5
174	3240.07
175	3243.1
176	3244.84
177	3248.86

Appendices References

1. Atkins, P. W.; Friedman, R. S. *Molecular Quantum Mechanics*, 4th ed; Oxford University Press: New York, NY, **2005**.
2. Szabo, A.; Ostlund, N. S. *Modern Quantum Chemistry: Introduction to Advanced Electronic Structure Theory*; Dover Publications: Mineola, NY, **1996**.
3. Koch, W.; Holthausen, M. C. *A Chemist's guide to Density Functional Theory*, 2nd ed; Wiley-VHC Verlag: Weinheim, Germany, **2002**.
4. Car, R. *Quant. Struct.-Act. Relat.* **2002**, *21*, 97.
5. Sun, Y. Y.; Lee, K.; Wang, L.; Kim, Y.; Chen, W.; Chen, Z.; Zhang, S. B. *Phys. Rev. B* **2010**, *82*, 073401.
6. Argaman, N.; Makov, G. *Amer. J. Phys.* **2000**, *68*, 69.
7. Hohenberg, P.; Kohn, W. *Phys. Rev.* **1964**, *136*, B864.
8. Kohn, W.; Sham, L. J. *Phys. Rev.* **1965**, *140*, A1133.
9. Parr, R. G.; Yang, W. *Density Functional Theory of Atoms and Molecules*; Oxford University Press: New York, NY, **1989**.
10. Stephens, P. J.; Devlin, J. F.; Chabalowski, C. F.; Frisch, M. J. *J. Phys. Chem.* **1994**, *98*, 11623.
11. Becke, A. D. *J. Chem. Phys.* **1993**, *98*, 5648.